SYNTHESIS OF ANISOTROPIC NANOSTRUCTURES AT THE AIR-WATER INTERFACE AND THEIR CHARACTERIZATION

RENU PASRICHA

UNDER THE GUIDANCE OF

Dr. MURALI SASTRY

CENTRE FOR MATERIAL CHARACTERIZATION

NATIONAL CHEMICAL LABORATORY

PUNE 411 008

INDIA

MARCH 2007

SYNTHESIS OF ANISOTROPIC NANOSTRUCTURES AT THE AIR-WATER INTERFACE AND THEIR CHARACTERIZATION

THESIS SUBMITTED TO

UNIVERSITY OF PUNE

FOR THE DEGREE OF

DOCTOR OF PHILOSOPHY

IN

PHYSICS

BY

RENU PASRICHA

CENTRE FOR MATERIAL CHARACTERIZATION
NATIONAL CHEMICAL LABORATORY
PUNE-411008
INDIA

MARCH 2007

Dedicated to my
husband Kamal and my children
Kanika and Aneesh

CERTIFICATE

This is to certify that the work discussed in the thesis entitled **"SYNTHESIS OF ANISOTROPIC NANOSTRUCTURES AT AIR-WATER INTERFACE AND THEIR CHARACTERIZATION**.**"** by **RENU PASRICHA** submitted for the degree of *Doctor of Philosophy in Physics* was carried out under my supervision at the Centre for Material Characterization and the Materials Chemistry Divisions of the National Chemical Laboratory, Pune, India. Such materials as have been obtained by other sources have been duly acknowledged in this thesis. To the best of my knowledge, the present work or any part there of, has not been submitted to any other University for the award of any other degree or diploma.

Date:
Place: Pune

Dr. Murali Sastry
(Research Guide)

CANDIDATE'S DECLARATION

I, Renu Pasricha, hereby declare that the work incorporated in this thesis entitled **"SYNTHESIS OF ANISOTROPIC NANOSTRUCTURES AT AIR-WATER INTERFACE AND THEIR CHARACTERIZATION."** submitted for the degree of *Doctor of Philosophy in Physics* has been carried out by me at the Centre for Material Characterization and the Materials Chemistry Divisions of the National Chemical Laboratory of the National Chemical Laboratory, Pune, India under the joint supervision of Dr. Murali Sastry. Such materials as have been obtained by other sources have been duly acknowledged in this thesis. The work is original and has not been submitted in part or full by me for award of any other degree or diploma in any other University.

Date: **Renu Pasricha**
Place: Pune (Research Student)

No duty is more urgent than that of returning thanks.
Saint Ambrose

ACKNOWLEDGEMENT

A journey is easier when you travel together. This thesis is the result of the work in which I have been accompanied and supported by many people. I take this opportunity to acknowledge them and extend my sincere gratitude for helping me make this Ph.D. thesis a possibility.

"For the things we have to learn before we can do them, we learn by doing them." "But to succeed... You need to find something to hold on to, something to motivate you, something to inspire you." To me, Dr. Murali Sastry has provided the utmost inspiration and motivation to take up the challenge of entering an alien field and completing the task presented here. It is a pleasant opportunity for me to express my gratitude and my sincere thanks to my mentor for introducing me to the wonderful field of nanoscience and providing me with an opportunity and resources to work under his valuable guidance. His ceaseless enthusiasm, constructive criticism, benign attention, dedication to work has had a profound influence on me. Working with him, I have learned to tackle science in an enjoyable manner. I can hardly express my gratitude to him for adjusting the sails of my professional life smoothly and giving it a direction. "Motivation is the art of getting people to do what you want them to do because they want to do it." His motivation in the right direction has led to what I am able to present today. In my association with him over the past six years I have seen his enthusiasm and dedication touching and inspiring a number of students. And I hope the journey continues….. Thanks for everything, Sir……

I'm grateful to Dr. S. Sivaram, Director, NCL, Pune for providing me with the opportunity and by permitting me to carry out the research work.

My special words of thanks should also go to Dr. Mohan Bhadbade, Head CMC for always being so kind, helpful and motivating. He has always been there for me whenever I needed it the most. His constant guidance, sincerity, patience, cooperation and support have always kept me going. I owe him a lot of gratitude for always being there for me and I feel privileged to be associated with a person like him during my life.

I am highly indebted to Dr. Sainkar former Head CMC for his advice, support and permission to use all the available facilities in the division and for his constant encouragement.

It is indeed a pleasure to thank Dr. Rajeev Kumar and Dr. Ogale for their constant support and encouragement all through. It was always good to know that they are there for all the guidance and help I needed.

I am grateful to Dr. Ganesh for being in the referee panel despite his busy schedule. I express my heart-felt gratitude to Dr. Absar Ahmad for being a wonderful colleague, a dear friend and for his constant support during the course of my thesis.

I wish to thank Dr. A. B. Mandale, Dr. Patil and Dr. Mitra for all the prompt XPS characterizations required during my research work. I am grateful to the entire staff of the Center for Materials Characterization, NCL, which is like an extended family for me, for having provided me with their help, support and encouragement.

I am honored to have an innumerable number of friends and well wishers here in NCL. I would like to express my appreciation to my friends and colleagues, Rajesh and Dr Prasad for their patience and support at all times and their valuable scientific suggestions. I wish to thank my other colleagues at NCL: Dr. Shubhangi, Dr. Dongre, Ms Anuya, Dr. Veedavati Puranik Dr. Guru, Dr. Ashish, Dr. Mula, Dr. Veda, Manoj, for their wonderful company. Mr Gholap needs a special word of

appreciation for his help in sharing the responsibility of running the microscopy facility and giving me ample time to finish writing my thesis work.

I would like to take this opportunity to thank all my lab mates and the members of the nanoscience group who have helped me in all possible ways. Thank-you, Dr.Ashvani, Dr. Anand, Dr. Saikat, Dr. Sumant, Dr. Debabrata, Dr. Kannan, Dr. Shankar, Dr. Anita, Hrushikesh, Minakshi, Ambarish, Tanushree, Akhilesh, Vipul, Sourabh, Atul, Ritwik, Neeta, Mrs Suguna, Neha, Sudershan, Priyanka, Maggi, Sanjay for giving me the feeling of being at home in the lab. A very special thanks to Manasi, Pratap , Amit, Deepti, Dr Sumant and Dr Anita for spending their valuable time proof-reading the chapters and suggesting valuable corrections in the thesis. I am grateful to Amit , Dr. Anita, Dr. Kannan and Pratap for their support in the experimental work and making work a pleasure. Thank you, Dr. Ashvani and Dr. Sumant for encouraging me to take up the task.

The cooperation I received from other faculty members and support staff of the Centre of Material Characterization especially Mr. Gangophadyaye is gratefully acknowledged. I will be failing in my duty if I do not mention the library staff and administrative staff of NCL for their timely help.

I would like to acknowledge my other friends for their moral support and motivation, which drives me to give my best. Suman, Vinita, Suren, Amita, Vijay, Shaarda, Priya, Sashank, Savita, Sunil, Sadhak, Kumud, Poonam, Srikant, Seema, Harpal, Sushma, Ruta, Asha, ….the list is endless…thanks to one and all. I find myself lucky to have friends like them in my life.

My acknowledgement will never be complete without the special mention of Mr M.D. Nair, for teaching me, "Nothing is impossible in life, success is just a hand away; all you need to do is stretch your arm."

The thesis could not have been completed without the endless love and blessings from my family. I wish to thank my parents, who taught me the value of integrity, hard work and discipline,, my husband, who rendered me enormous support during the whole tenure of my research work, my children , Kanika and Aneesh for their endless patience and unconditional love during the period of thesis writing. I also wish to thank my brothers, my co-sisters, brother-in law and sister-in laws, uncles and aunts for their unwavering faith in my capabilities, which has always encouraged me to go ahead, especially during difficult times. I should also thank my late mother-in-law, who I feel must be giving her blessing to me all along the course of this work. My heartfelt thanks to my uncle, Mr Kuldarshan, for showing undoubting faith in me and my efforts..

Last but not the least, my housekeeper, Joyce deserves a special mention for running the house smoothly during my busy schedule..

The chain of my gratitude would be definitely incomplete if I forget to thank the first cause of this chain. I thank the Almighty for giving me the strength and patience to work through all these years so that today I can stand proud with my head held high.

-- Ms. Renu Pasricha
March, 2007

Table of Contents

Chapter I: Introduction

Chapter II: Characterization techniques

Chapter III: Assembly of hydrophobized gold nanoparticles at the air-water interface by varying the surface tension

List of Publications

Chapter 1

Introduction

By far the best proof is experience (Francis Bacon)

This chapter provides an introduction to the thesis by describing the stimulating properties of material in the nano-regime and then moves onto a brief overview about synthesis of nanoparticles by different methods. It gives a brief outline on the importance of anisotropic nanostructures with respect to their properties and efforts that have been made to synthesize them. It then moves to the interest and ways to assemble nanoparticles in two-dimensional (2D) and three-dimensional (3D) ordered structures. The work in the thesis is mainly based on assembly and synthesis of anisotropic nanostructures at air-water interface. The chapter finally illustrates the chapter-wise description of the work.

"The difference with nano is in the approach to doing things. Nano is more like what nature does in building things from the ground up, rather than from the top down, as we have done in the past. Traditionally, we have taken a piece of bulk material and milled it down into a product. With nano, we build things atom by atom, molecule by molecule. So there's a basic difference in the approach. We've seen some surprises. And we expect to see more as this technology develops."

Dr. Diehl

Size Matters! Shape Matters too!!

1.1 Nanoscience

"Nanoscience" is the area of science where the dimensions play a critical role. It is the science of objects that are intermediate in size between the largest molecules and the smallest structures that can be fabricated by current photolithography; i.e. the science of objects with smallest dimensions ranging from a few nanometers to less than 100 nanometers [1-3]. In *chemistry*, this range of sizes has historically been associated with colloids, micelles, polymer molecules, phase-separated regions in block copolymers, and similar structures. More recently, structures such as buckytubes, silicon nanorods, and compound semiconductor quantum dots have emerged as interesting classes of nanostructures. In *physics*, nanoscience is most often associated with quantum behavior, and the behavior of electrons and photons in nanoscale structures. *Biology and biochemistry* also have a deep interest in nanostructures as components of the cell; many of the most interesting structures in biology—from DNA and viruses to subcellular organelles and gap junctions—can be considered as nanostructures [4, 5].

The term "nano" comes from a Greek prefix, meaning dwarf. A nanometer is one billionth of a meter. Nanoscale objects have atleast one dimension that measures between 1-99 nm. Nanotechnolgy, the art of building machines one atom at a time was first described by Nobel laureate physicist Richard Feynman in 1959, when he described the future in a ground breaking talk about the physical possibilities for "making, manipulating, visualizing and controlling things on a small scale," and imagining that in decades to come, it might be possible to arrange atoms "the way we want". He was the one to suggest that the laws of physics would allow people to use small to make smaller machines eventually onto the atomic level [6]. However, Norio Taniguchi gave the term 'nanotechnology' [7] for the colloidal particles. Ever since the report of Faraday [6], several different approaches have been developed towards the synthesis of colloidal noble metal nanoparticles by physical, chemical and biological routes.

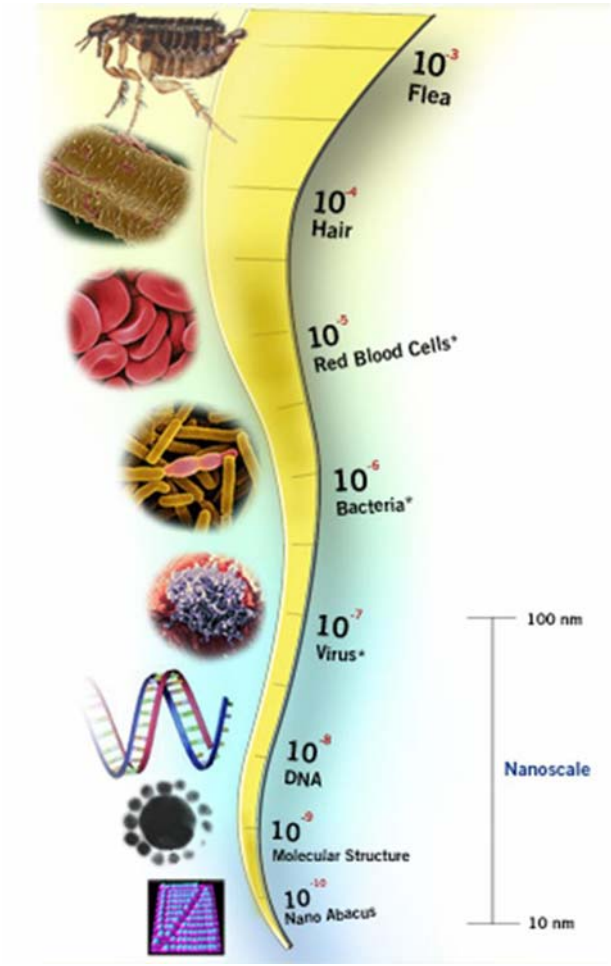

Figure 1.1 *Picture represents the relative sizes of various naturally occurring objects/ species in meters. Courtesy: Dennis Kunkel Microscopy Inc.*

These very small structures (Fig 1.1) are intensely interesting for many reasons [1b]. *First*, many of their properties mystify and excite us. How do the gold nanoparticles have different colours [8]? How do electrons move through organometallic nanowires [9]? *Second*, they are challenging to make. Molecules are easily synthesized in large quantities, and can be characterized thoroughly. Colloids and micelles and crystal nuclei have always been more difficult to prepare and to characterize; developing a "synthetic chemistry" of colloids that is as precise as that used to make molecules is a wonderful challenge for chemistry [10,11]. Synthesizing or fabricating ordered arrays and patterns of colloids poses a different and equally fascinating set of problems [12]. *Third*, because many nanoscale structures have been inaccessible, studying these structures leads to new

phenomena [13-15]. Very small particles, or large, ordered, aggregates of molecules or atoms, are simply not structures that science has been able to explore carefully. *Fourth*, nanostructures are in a range of sizes in which quantum phenomena would be expected to be important. [16]. *Fifth*, the nanometer-sized, functional structures that carry out many of the most sophisticated tasks of the cell are one frontier of biology. *Sixth*, nanostructures will be the basis of nanoelectronics and –photonics [17, 18] and will be a part of the revolution in the field.

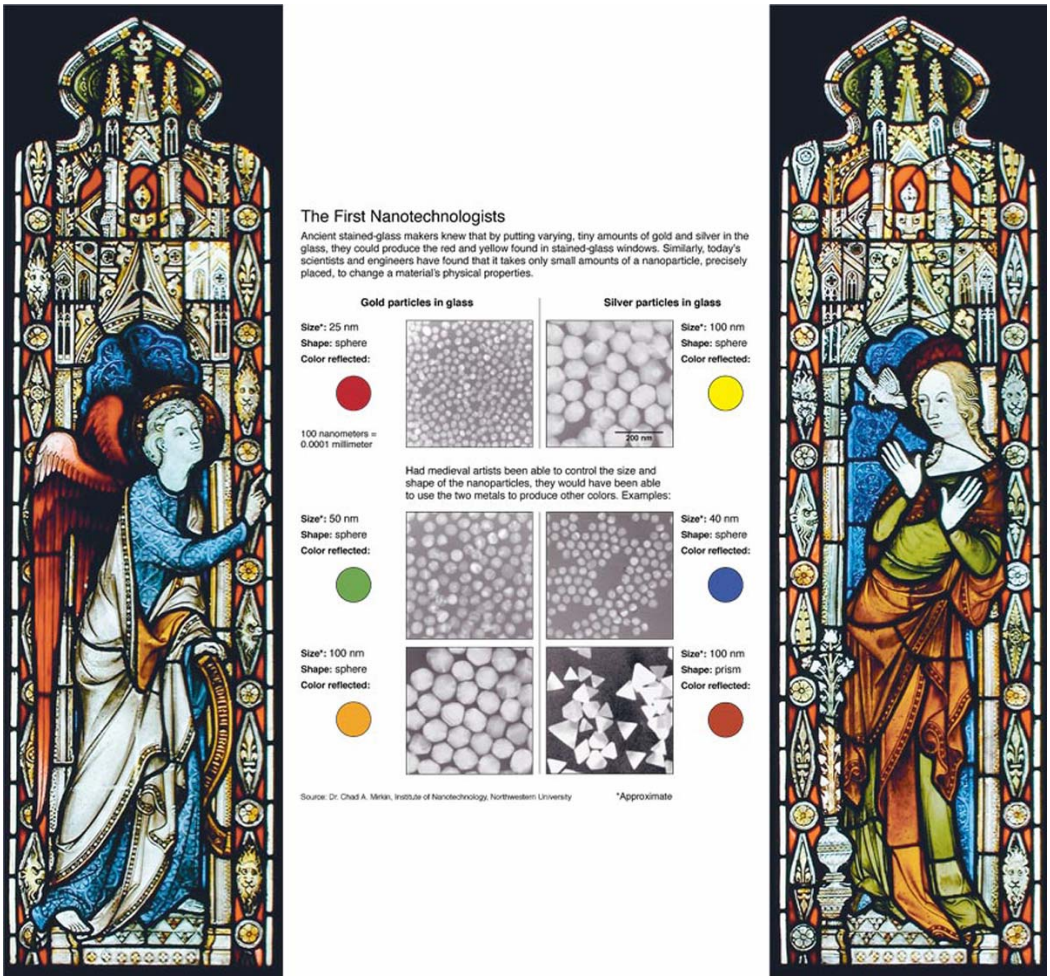

Figure 1.2 *Picture of a wall from the Medieval Ages showing the use of gold and silver colloids. Source: Dr Chad A. Mirkin, Institute of Nanotechnology, Northwestern University.*

The fascination started about 4000 years back, but is it only recently that the interesting terms like Nanoparticles, Nanostructures, Nanoscience and Nanotechnology

have become the most frequently used terms in material science. The earliest preparations of nanoparticles, particularly colloidal gold, date back to the early Vedic period in India, some 4000 years ago [19]. Interestingly, the applications of the so-called gold bhasma were medicinal. Besides the medicinal properties, we do have a very prominent example of the use of metallic nanoparticles, gold and silver in the Medieval Ages because of their colorful colloidal solutions [20] as seen in Fig 1.2. They were used as pigments to give brilliant ruby red and yellow colors to the paintings and stained glasses used in cathedrals at that time. It was not only the noble matels, but during the Middle Ages, the Muslims who fought crusaders with swords of Damascus steel had an edge - a very high-tech one. Their sabres contained carbon nanotubes. The researchers think that the sophisticated process of forging and annealing the steel formed the nanotubes and the nanowires, and could explain the amazing mechanical properties of the swords [21].

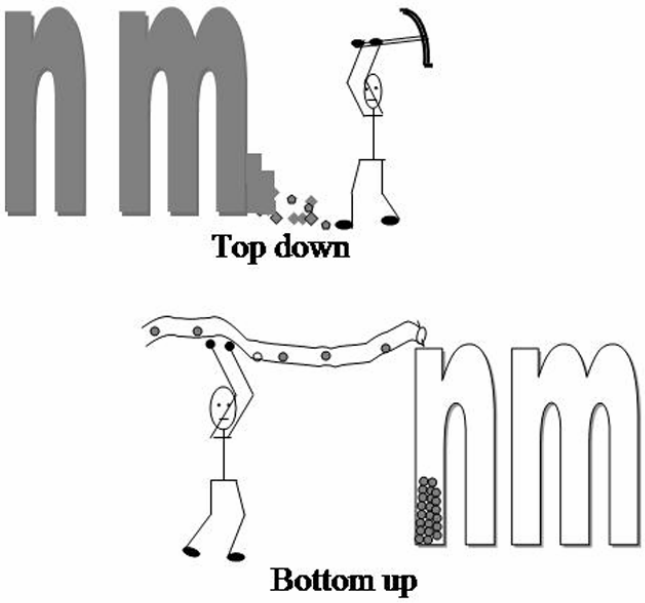

Fig 1.3 *Top down and Bottom up approach: Courtesy "Nanochemistry" by Ozin and Arsenault*

Top–down [22] and Bottom–up [23] are the two approaches that have been used for the synthesis of nanomaterials, fig 1.3. Top–down approach involves mainly physical methods where a bulk material is sliced into pieces till the desired size is achieved. Lithographic techniques, laser induced chemical etching and ball milling fall in to this

category [22]. However, these methods are effective only down to the micrometer level. Reaching nanometer scale makes these methods more expensive and technically difficult. The bottom–up approaches mainly involve chemical and biological methods to make nanostructures and nanoparticles. These involve controlled condensation of solute molecules that is formed during a chemical reaction. The restriction of the condensation or the growth leads to the formation of particles of desired size and shape [1b, 23]. However unlike the chemical synthesis of molecules of a desired structure, the synthesis of nanomaterials with uniform size and shape is difficult. Thus, large scale synthesis of nanomaterials remains a challenge.

In attempts to create miniaturized materials it has been realized that materials in nanodimensions exhibit properties very different to their bulk counterparts. Increasing knowledge about the unique properties of nanoparticles has lead to renewed interest in them for potential applications. The applications of nanoparticles extend to wide-ranging areas such as catalysis [24], biosensors [25], diagnostics [26], cell labeling [27], solar cells [28], fuel cells [29], photonic bandgap materials [30], single electron transistors [31], nonlinear-optical devices [32] and surface enhanced Raman spectroscopy [33]. The realization of their various potential applications is only limited by our imagination [34]. In the case of nanomaterials, the size [35], shape [36], surface composition [37], dielectric environment of the particle [38] and the interparticle interactions [39] are the key factors that can modulate the chemical, optical, magnetic and electronic properties.

1.2 Properties of metal nanoparticle

As stated above, the first and foremost reason of fascination with nanomaterials is their properties. The structural arrangement of atoms and the length scales of the material are the two important parameters, which when tuned properly at the nanometer scale, could lead to variation in the properties of the material [40], compared to its bulk. With material properties being characterized by the length scale of a material, fabricating materials with at least one dimension in the nanometer scale confines the electronic structure in that dimension. Consequently the confinement of electronic

structure becomes a function of the size and shape of the material. Hence any variation in size and shape of the material may manifest itself as a property change.

1.2.1 High surface-to-volume ratio (S/V)

Two key factors controlling the properties of nanomaterials are the size and surface characteristics of nanoparticles [41]. These two factors are interrelated because the *S*/*V* ratio increases as the size decreases. For a spherical particle, the *S*/*V* ratio is inversely proportional to its radius, *R* (*S*/*V*= 3/*R*). It is clear that the surface of nanoparticles plays an important role in their fundamental properties, from structural transformation via light emission to solubility. The surface atoms are chemically more active compared to the bulk atoms because they usually have fewer adjacent coordinate atoms and unsaturated sites or more dangling bonds. At the same time, the imperfection of the particle surface induces additional electronic states in the band gap, which act as electron or hole trap centers. As the size of the materials decreases, the surface to-volume ratio increases and the surface effects become more apparent and thereby easier to explore. In addition, the surface states near the gap can mix with the intrinsic states to a substantial extent, and these effects may also influence the spacing of the energy levels of nanoparticles [41]. In a system containing only a few hundred atoms, a large fraction of these atoms will be located on the surface. Because surface atoms tend to be coordinatively unsaturated, there is a large energy associated with this surface.

1.2.2 Size and shape dependant catalytic properties

The field of nanocatalysis (in which nanoparticles are used to catalyze reactions) has undergone an exponential growth during the past decade. As nanoparticles have a large surface-to-volume ratio compared to bulk materials, they are attractive to use as catalysts, catalysis being a surface phenomenon. The potential of using different shapes to catalyze different reactions has been discussed by El-Sayed and coworkers [42]. Recently, it has been shown that the activities of platinum nanoparticles of different shapes are indeed different for the same electron-transfer reaction in colloidal solution [43]. This potential shape dependent catalysis adds to the advantage of using nanoparticles as catalysts. In addition to being small they have corners and edges, this

makes the surface atoms of the nanoparticles unstable during the chemical reaction they catalyze, and the shape changes could occur [44]. The reactant molecules also show differential affinity in adsorption towards different faces of the catalyst. Hence metal nanoparticles of different shapes covered by different faces could be used to increase the selectivity of a catalyst [45]. Hydrogenation reactions [46-50] are the most common reactions that have been conducted using transition metal nanoparticles in colloidal solution.

1.2.3 Mechanical properties

Mechanical properties of a material depend strongly on the density of dislocations, grain size and the surface interface-to-volume ratio. The strength and hardness of the material could be severely affected if any decrease in grain size. As compared to the bulk, a nanoparticle has more defects due to the high surface to volume ratio. However the capability of a nanomaterial to undergo extensive tensile deformation without destroying the structure is well reported and is called superplasticity. Grain boundary diffusion and sliding observed in nanomaterials are the two key requirements for superplasticity [51].

1.2.4 Magnetic properties

The magnetic properties of nanoparticles differ from those of bulk in two ways. The large surface to volume ratio results in a different local environment for the surface atoms in their magnetic coupling / interaction with neighboring atoms, leading to the mixed volume and surface magnetic characteristics. Unlike bulk ferromagnetic materials, which usually form multiple magnetic domains, several small ferromagnetic particles could consist of only a single magnetic domain. In the case of a single particle being a single domain, the superparamagnetism occurs, in which the magnetizations of the particles are randomly distributed and they are aligned only under an applied magnetic field, and the alignment disappears once the external field is withdrawn. These could have important implications and for example, in ultra-compact information storage where the size of the domain determines the limit of storage density [52].

1.2.5 Biocompatibility

One of the important aspects in the study of nanoscience and nanotechnology is to assess the cytotoxicity levels of nanoparticles in living systems. Nanoparticles have been used for various biological applications and otherwise [53]. They have found potential future in the fields of biodiagonostics [54], therapeutics [55], drug delivery [56], bioimaging [57], immunostaining [58] and biosensing [59]. Thus, it becomes an important issue to study the short and long term effect of size, shape, and surface functional groups on the bioavailability, uptake, subcellular distribution, metabolism, and degradation of these different nanostructures. Some of the efforts made towards this aim are the studies using carbon nanostructures [60], CdSe quantum dots [61] and gold nanoparticles [62]. Sastry et al. [62g] have studied the uptake of gold nanoparticles by mammalian cells by pinocytosis and its compartmentalization in lysosomal bodies. With high scattering cross-section of gold nanoparticle in the near infrared region, they are also being considered for use as intravenous contrast enhancers in medical imaging [63].

1.2.6 Melting point

The melting point of the nanocrystals has a direct relation with the size of the nanoparticles i.e. smaller is the size of a nanoparticle; lower will be the melting point [64]. The surface atoms in the solid phase are coordinatively unsaturated and thus high amount of surface energy is associated with them and the surface energy is always lower in the liquid phase as compared to the solid phase. The process of melting starts from the surface and thus, the nanoparticle system is much more stable in the liquid phase due to reduced surface energy [65]. A dramatic decrease in the melting point is observed in the nanoparticles that are smaller than 3-4 nm in size [66].

1.2.7 Optical property

Optical properties have specifically gained an indispensable status in the study of the noble metal nanostructures. This is due to the fact that they show size, shape and composition dependent absorption profile, owing to their surface plasmon characteristics [67]. Mie theory describes the light absorption characteristic of spherical metal nanoparticles [67a], which shows that in the size range 3 to 10 nm, the absorption does

not depend strongly on the size of the particle. This is due to the fact that the higher order terms in the Mie formula become insignificant in this size range. Thus, only the dipole term becomes relevant, which depends only on the total metal concentration and not the size of the particles. The absorption spectrum of particles in a given solvent can be calculated from the optical constants of the bulk metal [68].

Gold and silver nanoparticles have a transverse plasmon absorption in the visible region of electromagnetic radiation, which is due to collective coherent excitation of conduction-band electrons on interaction with the incoming electromagnetic radiation [69]. The movement of the electrons under the influence of electric field vector of the incident light leads to a dipole oscillations across the particle. The positive polarization charge acts as a restoring force, which causes the electrons to oscillate. Thus, the electron density within the surface layer, the thickness of which is about equal to the screening length of few angstroms, oscillate whereas the density in the interior of the particle remains constant ("surface plasmon"). Therefore, any change in the electron density of this surface layer will lead to changes in the plasmon absorption [70]. Higher order modes become more dominant with increasing particle size, causing the plasmon absorption band to red shift and resulting in increased bandwidth. In the case of larger particles, the light cannot polarize the nanoparticles homogeneously and retardation effects lead to the excitation of higher order modes. Within the size range of 25 nm, the nanoparticles can be treated within the dipolar approximation and the absorption profile is independent of the particle size. Though, it has been reported that below the size limit of 10 nm the particles start showing size dependence of the plasmon resonance band and ultimately disappear for particles of size less than 2 nm. This is attributed to the decreasing validity of the free electron gas model assumption [69, 70].

Gans extended the Mie theory within the dipole approximation to explain the optical absorption of the cylindrical and oblate nanoparticles [71]. The plasmon resonance for nanorods shows two bands; the high energy band for the out of plane transverse plasmon resonance and the low energy band corresponding to the in-plane longitudinal plasmon resonance along the axis of the nanorods. The transverse plasmon

band shows a linear relation with the aspect ratio (ratio of length to width of nanorods) and the dielectric constant of the medium [69, 70]. With an increase in the aspect ratio, the energy separation between the two plasmon bands also increases [72]. Similarly, triangular nanoparticles also show two absorption bands corresponding to the transverse and longitudinal plasmon resonance. In certain cases, another peak in between the two plasmon peaks has also been reported which has been attributed to the in-plane quadrupole mode of plasmon resonance [73]. Several attempts have been made towards successful synthesis of anisotropic metal nanostructures such as rods [74], disks [75], triangular prisms [76], multipods [77], cubes [78] and nanoshells [79] and their optical properties have been studied.

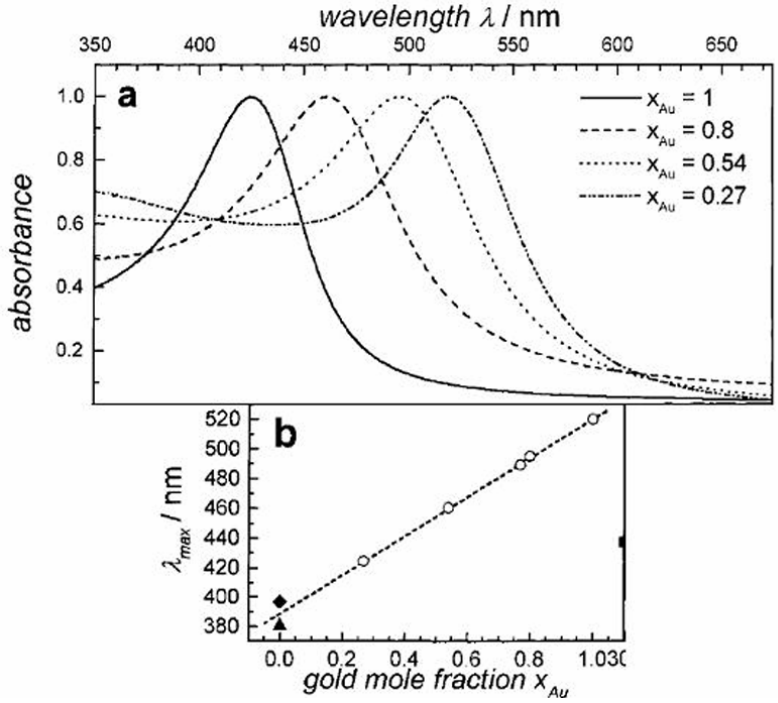

Fig 1.4 *Effect of gold-silver alloy formation on the surface plasmon absorption. Part (a) shows the UV-vis absorption spectra of spherical gold-silver alloy nanoparticles of varying composition. The gold mole fraction xAu varies between 1 and 0.27. The plasmon absorption maximum blue-shifts with decreasing xAu. This fact is further illustrated in part (b) where the plasmon band maximum is plotted as a function of the gold mole fraction xAu [84].*

While the peak position of the surface plasmon absorption of spherical gold nanoparticles is only weakly size-dependent, it varies strongly as a function of the composition for gold-silver alloy nanoparticles [80-84]. This is illustrated in Fig. 1.4

which gives the absorption spectra of pure gold and gold-silver alloy nanoparticles. As seen the maximum of the plasmon absorption clearly blue-shifts with decreasing gold mole fraction. This is also shown in Fig 1.4b, where the plasmon maximum is plotted as a function of gold mole fraction. A linear relationship is found experimentally [84-86]. This dependence of the plasmon band maximum on the alloy composition makes this system easily tunable for optical applications requiring a certain absorption spectrum.

The position and shape of the plasmon absorption of spherical metallic nanoparticles depend not only on their composition and, hence, on the correct form of the material dielectric function, but also on the dielectric function of the surrounding. Increase in the dielectric function of the surrounding medium leads to an increase in the plasmon band intensity and bandwidth as well as to a red shift of the plasmon band maximum [87]. Changing the surrounding medium to one with a higher dielectric constant and therefore enhancing the plasmon absorption is known as immersion spectroscopy [87].

1.2.8 Electronic property

The electrical conductivity of bulk metal is dependent on the band structure and mobility of the electrons. The expression for mobility of an electron is given as,

$$\mu = \frac{e.\lambda}{4\pi\varepsilon_0 m_e V_F} \qquad \text{..... (1.1)}$$

where λ is the mean free path of the electron between two successive collisions, m_e being effective mass of electron in the lattice, V_F the speed of electron (Fermi speed) and ε_0 the dielectric constant of the medium. The collective motion of electrons in the bulk phase obeys Ohm's law [88]. However, when the size of the metal approaches the nanometer scale, the finite size leads to unique electronic properties and Ohm's law is not necessarily obeyed.

The electrical charge transport in discontinuous metal nanoparticles film/cluster depends on two factors: the charging energy (E_{ch}), which is determined by the capacitance of the particles and the tunnel coupling between the particles, which is a function of the distance between the nanoparticles. The tunneling current (I) has been

found to be dependent on the separation between the particles (x) and the barrier height, φ (work function). It can be expressed as

$$I \alpha e^{\frac{-2x}{\hbar\sqrt{2m\varphi}}} \quad \ldots\ldots\ldots (1.2)$$

The electrical behavior of such films has been extensively studied in the past [89] and it has been shown that the activation energy for charge transport in such 3-D nanoparticles arrangement depends simply on the separation between the nanoparticles rather than the chemical nature of the molecule between them [90]. The temperature dependent electron conduction in such systems have been seen to follow the Arrhenius type activated electron tunneling behavior which follows the following relation [91],

$$\sigma(T) = \sigma_0 . e^{\frac{-E_A}{k_B . T}} \quad \ldots\ldots\ldots (1.3)$$

where E_A is the activation energy, k_B is the Boltzmann's constant and T is the temperature. This shows the characteristic hopping transport between nearest neighboring particles. The activation energy (E_A) becomes temperature dependent when the measuring temperature is decreased and at very low temperatures, the conductivity follows the variable-range hopping (VRH) model given by Mott [92],

$$\sigma(T) = \sigma_0 . e^{\left(\frac{-T_0}{T}\right)^{\gamma}} \quad \ldots\ldots\ldots (1.4)$$

where γ=1/(D+1) in D dimensions of the conduction path. Though γ is expected to have the value equal to ¼ for 3D nanoparticles, its value is mostly found to be ½ (D=1) for compact metal-cluster compounds. The temperature range, where the nearest-neighbor hopping to variable-conduction hopping transition is observed, has been found to be dependent on the particle size and the degree of disorder.

The dependence of the electrical conductivity of such 3D nanoparticles assembly on temperature and applied electric field has been studied using several theoretical models for electron hopping to finally confirm that the experimental results could be explained by thermally activated stochastic multiple site hopping process. However, at

higher temperatures, nearest-neighbor hopping dominates [93]. It is important to understand that at low temperatures, the number of charge carriers participating in the hopping process is independent of the temperature where as at higher temperatures, where k_BT term becomes comparable to the charging energy (E_{ch} is determined by the capacitance of the particles and thus is depecdent on particle size and interparticle space) of the metal nanoparticle, further thermally excited charge carriers participate in the hopping process. It has also been shown that for room temperature measurements, where Arrhenius-type thermal activation exists, the nearest-neighbor hopping is a strong function of the interparticle spacing when the particle size is fixed [91].

Wuelfing, Murray and coworkers have proposed that the cell constant, i.e. the geometry parameter of the sample, must be known precisely in order to discriminate between a temperature-independent tunneling and the thermally activated over-barrier process [94]. They have suggested an Arrhenius-type activated tunneling model to describe the transport phenomenon through a 3D network of ligand-stabilized gold nanoparticles. The relation governing this phenomenon is given as,

$$\sigma(\delta,T) = \sigma_0 .e^{-\beta\delta} .e^{\frac{-E_A}{k_BT}} \quad \text{..... (1.5)}$$

where β is the electron tunneling coefficient, δ is the average interparticle distance and the expression $\sigma_0 . e^{-\beta\delta}$ gives the conductivity when $k_BT >> E_A$. The first term in the above expression gives the electron tunneling between particles through the ligand shell and depends exponentially on the length of the surface capping molecule as long as the Fermi level of the particles lies between the highest occupied molecular orbital (HOMO)-lowest unoccupied molecular orbital (LUMO) gap of the capping molecule.

Thus, in general, it can be concluded that the electrical conduction within the 3D nanoparticle assemblies depends on the particles size, the interparticle spacing as well as the nature of the capping agent and its electronic structure. So, selective adsorption of gas molecules on such hybrid nano-assemblies can be easily exploited to fabricate chemiresistors for sensing chemical vapors.

1.3 Preparation of nanoparticles of different shapes

1.3.1 Nucleation and particle growth

The chemical growth of bulk or nanometer-sized materials inevitably involves the process of precipitation of a solid phase from solution. For a particular solvent, there is certain solubility for a solute, whereby addition of any excess solute will result in precipitation and formation of nanocrystals. Thus, in the case of nanoparticle formation, for nucleation to occur, the solution must be supersaturated either by directly dissolving the solute at higher temperature and then cooling to low temperatures or by adding the necessary reactants to produce a supersaturated solution during the reaction [95, 96]. The precipitation process then basically consists of a nucleation step followed by particle growth stages [97, 98]. Nucleation happens due to the driving force of the thermodynamics because the supersaturated solution is not energetically stable.

After the nuclei are formed from the solution, they grow via molecular addition, which relives the supersaturated step. When the concentration drops below the critical level, nucleation stops and the particles continue to grow by molecular addition until the equilibrium concentration of the precipitated species is reached. Uniformity of the size distribution is achieved through a short nucleation period that generates all of the particles obtained at the end of the reaction followed by a self-sharpening growth process. At this stage, the smaller particles grow more rapidly than the larger ones because the free energy driving force is larger for smaller particles than for larger ones if the particles are slightly larger than the critical size. At this stage, focusing in size occurs [95]. Nearly monodisperse size distribution can be obtained at this stage by either stopping the reaction (nucleation and growth) quickly or by supplying reactant source to keep a saturated condition during the course of the reaction.

1.3.2 Preparation Methods

The following methods are used commonly for the synthesis of nanoparticles.

- Physical methods

Physical techniques are directly used to form nanoparticles (like Laser ablation) or induce chemical reactions to form nanoparticles (Sonochemical and Photochemical methods)

- Chemical methods

It involves the reduction of metal ions with different reducing agents in the presence of a capping agent. Though chemical synthesis dates back to the middle ages [99], Faraday method of making gold nanoparticles in carbon disulphide by the reduction of chloroaurate ions by phosphorous vapors is the well known example for this method [100].

- Biological Methods

Employing fungus, bacteria and leaf extract to reduce metal ions to form metal nanoparticles.

The physical routes mainly include vapor deposition [101], thermal decomposition [102], spray pyrolysis [103], photoirradiation [104], laser ablation [105], ultrasonication [106], radiolysis [107] and solvated metal atom dispersion [108].

However, chemical methods for synthesis of metal nanoparticles have been more popular and have gained wide acceptance. Some of the common chemical routes include sol-gel method [109], solvothermal synthesis [110], micelles based synthesis [111] and galvanic replacement reaction [112]. Chemical reduction has been the most popular route towards synthesis of metal nanostructures due to easy protocols and the exquisite shape and size control provided by this method. The control of size, shape, stability and the assembly of nanoparticles have been achieved by using different capping agents, solvents and templates. Various types of capping agents have been used ranging from ions [113] to polymeric molecules [114] and even biomolecules [115]. Ever since the first report by Brust et al. [116] for the synthesis of monolayer-protected clusters (MPCs), several advances have been made in this field and a variety of capping agents have been used to prepare MPCs [117] soluble in non-polar organic as well as polar solvents. Although water has been used primarily for synthesis protocols, several reports on use of organic solvents [105a, 118], ionic liquids [114g, 119] and super critical fluids [120] are also

available. Similarly, different templates such as micelles [121], polymers [122], mesoporous materials [123], carbon nanotubes (CNTs) [124], biomolecules [125] and microorganisms [126] have been used for the synthesis of nanoparticles on the surface or in confined spaces.

Although, over the past several decades, physical and chemical methods have dominated the synthesis of nanostructures, recently considerable attention has been paid towards the use of biological systems. Biological systems have been known to fabricate intricate structures at the micro and nano scales with precise control in normal environmental conditions. The exquisite siliceous exoskeletons of the diatoms and radilarians [127] and calcareous structures synthesized by the coccoliths [128] are micro scale materials, which have attracted tremendous interest. Besides, magnetite particles found in the magnetosomes [129] of the magnetic bacteria [130] are a wonderful example of functional nanomaterials that helps the microorganism to navigate in the earth's geomagnetic field. This fact has lured scientists to understand the underlying mechanisms used by the biological systems and thus, explore the biomimetic approach towards synthesis of nanomaterials.

Fig 1.5 shows a basic map of some of the topological colloid-based objects that are being devised, designed, and synthesized by various groups. By no means is this scheme comprehensive; it illustrates the four basic concepts for particle modification, which are size control, shape manipulation, layered structures, and nanocrystal ordering. Combinations of these four processes can be readily envisaged. Three of these four pathways from single nanocrystals to more complex materials are well understood mechanistically. Size control is determined by nucleation and growth kinetics and the efficacy of capping agents in preventing Ostwald ripening and coalescence. Colloid structuring is largely controlled through manipulation of colloid and surface forces such as double layer repulsion, capillary forces, sedimentation, and electrophoresis or magnetophoresis. Finally, layered colloids can be synthesized when there is sufficient control over deposition and nucleation within a nanocrystal system. Shape control is the

exception. Shape control is the inorganic equivalent to branching in polymers and is still in its infancy.

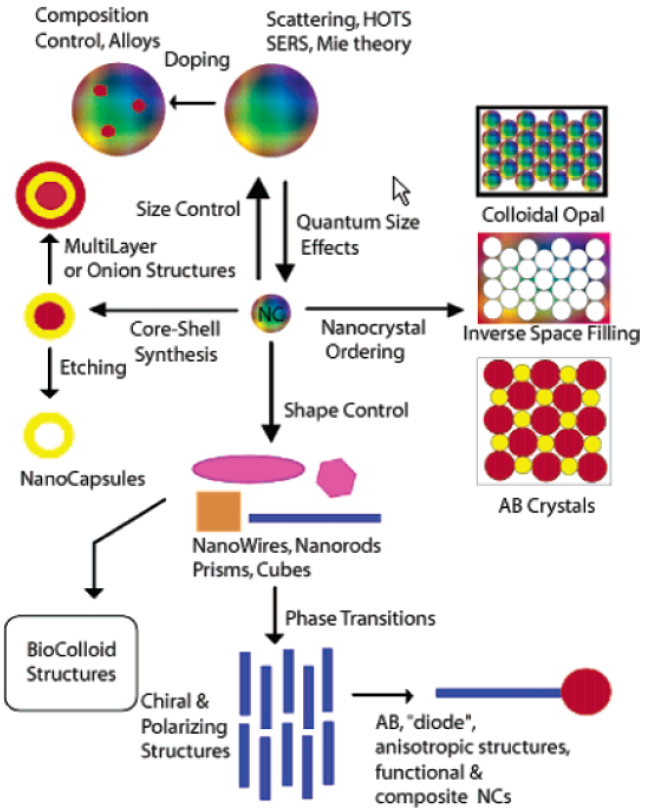

Figure 1.5 *Basic aspect of Nanocrystal topology [131]*

It has been now recognized that nanoparticle shape plays a crucial role in determining their optical/electronic properties [75a-76a-d, 132-133] as well as their catalytic activity [36, 42, 43] in addition to the size of the nanoparticle. Consequently, there is much current interest in developing experimental protocols for the synthesis of metal and semiconductor nanoparticles of different shapes. Nanorods/wires of silver [74d, 134] and gold [74a, 104q, 135], nanoprisms (nanotriangles) and nanoplates of silver [75a- 76a-d, 132] and gold [10d, 74a], and tetrapods of gold [76g, 136] are some of the interesting metallic nanocrystalline shapes that can now be routinely synthesized in the laboratory. From a purely fundamental angle, the ability to control the shape of nanocrystals is particularly exciting and has led to the first observation of two distinct quadrupole plasmon resonance modes in silver nanoprisms [76a]. Distortion of the

spherical symmetry in nanoparticles results in the introduction of anisotropy in the properties of the nanoparticles. In the context of plasmon vibration modes in such 'anisotropic" particles , an increase in the aspect ratio of silver and gold nanoparticles also leads to a shift in the in-plane surface plasmon absorption band to larger wavelengths that could be located well into the near infrared region (NIR) of the electromagnetic spectrum which is expected to be of significance in cancer hyperthermia [137] and in the new cell imaging technique of plasmon resonance tomography [138]. Large aspect-ratio metal nanorods and nanowires are expected to play an important role in the emerging area of plasmonics [139].

1.3.3 Anisotropic nanostructures

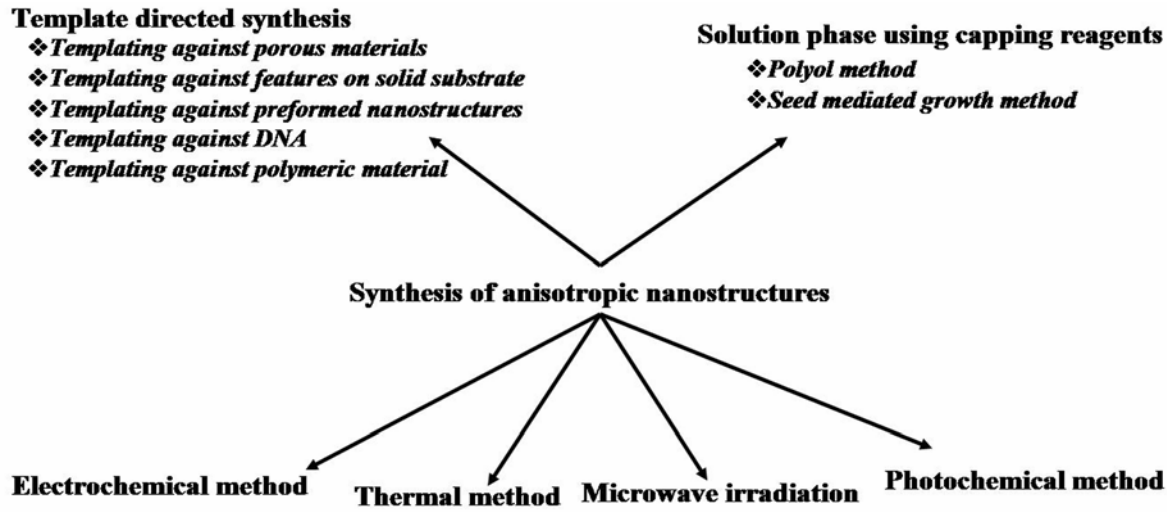

Figure 1.6 *Diagram showing the various approaches undertaken for synthesis of anisotropic nanostructures.*

Fig 1.6 shows the various approaches adopted for the generation of anisotropy. Anisotropy has thus been achieved either through photochemical reduction [74e, 76a, f, 140], by thermal methods [76d] or using electrochemical methods [72b, 74b]. Apart from these, sonochemical assisted synthesis [141] and microwave irradiation [142] techniques have also been used for the synthesis of 2-D silver nanoplates.

One of the best and common procedures for obtaining control over the shape of the nanoparticles is by using a template. The templates can be like porous alumina used for the synthesis of arrays of Au [143] and Ag [143] nanotubes, polycarbonate membrane

for the preparation of Au and Ag nanorods [144b], mesoporous silica template for the development of highly ordered mesostructured nanowires and nanowire arrays [144c] and use of multiwalled carbon nanotubes as a template for assembly of gold nanoparticles leading to nanowire formation [144d]. Templateing can also be done against features on solid substrate (patterned by lithography) for the growth of Au, Ag, Pd and Cu nanowires [145]. Yet another possibility is of templating against polymeric materials, which has been used for the synthesis of Ag nanowires [146a, b], Au nanowires and nanosheets [146c] and Ag nanodisks [146d]. Templateing against DNA has resulted in the synthesis of nanowire of Au [147a], Ag [147b], Pt [147c] and Pd [147d]. One of the common templates is a *preformed nanostructure.*

1.3.3.1 Templating against preformed nanostructures

Templating against nanostructures (anisotropic), pre-synthesized using other methods provides a generic and powerful approach to bring in anisotropy in nanostructures. With this simple approach, Xia and co-workers have synthesized highly crystalline nanotubes of metals such as Au, Pt and Pd via galvanic displacement reaction between Ag nanowires and appropriate precursors of these metals in the aqueous medium [112]. In this process, when silver nanowires are dispersed into an aqueous $HAuCl_4$ solution, they are immediately oxidized to silver ions. The resultant Au atoms are confined to the vicinity of the template surface. Once their concentration reaches a critical value, the Au atoms nucleate and grow into small clusters, and eventually evolve into a sheath-like structure around the silver template. Other significant works are gold and silver nanoframes by Mirkin's group [148a], Au, Ag, Pt and Pd nanowires by Yang and co-workers [148b] and gold nanoshells in organic as well as aqueous medium by Sastry and coworkers and others [112].

1.3.3.2 Use of capping agents

Yet another common means of synthesis of anisotropic nanostructures is solution phase methods based on capping reagents. It is now well understood that one can control the shape of a crystal by introducing appropriate capping reagents to change the free energies of the various crystallographic surfaces and thus to alter their growth rates.

Polyol method has been demonstrated by Xia and coworkers for the large-scale synthesis of silver nanowires [149]. Varying the reaction condition leads to change in morphology and aspect ratios of silver nanostructures [150]. Liz-Marzan and coworkers have reported the synthesis of Ag nanoprisims [76c]. Apart from silver, polyol synthesis method has also been utilized for anisotropic nanostructure growth of other metals such as gold [151] and platinum [152]. Besides polyol method, the synthesis of gold nanorods/wires with relatively high aspect ratios by aqueous seeded growth method has been established by Murphy's group [74]. El-Sayed and coworkers have shown increase in nanorod yield [153] and Chen and coworkers have shown that seed mediated growth process can also be employed for large-scale synthesis of silver nanoplates/nanodisks [75a, 76b].

1.4 Two-dimensional (2D) and three-dimensional (3D) organization of nanoparticles

Nanoparticles with physical and chemical functional specificity and selectivity, naturally makes them as ideal building blocks for two and three dimensional cluster self-assembled superlattice structures (in powder, thin film, and solid bulk form), in which the particles behave like well-defined molecular matter, arranged with long-range translational and even orientational order [154]. Well-defined ordered solids prepared from tailored nanocrystalline building blocks provide new opportunities to optimize and enhance the properties and performance of the materials. This is a new initiative in research on cluster engineered materials [155]. Moreover, the ability to assemble particles into well-defined two- and three-dimensional spatial configurations should produce interesting properties such as new collective physical behavior [156], and the development of a general procedure for the fabrication of "quantum" crystals is a major challenge of future research. The fabrication of such crystals of particles would, for example, lead to the production of optical gratings [157], optical filters [158], antireflective surface coating [159], selective solar absorbers [160], and data storage and microelectronic devices [161].

There is a plethora of reports regarding the organization of nanoparticles using various approaches. Alivisatos and coworkers [162], Sastry and co-workers [163], Rao, Natan and Bawendi and coworkers [164] have used self assembled monolayer to

immobilize the nanoparticles. Sastry and coworkers have further shown the control over the nanoparticle density by pH-dependent modulation [163]. Gersig and Mulveney [25a, 165] have shown that particles can form well-ordered 2D lattices of gold nanoparticles by the use of electrophoretic deposition. Few groups have shown 2D [166] and Kamat and coworkers have shown a 3D organization [167] of Pt nanoparticles by the same technique. Spontaneous organization by solvent evaporation has been used by several groups [168] for the spontaneous formation of self-assembled structures while deposited from a solution phase onto a solid substrate. The influence of the solvent evaporation process on 2D and 3D assembly of silver nanoparticles has been studied in great detail by Pileni and coworkers [168c-d, 169]. 2D and 3D assembly of gold and silver nanoparticles [170], ordered arrays of nanoparticles from bimodal distribution of sizes of the same metal [171a] and also of different metals [171b] have been shown. It has also been shown that along with stabilizing the nanoparticles in solution, the capping material also controls the interparticle distances of self-assembled structures [169, 172, and 173]. Besides this DNA is a hot favourite for the 3D assembly of nanoparticles. High control over the optical, mechanical and electrical properties of the hybrid bioinorganic materials was demonstrated for gold nanoparticles with DNA independently by Mirkin and coworkers [174] as well as Alivisatos and coworkers [175]. Arrays of nanoparticles have also been created using the inherent repeating patterns of bacterial S-layer proteins [176]. Nanosphere lithography, a “top down” approach developed by Van Duyne et al. [177 a-e] is another mean of generating ordered arrays of nanostructures. Mirkin’s group uses dip-pen lithography to generate arrays of Au nanostructures [177f-g]. Surface modified polymers for the 2D assembly of nanoparticles have been shown by Natan and coworkers [178]. Other groups have also shown assembly using polyelectrolyte thin film [179a] or using poly (vinylpyridine) [179b]. Kawasaki et al. have demonstrated that Ag and Au island films sputter-deposited on mica could be converted to a dense monolayer or 2D array of spherical nanoparticles without aggregation by post deposition nanosecond laser irradiation [180].

1.4.1 Organization at the air-water interface

Fendler et al pioneered the use of the air-water interface for the synthesis as well as assembly of nanoparticles employing Langmuir-Blodgett technique. Further, the technique was successively used by other groups for formation of colloidal particulate films of different technologically important materials. This versatile field offers variety of modes of assembly and synthesis; a few particulars of the research in this area have been discussed in following sections.

Immobilization of nanoparticles at air-water interface using electrostatic interaction

This strategy consists of spreading of oppositely charged Langmuir monolayer on the surface of aqueous solution of charged colloidal particles. The electrostatic immobilization of negatively charged carboxylic acid derivatized gold [181a], silver [181b,c] and cadmium sulphide [181c] nanoparticles at the air-water interface using positively charged fatty amine Langmuir monolayer has been studied in detail by Sastry and co-workers. The advantage of this approach for the 2D assembly of nanoparticles is that by varying the charge on the amine molecules through colloidal subphase pH, one can control the degree of cluster incorporation into the Langmuir monolayer.

Spreading surfactant stabilized nanoparticles on aqueous subphase

The air-water interface has been used for the assembly of nanoparticles synthesized *ex-situ* in solution. This method involves three steps: 1) synthesis of colloidal particles in the aqueous phase, 2) hydrophobization of aqueous colloidal particles by phase transferring them to organic phase using suitable phase transfer agent 3) spreading of hydrophobized nanoparticles (monolayer protected clusters, MPCs) on aqueous subphase in a Langmuir trough and formation of their mono/multilayer onto suitable substrates using LB technique. Fendler's group has shown the formation of compact, ordered arrays of MPCs of silver [182a], platinum [182b], palladium [182b] CdS [182c, d], lead zirconium titanate [182e] Fe_2O_3 [182f], TiO_2 [182g]. Apart from spherical nanoparticles, formation of superlattices of C_{60} molecules [183] and the 2D assembly of anisotropic nanostructures such as silver nanowires [184a] and barium chromate nanorods [184b] has also been demonstrated by this technique.

Reduction of metal ions under Langmuir monolayer

This is where the air-water interface plays an active role. Formation of nanoparticulate films of cadmium sulphide [185], lead sulphide [185, 186a] zinc sulphide [186a], and cadmium selenide [186b] has been established via the slow infusion of reactant gas (reducing agent) by this technique. Factors such as nature of the surfactant, surface pressure and the temperature affect the morphology of the nanocrystallites formed under the monolayer. A similar strategy was also shown to be applicable for the generation of silver [187a] and gold [187b] nanoparticulate films under suitable surfactant monolayers. Another active role of the air-water interface is where either the monolayer or the subphase acts as a reducing agents and nanoparticles (anisotropic or spherical) are synthesized at the interface [187 c-e]. Sastry and coworkers have shown how the symmetry-breaking nature of the air-water interface can be exploited to build anisotropic nanostructures by carrying out the reduction of precursor metal ions preferentially at the interface**.** This has been achieved either by constraining the precursor metal ions (formation of flat gold nanostructures by reduction of a monolayer of hydrophobic gold ions with anthranilic acid in the subphase [187c]) or the reducing agent (formation of flat gold nanosheets by the reduction of gold ions in the subphase by hexadecylaniline [187d] /alkylated tyrosine Langmuir monolayer [187e]) to the air-water interface thus confining the reduction of metal ions strictly to the interface.

1.4.2 Chemical/photochemical generation of nanoparticles within Langmuir-Blodgett films

In this method, the spreading of fatty acid Langmuir monoalyer on the surface of aqueous metal ion solution subphase results in the formation of precursor metal carboxylates at the air-water interface. The LB film with incorporated metal ions deposited on suitable substrate is then exposed to suitable reactant gas (reducing agent) in a sealed cell to form the nanoparticles. Reports on the synthesis of nanoparticles in LB matrices include photoreduction of gold ions complexed with octadecylamine/ hexadecylaniline [188], synthesis of size quantized CdS [189a, b], PbS [189c, d] and CdSe [189e], CdTe [189f] nanoparticles by exposure of the film to H_2S (or H_2Se, H_2Te respectively).

1.5 Outline of the thesis

Self-organization of colloidal nanoparticles via the LB technique has proven to be a straightforward and highly reproducible method for the production of uniform 2D structures for a variety of different types of nanoparticles [181-184]. An important aspect of nanotechnology is formation of thin films or patterns of nanoparticles that can be realized either by assembling the nanoparticles or synthesizing nanoparticles in a two dimensionally confined space.

It is also recognized that nanoparticle shape plays an important role in modulating its electronic and chemical properties. Shape anisotropy in nanostructures is achieved by the various routes described earlier. Owing to the fact that air-water interface has intrinsic anisotropy; it could be a model system for the generation of anisotropic nanostructures. However, surprisingly, the use of air-water interface for achieving nanoparticle shape control remains largely unexplored and underexploited.

Besides the passive role played by the air water interface in assembly of nanoparticles, an exciting option is to design experiments wherein the air-water interface is dynamic and permits reactions involving nanoparticles. Progress in this direction was made by Chen and co-workers [190]. The galvanic exchange reaction between sacrificial nanoparticles (which act as a template) and other suitable metal ions often results in the formation of hollow nanostructures [112] with interesting application potential. An interesting possibility that has not been addressed so far is to study transmetallation reactions involving nanoparticles assembled on suitable surfaces/interfaces with appropriate metal ions. An important motivation for such a study is the possibility of interconnecting close-packed nanoparticles assembled on surface/interfaces through transmetallation reactions leading to electrically conducting structures over large length scales. In this context, the air-water interface could be an excellent candidate to follow in real time transmetallation reactions between hydrophobic nanoparticles assembled in close packed structures on water and aqueous metal ions present in the subphase or vise versa.

An important aspect of the work is that new protocols have been developed for the synthesis of anisotropic nanostructures, which involve constrained growth of the nanocrystals within the confined plane of the Langmuir monolayer. These protocols are different from existing air-water interface wet-chemistry methods where the role of the Langmuir monolayer is passive.

The work described in this thesis covers the formation of 2D arrays of gold nanoparticles on the air water interface by variation of the surface tension and rate of evaporation. Thereon, the long range ordered arrays of closely packed nanoparticles formed in the presence of anionic and cationic monolayer have been used to study the galvanic exchange reaction at the interface. The transmetallation reaction has been studied by using sacrificial silver nanoparticles in an aqueous subphase and hydrophobized monolayer. The beauty of electrostatic interaction has been exploited for the separation and arrangement of triangles from their spherical counterparts. The mechanism of galvanic exchange reaction at the air water interface has been studied using Ni nanoparticles and Pt ions which at the end of reaction yield a catalytically active product.

The thesis consists of *six chapters*. ***Chapter one*** is an introduction to the thesis and gives a brief overview about the interest in assembling nanoparticles in 2D and 3D ordered assemblies, how their collective properties vary with different parameters and several methods available in the literature for the same. It also discusses the importance of anisotropic nanostructures with respect to their optical and catalytic properties and different routes of synthesis of anisotropic nanostructures. There is an insight to using the transmetallation reaction for the synthesis of metal nanoparticles. It also describes the methods of using transmetallation reaction at air water interface for the synthesis of anisotropic nanostructures.

Chapter two describes the experimental characterization techniques that have been consistently used for the depiction of the work. UV-visible Spectroscopy, Fourier Transform Infrared Spectroscopy (FTIR), Transmission Electron Microscopy (TEM), High resolution transmission Electron Microscopy (HRTEM), Energy Dispersive

Analysis of X-ray (EDAX), X-Ray photoemission spectroscopy (XPS) and I-V measurement are some of the techniques which have been extensively used to illustrate the formation of nanoparticles and their properties. The physical principles of different techniques and their application to understanding the various aspects of formation of the nanocomposites have been delineated.

Chapter three describe the finding on how solvents, surfactants and surface pressure play an important role in the formation of 2D superlattice of gold nanocrystals. Specifically, it has been shown that the morphology of the domain structures in gold nanocrystal arrays is determined by a competition between the 2D superlattice formation and solvent evaporation. It has been demonstrated that by controlling the spreading and subsequent evaporation process of the solvent, long-range-ordered nanocrystal superlattices can be prepared routinely, with domain size of several microns. Two different surfactants, one anionic (stearic acid) and other cationic (octadecylamine), of opposite charges have been used to form the monolayer for reducing the surface tension. To take into consideration the effect of solvent polarity on the rate of evaporation, a polar (chloroform) and a nonpolar (benzene) organic solvent with different rates of evaporation have been used for dispersing nanoparticles.

Chapter four describes the electrostatically controlled complexation of lemon grass reduced triangular gold colloidal particles in Langmuir monolayer films and demonstrating that compact, lamellar multilayer gold colloidal particle films can be transferred to solid supports by the LB method. More specifically, we have investigated the complexation of lemon grass reduced triangular gold colloidal particles in octadecylamine (ODA) monolayer and also the size and shape selectivity of the monolayer using transmission electron microscopy (TEM), UV-vis absorption, Brewster angle microscopy and Fourier transform infrared (FTIR) spectroscopy. Another interesting observation from this investigation was the dependence of the colloidal solution pH at which the cluster incorporation into the ODA matrix occurred. This indicates that the energetic of ionization of the amine groups on the monolayer is pH dependent and also is strongly affected by the nanoscale curvature of the particles.

Chapter five discusses the galvanic exchange reaction between sacrificial silver particles and gold ions under different conditions. We show the formation of nanostructures with interesting morphologies at the air water interface, by using gold ions in an aqueous subhase and hydrophobized silver nanoparticles with and without ionizable lipid monolayer.

The galvanic exchange reaction between Ag nanoparticles and gold ions was also carried out at the liquid liquid interface. Addition of chloroauric acid to close packed silver nanoparticle arrangement at the interface achieved by a simple reaction (without using linkers) where tyrosine-reduced silver nanoparticles were stirred with dodecylamine in chloroform led to the formation of interlinked bimetallic flat nanostructures. When deposited on substrates, these films show a transition from semiconductor to metallic behaviour upon completion of reaction and are an excellent candidate for ammonia sensing. The thin films were cast onto carbon-coated copper grids and glass slides and were characterized by Transmission Electron Microscope (TEM) and X-ray Diffraction (XPS) measurements respectively. This strategy opens up an exciting methodology of synthesizing flat nanostructures at the liquid-liquid interface.

To investigate the effect of halide ions (chloride, bromide and iodide) on the morphology of the nanostructures during the galvanic exchange reaction, the same was also carried out in aqueous medium in the presence of halide ions. The exercise resulted in formation of nanoshells with thin walls in the presence of bromide ions.

Chapter six describes synthesize of porous nanoparticles of platinum by transmetallation between sacrificial Ni nanoparticles and chloroplatinic acid (H_2PtCl_6) in solution. Catalytic activity shown by this system for hydrogenation of nitrobenzene to aniline, as a test reaction is very high compared to conventional catalysts. The reaction is quite fast and completed within ten minutes of addition of H_2PtCl_6 into the Ni solution. Thus in urge to have an idea regarding the mechanism of the reaction and to form assembled Pt nanostructures we performed the reaction the at air water interface where the constrained environment can effect the rate of the transmetallation reaction. The chapter describes the mechanistic approach to a facile, efficient, and economical

controlled synthesis of assembly of porous Pt nanoparticles at the air water interface. The synthesized porous Pt nanoparticles have an effective diameter of 38nm and 80nm and they are an assembly of discrete Pt nanoparticles having a very small dimension of 2nm.

The ***seventh chapter*** summarizes the work presented in the thesis and emphasizes on the possible further research in this area.

References:

(1) (a) Dowling, A. et al., Nanoscience and nanotechnologies: opportunities and uncertainties, A Report by The Royal Society & The Royal Academy of Engineering, London, July **2004**. (b) George M. Whitesides, G.M. *Small* **2005**, *1*, 172

(2) Poole, C.P.; Jr., Owens, F. J.; *Introduction to Nanotechnology*, Wiley-Interscience, Hoboken, NJ, **2003**.

(3) Lieber, M. *MRS Bull*. **2003**, *28*, 486.

(4) Bam ford, H. *Curr. Biol*. **2000**, *10*, R558.

(5) Service, R.F. *Science* **2002**, *298*, 2322.

(6) Feynman, R. P. *Eng. Sci.* **1960**, *23*, 22.

(7) Taniguchi, N. **1974**. On the Basic Concept of 'Nano-Technology'. In: *Proceedings of the international conference on production engineering. Tokyo, Part II,* Japan Society of Precision Engineering, **1974**: 18-23: Tokyo: JSPE

(8) (a) Ostwald, W. *Kolloid Z.***1909**, *4*, 5. (b) Daniel, M.; Astruc, D. *Chem. Rev.* **2004**, *104*, 293.

(9) Wang, K. L. J. *Nanosci. Nanotechnol*. **2002**, *2*, 235.

(10) Mammen, M.; Choi, S.-K.; Whitesides, G. M. *Angew. Chem*. **1998**, *110*, 2908; Angew. *Chem. Int. Ed*. **1998**, *37*, 2755.

(11) Craver, C.; Carraher, C.; Applied Polymer Science: 21st Century, *Elsevier*, Amsterdam, **2000**.

(12) Redl, F. X.; Cho, K.S.; Murray, C.B.; O'Brien, S. *Nature* **2003**, *423*, 968.

(13) Al'tshuler, B. L.; Lee, P. A.; *Phys. Today* **1988**, *36*, 41.

(14) Likharev, K.K. IBM *J. Res. Develop*. **1988**, *32*, 144.

(15) M. G. Bawendi, M. L. Steigerwald, L. E. Brus, *Annu. Rev. Phys. Chem*. **1990**, *41*, 477.

(16) Hey, T.; Walters, P. The New Quantum Universe, Cambridge University Press, Cambridge, UK, **2003**.

(17) R. T. Bate, *Sci. Am*. **1988**, *258*, 96.

(18) Goldhaber-Gordon, D.; Montemerlo, M.S.; Love, J.C.; Opiteck, G.J.; Ellenbogen, J.C. *Proc. IEEE* **1997**, *85*, 521.

(19) Swami Sivananda, *Practice of Ayurveda* **2006**, Divine life society Publishers

(20) Kerker, M. *J. Colloid Int. Sci*. **1985**, *105*, 297

(21) Reibold, P.; Paufler, P.; Levin, A.A.; Kochmann, W.; PÃ¤tzke, N.; Meyer, D.C. *Nature*, *444*, 286.

(22) September issue of *Scientific American*, **2001**.

(23) (a) Fendler, J. H.; Meldrum, F. C. *Adv. Mater*. **1995**, *7*, 607. (b) Schmid, G. *Chem. Rev*. **1992**, *92*, 1709.

(24) (a) Roucoux, A.; Schulz, J.; Patin, H. *Chem. Rev.* **2002,** *102,* 3757. b) Lewis, L. N. *Chem. Rev.* **1993**, 93, 2693.

(25) (a) Niemeyer, C. M. *Angew. Chem. Int. Ed.* **2001**, *40*, 4128. (b) Niemeyer, C. M. *Angew. Chem. Int. Ed.* **2003**, *42*, 5974. (c) Parak, W. J.; Gerion, D.; Pellegrino, T.; Zanchet, D.; Micheel, C.; Williams, S. C.; Bodreau, R.; Gros, M. A. L.; Larabell, C. A.; Alivisatos, A. P. *Nanotechnology* **2003**, *14*, R15. (d) Caski, A.; Maubach, G.; Born, D.; Reichert, J.; Fritzsche, W. *Single Mol.* **2002**, *3*, 275.

(26) Rosi, N. L.; Mirkin, C. A. *Chem. Rev.* **2005**, *105*, 1547.

(27) (a) Parak, W. J.; Pellegrino, T.; Plank, C. *Nanotechnology* **2005**, *16*, R9; (b) Bruchez, M.; Moronne, Jr., M.; Gin, P.; Weiss, S.; Alivisatos, A. P. *Science* **1998**, *281*, 2013; (c) Chan, W. C. W.; Nie, S. M. *Science* **1998**, *281*, 2016.

(28) (a) Hagfeldt, A.; Graetzel, M. *Acc. Chem. Res.* **2000**, *33*, 269. (b) Bueno, J. T.; Shchukina, N.; Ramos, A. A. *Nature*. **2004**, *430*, 326.

(29) Fichtner, M. *Adv. Eng. Mater.* **2005**, *7*, 443.

(30) Moran, C. E.; Steele, J. M.; Halas, N. J. *Nano Lett*. **2004**, *4*, 1497.

(31) (a) Simon, U. In *Nanoparticles: From Theory to Application*, Schmid, G., Ed. Wiley-VCH, Weinheim, 2004. (b) *Nanomaterials: Synthesis, Properties, and Applications*, edited by A. S. Edelstein and R. C. Cammarata (Institute of Physics Publishing, Bristol, U.K., **1996**).

(32) (a) Maier, S. A.; Brongersma, M. L.; Kik, P. G.; Meltzer, S.; Requicha, A. A. G.; Atwater, H. A. *Adv. Mater.* **2001**, *13*, 1501. (b) Maier, S. A.; Brongersma, M. L.; Kik, P. G.; Atwater, H. A. *Phys. Rev. B*, **2002**, *65*, 193408. (c) Wang, Y. *Acc. Chem. Res.* **1991**, *24*, 133. (b) Yoffe, A. D. *Adv. Phys.* **1993**, *42*, 173.

(33) Li, X.; Xu, W.; Zhang, J.; Jia, H.; Yang, B.; Zhao, B.; Li, B.; Ozaki, Y. *Langmuir* **2004**, *20*, 1298.

(34) (a) Rouvray, D. *Chem. Br.* **2000**, *36*, 46. (b) Lawton, G. *Chem. Ind. (London)* 2001, 174. (c) Havancsak, K. *Mater. Sci. Forum* 2003, *414*, 85. (d) Mazzola, L. *Nature Biotech.* **2003**, *21*, 1137. (e) Hayat, M. A. Ed.; *Colloidal Gold: Principles, Methods and Application*; Academic Press: San Diego, 1989; Vol 1. (f) Alivisatos, P. *Nature Biotech.* **2004**, *22*, 47.

(35) (a) Brust, M.; Kiely, C. J. *Colloids Surf. A: Physicochem. Eng. Asp.* **2002**, *202*, 175. (b) Link, S.; El-Sayed, M. A. *J. Phys. Chem. B* **1999**, *103*, 4212. (c) Brus, L. E. *J. Chem. Phys.* **1983**, *79*, 5566. (d) J. P. Borel, *Surf. Sci.* **1981**, *106*, 1 (e) Dick, K.; Dhanasekaran, T.; Zhang, Z.; Meisel, D. *J. Am. Chem. Soc.*, **2002**, *124*, 2312. (f) Glinka, Y. D.; Lin, S. –H.; Hwang, L. –P.; Chen, Y. –T.; Tolk, N. H. *Phys. Rev. B*, **2001**, *64*, 085421. (g) Eychmüller, A. *J. Phys. Chem. B* **2000**, *104*, 6514. (h) Buffat, P.; Borel, J. P. *Phys. Rev. A* **1976**, *13*, 2287. (i) Skomski, R *J. Phys.: Condens. Matter* **2003**, *15*, R841. (j) McHale, J. M.,; Auroux, A.,; Perotta, A. J.; Navrotsky, A. *Science* **1997**, *277*, 788. k) Zhang, H.; Banfield, J. F. *J. Mater. Chem.* **1998**, 8, 2073.

(36) (a) El-Sayed, M. A. *Acc. Chem. Res.* **2001**, *34*, 257. (b) Link, S.; El-Sayed, M. A. *J. Phys. Chem. B* **1999**, *103*, 8410. c) Burda, C.; Chen, X.; Narayanan, R.; El-Sayed, M. A. *Chem. Rev.* **2005**, *105*, 1025.

(37) (a) Chen, S.; Huang, K. *Langmuir* **2000**, *16*, 2014. (b) Li, D.; Li, J. *Chem. Phys. Lett.* **2003**, *372*, 668. (c) Chen, S.; Ingram, R. S.; Hostetler, M. J.; Pietron, J. J.; Murray, R. W.; Schaaff, T. G.; Khoury, J. T.; Alvarez, M. M.; Whetten, R. L. *Science* **1998**, *280*, 2098. (d) Miles, D. T.; Murray, R. W. *Anal. Chem.* **2003**, *75*, 1251 (e) Chen, S.; Pei, R. *J. Am. Chem. Soc.* **2001**, *123*, 10607. (f) Quinn, B. M.; Liljeroth, P.; Ruiz, V.;

Laaksonen, T.; Kontturi, K. *J. Am. Chem. Soc.* **2003**, *125*, 6644. (g) Zhang, P.; Sham, T. K. *Appl. Phys. Lett.* **2002**, *81*, 736.

(38) (a) Templateon, A. C.; Pietron, J. J.; Murray, R. W.; Mulvaney, P. *J. Phys. Chem. B* **2000**, *104*, 564. (b) Itoh, T.; Asahi, T.; Masuhara, H. *Appl. Phys. Lett.* **2001**, *79*, 1667. (c) Rechberger, W.; Hohenau, A.; Leitner, A.; Krenn, J. R.; Lamprecht, B.; Aussenegg, F. R. *Opt. Commun.* **2003**, *220*, 137. (d) Link, S.; Mohamed, M. B.; El-Sayed, M. A. *J. Phys. Chem. B* **1999**, *103*, 3073. (e) Yan, B.; Yang, Y.; Wang, Y. *J. Phys. Chem. B* **2003**, *107*, 9159. (f) Swanson, N. L.; Billard, B. D. *Nanotechnology* **2003**, *14*, 353.

(39) (a) Su, K.-H.; Wei, Q.-H.; Zhang, X.; Mock, J. J.; Smith, D. R.; Schultz, S. *Nano Lett.* **2003**, *3*, 1087. (b) Xu, H.; Bjerneld, E. J.; Kall, M.; Borjesson, L. *Phys. Rev. Lett.* **1999**, *83*, 4357. (c) Kottmann, J. P.; Martin Oliver, J. F. *Opt. Lett.* **2001**, *26*, 1096. (d) Kelly, K. L.; Coronado, E.; Zhao, L. L.; Schatz, G. C. *J. Phys. Chem. B* **2003**, *107*, 668. (e) Jensen, T.; Kelly, L.; Lazarides, A.; Schatz, G. *Cluster Sci.* **1999**, *10*, 295. (f) Al-Rawashdeh, N.; Foss, C. A., Jr. *Nanostruct. Mater*. **1997**, *9*, 383. (g) Schmid G.; Simon U. *Chem. Commun.*, **2005**, *6*, 697.

(40) Heath, J. R. *Science* **1995**, *270*, 1315.

(41) (a) Murray, C. B.; Norris, D. J.; Bawendi, M. G. *J. Am. Chem. Soc.* **1993**, *115*, 8706. (b) Alivisatos, A. P. *J. Phys. Chem.* **1996**, *100*, 13226. (c) Nirmal, M.; Brus, L. *Acc. Chem. Res.* **1999**, *32*, 407. (d) Schmid, G. Metals. In *Nanoscale Materials in Chemistry*; Klabunde, (e) K. J., Ed.; Wiley-Interscience: New York, 2001; Chapter 2, p 15. (f) Alivisatos, A. P. *Endeavour* **1997**, *21*, 56.

(42) Ahmadi, T. S.; Wang, Z. L.; Green, T. C.; Henglein, A.; El-Sayed, M. A. *Science* **1996**, *272*, 1924.

(43) Narayanan, R.; El-Sayed, M. A. *Nano Lett.* **2004**, *4* (7), 1343.

(44) Narayanan, R.; El-Sayed, M. A. *J. Phys. Chem. B* **2004**, *108* (18), 5726.

(45) Wang, Z. L.; Ahmad, T. S.; El-Sayed, M. A. *Surf. Sci*., **1997**, *380*, 302.

(46) Ohde, H.; Ohde, M.; Wai, C. M. *Chem. Commun.* **2004**, *8*, 930.

(47) Fonseca, G. S.; Umpierre, A. P.; Fichtner, P. F. P.; Teixeira, S. R.; Dupont, J. *Chem. Eur. J.* **2003**, *9* (14), 3263.

(48) Adlim, M.; Abu Bakar, M.; Liew, K. Y.; Ismail, J. *J. Mol. Catal. A: Chem.* **2004**, *212* (1-2), 141.

(49) Semagina, N. V.; Bykov, A. V.; Sulman, E. M.; Matveeva, V. G.; Sidorov, S. N.; Dubrovina, L. V.; Valetsky, P. M.; Kiselyova, O. I.; Khokhlov, A. R.; Stein, B.; Bronstein, L. M. *J. Mol. Catal. A: Chem.* **2004**, *208* (1-2), 273.

(50) Anderson, K.; Cortinas Fernandez, S.; Hardacre, C.; Marr, P. C. *Inorg. Chem. Commun.* **2003**, *7* (1), 73.

(51) Weertman, J. R.; Averback, R. S.; in *Nanomaterials: Synthesis, properties and applications*, eds. Edelstein, A. S.; Cammarata, R. C. London, Institute of Phys. Publ., **1996**, chapter *13*, 323.

(52) Auschalorn, D. D.; Di Vincenzo, D. P. Smyth, J. F. *Science*, **1992**, *258*, 414.

(53) (a) Glomm, W.R. *J. Dispersion Sci. Technol.* **2005**, *26*, 389. (b) Salata, O.V. *J. Nanobiotechnology* **2004**, *2*, 3. (c) West, J.L.; Halas, N.J. *Curr. Opin. Biotechnol.* **2000**, *11*, 215. (d) Katz, E.; Willner, I. *Angew. Chem. Int. Ed.* **2004**, *43*, 6042.

(54) Rosi, N.L.; Mirkin, C.A. *Chem. Rev.* **2005,** *105*, 1547.

(55) (a) Shaw III, C.F. *Chem. Rev.* **1999,** *99,* 2589. (b) Pissuwan, D.; Valenzuela, S.M.; Cortie, M.B. *Trends Biotechnol.* **2006**, *24*, 62.

(56) (a) Emerich, D.F.; Thanos, C.G. *Biomol. Eng.* **2006**, *23*, 171. (b) Niemeyer C.M. *Angew. Chem. Int. Ed.* **2001**, *40*, 4128. (c) Sanford, J.C.; Smith, F.D.; Russell, J.A. *Methods Enzymol.* **1993**, *217*, 483.

(57) (a) Sharma, P.; Brown, S.; Walter, G.; Santra, S.; Moudgil, B. *Adv. Colloid Interface Sci.* **2006**, *123-126*, 471. (b) Bielinska, A.; Eichman, J.D.; Lee, I.; Baker, J.R., Jr.; Balogh, L. *J. Nanopart. Res.* **2002**, *4*, 395.

(58) Roth, J. *Histochem. Cell Biol.* **1996**, *106*, 1.

(59) Olofsson, L.; Rindzevicius, T.; Pfeiffer, I.; Kall, M.; Hook, F. *Langmuir* **2003**, *19*, 10414.

(60) (a) Warheit, D.B.; Laurence, B.R.; Reed, K.L.; Roach, D.H.; Reynolds, G.A.; Webb, T.R. *Toxicol. Sci.* **2004**, *77*, 117. (b) Lam, C.W.; James, J.T.; McCluskey, R.; Hunter, R.L. *Toxicol. Sci.* **2004**, *77*, 126. (c) Kam, N.W.S.; Jessop, T.C.; Wender, P.A.; Dai, H. *J. Am. Chem. Soc.* **2004**, *126*, 6850.

(61) (a) Ballou, B.; Lagerholm, B.C.; Ernst, L.A.; Bruchez, M.P.; Waggoner, A.S.; Larson, D.R.; Zipfel, W.R.; Williams, R.M.; Clark, S.W.; Wise, F.W.; Webb, W.W.; Wu, X.; Liu, H.; Liu, J.; Haley, K.N.; Treadway, J.A.; Larson, J.P.; Ge, N.; Peale, F. *Bioconjugate Chem.* **2004**, *15*, 79. (b) Derfus, A.M.; Chan, W.C.; Bhatia, S.N. *Nano Lett.* **2004**, *4*, 11. (c) Larson, D.R.; Zipfel, W.R.; Williams, R.M.; Clark, S.W.; Bruchez, M.P.; Wise, F.W.; Webb, W.W.; Wu, X.; Liu, H.; Liu, J.; Haley, K.N.; Treadway, J.A.; Larson, J.P.; Ge, N.; Peale, F. *Science* **2003**, *300*, 1434. (d) Wu, X.; Liu, H.; Liu, J.; Haley, K.N.; Treadway, J.A.; Larson, J.P.; Ge, N.; Peale, F.; Bruchez, M.P. *Nat. Biotechnol.* **2003**, *21*, 41.

(62) (a) Thomas, M.; Klibanov, A.M. *Proc. Natl. Acad. Sci. USA* **2003**, *100*, 9138. (b) Tkachenko, A.G.; Xie, H.; Coleman, D.; Glomm, W.; Ryan, J.; Anderson, M.F.; Franzen, S.; Feldheim, D.L. *J. Am. Chem. Soc.* **2003**, *125*, 4700. (c) Tkachenko, A.G.; Xie, H.; Liu, Y.; Coleman, D.; Ryan, J.; Glomm, W.; Shipton, M.K.; Franzen, S.; Feldheim, D.L. *Bioconjugate Chem.* **2003**, *14*, 482. (d) Hillyer, J.F.; Albrecht, R.M. *J. Pharm. Sci.* **2001**, *90*, 1927. (e) Tsoli, M.; Kuhn, H.; Brandau, W.; Esche, H.; Schmid, G. *Small* **2005**, *1*, 841. (f) Connor, E.E.; Mwamuka, J.; Gole, A.; Murphy, C.J.; Wyatt, M.D. *Small* **2005**, *1*, 325. (g) Shukla, R.; Bansal, V.; Chaudhary, M.; Basu, A.; Bhonde, R.R.; Sastry, M. *Langmuir* **2005,** *21,* 10644.

(63) Sokolov, K.; Follen, M.; Aaron, J.; Pavlova, I.; Malpica, A.; Lotan, R. Kortum, R. R. *Cancer Research* **2003**, *63*, 1999.

(64) Qi, W.H.; Wang, M.P.; Su, Y.C. J. Mater. Sci. Lett. **2002**, *21*, 877.

(65) (a) Buffat, P.; Borel, J.-P. *Phys. Rev. A* **1976**, *13*, 2287. (b) Castro, T.; Reifenberger, R.; Choi, E.; Andres, R.P. *Phys. Rev. B* **1990**, *42*, 8548. (c) Beck, R.D.; St. John, P.; Homer, M.L.; Whetten, R.L. *Science* **1991**, *253*, 879. (d) Martin, T.P.; Naher, U.; Schaber, H.; Zimmermann, U. *J. Chem. Phys.* **1994**, *100*, 2322.

(66) (a) Couchman, P.R.; Jesser, W.A. *Nature* **1977**, *269*, 481. (b) Ercolessi, F.; Andreoni, W.; Tosatti, E. *Phys. Rev. Lett.* **1991**, *66*, 911.

(67) (a) Mie, G. *Ann. Phys*. **1908**, *25*, 377. (b) Greighton, J.A.; Eadon, D.G. *J. Chem. Soc. Faraday Trans.* **1991**, *87*, 3881. (c) Mulvaney, P. *Langmuir* **1996**, *12*, 788.

(68) Johnson, P.B.; Christy, R.W. *Phys. Rev. B* **1972**, *6*, 4370.

(69) Link, S; El-Sayed, M.A. *Annu. Rev. Phys. Chem.***2003**, *54*, 331.

(70) Burda, C.; Chen, X.; Narayanan, R.; El-Sayed, M.A. *Chem. Rev.* **2005**, *105*, 1025.

(71) Gans, R. *Ann. Phys.* **1915**, *47*, 270.

(72) (a) van der Zande, B.M.I.; Bohmer, M.R.; Fokkink, L.G.J.; Schonenberger, C. *J. Phys. Chem. B* **1997**, *101*, 852. (b) Yu, Y.Y.; Chang, S.S.; Lee, C.L.; Wang, C.R.C. *J. Phys. Chem. B* **1997**, *101*, 6661.

(73) Millstone, J.E.; Park, S.; Shuford, K.L.; Qin, L.; Schatz, G.C.; Mirkin, C.A. *J. Am. Chem. Soc.* **2005**, *127*, 5312.

(74) (a) Busbee, B D.; Obare, S.O.; Murphy; C.J *Adv. Mater.* **2003**, *15*, 414. (b) Chang, S.-S.; Shih, C.-W.; Chen, C.-D.; Lai, W.-C.; Wang, C.R.C. *Langmuir* **1999**, *15*, 701. (c) Chemseddine, A.; Moritz, T. *Eur. Inorg. Chem.* **1999**, 235. (d) Jana, N.R.; Gearheart, L.; Murphy, C.J. *Chem. Commun.* **2001**, 617. (e) Kim, F.; Song, J.H.; Yang, P. *J. Am. Chem. Soc.* **2002**, *124*, 14316. (f) Tang, Z.; Kotov, N.A.; Giersig, M. *Science* **2002**, *297*, 237. (g) Xia, Y.N.; Yang, P.D.; Sun, Y.G.; Wu, Y.Y.; Mayers, B.; Gates, B.; Yin, Y.D.; Kim, F.; Yan, Y.Q.; *Adv. Mater.* **2003**, *15*, 353.

(75) (a) Chen, S.; Fan, Z.; Carroll, D.L. *J. Phys. Chem. B* **2002**, *106*, 10777. (b) Hao, E.; Kelly, K.L.; Hupp, J.T.; Schatz, G.C. *J. Am.Chem. Soc.* **2002**, *124*, 15182. (c) Maillard, M.; Giorgio, S.; Pileni, M.-P. *Adv. Mater.* **2002**, *14*,1084. (d) Puntes, V.F.; Zanchet, D.; Erdonmez, C.K.; Alivisatos, A.P. *J. Am. Chem. Soc.* **2002**, *124*, 12874. (e) Maillard, M.; Huang, P.; Brus, L. *Nano Lett.* **2003**, *3*, 1611.

(76) (a) Jin, R.; Cao, Y.; Mirkin, C.A.; Kelly, K.L.; Schatz, G.C.; Zheng, J.G. *Science* **2001**, *294*, 1901. (b) Chen, S.; Carroll, D.L. *Nano Lett.* **2002**, *2*, 1003. (c) I. Pastoriza-Santos, L.M. Liz-Marźan, *Nano Lett.* **2002**, *2*, 903. (d) Y. Sun, B. Mayers, Y. Xia, *Nano Lett.* **2003**, *3*, 675. (e) Yang, J.; Fendler, J.H. *J. Phys. Chem* **1995**, *99*, 5505. (f)

Jin, R.; Cao, Y.; Hao, E.; Metraux, G.; Schatz, G.C.; Mirkin, C.A. *Nature* **2003**, *425*, 487. (g) Shankar, S.S.; Rai, A.; Ankamwar, B.; Singh, A.; Ahmad, A.; Sastry, M. *Nat. Mater.* **2004**, ***3,*** 482

(77) (a) Lee, S.-M.; Jun, Y.-W.; Cho, S.N.; Cheon, J. *J. Am. Chem.Soc.* **2002**, *124*, 11244. (b) Chen, S.; Wang, Z.L.; Ballato, J.; Foulger, S.H.; Carroll, D.L. *J. Am. Chem. Soc.* **2003**, *125*, 16186. (c) Manna, L.; Milliron, D.J.; Meisel, A.; Scher, E.C.; Alivisatos, A.P. *Nature Mater.* **2003**, *2*, 382. (d) Manna, L.; Scher, E.C.; Alivisatos, A.P. *J. Am. Chem.Soc.* **2000**, *122*, 12700. (e) Hao, E.; Bailey, R.C.; Schatz, G.C.; Hupp, J.T.; Li, S. *Nano Lett.* **2004**, *4*, 327.

(78) (a) Sun, Y.; Xia, Y. *Science* **2002**, *298*, 2139. (b) Ahmadi, T.S.; Wang, Z.L.; Green, T.C.; Henglein, A.; El-Sayed, M.A. *Science* **1996**, *272*, 1924.

(79) (a) Oldenburg, S.J.; Jackson, J.B.; Westcott, S.L;. Halas, N.J. *Appl. Phys. Lett.* **1999**, *75*, 897. (b) Jackson, J.B.; Halas, N.J. *J. Phys. Chem. B* **2001**, *105*, 2743. (c) Graf, C.; Blaaderen, A.v. *Langmuir* **2002**, *18*, 524. (d) Pordan, E.; Nordlander, P. *Nano Lett.* **2003**, *3*, 543. (e) Oldenburg, S.J.; Averitt, R.D.; Westcott, S.L.; Halas, N.J. *Chem. Phys. Lett.* 1998, *288*, 243. (f) Jin, Y.; Dong, S. *J. Phys. Chem. B* **2003**, *107*, 12902.

(80) Papavassiliou, G. C. *J. Phys. F: Met. Phys.* **1976**, *6*, L103.

(81) Sinzig, J.; Radtke, U.; Quinten, M.; Kreibig, U. *Z. Phys. D* **1993**, *26*, 242.

(82) Teo, B. K.; Keating, K.; Kao, Y.-H. *J. Am. Chem. Soc.* **1987**, *109*, 3494.

(83) Treguer, M.; de Cointet, C.; Remita, H.; Khatouri, J.; Mostafavi, M.; Amblard, J.; Belloni, J.; de Keyzer, R. *J. Phys. Chem. B* **1998**, *102*, 4310.

(84) Link, S.; Wang, Z. L.; El-Sayed, M. A. *J. Phys. Chem. B* **1999**, *103*, 3529.

(85) Carey Lea, M. *Am. J. Sci.* **1889**, *37*, 476.

(86) Mulvaney, P.; Giersig, M.; Henglein, A. *J. Phys. Chem.* **1993**, *97*, 7061.

(87) Kreibig, U.; Vollmer, M. *Optical Properties of Metal Clusters*; Springer: Berlin, **1995**.

(88) Schmid, G. *Metals: In Nanoscale Materials in Chemistry*; (Ed. Klabunde, K.J.), Wiley-Interscience: New York, **2001**, *Chapter 2*, 15.

(89) (a) Schön, G.; Simon, U. *Colloid Polym. Sci.* **1995**, *273*, 101. (b) Schön, G.; Simon, U. *Colloid Polym. Sci.* **1995**, *273*, 202.

(90) Simon, U.; G. Schön, *Handbook of Nanostructured Materials and Nanotechnology* (Ed.: H. S. Nalwa), Academic Press **2000**, *Vol. 3*, 131.

(91) Torma, V.; Vidoni, O.; Simon, U.; Schmid, G. *Eur. J. Inorg. Chem.* **2003**, 1121.

(92) Mott, N.F. *Philos. Mag.* **1969**, *19*, 835.

(93) (a) Dyre, J.C.; *Phys. Rev. B* **1993**, *47*, 9128. (b) Dyre, J.C. *Phys. Rev. B* **1994**, *49*, 11709.

(94) (a) Wuelfing, W.P.; Green, S.J.; Pietron, J.J.; Cliffel, D.E.; Murray, R.W. *J. Am. Chem. Soc.* **2000**, *122*, 11465. (b) Wuelfing, W.P.; Murray, R.W. *J. Phys. Chem. B* **2002**, *106*, 3139.

(95) Peng, X.; Wickham, J.; Alivisatos, A. P. *J. Am. Chem. Soc.* **1998**, *120*, 5343.

(96) Murray C. B.; Kagan, C. R.; Bawendi, M. G. *Annu. Rev. Mater. Sci.* **2000**, *30*, 545.

(97) Pamplin, B. R. *Crystal Growth*; Pergamon Press: New York, **1975**.

(98) Jiang, Y. Forced Hydrolysis and Chemical Co-Precipitation. In *Handbook of Nanophase and Nanostructured Materials*; Wang, Z. L., Liu, Y., Zhang, Z., Eds.; Kluwer Academic: New York, **2003**; p 59.

(99) Helcher, H. H. ; *J. Herbord Klossen: Breslau and Leipzig*, **1718**.

(100) Faraday, M. *Philos. Trans*. **1857**, *147*, 145.

(101) Wegner, K.; Walker, B.; Tsantilis, S.; Pratsinis, S.E. *Chem. Eng. Sci.* **2002**, *57*, 1753. (b) Choi, C.J.; Tolochko, O.; Kim, B.K. *Mater. Lett.* **2002**, *56*, 289. (c) Wang, Z.H.; Choi, C.J.; Kim, J.C.; Kim, B.K.; Zhang, Z.D. *Mater. Lett.* **2003**, *57*, 3560. (d) Oha, S.; Choi, C.; Kwon, S.; Jin, S.; Kim, B.; Park, J. *J. Magn. Magn. Mater.* **2004**, *280*, 147. (e) Chevallier, J. *Thin Solid Films* **1977**, *40*, 223. (f) Perekrestov, V.I. *Tech. Phys. Lett.* **2005**, *31*, 830.

(102) (a) Wang, Y.; Zhang, L.; Meng, G.; Liang, C.; Wang, G.; Sun, S. *Chem.Commun.* **2001**, 2632. (b) Teng, X.; Black, D.; Watkins, N.J.; Gao, Y.; H. Yang, *Nano Lett.* **2003**, *3*, 261. (c) Wang, Y.; Herricks, T.; Xia, Y. *Nano Lett.* **2003**, *3*, 1163. (d) Hou,

Y.; Kondoh, H.; Kogure, T.; Ohta, T. Chem. Mater. **2004,** *16,* 5149. (e) Lee, D.K.; Kang, Y.S. *ETRI Journal* **2004**, *26*, 252.

(103) (a) Kim, J.H.; Germer, T.A.; Mulholland, G.W.; Ehrman, S.H. *Adv. Mater.* **2002**, *14*. 518. (b) Mädler, L.; Kammler, H.K.; Mueller, R.; Pratsinis, S.E. *J. Aerosol Sci.* **2002**, *33*, 369. (c) Okuyama, K.; Lenggoro, I.W. *Chem. Eng. Sci.* **2003**, *58*, 537. (d) Mueller, R.; Mädler, L.; Pratsinis, S.E. Chem. Eng. Sci. 2003, 58, 1969. (e) Suh, W.H.; Suslick, K.S. *J. Am. Chem. Soc.* **2005**, 127, 12007.

(104) (a) Zhou, Y.; Wang, C.Y.; Zhu, Y.R., Chen, Z.Y. *Chem. Mater.* **1999**, *11*,2310. (b) Li, H.X.; Lin, M.Z.; Hou, J.G. *J. Crystal Growth* **2000**, *212*, 222. (c) Mallick , K.; Wang , Z.L.; Pal, T. *J. Photochem. Photobiol. A* **2001**, *140*, 75. (d)Chen, W.X.; Lee, J.Y.; Liu, Z. *Chem. Commun.* **2002**, 2588. (e) Mandal, M.; Kundu, S.; Ghosh, S.K.; Pal, T. *Bull. Mater. Sci.* **2002**, *25*, 509. (f) Yin, H.; Yamamoto, T.; Wada, Y.; Yanagida, S. *Mater. Chem. Phys.* **2004**, *83*, 66. (g) Zhua, H.; Zhang, C.; Yin, Y. *J. Crystal Growth* **2004**, *270*, 722. (h) Kimling, J.; Maier, M.; Okenve, B.; Kotaidis, V.; Ballot, H.; Plech, A. *J. Phys. Chem. B* **2006,** *110,* 15700. (i) Sakamoto, M.; Tachikawa, T.; Fujitsuka, M.; Majima, T. Langmuir, **2006**, *22,* 6361. (j) Jia, H.; Xu, W.; An, J.; Li, D.; Zhao, B. *Spectrochimica Acta A* **2006**, *64*, 956. (k) Itakura, T.; Torigoe, K.; Esumi, K. *Langmuir* **1995**,*11*, 4129. (l) Ershov, B. G.; Henglein, A. *J. Phys. Chem.* **1993**, *97*, 3434. (m) Gutierrez, M.; Henglein, A. *J. Phys. Chem.* **1993**, *97*, 11368. (n) Torigoe, K.; Esumi, K. *Langmuir* **1993**, *9*, 1664. (o) Torigoe, K.; Esumi, K. *Langmuir* **1992**, *8*, 59. (p) Esumi, K.; Matsuhisa, K.; Torigoe, K. *Langmuir* **1995**, *11*, 3285. (q Marignier, J. L.; Belloni, J.; Delcourt, M. 0.; Chevalier, J. P. *Nature* **1985**, *317*, 344.

(105) (a) Amendola, V.; Polizzi, S.; Meneghetti, M. *J. Phys. Chem. B* **2006,** *110,* 7232. (b) Amendola, V.; Rizzi, G.A.; Polizzi, S.; Meneghetti, M. *J. Phys. Chem. B* **2005**, *109*, 23125. (c) Balchev, I.; Minkovski, N.; Marinova, Ts.; Shipochka, M.; Sabotinov, N. *Mater. Sci. Eng. B* **2006**, *135*, 108. (d) Becker, M.F.; Brock, J.R.; Cai, H.; Henneke, D.E.; Keto, J.W.; Lee, J.; Nichols, W.T.; Clicksman, H.D. *Nanostruct. Mater.* **1998**, *10*, 853. (e) Mafuné, F.; Kohno, J.; Takeda, Y.; Kondow, T. *J. Phys. Chem. B* **2000,**

104, 9111. (f) Mafuné, F.; Kohno, J.; Takeda, Y.; Kondow, T. *J. Phys. Chem. B* **2000**, *104*, 8333. (g) Mafuné, F.; Kohno, J.; Takeda, Y.; Kondow, T.; Sawabe, *J. Phys. Chem. B* **2001**, *105*, 5114. (h) Mafuné, F.; Kohno, J.; Takeda, Y.; Kondow, T. *J. Phys. Chem. B* **2002**, *106*, 7575. (i) Zhu, X.P.; Suzuki, T.; Nakayama, T.; Suematsu, H.; Jiang, W.; Niihara, K. *Chem. Phys. Lett.* **2006**, *427*, 127. (j) Cai, H.; Chaudhary, N.; Lee, J.; Becker, M.F.; Brock, J.R.; Keto, J.W. *J. Aerosol Sci*. **1998**, *5/6*, 627.

(106) (a) Chen, W.; Cai, W.; Lei, Y.; Zhang, L. *Mater. Lett.* **2001**, *50*, 53. (b) Chen, W.; Cai, W.; Zhang, L.; Wang, G.; Zhang, L. *J. Colloid Interface Sci.* **2001**, *238*, 291. (c) Dhas, N.A., Raj, C.P., Gedanken, A. *Chem. Mater.* **1998,** *10,* 1446. (d) Fujimoto, T.; Terauchi, S.; Umehara, H.; Kojima, I.; Henderson, W. *Chem. Mater.* **2001,** *13,* 1057. (e) Fujimoto, T.; Mizukoshi, Y.; Nagata, Y.; Maeda, Y.; Oshima, R. Scripta Mater. 2001, 44, 2183. (f) Nemamcha, A.; Rehspringer, J.; Khatmi, D. *J. Phys. Chem. B* **2006,** *110,* 383. (g) Okitsu, K.; Mizukoshi, Y.; Bandow, H.; Yamamoto, T.A.; Nagata, Y.; Maeda, Y. *J. Phys. Chem. B* **1997,** *101,* 5470. (h) Pol, V.G.; Grisaru, H.; Gedanken, A. *Langmuir* **2005,** *21,* 3635. (i) Salkar, R.A.; Jeevanandam, P.; Aruna, S.T.; Koltypin, Y.; Gedanken, A. *J. Mater. Chem.* **1999**, *9*, 1333. (j) Su, C.; Wu, P.; Yeh, C. *J. Phys. Chem. B* **2003,** *107,* 14240. (k) Suslick, K.S.; Fang, M.; Hyeon, T. *J. Am. Chem. Soc.* **1996,** *118,* 11960. (l) Wu, C.; Mosher, B.P.; Zeng, T. *Chem. Mater.* **2006**, *18*, 2925.

(107) (a) Kurihara, K.; Kizing, J.; Stenius, P.; Fender, J. H. *J. Am. Chem.Soc.* **1983**, *105*, 2574. (b) Mulvaney, P.; A. Henglein, *J. Phys. Chem.* **1990**, *94*, 4182. (c) Joshi, S.S.; Patil, S.F.; Iyer, V.; Mahumuni, S. Nanostruct. Mater. **1998**, *7*, 1135. (d) Henglein, A.; Meisel, D. Langmuir **1998,** *14,* 7392. (e) Gachard, E.; Remita, H.; Khatouri, J.; Keita, B.; Nadjo, L.; Belloni, J. *New J. Chem.* **1998**, 1257. (f) Henglein, A.; Giersig, M. *J. Phys. Chem. B* **1999,** *103,* 9533. (g) Dimitrijevic, N.M.; Bartels, D.M.; Jonah, C.D.; Takahashi, K.; Rajh, T. *J. Phys. Chem. B* **2001,** *105,* 954. (h) Doudna, C.M.; Bertino, M.F.; Blum, F.D.; Tokuhiro, A.T.; Lahiri-Dey, D.; Chattopadhyay, S.; Terry, J. *J. Phys. Chem. B* **2003**, *107,* 2966.

(108) (a) Stoeva, S.I.; Prasad, B.L.V.; Uma, S.; Stoimenov, P.K.; Zaikovski, P.; Sorensen, C.M.; Klabunde, K.J. *J. Phys. Chem. B* **2003,** *107,* 7441. (b) Ponce, A.A.; Klabunde, K.J. *J. Mol. Catal.*2005, 225, 1. (c) Smetana, A.B.; Klabunde, K.J.; Sorensen C.M. *J. Colloid Interface Sci.* **2005**, *284*, 521. (d) Klabunde, K. J.; Timms, P. S.; Skell, P. S.; Ittel, S. *Inorg. Synth.* **1979**, *19*, 59. (e) Davis, S. C.; Klabunde, K. J. *Chem. Rev.* **1982**, *82*, 153. (f) Stoeva, S.; Klabunde, K.J.; Sorensen, C.M.; Dragieva, I. *J. Am. Chem. Soc.* **2002**, *124*, 2305.

(109) (a) Armelao, L.; Bertoncello, R.; De Dominicis, M. *Advanced Materials* **1997**, *9*, 736. (b) Devarajan, S.; Bera, P.; Sampath, S. *J. Colloid Interface Sci.* **2005**, *290*, 117. (c) Shukla, S.; Seal, S. Nanostruct. Mater. 1999, 11, 1181.

(110) (a) Gao, F.; Lu, Q.; Komarneni, S. *Chem. Mater.* **2005,** *17,* 856. (b) Rosemary, M.J.; Pradeep, T. *J. Colloid Interface Sci.* **2003**, *268*, 81.

(111) (a) Bronstein, L.M.; Chernyshov, D.M.; Timofeeva, G.I.; Dubrovina, L.V.; Valetsky, P.M.; Obolonkova, E.S.; Khokhlov, A.R. *Langmuir* **2000**, *16*, 3626. (b) Bronstein, L.M.; Sidorov, S.N.; Valetsky, P.M.; Hartmann, J.; Cölfen, H.; Antonietti, M. *Langmuir* **1999**, *15*, 6256. (c) Lee, C.-L.; Wan, C.-C.; Wang, Y.-Y. *Adv. Funct. Mater.* **2001**, *11*, 344.

(112) (a) Sun, Y.; Xia, Y. *J. Am. Chem. Soc.* **2004**, *126*, 3892 (b) Sun, Y.; Mayers, B. T.; Xia, Y. *Adv. Mater.* **2003**, *15*, 641 (c) Sun, Y.; Xia, Y. *Nano Lett.* **2003**, *3*, 1569 (d) Jin, Y.; Dong, S. *J. Phys. Chem. B* **2003,** *107,* 12902 (e) Sun, Y.; Mayers, B.T.; Xia, Y. *Nano Lett.* **2002**, *2*, 481 (f) Chen, J.; Saeki, F.; Wiley, B.J.; Cang, H.; Cobb, M.J.; Li, Z.Y.; Au, L.; Zhang, H.; Kimmey, M.B.; Li, X.D.; Xia, Y. *Nano Lett.* **2005**, *5*, 473. (g) Shukla, S.; Priscilla, A.; Banerjee, M.; Bhonde, R.R.; Ghatak, J.; Satyam, P.V.; Sastry, M. *Chem. Mater.* **2005**, *17*, 5000. (h) Liang, H.-P., Guo, Y.-G., Zhang, H.-M., Hu, J.-S., Wan, L.-J.,. Bai, C.-L *Chem. Commun.* **2004**, 1496. (i) Selvakannan, P. R.; Sastry, M. *Chem. Commun.* **2005**, 1684

(113) (a) Cliffel, D. E.; Zamborini, F. P.; Gross, S. M.; Murray, R. W. *Langmuir* **2000**, *16*, 9699. (b) Yonezawa, T.; Onoue, S.; Kimizuka, N. *Langmuir* **2000**, *16*, 5218. (c) Thomas, K.G.; Zajicek, J.; Kamat, P.V. *Langmuir* **2002,** *18,* 3722.

(114) (a) Henhar, R.S.; Norstern, T.B.; Rotello, V.M. *Adv. Mater.* **2005**, *17*, 657. (b) Cheng, J.; Teply, B.A.; Sherifi, I.; Sung, J.; Luther, G.; Gu, F.X.; Levy-Nissenbaum, E.; Radovic-Moreno, A.F.; Langer, R.; Farokhzad, O.C. *Biomaterials* **2007**, *28*, 869. (c) Hoppe, C.E.; Lazzari, M.; Pardiñas-Blanco, I.; López-Quintela, M.A. *Langmuir* **2006,** *22,* 7027. (d) Qian, X.F.; Yin, J.; Feng, S.; Liu, S.H.; Zhu, Z.K. *J. Mater.Chem.* **2001**, *11*, 2504. (e) Sidorov, S.N.; Bronstein, L.M.; Valetsky, P.M.; Hartmann, J.; Cölfen, H.; Schnablegger, H.; Antonietti, M. *J. Colloid Interface Sci.* **1999**, *212*, 197. (f) Xiong, Y.; Washio, I.; Chen, J.; Cai, H.; Li, Z.–Y.; Xia, Y. *Langmuir* **2006,** *22,* 8563. (g) Mu, X.; Evans, D.G.; Kou, Y. *Catal. Lett.* **2004**, *97*, 151.

(115) (a) Selvakannan, PR.; Mandal, S.; Phadtare, S.; Pasricha, R.; Sastry, M. *Langmuir* **2003,** *19,* 3545. (b) Selvakannan, PR.; Mandal, S.; Phadtare, S.; Gole, A.; Pasricha, R.; Adyanthaya, S.D.; Sastry, M. *J. Colloid Interface Sci.* **2004**, *269*, 97. (c) Zhong, Z.; Patskovskyy, S.; Bouvrette, P.; Luong, J.H.T.; Gedanken, A. *J. Phys. Chem. B* **2004,** *108,* 4046. (d) Huang, Y.-F.; Lin, Y.-W.; Chang, H.-T. *Nanotechnology* **2006**, *17*, 4885. (e) Naka, K.; Itoh, H.; Tampo, Y.; Chujo, Y. *Langmuir* **2003,** *19,* 5546. (f) Fan, J.; Chen, S.; Gao, Y. *Colloids Surf. A* **2003**, *28*, 199. (g) Fujiki, Y.; Tokunaga, N.; Shinkai, S.; Sada, K. *Angew. Chem. Int. Ed.* **2006**, *45*, 4764. (h) Aubin-Tam, M.; Hamad-Schifferli, K *Langmuir* **2005,** *21,* 12080. (i) You, C.-C., De, M., Han, G., Rotello, V.M. *J. Am. Chem. Soc.* **2005**, *127*, 12873. (j) Bhargava, S.K.; Booth, J.M.; Agrawal, S.; Coloe, P.; Kar, G. *Langmuir* **2005,** *21,* 5949. (k) Sanyal, A.; Mandal, S.; Sastry, M. *Adv. Funct. Mater.* **2005**, *15*, 273. (l) Selvakannan, PR.; Swami, A.; Srisathiyanarayanan, D.; Shirude, P.S.; Pasricha, R.; Mandale, A.B.; Sastry, M. *Langmuir* **2004,** *20,* 7825. (m) Joshi, H.; Shirude, P.S.; Bansal, V.; Ganesh, K.N.; Sastry, M. *J. Phys. Chem. B* **2004,** *108,* 11535.

(116) Brust, M.; Walker, M.; Bethell, D.; Schiffrin, D. J.; Whyman, R. *J. Chem. Soc., Chem. Commun*. **1994**, 801.

(117) (a) Ye, H.; Scott, R. W. J.; Crooks, R. M. *Langmuir* **2004**, *20*, 2915. (b) Yee, C.; Scotti, M.; Ulman, A.; White, H.; Tafailovich, M.; Sokolov, J. *Langmuir* **1999**, *15*, 4314. (c) Hasan, M.; Bethell, D.; Brust, M. *J. Am. Chem. Soc.* **2002**, *124*, 1132. (d)

Brust, M.; Stuhr-Hansen, N.; Norgaard, K.; Christensen, J. B.; Nielsen, L. K.; Bjornholm, T. *Nano Lett.* **2001**, *1*, 189. (e) Rautaray, D.; Kumar, P. S.; Wadgaonkar, P. P.; Sastry, M. *Chem. Mater.* **2004**, *16*, 988. (f) Kumar, A.; Mandal, S.; Selvakannan, P. R.; Pasricha, R.; Mandale, A. B.; Sastry, M. *Langmuir* **2003**, *19*, 6277. (g) templateon, A. C.; Chen, S.; Gross, S. M.; Murray, R.W.*Langmuir* **1999**, *15*, 66. (h) templateon, A. C.; Cliffel, D. E.; Murray, R. W. *J. Am. Chem. Soc.* **1999**, *121*, 7081. (i) Wuelfing, W. P.; Gross, S. M.; Miles, D. T.; Murray, R.W. *J. Am.Chem. Soc*. **1998**, *120*, 12696. (j) Schaff, T. G.; Knight, G.; Shaffigulin, M. N.; Borkman, R. F.; Whetten, R. L. *J. Phys. Chem. B* **1998**, *102*, 10643. (k) Brust, M.; Fink, J.; Bethell, D.; Schiffrin, D. J.; Kiely, C. J. *J. Chem. Soc., Chem. Commun*. **1995**, 1655. (l) Johnson, S. R.; Evans, S. D.; Brydson, R. *Langmuir* **1998**, *14*, 6639. (m) Chen, S.; Kimura, K. *Langmuir* **1999**, *15*, 1075. (n) Shon, Y. S.; Wuelfing, W. P.; Murray, R. W. *Langmuir* **2000**, *17*, 1255. (o) Huang, J.; He, C.; Liu, X.; Xiao, Y.; Mya, K. Y.; Chai, J. *Langmuir* **2004**, *20*, 5145. (p) Huang, J.; Liu, Z.; Liu, X.; He, C.; Chow, S.Y.; Pan, J. *Langmuir* **2005,** *21,* 699. (q) Schmid, G.; Lehnert, A. *Angew. Chem. Int. Ed. Engl.* **1989**, *28*, 780. (r) Schmid, G. *Chem. Rev.* **1992**, *92*, 1709. (s) Naka, K.; Yaguchi, M.; Chujo, Y. *Chem. Mater.* **1999**, *11*, 849. (t) Leff, D.V.; Brandt, L.; Heath, J.R. *Langmuir* **1996**, *12*, 4723. (u) Brown, L.O.; Hutchison, J.E. *J. Phys. Chem. B.* **2001**, *105*, 8911. (v) Stevenson, K.A.; Muralidharan, G.; Maya, L.; Wells, J.C.; Barhen, J.; Thundat, T. *J. Nanosci. Nanotech.* **2002**, *2*, 397. (w) Murakoshi, K.; Nakato, Y. *Adv. Mater.* **2000**, *12*, 791.

(118) (a) Brust, M.; Fink, J.; Bethell, D.; Schiffrin, D. J.; Kiely, C. J. *J. Chem. Soc., Chem. Commun*. **1995**, 1655. (b) Knecht, M.R.; Garcia-Martinez, J.C.; Crooks, R.M. *Langmuir* **2005,** *21,* 11981. (c) Cardenas-Trivino, G.; Klabunde, K. J.; Dale, E. B. *Langmuir* **1987**, *3*, 986. (d) Mandal, S.; Das, A.; Srivastava, R.; Sastry, M. *Langmuir* **2005,** *21,* 2408. (e) Schlotterbeck, U.; Aymonier, C.; Thomann, R.; Hofmeister, H.; Tromp, M.; Richtering, W.; Mecking, S. *Adv. Funct. Mater.* **2004**, *14*, 999. (f) Cozzoli, P.D.; Comparelli, R.; Fanizza, E.; Curri, M.L.; Agostiano, A.; le Laub, D. *J. Am. Chem. Soc.* **2004**, *126*, 3868.

(119) (a) Kim, K.-S.; Demberelnyamba, D.; Lee, H. *Langmuir*, **2004**, *20*, 556. (b) Wang, Y.; Yang, H. *Chem. Commun.* **2006**, 2545. (c) Zhao, D.; Fei, Z.; Ang, W.H.; Dyson, P.J. *Small* **2006**, *2*, 879. (d) Scheeren, C.W.; Machado, G.; Teixeira, S.R.; Morais, J.; Domingos, J.B.; Dupont, J. *J. Phys. Chem. B* **2006,** *110,* 13011.

(120) (a) Sun, Y.; Riggs, J.E.; Rollins, H.W.; Guduru, R. *J. Phys. Chem. B* **1999,** *103,* 77. (b) Cason, J.P.; Roberts, C.B. *J. Phys. Chem. B* **2000**, *104,* 1217. (c) Cason, J.P.; Khambaswadkar, K.; Roberts, C.B. *Ind. Eng. Chem. Res.* **2000,** *39,* 4749. (d) Ohde, H.; Hunt, F.; Wai, C.M. *Chem. Mater.* **2001,** *13,* 4130. (e) N.Z. Clarke, C. Waters, K.A. Johnson, J. Satherley, D.J. Schiffrin, *Langmuir* **2001,** *17,* 6048. (f) Morley, K.S.; Marr, P.C.; Webb, P.B.; Berry, A.R.; Allison, F.J.; Moldovan, G.; Brown, P.D.; Howdle, S.M. *J. Mater.Chem.***2002**, *12*, 1898. (g) X.-R. Ye, Y. Lin, C. Wang, M.H. Engelhard, Y. Wang, C.M. Wai, *J . Mater. Chem.***2004**, *14*, 908. (h) Morley, K.S.; Licence, P.; Marr, P.C.; Hyde, J.R.; Brown, P.D.; Mokaya, R.; Xia, Y.; Howdle, S.M. *J. Mater. Chem.* **2004**, *14*, 1212. (i) Esumi, K.; Sarashina, S.; Yoshimura, T. *Langmuir* **2004,** *20,* 5189. (j) Hou, Z.; Theyssen, N.; Brinkmann, A.; Leitner, W. *Angew. Chem. Int. Ed.* **2005**, *44*, 1346. (k) Sun, Z.; Fu, L.; Liu, Z.; Han, B.; Liu, Y.; Du, J. *J. Nanosci. Nanotechnol.* **2006**, *6*, 691.

(121) (a) Bronstein, L.; Krämer, E.; Berton, B.; Burger, C.; Förster, S.; Antonietti, M. *Chem. Mater.* **1999,** *11,* 1402. (b) Jana, N.R. *Small* **2005**, *1*, 875. (c) Pileni, M.P. *Supramol. Sci.* **1998**, *5*, 321. (d) Pileni, M.P.; Ninham, B.W.; Gulik-Krzywicki, T.; Tanori, J.; Lisiecki, I.; Filankembo, A. *Adv. Mater.* **1999**, *11*, 1358. (e) Pileni, M.P.; Gulik-Krzywicki, T.; Tanori, J.; Filankembo, A.; Dedieu, J.C. *Langmuir* **1998,** *14,* 7359.

(122) (a) Balogh, L.; Valluzzi, R.; Laverdure, K.S.; Gido, S.P.; Hagnauer, G.L.; Tomalia, D.A. *J. Nano. Res.* **1999**, *1*, 353. (b) Zhao, M.; Crooks, R.M. *Angew. Chem. Int. Ed.* **1999**, *38*, 364. (c) Chechik, V.; Zhao, M.; Crooks, R.M. *J. Am. Chem. Soc.* **1999,** *121,* 4910. (d) Zhao, M.; Sun, L.; Crooks, R.M. *J. Am. Chem. Soc.* **1998,** *120,* 4877. (e) Niu, Y.; Crooks, R.M. *Chem. Mater.* **2003,** *15,* 3463. (f) Scott, R.W.J.; Wilson, O.M.; Crooks, R.M. *J. Phys. Chem. B* **2005,** *109,* 692.

(123) (a) Fukuoka, A.; Higuchi, T.; Ohtake, T.; Oshio, T.; Kimura, J.; Sakamoto, Y.; Shimomura, N.; Inagaki, S.; Ichikawa, M. *Chem. Mater.* **2006,** *18,* 337. (b) Fukuoka, A.; Araki, H.; Sakamoto, Y.; Sugimoto, N.; Tsukada, H.; Kumai, Y.; Akimoto, Y.; Ichikawa, M. *Nano Lett.* **2002**, *2*, 793. (c) Fukuoka, A.; Araki, H.; Kimura, J.; Sakamoto, Y.; Higuchi, T.; Sugimoto, N.; Inagaki, S.; Ichikawa, M. *J. Mater. Chem.* **2004**, *14*, 752. (d) Joo, S.H.; Choi, S.J.; Oh, I.; Kwak, J.; Liu, Z.; Terasaki, O.; Ryoo, R. *Nature* **2001**, *412*, 169.

(124) (a) Chen, P.; Wu, X.; Lin, J.; Tan, K.L. *J. Phys. Chem. B.* **1999**, *103*, 4559. (b) Quinn, B.M.; Dekker, C.; Lemay, S.G. *J. Am. Chem. Soc.* **2005**, *127*, 6146. (c) Guo, D.J.; Li, H.L. *J. Colloid Interface Sci.* **2005**, *286*, 274. (d) Qu, J.; Shen, Y.; Qu, X.; Dong, S. *Chem. Commun.* **2004**, 34. (e) Day, T.M.; Unwin, P.R.; Wilson, N.R.; Macpherson, J.V. *J. Am. Chem. Soc.* **2005**, 127, 10639. (f) Govindaraj, A.; Satishkumar, B.C.; Nath, M.; Rao, C.N.R. *Chem. Mater.* **2000,** *12,* 202. (g) Kyotani, T.; Tsai, L.; Tomita, A. *Chem. Commun*. **1997**, 701. (h) Pradhan, B.K.; Kyotani, T.; Tomita, A. Chem. Commun. **1999**, 1317. (i) Sloan, J.; Wright, D.M.; Woo, H.-G.; Bailey, S.; Brown, G.; York, A.P.E.; Coleman, K.S.; Hutchison, J.L.; Green, M.L.H. *Chem. Commun.* **1999**, 699.

(125) (a) Wong, K.K.W.; Douglas, T.; Gider, S.; Awschalom, D.D.; Mann, S. *Chem. Mater.* **1998**, *10*, 279. (b) He, J.; Kunitake, T. *Chem. Mater.* **2004,** *16,* 2656. (c) Mark, S.S.; Bergkvist, M.; Yang, X.; Angert, E.R.; Batt, C.A. Biomacromolecules **2006,** *7*, 1884. (d) Willner, I., Baron, R., Willner, B. *Adv. Mater.* **2006**, *18*, 1109. (e) Zhu, H.; John, G.; Wei, B. *Chem. Phys. Lett.* **2005**, *405*, 49. (f) Klem, M.T.; Willits, D.; Solis, D.J.; Belcher, A.M.; Young, M.; Douglas, T. *Adv. Funct. Mater.* **2005**, *15*, 1489.

(126) (a) Pollmann, K.; Merroun, M.; Raff, J.; Hennig, C.; Selenska-Pobell, S. *Lett. Appl. Microbiol.* **2006**, *43*, 39. (b) Douglas, T.; Young, M. *Nature* **1998**, *393*, 152. (c) Konishi, Y.; Tsukiyama, T.; Ohno, K.; Saitoh, N.; Nomura, T.; Nagamine, S. *Hydrometallurgy* **2006**, *81*, 24. (d) Nam, K.T.; Kim, D.-W.; Yoo, P.J.; Chiang, C.-Y.; Meethong, N.; Hammond, P.T.; Chiang, Y.-M.; Belcher, A.M. *Science* **2006**, *312*,

885. (e) Lee, S.-K.; Yun, D.S.; Belcher, A.M. *Biomacromolecules* **2006,** *7*, 14. (f) Peelle, B.R.; Krauland, E.M.; Wittrup, K.D.; Belcher, A.M. *Langmuir* **2005,** *21,* 6929. (g) Reiss, B.D.; Mao, C.; Solis, D.J.; Ryan, K.S.; Thomson, T.; Belcher, A.M. *Nano. Lett.* **2004**, *4*, 1127.

(127) (a) Mann, S. *Nature*, **1993**, *365*, 499. (b) Oliver, S.; Kupermann, A.; Coombs, N., Lough, A.; Ozin, G.A. *Nature*, **1995**, *378*, 47. (c) Kröger, N.; Deutzmann, R.; Sumper, M., *Science*, **1999**, *286*, 1129.

(128) Young, J.R.; Davis, S.A.; Bown, P.R.; Mann, S. *J. Struct. Biol.* **1999**, *126***,** 195.

(129) Balkwill, D.; Marata, D.; Blakemore, R.P. *J. Bacteriol.* **1980**, *141*, 1399.

(130) (a)Lovley, D.R.; Stolz, J.F.; Nord, G.L.; Phillips, E.J.P. *Nature*, **1987**, *330*, 252. (b) Spring, H.; Schleifer, K.H. *Sys. Appl. Microbiol*. **1995**, *18*, 147. (c) Dickson, D.P.E. *J. Magn. Magn. Mater.* **1999**, *203*, 46.

(131) Luis M. Liz-Marza´n, L.M.; Mulvaney, P *J. Phys. Chem. B,* **2003***, 107,* 7312

(132) (a) Germain, V.; Li, j.; Ingert, D.; Wang, Z.L.; Pileni, M.P. *J. Phys. Chem. B*, **2003**, *107*, 7492 (b) Okada, N.; Hamanaka, Y.; Nakamura, a.; P.-Santos, I.; Liz-Marzan, L.M. *J. Phys. Chem. B*, **2004**, *108*, 8751.

(133) (a) Huang, T.; Murray, R.W. *J. Phys. Chem. B*, **2001**, *105*, 12498 (*b*) McLellan, J. M.; Geissler, M.; Xia, Y. *J. Am. Chem. Soc.*, **2004**, *126*, 10830.

(134) (a) Chung, S.-W.; Markovich, G.; Heath, J.R. *J. Phys. Chem. B*, **1998**, *102*, 6685 (*b*) Sun, Y.; Yin, Y.; Mayers, B.T.; Herricks, T.; Xia, Y. *Chem. Mater.*, **2002**, *14*, 4736 (*c*) Caswell, K.K.; Bender, C.M.; Murphy, C.J. *Nano Lett.*, **2003**, *3*, 667 .

(135) (a) Jana, N.R.; Gearheart L.; Murphy, C.J. *J. Phys. Chem. B*, **2001**, *105*, 4065; (b) Brown, K. R.; Walter, D. G.; Natan, M.J. *Chem. Mater.*, **2000**, *12*, 306 (*c*) Johnson, C. J.; Dujardin, E.; Davis, S.A.; Murphy, C.J.; Mann, S. *J. Mater. Chem.*, **2002**, *12*, 1765.

(136) (a) Malikova, N.; Pastoriza-Santos, I.; Schierhorn, M.; Kotov, N.A.; Liz-Marzan, L.M. *Langmuir***, 2002**, *18*, 3694 .

(137) (a) Liu, H.; Alivisatos, A.P. *Nano Lett.*, **2004**, *4*, 2397 (b) Chen, S.; Wang, Z.L.; Ballato, J.; Foulger, S.H.; Carroll, D.L. *J. Am. Chem. Soc.*, **2003**, *125*, 16186 .

(138) Chen, J.; Saeki, F.; Wiley, B.J.; Cang, H.; Cobb, M.J.; Li, Z.-Y.; Au, L.; Zhang, H.; Kimmey, M.B.; Li, X.; Xia, Y. *Nano Lett.*, **2005**, *5* 473

(139) (a) Maier, S. A.; Broongersma, M.L.; Kik, P.G.; Meltzer, S.; Requicha, A. A. G.; Koel, B.E.; Atwater, H.A. *Adv. Mater.*, **2001**, *13*, 1501 (b) Radloff , C.; Halas, N.J. *Nano Lett.*, **2004**, *4*, 1323 .

(140) Callegari, A.; Tonti, D.; Chergui, M. *Nano Lett*. **2003**, *3*, 1565.

(141) Jiang, Li-Peng; Shu, X.; Zhu, J-M.; Zhang, J-R; Zhu, Ju-J; Chen, H-Y *Inorg. Chem.* **2004**, *43*, 5877.

(142) Tsuji, M.; Hasimoto, M.; Nishizawa, Y.; Tsuji, T. *Chem. Lett.* **2003**, *32*, 1114.

(143) (a) Qu, L.; Shi, G.; Wu, X.; Fan, B. *Adv. Mater*. **2004**, *16*, 1200. (b) Hou, S.; Harrell, C. C.; Trofin, L.; Kohli, P.; Martin, C. R. *J. Am. Chem. Soc.* **2004**, *126*, 5674. (c) Go1ring, P.; Pippel, E.; Hofmeister, H.; Wehrspohn, R. B.; Steinhart, M.; Go1sele, U. *Nano Lett*. **2004**, *4*, 1121. (d) Choi, J.; Sauer, G.; Nielsch, K.; Wehrspohn, R.B.; Go¨sele, U. *Chem. Mater.* **2003**, *15,* 776.

(144) (a) Lahav, M.; Sehayek, T.; Vaskevich, A.; Rubinstein, I. *Angew. Chem. Int. Ed*. **2003**, *42*, 5576. (b) Cepak, V. M.; Martin, C. R. *J. Phys. Chem. B* **1998**, *102,* 9985. (c) Wu, Y.; Livneh, T.; Zhang, Y. X.; Cheng, G.; Wang, J.; Tang, J.; Moskovits, M.; Stucky, G. D. *Nano Lett.* **2004**, *4*, 2337. (d) Sainsbury, T.; Fitzmaurice, D. *Chem. Mater*. **2004**, *16,* 2174.

(145) (a) Penner, R. M. *J. Phys. Chem. B* **2002**, *106,* 3339. (b) Walter, E. C.; Murray, B. J.; Favier, F.; Kaltenpoth, G.; Grunze, M.; Penner, R. M. *J. Phys. Chem. B* **2002**,*106*, 11407.

(146) (a) Zhang, D.; Qi, L.; Ma, J.; Cheng, H. *Chem. Mater*. **2001,** *13,* 2753. (b) Cornelissen, J. J. L. M.; Heerbeek, R. V.; Kamer, P. C. J.; Reek, J. N. H.; Sommerdijk, N. A. J. M.; Nolte, R. J. M. *Adv. Mater*. **2002**, *14*, 489. (c) Kim, U. K.; Cha, S. H.; Shin, K.; Jho, J. Y.; Lee, J. C. *Adv. Mater.* **2004**, *16*, 459. (d) Hao, E.; Kelly, K. L.; Hupp, J. T.; Schatz, G. C. *J. Am. Chem. Soc*. **2002**, *124*, 15182.

(147) (a) Patolsky, F.; Weizmann, Y.; Lioubashevski, O.; Willner, I. *Angew. Chem. Int. Ed*. **2002**, *41*, 2323. (b) Braun, E.; Eichen, Y.; Sivan, U.; Yoseph, G. B. *Nature* **1998**,

391, 775. (c) Ford, W. E.; Harnack, O.; Yasuda, A.; Wessels, J. M. *Adv. Mater*. **2001**, *13*, 1793. (d) Deng, Z.; Mao, C. *Nano Lett*. **2003**, *3*, 1545.

(148) (a) Me´traux, G. S.; Cao, Y. C.; Jin, R.; Mirkin, C. A. *Nano Lett*. **2003**, *3*, 519. (b) Song, J. H.; Wu, Y.; Messer, B.; Kind, H.; Yang, P. *J. Am. Chem. Soc.* **2001,** *123,* 10397.

(149) (a) Sun, Y.; Mayers, B.; Herricks, T.; Xia, Y. *Nano Lett*. **2003**, *3*, 955. (b) Sun, Y.; Yin, Y.; Mayers, B. T.; Herricks, T.; Xia, Y. *Chem. Mater.* **2002**, *14,* 4736. (c) Sun, Y.; Gates, B.; Mayers, B.; Xia, Y. *Nano Lett.* **2002**, *2*, 165. (d) Sun, Y.; Xia, Y. *Adv. Mater.* **2002**, *14*, 833.

(150) Wiley, B.; Herricks, T.; Sun, Y.; Xia, Y. *Nano Lett*. **2004**, *4*, 1733.

(151) Kim, F.; Connor, S.; Song, H.; Kuykendall, T.; Yang, P. *Angew. Chem. Int. Ed*. **2004**, *43*, 3673.

(152) (a) Chen, J.; Herricks, T.; Geissler, M.; Xia, Y. *J. Am. Chem. Soc.* **2004**, *126*, 10854. (b) Herricks, T.; Chen, J.; Xia, Y. *Nano Lett*. **2004**, *4*, 2367.

(153) Nikoobakht, B.; El-Sayed, M. A. *Chem. Mater.* **2003**, *15,* 1957.

(154) R. L. Whetten, R.L.; Khoury, J.T.; Alvarez, M.M.; Murthy, S.; Vezmar, I.;Wang, Z.L.; Cleveland, C.C.; Luedtke, W.D.; Landman, U. *Adv. Mater*. **1996**, *8*, 428.

(155) Wang, Z.L. Adv. Mater. **1998**, *10*, 13

(156) Heitmam, D.; Kotthaus, J. P. *Phys. Today* **1993**, *56*.

(157) (a)Xia, Y.; Kim, E.; Mrksich, M.; Whitesides, G. M. *Chem. Mater.***1996**, *8*, 601.(b) Kumar, A.; Whitesides, G. M. *Science* **1994**, *263*, 60.

(158) Asher, S. A. U. S. Patents 4, 627, 689 and 4, 632, 517.

(159) (a)Yoldas, B. E.; Partlow, D. P. *Appl. Opt.* **1984**, *23*, 1418.(b) Hinz, P.; Dislich, H. *J. Non-Cryst. Solids* **1986**, *82*, 411.

(160) Hahn, R. E.; Seraphin, B. O. In *Physics of Thin Film*, Academic: New York, **1978.**

(161) Kastner, M. A. *Phys. Today* **1993**, 24.

(162) Colvin, V. L.; Goldstein, A. N.; Alivisatos, A. P. *J. Am. Chem. Soc.* **1992**, *114,* 5221.

(163) (a) Gole, A.; Sainkar, S. R.; Sastry, M. *Chem. Mater.* **2000**, *12,* 1234. (b) Bandyopadhyay, K.; Patil, V.; Vijayamohanan, K.; Sastry, M. *Langmuir* **1997,** *13,* 5244. (c) Sastry, M. *Colloids and Colloid Assemblies: Synthesis, Modification, Organization and Utilization of Colloid Particles* ed. F. Caruso, Wiley-VCH, Berlin Chapter 12. **2003**, 369-397. (d) Sastry, M. *Handbook of Surfaces and Interfaces of Materials*, Ed. H.S. Nalwa, Nanostructured Materials, Micelles and Colloids, Academic Press**,** Volume 3, Chapter 2, **2001**, 87-119.

(164) (a) Rao, C. N. R.; Kulkarni, G. U.; Thomas, P. J.; Ed-wards, P. P. *Chem. Soc. Rev*. **2000**, *29*, 27. (b) Musick, M. D.; Keating, C. D.; Keefe, M. H.; Natan, M. J. *Chem. Mater*. **1997**, *9*, 1499. (c) Murray, C. B.; Kagan, C. R.; Bawendi, M. G. *Science* **1995**, *270*, 1335.

(165) Giersig, M.; Mulvaney, P. *J. Phys. Chem.* **1993,** *97,* 6334. (b) Giersig, M.; Mulvaney, P. *Langmuir* **1993**, *9*, 3408.

(166) Teranishi, T.; Hosoe, M.; Tanaka, T.; Miyake, M. *J. Phys. Chem. B* **1999**, *103,* 3818.

(167) Chandrasekharan, N.; Kamat, P. V. *Nano Lett*. **2001**, *1*, 67.

(168) (a) Korgel, B. A.; Fullam, S.; Connoly, S.; Fitzmaurice, D. *J. Phys. Chem. B* **1998**, *122*, 4640. (b) Harfenist, S. A.; Wang, Z. L.; Alvarez, M. M.; Vezmar, I.; Whetten R. L. *J. Phys. Chem.* **1996**, *100*, 13904. (c) Pileni, M. P. *Langmuir* **1997**, *13*, 3266. (d) Pileni, M. P. *New J. Chem*. **1998**, *22*, 693. (e) Nikoobakht, B.; Wang, Z. L.; El-Sayed, M. A. *J. Phys. Chem. B* **2000**, *104*, 8635.

(169) Pileni, M. P. *J. Phys. Chem. B* **2001**, *105,* 3358.

(170) (a) Selvakannan, PR.; Mandal, S.; Pasricha, R.; Sastry, M. *J. Colloid Int. Sci*. **2004**, *279*, 124. (b) Sarathy, K. V.; Raina, G.; Yadav, R. T.; Kulkarni, G. U.; Rao, C. N. R. *J. Phys. Chem. B* **1997**, *101,* 9876. (c) Brown, L. O.; Hutchison, J. E. *J. Phys. Chem. B* **2001**, *105,* 8911. (d) He, S.; Yao, J.; Jiang, P.; Shi, D.; Zhang, H.; Xie, S.; Pang, S.; Gao, H.; *Langmuir* **2001**, *17,* 1571. (e) Zhao, S.Y.; Wang, S.; Kimura, K. *Langmuir* **2004**, *20,* 1977. (f) Stoeva, S.; Klabunde, K. J.; Sorensen, C.M.; Dragieva, I. *J. Am. Chem. Soc*. **2002**, *124*, 2305. (g) Liu, S.; Zhu, T.; Hu, R.; Liu, Z. *Phys. Chem. Chem. Phys*. **2002**, *4*, 6059.

(171) (a) Kiely, C. J.; Fink, J.; Brust, M.; Bethell D.; Schiffrin, D. J. *Nature* **1998**, *396*, 444. (b) Kiely, C. J.; Fink, J., Zheng, J. G.; Brust, M.; Bethell D.; Schiffrin, D. J. *Adv. Mater*. **2000**, *12*, 640.

(172) (a) Collier, C. P.; Vossmeyer, T.; Heath, J. R. *Ann. Rev. Phys. Chem*. **1998**, *49*, 71. (b) Wang, Z. L. *Adv. Mater*. **1998**, *10*, 13.

(173) Andres, R. P.; Bielefeld, J. D.; Henderson, J. I.; Janes, D. B.; Kolagunta, V. R. *Science* **1996**, *273*, 1690.

(174) (a) Elghanian, R.; Storhoff, J. J.; Mucic, R. C.; Letsinger, R. L.; Mirkin, C. A. *Science* **1997**, *277*, 1078. (b) Mitchell G. P.; Mirkin, C. A.; Letsinger, R. L. *J. Am. Chem. Soc*. **1999**, *121*, 8122. (c) Taton, T. A.; Mirkin, C. A.; Letsinger, R. L. *Science* **2000**, *289*, 1757. (d) Storhoff, J. J.; Mirkin, C. A. *Chem. Rev*. **1999**, *99*, 1849.

(175) Alivisatos, A. P.; Johnsson , K. P.; Peng, X.; Wilson, T. E.; Loweth, C. J. *Nature* **1996**, *382*, 609.

(176) (a) Shenton, W.; Pum, D.; Sleytr, B.; Mann, S. *Nature* **1997**, *389*, 585. (b) Bergkvist, M.; Mark, S. S.; Yang, X.; Angert, E. R.; Batt, C. A. *J. Phys. Chem. B* **2004**, *108,* 8241.

(177) (a) Hulteen, J. C.; van Duybe, R. P. *J. Vac. Sci. Tech. A* **1995**, *13*, 1533. (b) Haynes, C. L.; van Duybe, R. P.; *J. Phys. Chem. B* **2001**, *105*, 5599. (c) Hulteen, J. C.; Treichel, D. A.; Smith, M.T.; Duval, M. L.; Jensen, T.R.; van Duyne, R. P. *J. Phys. Chem. B* **1999**, *103,* 3854. (d) Haynes, C. L.; McFarland, A. D.; Smith, M.T.; Hulteen, J. C.; van Duyne R. P. *J. Phys. Chem B* **2002**, *106*, 1898. (e) Ormonde, A. D.; Hicks, E. C. M.; Castillo, J.; van Duyne, R. P. *Langmuir* **2004**, *20,* 6927 (f) Zhang H.; Mirkin, C.A. *Chem. Mater.* **2004**, *16,* 1480. (g) Zhang H.; Li, Z.; Mirkin, C.A. *Adv. Mater*. **2002**, *14*, 1472

(178) (a) Freeman, R. G.; Grabar, K. C.; Alison, K. G.; Bright, R. M.; Davis, J. A.; Guthrie, A. P.; Hommer, M. B.; Jackson, M. A.; Smith, P.C.; Walter, D. G.; Natan, M. J. *Science* **1995**, *267*, 1629. (b) Grabar, K. C.; Allison, K.J.; Baker, B. E.; Bright, R. M.; Brown, K.R.; Freeman, R. G.; Fox, A. P.; Keating, C. D.; Musik, M. D.; Natan, M. J. *Langmuir* **1996**, *12*, 2353. (c) Grabar, K. C.; Freeman, R. G.; Hommer,

M. B.; Natan, M. J. *Anal. Chem*. **1995**, *67*, 735. (d) Bright, R. M.; Walter, D. G.; Musik, M. D.; Jackson, M. A.; Allison, K.J.; Natan, M. J. *Langmuir*, **1996**,*12*, 810.

(179) (a)Peschel, S.; Schmid, G. *Angew. Chem. Int. Ed.* **1995**, *34*, 1442 (b) Malynych, S.; Luzinov, I.; Chumanov, G. *J. Phys. Chem. B* **2002**, *106,* 1280.

(180) Kawasaki, M.; Hori, M. *J. Phys. Chem. B* **2003**, *107,* 6760.

(181) (a)Mayya, K. S.; Patil, V.; Sastry, M. *Langmuir* **1997**, *13,* 2575 (b) Sastry, M.; Mayya, K. S.; Patil, V.; Paranjape, D. V.; Hegde, S. G. *J. Phys. Chem. B* **1997,** *101,* 4954. (c) Mayya, K. S.; Sastry, M. *Langmuir* **1998,** *14,* 74 (d) Mayya, K.S.; Patil, V.; Madhu Kumar P.; Sastry, M. *Thin Solid Films* **1998,** *312*, 308.

(182) (a)Meldrum, F. C.; Kotov, N. A.; Fendler, J. H. *Langmuir* **1994***, 10,* 2035. (b) Meldrum, F.C.; Kotov, N. A.; Fendler, J. H. *Chem. Mater.* **1995**, *7,* 1112. (c) Kotov, N. A.; Meldrum, F. C.; Wu, C.; Fendler, J. H. *J. Phys. Chem.* **1994**, *98*, 2735. (d) Tian, Y.; Fendler, J.H. *Chem. Mater.* **1996**, *8,* 969. (e) Kotov, N. A.; Zavala, G.; Fendler, J. H. *J. Phys. Chem.* **1995,** *99,* 12375. (f) Meldrum, F. C.; Kotov, N. A.; Fendler, J. H. *J. Phys. Chem.* **1994***, 98,* 4506. (g) Kotov, N. A.; Meldrum, F.C.; Fendler, J.H. *J. Phys. Chem.* **1994***, 98,* 8827.

(183) Ganguly, P.; Paranjape, D.V.; Patil, K.R.; Chaudhari, S. K.; Kshirsagar, S.T. *Indian J. Chem. A* **1992**, *31*, F42.

(184) (a)Tao, A.; Kim, F.; Hess, C.; Goldberger, J.; He, R.; Sun, Y.; Xia, Y.; Yang P. *Nano Lett.* **2003**, *3*, 1229. (b) Kim, F.; Kwan, S.; Akana, J.; Yang, P. *J. Am. Chem. Soc.* **2001**, *123,* 4360.

(185) (a) Kyunghee, C. Y.; Fendler, J.H. *Langmuir* **1990**, *6*, 1519. (b) Yang, J.; Meldrum, F.C.; Fendler, J. H. *J. Phys. Chem.* **1995***, 99,* 5500. (c) Zhao, X. K.; Xu, S.; Fendler, J. H. *Langmuir* **1991**, *7*, 520. (d) Zhao, X. K.; Fendler, J. H. *Chem. Mater* **1991,** *3,* 168. (e) Zhao, X. K.; Fendler, J. H. *J. Phys. Chem.* **1991**, *95,* 3716. (f) Zhao, X. K.; McCormick, L. D.; Fendler, J. H. *Chem. Mater.* **1991**, *3*, 922. (g) Yuan, Y.; Cabasso, I.; Fendler, J.H.; *Chem. Mater.* **1990**, *2*, 226. (h) Yang, J.; Meldrum, F.C.; Fendler J. H. *J. Phys. Chem.* **1995***, 99,* 5500.

(186) (a) Zhao, X. K.; Yang, J. L.; McCormick, D.; Fendler, J. H. *J. Phys. Chem.* **1992,** *96*, 9933. (b) Yang, J.; Fender, J. H. *J. Phys. Chem.* **1995**,*99,* 5505. (b) Zhao, X. K.; McCormick, L.D.; Fendler J. H. *Langmuir* **1991**, *7,* 1255.

(187) (a)Yi, K. C.; Horvolgyi, Z.; Fendler, J. H. *J. Phys. Chem*. **1994**, *98*, 3872. (b) Yi, K. C.; Mendieta, V. S.; Castaiiares, R.L.; Meldrum, F.C.; WU, C.; Fendler, J. H. *J. Phys. Chem.* **1995**, *99,* 9869. (c) Swami, A.; Kasture, M.; Pasricha, R.; Sastry, M. *J. Mater.Chem.* **2004**, *14*, 709. (d) Swami**,** A.; Kumar, A.; Selvakannan, PR.; Mandal, S.; Pasricha, R.; Sastry, M. *Chem. Mater*. **2003**, *15*, 17. (e) D'Costa, M.; Pasricha, R.; Sastry, M. *J. Mater. Chem.* **2004**, 14, 2696.

(188) Ravaine, S.; Fanucci, G. E.; Seip, C.T.; Adair, J. H.; Talham, D.R. *Langmuir* **1998**, *14*, 708.

(189) (a) Smotkin, E. S.; Lee, C.; Bard, A. J.; Campion, A.; Fox, M. A.; Mallouk, T. E.; Webber, S. E; White, J. M. *Chem. Phys. Lett.* **1988**, *152*, 265. (b) Peng, X.; Lu, R.; Zhao, Y.Y.; Qu, L.; Chen, H.; Li T. *J. Phys. Chem.* **1994**, *98,* 7052. (c) Peng, X.; Guan, S.; Chai, X.; Jiang, Y.; Li, T. *J. Phys. Chem.* **1992**, *96,* 3170. (d) Zhu, R.; Min, G.; Wei, Y. *J. Phys. Chem.* **1992**, *96,* 8210. (e)Urquhart, R. S.; Furlong, D. N.; Gengenbach, T.; Geddes, N. J.; Griesert, F. *Langmuir* **1996**, *11*, 1127. (f) Grieser, F.; Furlong, D. N.; Scoberg, D.; Ichinose, I.; Kimizuka, N.; Kunitake, T. *J. Chem. Soc. Faraday Trans*. **1992**, *88*, 2207.

(190) Chen, S. *Ad*V. *Mater*. **2000**, *12*, 186. (b) Chen, S. *Langmuir* **2001**, *17*, 2878.

Chapter II

Characterization Techniques

This chapter discusses the basic working principle of the various characterization techniques, which were used during the course of the presented work.

The main emphasis of this thesis is on the synthesis and assembly of anisotropic nanoparticles at air-water interface and deposition of their films using Langmuir-Blodgett (LB) technique. The LB films of nanoparticles have been characterized by a host of techniques such as UV-vis spectroscopy, Fourier Transform Infrared spectroscopy (FTIR), X-ray photoemission spectroscopy (XPS), Transmission Electron Microscopy (TEM), High resolution Transmission Electron Microscopy (HTREM), Energy Dispersive X-ray analysis (EDAX) and Scanning Transmission Electron Microscopy (STEM). A lot of other techniques have also been used. This chapter is devoted in explaining the basic principles on which different techniques are based and their application in understanding various aspects of formation of the LB films.

2.1 Langmuir Blodgett (LB) technique

LB technique is one of the most promising techniques for preparing organic thin films [1] as it enables (a) the precise control of the monolayer thickness, (b) homogenous deposition of the monolayer over large areas on almost any kind of solid substrate and (c) the possibility to make multilayer structures with varying layer composition. For the work discussed in this thesis, LB technique has been extensively for the synthesis of anisotroic nanostructures by restricting the reduction of precursor metal ions at the two dimensional air-water interface.

Langmuir films

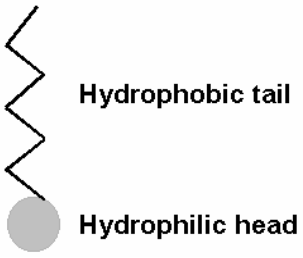

Figure 2.1 *A schematic of an amphiphilic molecule showing hydrophobic (long hydrocarbon chain) and hydrophilic (polar group) parts.*

Langmuir films consist of surface active materials or 'surfactants' trapped at the interface between two dissimilar phases, either liquid-liquid or liquid-gas. Surfactants are molecules which are amphiphilic in nature (Fig. 2.1) and consist of a hydrophilic (water

soluble) and hydrophobic (water insoluble) part. The hydrophobic part usually consists of hydrocarbon or fluorocarbon chains and the forces acting upon them are predominantly van der Waal's type ($1/r^{12}$ and $1/r^{6}$). While the hydrophilic part consists of a polar group (-OH, -COOH, $-NH_3^+$, $-PO_4^-(CH_2)_2NH_3^+$ etc.) and the forces acting upon them are predominantly coulomb type ($1/r^2$).

Amphiphilic molecules are trapped at the interface because they possess two very different types of bonding within the one molecular structure. The driving force behind the association is the reduction of the free energy of the system. Therefore, when a surfactant comes in contact with water it accumulates at the air-water interface causing a decrease in the surface tension of water. Many of these amphiphilic molecules insoluble in water can (with the help of a volatile and water insoluble solvent) easily spread on a water surface with hydrophilic 'head' groups pulling the molecule into the bulk of the water and the hydrophobic 'tail' groups pointing into the air. One molecule thick surface monolayer will only be achieved if the amphiphatic balance (that is balance between hydrophilic and hydrophobic parts) of the molecule is correct. Sweeping a barrier over the water surface causes the molecules to come closer together and eventually form a compressed, ordered monolayer. The film produced by such a method is known as a Langmuir film.

Pressure-Area Isotherm (π-A isotherm)

The most important indicator of the monolayer properties of an amphiphilic molecule is given by measuring the changes in surface tention upon compressing the monolayer. The reduction of surface tension is known as the surface pressure i.e. surface pressure is the lateral pressure that must be applied to prevent the film from spreading. Pressure readings are made by means of Wilhelmy plate attached to a microbalance. The plot of surface pressure versus area occupied per molecule is known as a 'pressure-area isotherm'(π-*A* – isotherm) because compression takes place at constant temperature (Fig. 2.2). The shape of isotherm is characteristic of the molecules making up the film and hence provides a two-dimensional 'fingerprint'. π-*A* isotherm gives information about the stability of the molecules in the two dimensional system, phase transitions and

conformational transitions. It also gives some idea of the amount of pressure that has to be applied to the film on the sub phase, to enable deposition of the LB film in the solid-like phase. Thus at appropriate pressure, the film can be transferred to the substrate.

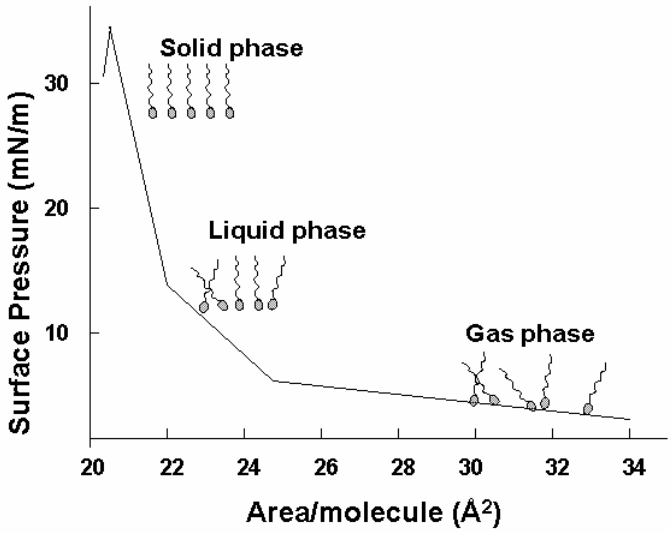

Figure 2.2 *A typical pressure- area (π-A) isotherm showing the various phase transitions of the floating monolayer*

Deposition of LB films

Langmuir film balance can also be used for building up highly organised multilayers of the amphiphile. This is accomplished by successively dipping a solid substrate up and down through the monolayer while simultaneously keeping the surface pressure constant by a computer controlled feedback system between the electrobalance measuring the surface pressure and the barrier moving mechanism. Consequently the floating monolayer is adsorbed to the solid substrate. In this way multilayer structures of hundreads of layers can be produced. These multilayer structures are commonly called Langmuir-Blodgett or simply LB films. The LB deposition is traditionally carried out in the 'solid' phase. The surface pressure is then high enough to ensure sufficient cohesion in the monolayer so that the monolayer does not fall apart during transfer to the solid substrate. This also ensures the build up of homogeneous multilayers. The surface pressure value that gives the best results depends on the nature of the monolayer. When the solid substrate is hydrophilic (glass, SiO_2 etc.) the first layer is deposited by raising

the solid substrate from the subphase through the monolayer, whereas if the substrate is hydrophobic (HOPG, silanized SiO_2 etc.) the first layer is deposited by lowering the substrate into the subphase through the monolayer.

The parameters affecting the type of LB film produced are, the nature of the spread film, the subphase composition and temperature, the surface pressure during the deposition and the deposition speed, the type and nature of the solid substrate and the time the solid substrate is stored in air or in the subphase between the deposition cycles.

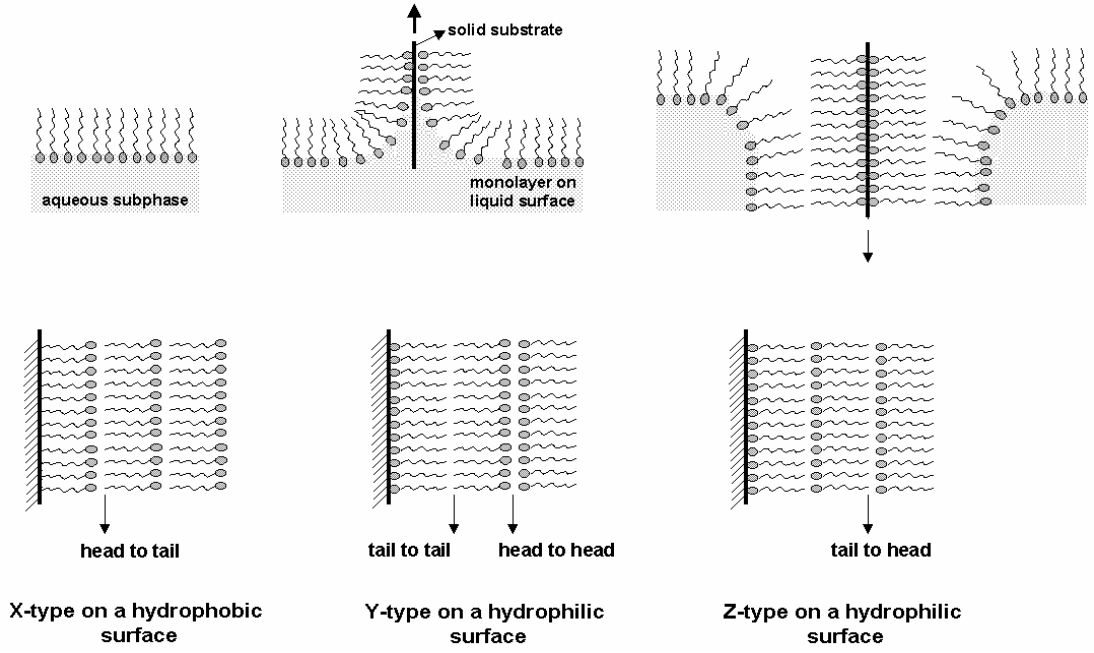

Figure 2.3 *A schematic showing different types of deposition of LB films*

The quantity and the quality of the deposited monolayer on a solid support is measured by a transfer ratio, given by:

$$TR = \frac{area\ of\ monolayer\ removed\ from\ the\ subphase\ at\ constant\ pressure}{area\ of\ substrate\ immersed\ in\ water}$$

For ideal transfer the TR is 1. Different kind of LB multilayers can be produced and/or obtained by successive deposition of monolayers on the same substrate. The most common type is Y-type multilayer, which is produced when the monolayer deposits to the solid substrate in both upward and downward movement of the substrate. When the monolayer deposits only during upward or downward movement, the multilayer structure

is called either Z-type or X-type (Fig. 2.3). An alternative way to deposit the monolayer is the Langmuir-Schaeffer (LS) technique. This technique differs from the vertical deposition technique described above only in the sense that the solid substrate is horizontally lowered in contact with the monolayer.

Nima LB trough, Model 611 was used for the present work. The photograph of the set up is shown in Fig 2.4. Pressure–area (π–*A*) isotherms were recorded at room temperature as a function of time from spreading the monolayer at a compression and expansion rate of 20 cm^2/min. A standard Wilhelmy plate was used for surface pressure sensing. Multilayer films of the nanoparticles of different thickness were formed by the LB technique at a constant surface pressure and a deposition rate of 25 mm/min with a waiting time of 180 s between dips on quartz slides, silicon (Si) (111) wafers and carbon-coated transmission electron microscopy (TEM) grids for UV–vis spectroscopy, Fourier transform infrared spectroscopy (FTIR) and transmission electron microscopy measurements, respectively. The quartz and Si (111) substrates were hydrophobized by depositing three monolayers of lead arachidate prior to transfer of the nanoparticle monolayers. The hydrophobization of the support resulted in better transfer ratios of the nanoparticle monolayers. For the LB films grown on different substrates, monolayer transfer was observed both during the upward and downward strokes of the substrate at close to unity transfer ratio.

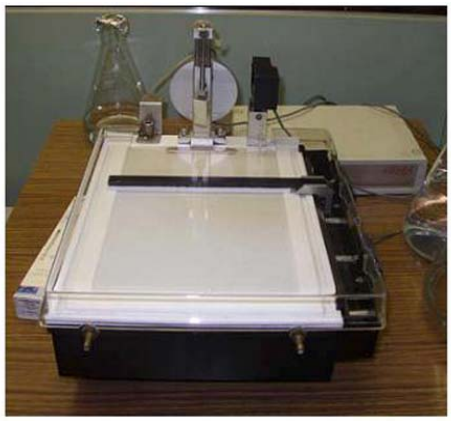

Figure 2.4 *Photograph of the Nima LB trough.*

2.2 UV-Vis-NIR spectroscopy

Absorption spectroscopy in the visible region has long been an important tool to the analyst [2]. Appearance of colour arises from the property of the colored material to absorb selectively and reflect its complementary colour which falls within the visible region of the electromagnetic spectrum.

Theory

The total energy of a molecule is the sum of its electronic energy, vibrational energy and rotational energy. The magnitude of these energies decreases in the following order: E_{elec}, E_{vib} and E_{rot}. Energy absorbed in the UV region produces changes in the electronic energy of the molecule resulting from transitions of valence electrons in the molecule. The relationship between the energy absorbed in an electronic transition and the frequency (ν), wavelength (λ) and wavenumber ($\bar{\nu}$) of radiation producing the transition is

$$\Delta E = h\nu = hc/\lambda = h\,\bar{\nu}\,c$$

where, h is Planck's constant, c is the velocity of light and ΔE is the energy absorbed in an electronic transition in a molecule from a low-energy state (ground state) to a high energy state (excited state). The energy absorbed is dependent on the energy difference between the ground state and the excited state; the smaller the difference in energy, the longer the wavelength of absorption. Since UV energy is quantized, the absorption spectrum arising from a single electronic transition should consist of a single, discrete line. A discrete line is not obtained since electronic absorption is superimposed on rotational and vibrational sublevels as shown in Fig. 2.5. The principal characteristics of an absorption band are its position and intensity. The position of an absorption band correspond to the wavelength of radiation whose energy is equal to that required for an electronic transition. The intensity of absorption is largely dependent on two factors: the probability of interaction between the radiation energy and the electronic system and the difference between the ground and excited state. The intensity of absorption may be expressed as transmittance (T), defined by

$$T = I/I_0$$

where I_0 is the intensity of the radiant energy striking the sample, and I is the intensity of the radiation emerging from the sample. A more convenient expression of absorption intensity is that derived from the Lambert-Beer law, which establishes a relationship between the absorbance, the sample thickness and the concentration of the absorbing species. The relationship is expressed as

$$A = abc$$

where, A is the measured absorbance, a is absorptivity , b is the cell-path length, and c is the analyte concentration.

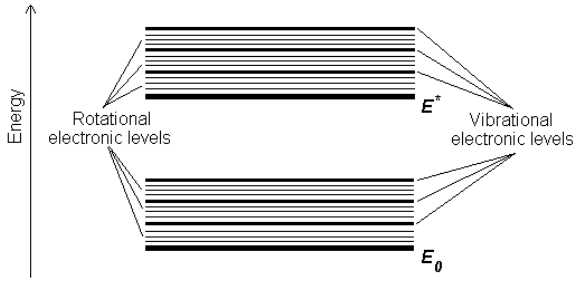

Figure 2.5 *Energy level diagram of a diatomic molecule*

On the other hand, light absorption by small metal particles is best described by Mie's theory [3]. The absorption spectrum of particles in a given solvent can be calculated from the optical constants of the bulk metal, although the absorption of the particles is often vastly different from that of the bulk metal itself [3]. The simplest case is when the particles are spherical and their size is small compared to the wavelength of light, and the particles are well separated in solution. At particle sizes between about 3 and 20 nm, there is not a strong dependence of the absorption spectra on particle size. This is because the particles are below the size at which higher order terms in the Mie formula for the absorption constant become significant. Thus, one has to regard only the dipole term, which depends only on the total metal concentration in the solution and not on particle size. The absorption coefficient in $mol^{-1}.L.cm^{-1}$ is calculated from the relation [3,4]

$$\alpha = \frac{18\pi}{\ln 10} \frac{10^5}{\lambda} \frac{Mn_0^3}{\rho} \frac{\varepsilon_2}{(\varepsilon_1 + 2n_0^2) + \varepsilon_2^2}$$

where, λ is the wavelength of light in nanometers, M and ρ are the molecular weight and density of the metal, n_o is the refractive index of the solvent and ε_1 and ε_2 are the real and imaginary parts of the dielectric constant of the metal. When the size of the particles becomes smaller than the mean free path of the electrons, the absorption bands are broadened; this is accounted for by using size-corrected values of ε_2 [4,5]

$$\varepsilon_2 = \varepsilon_{2(bulk)} + \left(\omega_p^2 / \omega^3\right)\left(V_F / R\right)$$

where ω is the light frequency, ω_p the plasmon frequency, v_F the electron velocity at the Fermi level and R the particle radius (R/V_F, mean time of the free movement of the electrons). Resonance with the incident light is reached at the wavelength, where the negative value of ε_1 of the metal is equal to twice the dielectric constant of the medium. For example, gold particles possess plasmon resonances in the visible range (~514 nm). When a small spherical metallic nanoparticle is irradiated by light, the oscillating electric field causes the conduction electrons to oscillate coherently. This is schematically pictured in Fig.2.6.

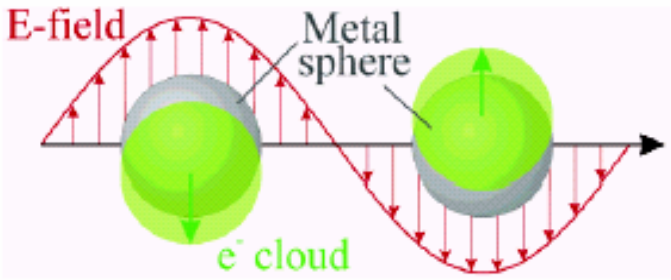

Figure 2.6 *Polarization of a spherical metal particle by the electrical field vector of the incoming light*

When the electron cloud is displaced relative to the nuclei, a restoring force arises from Coulomb attraction between electrons and nuclei that results in oscillation of the electron cloud relative to the nuclear framework. The oscillation frequency is determined by four factors: the density of electrons, the effective electron mass, and the shape and size of the charge distribution [5]. The collective oscillation of the electrons is called the dipole plasmon resonance of the particle (sometimes denoted "dipole particle plasmon

resonance" to distinguish from plasmon excitation that can occur in bulk metal or metal surfaces). Thus, the electron density within a surface layer, the thickness of which is about equal to the screening length of a few angstroms, oscillate, whereas the density in the interior of the particle remains constant ("surface plasmon"). Therefore, any changes in the electron density of this surface layer will lead to changes in the plasmon absorption.

In the spectrophotometer both deuterium and tungsten lamp is used as the source for characterization in the UV and visible regions respectively. However one xenon arc lamp can also be used which can serve the purpose for both UV and visible region. In such a dual beam spectrophotometer, light from either the visible or the ultraviolet source enters the grating monochromator before it reaches the filter. Broadband filters contained in a filter wheel are automatically indexed into position at the required wavelengths to reduce the amount of stray light and unwanted orders from the diffraction grating. The light from the source is alternatively split into one of two beams by a rotating mirror called a chopper as is shown in the schematic of Fig 2.7, one beam is passed through the sample and the other through the reference. Some double-beam instruments have two detectors, and the sample and reference beam are measured at the same time. In other instruments, the two beams pass through a beam chopper which blocks one beam at a time.

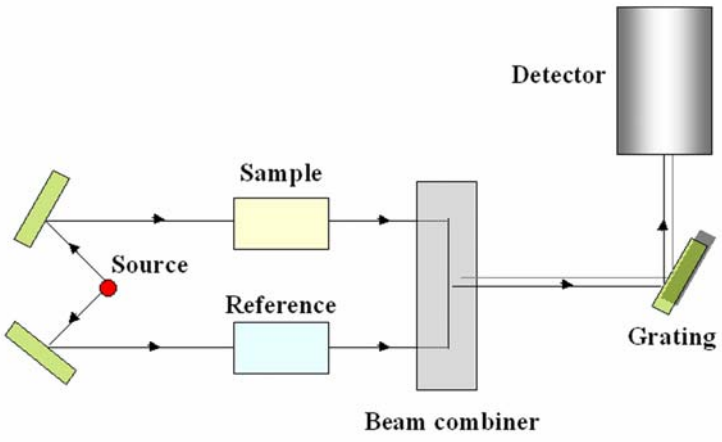

Figure 2.7 *A pictorial representation of the principle of UV-Vis spectrophotometer.*

The detector, which is often a photodiode, alternates between measuring the sample beam and the reference beam. UV–vis spectroscopy measurements of all the samples in the present case were performed on a Jasco V-570 UV/Vis/NIR spectrophotometer operated with a resolution of 1 nm.

2.3 Fourier transform infrared spectroscopy (FTIR)

Instrumentation

Modern spectrometers working in the infrared region generally use the Fourier transform technique for spectral detection and analysis. The essential part of an FTIR instrument is the Michelson's interferometer, which consists of static and a movable mirror as shown in Fig 2.8. The source is generally a Nernst filament consisting of a spindle of rare-earth oxides. The beam is then guided and made to pass through a beam splitter (a part of the interferometer, a component which reflects about half of the radiation that hits it and transmits the rest). The beam thus divided into 2 parts recombines again either constructively or destructively depending on the path difference created by the movable mirror. An actual signal thus consists of radiation spanning a large number of wave numbers and the total intensity is thus integration from the individual contributions.

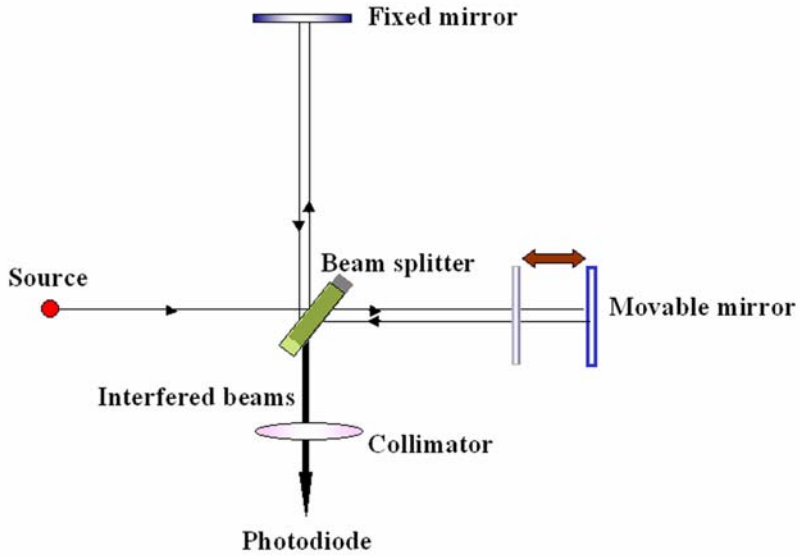

Figure 2.8 *Schematic showing the basic principle behind Michelson's interferometer*

Due to changes in the relative position of the moving mirror to the fixed mirror, an interference pattern is generated. The resulting beam then passes through the sample and is eventually focused on the detector. When this IR beam is directed through the sample, the amplitudes of a set of waves are reduced by absorption if the frequency of this set of waves is the same as one of the characteristic frequencies of the sample. The interferogram contains information over the entire IR region to which the detector is responsive. A mathematical operation known as Fourier transformation converts the interferogram (a time domain spectrum displaying intensity versus time within the mirror scan) to the final IR spectrum, which is the familiar frequency domain spectrum showing intensity versus frequency. The detector commonly used in the FTIR instruments is the pyroelectric substance, deuterated triglycine sulfate (DTGS). Other photoconductive detectors include indium antimonide (InSb) or mercury cadmium telluride (MCT), which are highly sensitive and have faster response time.

Principle

The atoms in a molecule do not remain in a fixed relative position and vibrate about some mean position. If there is a periodic alternation in the dipole moment due to this vibrational motion, then such mode of vibration is infrared (IR) active. The IR region of the electromagnetic spectrum is 100 μm – 1 μm wavelength. The vibrating molecule absorbs energy only from radiation with which it can coherently interact, i.e. the radiation of its own oscillation frequency. The appearance or non-appearance of certain vibrational frequencies gives valuable information about the structure of a particular molecule. The frequency of vibration is given by the relation:

$$\nu = \frac{1}{2\pi} \sqrt{\frac{k}{\mu}}$$

where, k is force constant; μ is reduced mass.

Silicon is the most commonly used substrate for IR measurements, for variety of reasons. It is chemically very stable and generally not very reactive even at high temperatures. It is excellent for optical studies of deposited films in the visible region using reflection techniques. It does not have strong lattice absorption bands in the useful regions of the

infrared and thus can be used for transmission studies in this region. To correct for the lattice absorption bands in silicon, a reference silicon sample is used as a reference.

Peak assignments for fatty amines from monolayer protected clusters

C-H Stretching region: The two bands at 2920 and 2850 cm^{-1} have been assigned to the antisymmetric (d^+) and symmetric (d^-) methylene (CH_2) stretching vibrations respectively and two weak bands at about 2960 and 2875 cm^{-1} to the asymmetric/degenerate and symmetric methyl (CH_3) stretching vibrations respectively. The position of the peaks and the increase in intensity of the methylene stretching vibrations relative to methyl stretching vibration with chain length indicates structural integrity of the molecule. More interestingly, actual peak values of the symmetric and antisymmetric CH_2 stretching vibrations can be used as a sensitive indicator of the ordering of the alkyl chains. For example, Nuzzo *et al* reported that the d^- and d^+ values for hexadecanethiolate monolayer on gold surface appear at 2920 and 2850 cm^{-1} respectively and concluded that the number of gauche defects in the methylene chains was small [6]. Similarly Porter et al. [7] reported that monolayer with chains longer than 6 carbon atoms in the alkyl chain, were highly ordered, whereas the smaller molecules resembled the liquid state, i.e., high density of gauche defects (d^+ and d^- - 2855 and 2924 respectively).

N-H vibrations Typical peaks for the free amine are seen at 3333 cm^{-1}. This band shifts to 3198 cm^{-1} on salt formation of primary amine [8]. NH_3 symmetric deformation band is observed at 1487 cm^{-1} in case of pure amine The NH_3 antisymmetric deformation appears in the region of 1587 cm^{-1} [9].

FTIR measurements of the LB films of nanoparticles in the present study were carried out in the diffuse reflectance mode at a resolution of 4 cm^{-1} on a Perkin-Elmer FTIR Spectrum One spectrophotometer.

2.4 X-ray photoelectron spectroscopy (XPS)

X-ray Photoelectron Spectroscopy known as XPS has been developed from the Fifties by Professor K. Siegbahn for which he was awarded the Physics Nobel Prize in 1981. XPS is surface science technique used to study the composition and electronic state of the surface region of a sample. Since, the technique provides a *quantitative analysis of*

the surface composition is sometimes known by the alternative acronym, ESCA (**E**lectron **S**pectroscopy for **C**hemical **A**nalysis).

Working Principle

XPS is based on well-known photoelectric effect (a single photon in/electron out process) first explained by Einstein in 1905. Photoelectron spectroscopy uses monochromatic sources of radiation (i.e. photons of fixed energy given by relation, $E = h\nu$). In XPS the photon is absorbed by an atom in a molecule or solid, leading to ionization and the emission of a core (inner shell) electron. The kinetic energy distribution of the emitted photoelectrons (i.e. the number of emitted photoelectrons as a function of their kinetic energy) can be measured using any appropriate electron energy analyser and a photoelectron spectrum can thus be recorded. The one way to look at the overall process of photoionization is follows :

$$A + h\nu = A^{+} + e-$$

Conservation of energy then requires that:

$$\mathbf{E(A) + h\nu = E(A^{+}) + E(e-)}$$

Since the electron's energy is present solely as kinetic energy (KE) this can be rearranged to give the following expression for the KE of the photoelectron:

$$\mathbf{KE = h\nu - (E(A^{+}) - E(A))}$$

The final term in brackets, representing the difference in energy between the ionized and neutral atoms, is generally called the *binding energy* (BE) of the electron - this then leads to the following commonly quoted equation:

$$\mathbf{KE = h\nu - BE}$$

the binding energies (BE) of energy levels in solids are conventionally measured with respect to the Fermi-level of the solid, rather than the vacuum level. This involves a small correction to the equation given above in order to account for the *work function* (ϕ) of the solid,

$$\mathbf{KE = h\nu - BE - \phi}$$

Employing photons with fixed energy $h\nu$, it is obvious that if kinetic energy KE and work function ϕ of the sample are measured and known, it is possible to measure binding

energy of electron in solid. Binding energies being characteristic of atoms, different elements present in the sample under investigation are identified. Electrons traveling through a material have a relatively high probability of experiencing inelastic collisions with locally bound electrons as a result of which they suffer energy loss and contribute to the background of the spectrum rather than a specific peak. Due to inelastic scattering process, the flux of photoelectrons emerging from the sample is much attenuated.

Why is the XPS technique surface sensitive?

The soft X-rays employed in XPS penetrate a substantial distance into the sample (~ μm). Thus this method of excitation imparts no surface sensitivity at the required atomic scale. However the photoelectrons can escape from only a very short distance beneath the surface (< 100 Å). The surface sensitivity thus arises from the emission and detection of the photoemitted electrons.

Chemical shift

The exact binding energy of an electron depends not only upon the level from which photoemission is occurring, but also upon:

(1) the formal oxidation state of the atom

(2) the local chemical and physical environment

changes in either (1) or (2) give rise to small shifts in the peak positions in the spectrum - so-called *chemical shifts.* Atoms of a higher positive oxidation state exhibit a higher binding energy due to the extra coulombic interaction between the photo-emitted electron and the ion core. This ability to discriminate between different oxidation states and chemical environments is one of the major strengths of the XPS technique.

The basic requirements for a XPS experiment are:

(1) x-ray source of fixed-energy radiation (usually Mg Kα with $h\nu$ = 1253.6 eV or Al Kα with $h\nu$ = 1486.6 eV)

(2) Concentric hemispherical analyser (CHA), which uses an electric field between two hemispherical surfaces to disperse the electrons according to their kinetic energy, and thereby measure the flux of emitted electrons of a particular energy.

(3) a high vacuum environment (to enable the emitted photoelectrons to be analysed without interference from gas phase collisions)

A closer look at the spectra from the core levels of *p, d and f levels* (example Au 4f or Ag 3d) shows the presence of a photoemission doublet. The reason for the formation of the doublet is the mixing of the spin and the angular momentum, commonly known as the spin-orbit coupling, it can be the Russell- Saunders (*l-s*) coupling or the *j-j* coupling. As for example since the value of *l* for d orbital is 2 hence the coupling will result in the *j value of* 5/2 (2+1/2) and 3/2 (2-1/2). Thus there will be 2 states of $d_{5/2}$ and $d_{3/2}$, the intensity of which depends on the multiplicity.

$$\text{Multiplicity} = 2j+1$$

Hence, for $d_{5/2}$, multiplicity = 2*(5/2)+1=6 and

for $d_{3/2}$, multiplicity = 2*(3/2)+1=4

Thus the ratio of the intensities of the peak will be 6:4 or 3:2 or 1.5:1.

For the work described in this thesis, the XPS spectra of C 1s, Au 4f, Ag 3d, and N 1s core levels were recorded from a LB film containing nanoparticles deposited on Si (111) substrate. XPS measurements were carried out on a VG Microtech ESCA 3000 instrument at a base pressure better than 1 x 10^{-9} Torr with un-monochromatized Mg Kα radiation (1253.6 eV energy). The measurements were made in the constant analyzer energy (CAE) mode at a pass energy of 50 eV and electron takeoff angle (angle between electron emission direction and surface plane) of 60°. This leads to an overall resolution of ~ 1 eV in the measurements. The chemically distinct components in the core level spectra were resolved by a non-linear least squares fitting algorithm after background removal by the Shirley method [10]. The core level binding energies (BE) were aligned with the adventitious carbon binding energy of 285 eV.

2.5 Transmission electron microscopy (TEM)

Specimen-Beam interaction

There are various processes in which a sample interacts with the incident electron beam. A cartoon of the various processes is shown in Figure 2.9. Specimen interaction is what makes Electron Microscopy possible. The energetic electrons in the microscope

strike the sample and various can occur. The reactions noted on the top side of he diagram are utilized when examining thick or bulk specimens (SEM) while the reactions oon the bottom side are those examined in thin or foil specimens (TEM). Specific interaction volume is the volume inside the specimen in which interactions occur while being struck with an electron beam.

This volume depends on the following factors:

(a) Atomic number of the material: higher atomic number materials absorb or stop more electrons and so have a smaller interaction volume.

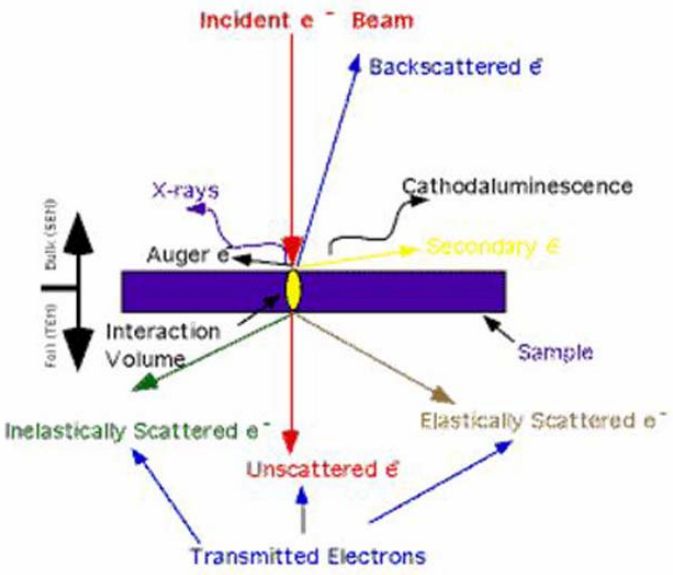

Figure 2.9 *A cartoon showing the possible effects after specimen-electron beam interaction.*

(b) Accelerating voltage being used; higher voltages penetrate farther into the sample and generate larger interaction volumes.

(c) Angle of incidence for the electron beam; the greater the angle (further from normal) the smaller the volume.

Working principle

In TEM analysis, a thin specimen is illuminated with electrons in which the electron intensity is uniform over the illuminated area. As the electrons travel through the specimen, they are either scattered by a variety of processes or they may remain unaffected by the specimen. The end result is that a nonuniform distribution of electrons

emerges from the exit surface of the specimen, that contains all the structural and chemical information about the specimen. Electron microscope is constructed to display this nonuniform distribution of electrons in two different ways.

Angular distribution of scattering can be viewed in the form of scattering patterns, usually called diffraction patterns, and spatial distribution of scattering can be observed as contrast in images of the specimen. The advantage of this arrangement is the possibility of directly viewing the area from which the diffraction pattern arises. The basic components of transmission electron microscope are shown in Fig. 2.10

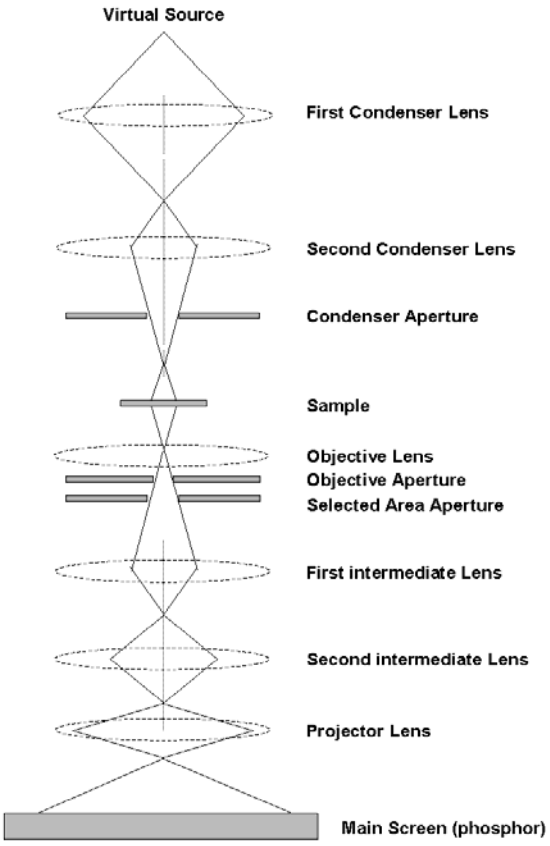

Figure 2.10 *Diagram showing the various elements of the TEM instrument*

A modern TEM is composed of an illumination system, a specimen stage, an objective lens system, the magnification system, the data recording system(s), and the chemical analysis system. The electron gun is the heart of the illumination system, which

typically uses LaB_6 or tungsten thermionic emission source or a field emission source. The LaB_6 gun gives a high illumination current, but the current density and the beam coherence are not as high as those of a field emission source. Field emission source is unique for performing high coherence lattice imaging, electron holography, and high spatial resolution microanalysis. The illumination system also includes the condenser lenses that are vitally important for forming a fine electron probe. The specimen stage is the key to carrying out structure analysis, because it can be used to perform in situ observations of phenomena induced by annealing, electric field, or mechanical stress, giving the possibility of characterizing the physical properties of individual nanostructures. The objective lens is the heart of a TEM which determines the limit of image resolution. The magnification system consists of intermediate lenses and projection lenses, and it gives a magnification upto 1.5 million. The data recording system tends to be digital with the use of a charge coupled device (CCD), allowing quantitative data processing and quantification. Finally, the chemical analysis system is the energy-dispersive X-ray spectroscopy (EDS) and electron energy loss spectroscopy (EELS), both can be used complementary to quantify the chemical composition of the specimen. EDS relies on the counting of X-rays emitted from the beam-illuminated specimen region as a function of the photon energy and it is probably the most precise microanalysis technique in TEM. EELS analyze the intensity distribution of the transmitted electrons as a function of their energy loss. It provides not only the chemical information on the specimen but also its electronic structure. A complementary application of the diffraction, imaging, and spectroscopy techniques available in a TEM is likely to give a more precise and reliable determination of the crystal structure. HRTEM used in the study does not have an EELS attached to it but it does have a STEM and EDAX facility.

Imaging and Diffraction in the TEM

The objective lens forms a diffraction pattern in the back focal plane with electrons scattered by the sample and combines them to generate an image in the image plane (intermediate image). Thus, diffraction pattern and image are simultaneously

present in the TEM. It depends on the intermediate lens which of them appears in the plane of the second intermediate image and magnified by the projective lens on the viewing screen. Switching from real space (image) to reciprocal space (diffraction pattern) is easily achieved by changing the strength of the intermediate lens, Fig 2.11.

In imaging mode, an objective aperture can be inserted in the back focal plane to select one or more beams that contribute to the final image (BF, DF, HRTEM). In selected area electron diffraction (SAED), an aperture in the plane of the first intermediate image defines the region of which the diffraction is obtained [11].

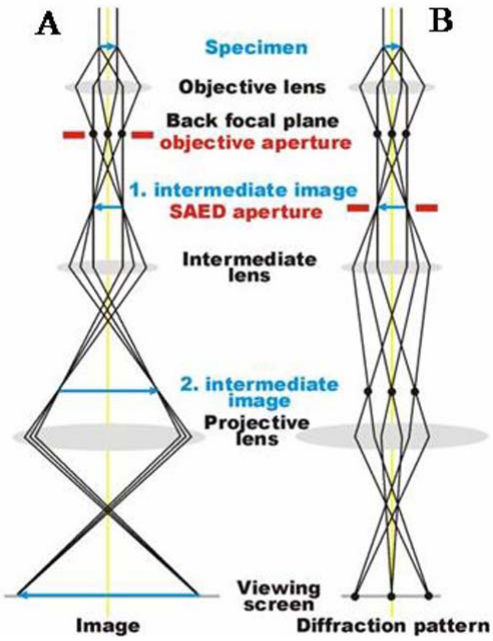

Figure 2.11 *Schematic of Imaging (A) and diffraction modes (B) in TEM Courtesy*: http://www.microscopy.ethz.ch/mtc.htm.

Image Modes in TEM

Principles of Image Formation

Fig 2.12 (A) shows the simplified representation of the ray path leading to the first intermediate image in the image plane of the objective lens. Electrons, which come from the condenser system of the TEM, are scattered by the sample, situated in the object plane of the objective lens. Electrons scattered in the same direction are focused in the

back focal plane, and, as a result, a diffraction pattern is formed there. Electrons coming from the same point of the object are focused in the image plane. In a TEM, the first intermediate image is magnified by further lenses (projective system).

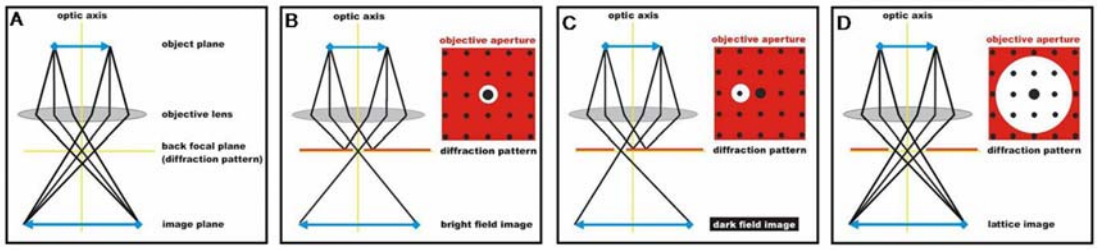

Figure 2.12 *Schematic showing the different modes of image formation Courtesy*: http://www.microscopy.ethz.ch/mtc.htm.

Bright field image (BF)

In the bright field (BF) mode of the TEM, an aperture is placed in the back focal plane of the objective lens which allows only the direct beam to pass. In this case, the image results from a weakening of the direct beam by its interaction with the sample. Therefore, mass-thickness and diffraction contrast contribute to image formation: thick areas, areas in which heavy atoms are enriched, and crystalline areas appear with dark contrast. It should be mentioned that the interpretation of images is often impeded by the simultaneous occurrence of the contrast-forming phenomena , Fig 2.12 (B).

Dark field image (BF)

In dark field (DF) images, the direct beam is blocked by the aperture while one or more diffracted beams are allowed to pass the objective aperture. Since diffracted beams have strongly interacted with the specimen, very useful information is present in DF images, e.g., about planar defects, stacking faults or particle size, Fig 2.12 (C).

Lattice Images (HRTEM)

To obtain lattice images, a larger objective aperture has to be selected that allows many beams including the direct beam to pass. The image is formed by the interference of the diffracted beams with the direct beam (phase contrast). If the point resolution of the microscope is sufficiently high and a suitable sample oriented along a zone axis, then

high-resolution TEM (HRTEM) images are obtained. In many cases, the atomic structure of a specimen can directly be investigated by HRTEM , Fig 2.12 (D).

The incident parallel electron beam, ideally a plane wave, interacts elastically while passing through the specimen, and the resulting modulations of its phase and amplitude are present in the electron wave leaving the specimen. The wave here, the object exit wave o(***r***), thus contains the information about the object structure. Unfortunately, the objective lens is not an ideal but has aberrations (astigmatism, spherical C_s and chromatic C_c aberration) that reduce image quality. The intensity distribution of the exit wave function is described by the contrast transfer function (CTF) [11].

Electron Diffraction (ED)

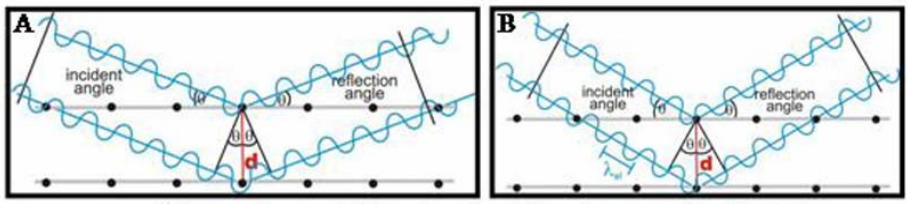

Figure 2.13 *Schematic showing the destructive (A) and constructive interference (B) of reflected waves. Courtesy*: http://www.microscopy.ethz.ch/mtc.htm

Electron diffraction is a collective elastic scattering phenomenon with electrons being scattering by atoms in a regular array (crystal). The incoming plane electron wave interact with the atoms, and secondary waves are generated which interfere with each other (analogous to the Huygens principle for diffraction of light). This occurs either constructively (reinforcement at certain scattering angles generating diffracted beams) or destructively (extinguishing of beams), Fig 2.13. As in X-ray diffraction (XRD), the scattering event can be described as a reflection of the beams at planes of atoms (lattice planes). The Bragg law gives the relation between interplanar distance d and diffraction angle Θ:

$$n\lambda = 2d\sin\Theta$$

Since the wavelength λ of the electrons is known, interplanar distances can be calculated from ED patterns. Furthermore, information about crystal symmetry can be obtained. Consequently, electron diffraction represents a valuable tool in crystallography.

2.5.1 Scanning Transmission Electron Microscope (STEM)

The principle of STEM is that an electron lens is used to focus a high energy beam of electron to form a small scanned electron probe a few angstrom in diameter. A thin specimen is used so that most electrons are transmitted with little lateral spreading, and a variety of signals from elastic and inelastic scattering events are recorded, allowing high spatial resolution analysis and imaging. Three types of detectors are used to obtain STEM images [11]:

1. **BF detector**

It is placed at the same site as the aperture in BF-TEM and detects the intensity in the direct beam from a point on the specimen, Fig 2.14 A.

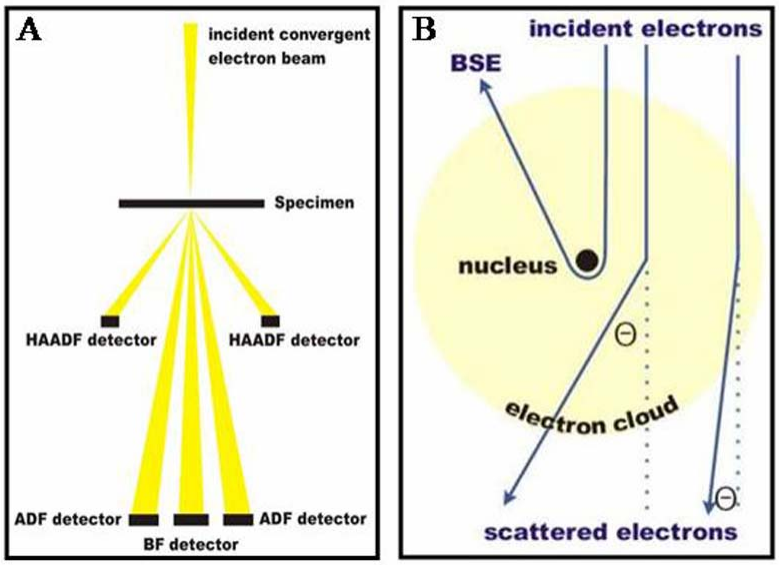

Figure 2.14 *schematic s showing the arrangement of various STEM detectors (A) and the elastic scattering of electrons by atom (B)* Courtesy: http://www.microscopy.ethz.ch/mtc.htm

2. **ADF detector**

The annular dark field (ADF) detector is a disk with a hole in its center where the BF detector is installed. The ADF detector uses scattered electrons for image formation,

similar to the DF mode in TEM. The measured contrast mainly results from electrons diffracted in crystalline areas but is superimposed by incoherent Rutherford scattering.

3. HAADF detector

The high annular dark field detector is also a disk with a hole, but the disk diameter and the hole are much larger than in the ADF detector. Thus it detects electrons that are scattered to higher angles and almost only incoherent Rutherfold scattering contributes to the image. Thereby Z, contrast is achieved.

Elastic Scattering of Electrons by Atoms and the contrast mechanism

An electron penetrating into the electron cloud of an atom is attracted by the positive potential of the nucleus (Columbic interaction), and its path is changed as a result. The closer the electron comes to the nucleus, the higher is the force and consequently the scattering angle. In rare cases, even complete backscattering can occur (back scattered electrons BSE). These interactions can be treated as elastic, which means that no energy is transferred from the scattered electron to the atom, Fig 2.14 B. This simple model helps to explain basic contrast mechanisms in TEM and STEM. The mass-thickness contrast is somehow related to the contrast in optical microscopy, but it is the local scattering power that determines contrast in TEM instead of absorption of light. The interaction of electrons with heavy atoms is stronger than with light atoms so that areas in which heavy atoms are localized appear with darker contrast than such with light atoms (mass contrast). In thick areas, more electrons are scattered of course; these areas appear dark (thickness contrast). In particular, the **mass-thickness contrast** is important in bright and dark field imaging.

The strong Coulomb interaction of the electrons with the potential of atom core, which leads to high angle scattering (designated as Rutherford scattering), is employed by **Z-contrast imaging** in STEM. By this method, small clusters (or even single atoms) of heavy atoms can be imaged in a matrix of light atoms since the contrast is proportional to Z^2 (Z: atomic number) [11].

If a crystalline specimen is transmitted by electrons, then Bragg diffractions happens as well. Each atom in such a regular arrangement acts as a scattering center. If a

crystal is oriented along a zone axis so that many electrons are strongly scattered to contribute to the reflections in the diffraction pattern, then only a few electrons pass without interactions and therefore this crystal appears with dark contrast in the BF image (**diffraction contrast**). In real specimen, all contrast mechanisms, namely mass-thickness and Bragg contrast, occur simultaneously, making interpretation sometimes difficult [12].

Mass-Thickness and Bragg Contrast

The interaction of electrons with heavy atoms is stronger than with light atoms. If the thickness is homogeneous, areas in which heavy atoms are concentrated appear with darker contrast than such with light atoms (mass contrast). Of course, more electrons are scattered in thick than in thin areas; thus, thick areas appear dark (thickness contrast). However, a thick area with light elements might have the same contrast as a thinner area with heavier atoms. If the sample has crystalline areas, many electrons are strongly scattered by Bragg diffraction (especially if the crystal is oriented along a zone axis with low indices), and this area appears with dark contrast in the BF image as well (diffraction contrast).

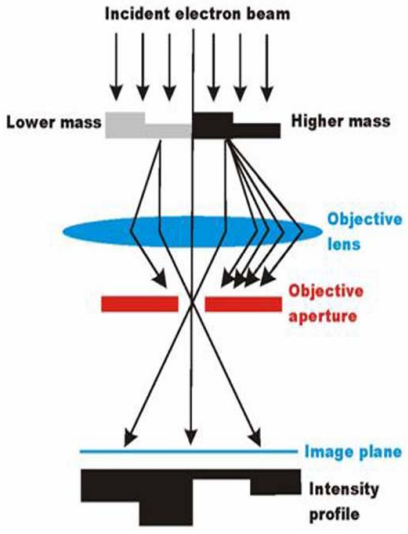

Figure 2.15 *Schematic showing the mass thickness contrasts: courtesy* http://www.microscopy.ethz.ch/mtc.htm

To summarize, independent of the reason for its scattering, all scattered electron beams are deflected away from the optical axis and blocked by the objective aperture, and thus the corresponding areas appear dark in the BF-image. Generally, mass-thickness contrast and Bragg contrast are important in bright and dark field imaging, Fig 2.15 shows a ray diagram for the same [11].

2.5.2 Energy Dispersive X-ray analysis (EDAX)

EDAX Analysis stands for Energy Dispersive X-ray analysis. It is sometimes referred to also as EDS or EDAX analysis. It is a technique used for identifying the elemental composition of the specimen, or an area of interest thereof. The EDX analysis system works as an integrated feature of a Transmission or Scanning electron microscope (SEM), and can not operate on its own without the latter.

During EDX Analysis, the specimen is bombarded with an electron beam inside the electron microscope. The bombarding electrons collide with the specimen atoms' own electrons, knocking some of them off in the process. A position vacated by an ejected inner shell electron is eventually occupied by a higher-energy electron from an outer shell. To be able to do so, however, the transferring outer electron must give up some of its energy by emitting an X-ray.

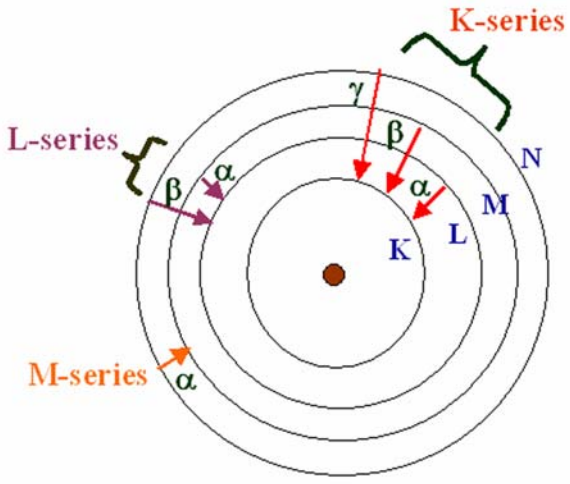

Figure 2.16 *Elements in an EDX spectrum are identified based on the energy content of the X-rays emitted by their electrons as these electrons transfer from a higher-energy shell to a lower-energy.*

The amount of energy released by the transferring electron depends on which shell it is transferring from, as well as which shell it is transferring to. Furthermore, the atom of every element releases X-rays with unique amounts of energy during the transferring process. Thus, by measuring the amounts of energy present in the X-rays being released by a specimen during electron beam bombardment, the identity of the atom from which the X-ray was emitted can be established.

The EDX spectrum is just a plot of how frequently an X-ray is received for each energy level. An EDX spectrum normally displays peaks corresponding to the energy levels for which the most X-rays had been received. Each of these peaks is unique to an atom, and therefore corresponds to a single element. The higher a peak in a spectrum, the more concentrated the element is in the specimen.

An EDX spectrum plot not only identifies the element corresponding to each of its peaks, but the type of X-ray to which it corresponds as well. For example, a peak corresponding to the amount of energy possessed by X-rays emitted by an electron in the L-shell going down to the K-shell is identified as a K-Alpha peak. The peak corresponding to X-rays emitted by M-shell electrons going to the K-shell is identified as a K-Beta peak. See Figure 2.16.

The TEM measurements were done on a JEOL model 1200EX instrument operated at an accelerating voltage of 120 kV. HRTEM/STEM and EDAX were done using **Tecnai G^2 F30 S-Twin** operating at an accelerating voltage of 300 kV

2.6 Contact angle measurements

***What is contact angle*?** Contact angle, θ, is a quantitative measure of the wetting of a solid by a liquid. It is defined geometrically as the angle formed by a liquid at the three phase boundary where a liquid, gas and solid intersect as shown in Fig. 2.17 It can be seen from this figure that low values of θ indicate that the liquid spreads, or wets well, while high values indicate poor wetting. If the angle θ is less than 90° the liquid is said to wet the solid. If it is greater than 90° it is said to be non-wetting. A zero contact angle represents complete wetting.

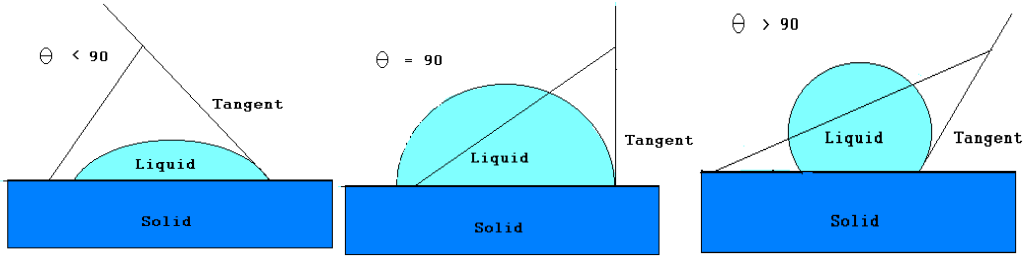

Figure 2.17 *Schematic showing the different contact angles of a liquid drops on solid substrate*

***How is contact angle measured*?** Two different approaches are commonly used to measure contact angles of non-porous solids, goniometry and tensiometry. Goniometry involves the observation of a sessile drop of test liquid on a solid substrate. Tensiometry involves measuring the forces of interaction as a solid is contacted with a test liquid.

Goniometry. Analysis of the shape of a drop of test liquid placed on a solid is the basis for goniometry. The basic elements of a goniometer include a light source, sample stage, lens and image capture. Contact angle can be assessed directly by measuring the angle formed between the solid and the tangent to the drop surface. Goniometry can be used in many situations where tensiometry cannot. One can use a great variety of solid substrates provided they have a relatively flat portion for testing and can fit on the stage of the instrument. Substrates with regular curvature, such as contact lenses are also easily analyzed. Testing can be done using very small quantities of liquid. It is also easy to test high temperature liquids such as polymer melts.

In the present study contact angle measurements of a sessile water drop (1 μL) were carried out on the nanoparticle multilayer films deposited on quartz substrates using a Rame-Hart 100 goniometer.

2.7 Brewster angle microscopy (BAM)

The imaging of thin films at the gas/liquid interface is generally considered to be of great importance in the study of such systems. There are many techniques that can be applied e.g. fluorescence microscopy, AFM to LB films, etc. Many of these techniques require the use of probe compounds in the system (such as a fluorescent dye for instance) or an appropriate modification of if (as in the case of AFM where an LB film has to be

formed). Although still useful there is always the uncertainty of whether the system under study is in its original state or not.

Brewster Angle: Sir David Brewster, a Scottish physicist, in his studies on polarized light discovered that when light strikes a reflective surface at a certain angle, the light reflected from that surface is polarized into a single plane. This angle is commonly referred to as Brewster angle as shown in Fig 2.18 [13]. When the beam arrives on the surface at this critical angle, the polarization degree of the reflected beam is 100 percent with the orientation of the electric vectors lying perpendicular to the plane of incidence and parallel to the reflected surface. The refracted ray is oriented at an angle of 90° from the reflected ray and is only partially polarized.

In other words the Brewster angle is defined as the angle at which the intensity of the vertical component of reflected linearly polarized light passes through a minimum. The Brewster angle is controlled by the refractive indices of the materials in the system. For example, the Brewster angles for the air/water, air/glass and air/diamond interfaces are 53°, 57° and 67.5° respectively.

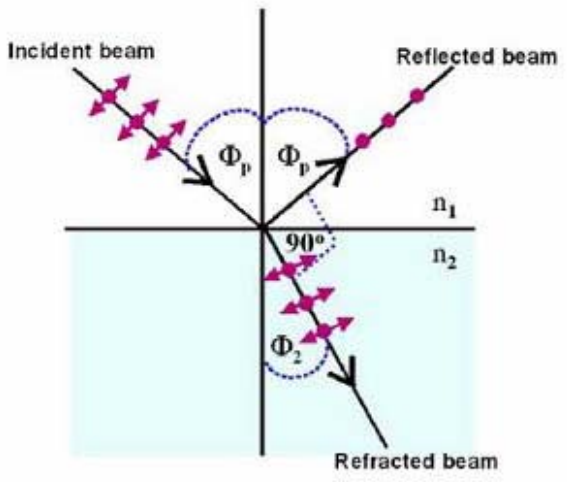

If μ is the refractive index, then, by Snell's law:

$$\frac{\eta_2}{\eta_1} = \mu = \frac{\sin \Phi_p}{\sin \Phi_2}$$

$$\mu = \frac{\sin \Phi_p}{\sin (90 - \Phi_p)}$$

$$\mu = \frac{\sin \Phi_p}{\cos \Phi_p}$$

$$\Phi_p = \tan^{-1} \mu$$

Φ_p = **Brewster Angle**

Figure 2.18 *Generation of Brewster Angle (Φ p) shown by the ray diagram.*

The existence of a Brewster angle is a pecularity of p-polarized light. The reflectivity coefficient rp vanishes at the Brewster angle and hence no light is reflected there. A monolayer at the air-water interface yields a certain amount of reflected light,

which is sufficient to produce an image. The internal structure of domains can be detected. This technique is in many respects superior to fluorescence microscopy, since it does not require any label which could have an undesired impact on the systems.

BAM allows direct observation of the films onto the water/air surface. This technique is sensitive to the surface density and to the anisotropy of phase domains in monolayers, where the reflectivity of a planar interface between two media depends on the polarization of the incident light and on the angle of incidence. For a Fresnel interface (an interface where the refractive index changes steeply) and for a polarization where the electric field is in the plane of incidence, the reflectivity vanishes at the Brewster angle. For a real interface, the reflected light intensity has a minimum at the Brewster angle, but does not vanish. However, the reflected intensity at the Brewster angle is strongly dependent on the interfacial properties and is particularly sensitive to monolayers at the interface. The reflectivity of a real interface at the Brewster angle for the mentioned polarization has three origins: (a) the thickness of the interface, (b) the roughness of real interfaces, and (c) the anisotropy of monolayers.The basis of this method is illustrated in figure 2.19. For a beam of p-polarised light (p- parallel to the plane of incidence) there is an angle of incidence *theta* at which no relfection occurs. This is called "Brewster angle" and is satisfying the relationship **tan(*theta*) = $n_{subphase}$ / n_{air}** , where **n** is the refractive index of the corresponding phase.

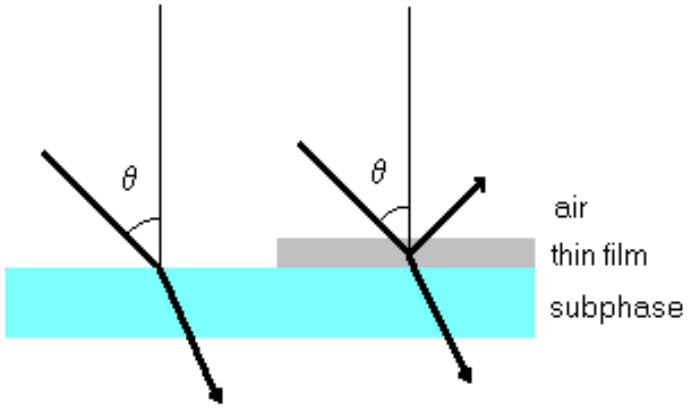

Figure 2.19 *Schematic showing the principal of BAM*

Introducing a thin film in between the two phases the optical properties of the system change so that a small amount of the incident intensity is reflected. In the general case it can be said that the reflected light can have a different from the incident light polarisation state. The reflected light can easily be "captured" by a detector like a CCD camera and in that way the film can be visualised.

A Brewster angle microscope (BAM) is comprised of a light source (laser), a set of one or two polarising filters of which the first is responsible for the polarisation of the beam prior to its reflection and the second is analysing the polarisation state of the reflected part of the beam and a light detector (a CCD camera).

2.8 Electrophoresis and Zeta Potential

Electrophoresis is the migration of charged molecules in solution in response to an electric field. Their rate of migration depends on the strength of the field; on the nett charge, size and shape of the molecules and also on the ionic strength, viscosity and temperature of the medium in which the molecules are moving. As an analytical tool, electrophoresis is simple, rapid and highly sensitive. It is the electromotive force (EMF) that is used to push or pull the molecules through the gel matrix; by placing the molecules in wells in the gel and applying an electric current, the molecules will move through the matrix at different rates, towards the anode if negatively charged or towards the cathode if positively charged (note that gel electrophoresis operates as an electrolytic cell; the anode is positive and the cathode is negative). Figure 2.20 shows the photograph of the setup used for electrophoresis.

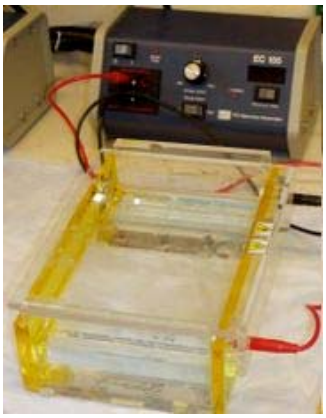

Figure 2.20 *set up used for Gel - electrophoresis*

Zeta potential, in Colloid Chemistry, refers to the electrostatic potential generated by the accumulation of ions at the surface of the colloidal particle which is organized into an electrical double-layer consisting of the Stern layer (The **Stern layer** is the layer of counterions that attach to a charged surface. These ions are temporarily bound and shield the surface charge) and the diffuse layer. The zeta potential of a particle can be calculated if the electrophoretic mobility of the sample is known by Henry's equation:

$$U_e = \frac{2\varepsilon\zeta f(ka)}{3\eta}$$

Where U_e is the electrophoretic mobility, is the dielectric constant of the sample, ζ is the zeta potential, $f(ka)$ is Henry's Function (most often used are the Huckel and Smoluchowski approximations of 1 and 1.5, respectively), and η is the viscosity of the solvent.

2.9 Conductivity measurement

Keithley 238 high current source measure unit has been used for all the electrical characterization. It can operate in two modes where it can functions as a current or a voltage source:

1. Source V Measure I: In this mode, the instrument functions as a voltage source and simultaneously measures the current given across the circuit. This instrument is capable of sourcing ±100μV to ±110 V. When programmed to source voltage, current measuring meter is connected in series with V source and output (Figure 2.21A).
2. Source I Measure V: Here, the instrument functions as a current source and measures the potential drop across the given circuit. This instrument is capable of sourcing ±100 fA to 1A. When programmed to source current, potential measuring meter is connected across (in parallel) with the current source and the output (Figure 2.21B).

The instrument functions in two operation modes namely DC mode and Sweep mode. The source measure unit operation (both DC and sweep modes) also consists of source delay measure (SDM) cycles. During each SDM cycles following steps occur,

1. Set the source output level.

2. Perform the delay.

3. Make the measurement.

The delay is used to allow the source to settle before the measurement is made. The total period of delay includes internal (default) delay and the user defined programmed delay. With the default delay enabled, a short delay is allowed for internal settings on the low current ranges. In dc operation a constant current or voltage is applied to the output. This operation consists of continuous series of SDM cycles. In each SDM cycle, the measured reading will be internally updated, making them available for display. In sweep operations the measure unit sweeps through the user defined list of points specifying source values and delay times for wave forms. An SDM cycle occurs in each programmed step. Each measurement taken is stored in sweep buffer.

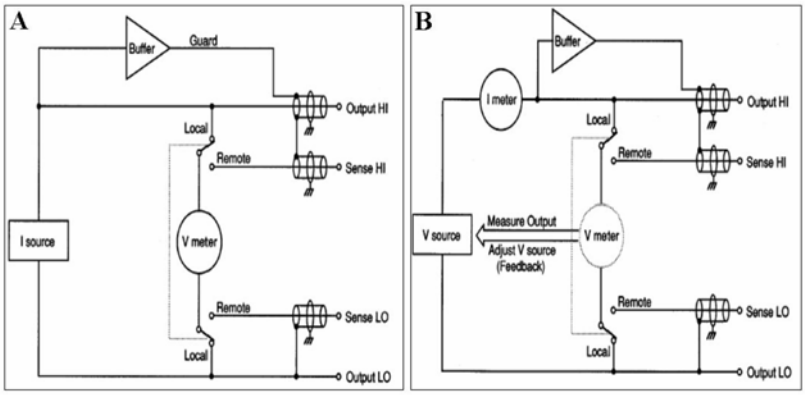

Figure 2.21 *Schematic showing the circuit diagram of conductivity meter: (A) Source I Measure V (B) Source V Measure I mode [10].*

There are six basic types of sweep waveforms available namely fixed level, linear staircase, log staircase, pulse, linear staircase pulse and log staircase pulse. The instrument is capable of being handled in 2 modes i.e. in “local mode” operated through the operating panels on the instrument or in “remote mode”. In remote mode different controls of the instrument are handled through computers, where according to our requirements programs can be written to perform the specific operation. Local mode has limitations in its application the measurement data is stored in the instruments memory, which is very limited. So in local mode it is not possible to perform the measurement for a long period. Remote sensing is a better alternative, which is achieved by interfacing the

instrument with computer by standard IEEE-488 bus connector. The programs written in TEST POINT programming environment were used for various DC and sweep mode electrical measurements. Besides, another program was written to make electrical measurement at fixed voltage as a function of time, which was used to measure conductivity variation on exposure to chemical vapors.

The electrical property measurements of the films were performed. Besides, the electrical properties of the silver film and silver-gold bimetallic film were also studies at room temperature and as a function of varying temperature to calculate the activation energy. All the above systems were also studied for change in the electrical property (at fixed voltage) as a function of time during exposure and removal of various chemical vapors to establish their application in chemical vapor sensing.

References

(1) Ulman, A. *An introduction to Ultrathin Organic Films: from Langmuir-Blodgett to Self-Assembly*, Academic Press, San Diego, CA, **1991**.

(2) Denney, R.C; Sinclair, R. *Visible and Ultraviolet Spectroscopy*. *Analytical Chemistry by open learning series*, John Wiley and Sons, USA.

(3) Mie, G. *Ann. Phys*. **1908**, *25*, 377.

(4) Mulvaney, P. *Langmuir* **1996**, *12*, 788. (b) Henglein, A. *J. Phys. Chem. B*. **1993**, *97*, 5457.

(5) Kelly, K. L.; Coronado, E.; Zhao, L.L.; Schatz, G. C. *J. Phys. Chem. B* **2003**, *107*, 668.

(6) Nuzzo, R.G.; Fusco, F.A.; Allara, D.L. *J. Am. Chem. Soc*. **1987**, *109*, 2358. (b) Nuzzo, R.G.; Dubois, L.H.; Allara, D.L. *J. Am. Chem. Soc*. **1990**, *112*, 558.

(7) Porter, M.D.; Bright, T.B.; Allara, D.L.; Chidsey, C.E.D. *J. Am. Chem. Soc*. **1987**, *109*, 3559.

(8) Bardosova, M.; Tregold, R.H.; Ali-Adib, Z. *Langmuir* **1995**, *11*, 1273. (b) Pal, S. *Ph. D thesis* University of Pune, **1996**.

(9) Ning, G.; Guangfu, Z.; Shiquan, X. *J. Mol. Struct*. **1992**, *275*, 85.

(10) Shirley, D. A. *Phys. Rev. B* **1972**, *5*, 4709.

(11) http://www.microscopy.ethz.ch/mtc.htm

(12) Hirsch, P. B.; Howie, A.; Nicholson, R. B.; Pashley, D. W.; Whelan, M. J. *Electron Microscopy of Thin Crystals*; Roberts E. Krieger Publishing Company: New York, **1977**.

(13) http://en.wikipedia.org/wiki/Brewster's angle

Chapter III

Assembly of hydrophobized gold nanoparticles at the air-water interface by varying the surface tension

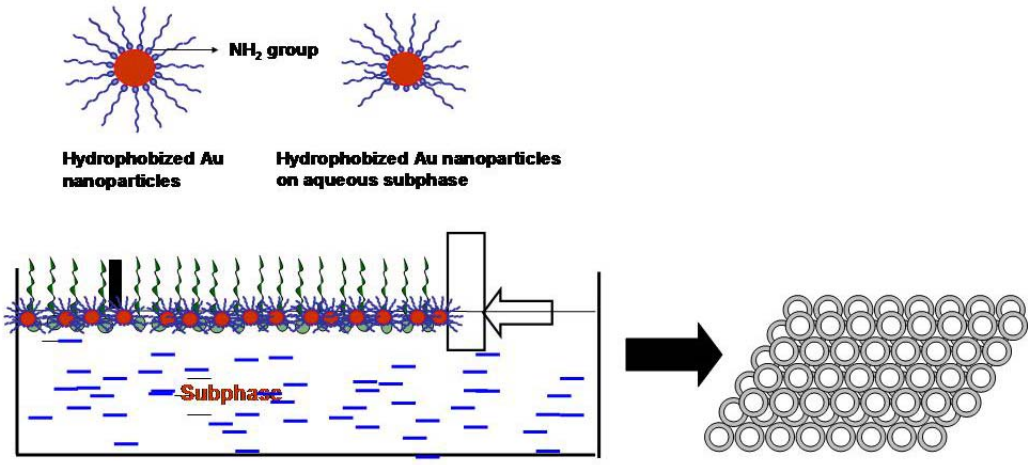

Periodicity is one of nature's fundamental beauties.* (*P. Ball)

Presence of monolayer of surfactant reduces the surface tension of the water subphase at the air water interface. In this chapter we have exploited this fact to modulate the assembly of nanoparticles at the air water interface. The chapter demonstrates the effect of deposition pressure, nature of lipid monolayer and solvent type in controlling the long range ordering of nanoparticles at the air- water interface.

Part of the work presented in this chapter has been communicated

(1) Pasricha, R.; Swami, A. and Sastry, M. *J. Nanosci Nanotech.*, **2007** (communicated).

3.1 Introduction

Nanophase and nanoparticle materials are the new generation of advanced materials that are expected to exhibit unusual chemical and physical properties different from those of either the bulk materials or single atoms [1]. Engineering of nanophase materials and devices is of vital interest in electronics [2], semiconductors and optics [3], catalysis [4], ceramics [5] and magnetism [6, 7]. The unique properties of nanophase materials are determined by their atomic scale structures, particularly the structures of interfaces and surfaces. In fact, studies of small particles and catalytically active particles have been a focused area of scientific research for decades.

It is only recently that a new idea has begun to be realized. Nanoparticles and the physical and chemical functional specificity and selectivity they possess, make them ideal building blocks for two- and three dimensional cluster self-assembled superlattice structures (in powder, thin film, and solid bulk form), in which the particles behave like well-defined molecular matter, arranged with long-range translational and even orientational order [8]. Well-defined ordered solids prepared from tailored nanocrystalline building blocks provide new opportunities to optimize and enhance the properties and performance of the materials. This is a new initiative in research on cluster engineered materials. Research has lead to the successful fabrication of self-assembled passivated nanocrystal superlattices (NCSs) or nanocrystal arrays (NCAs) of metal, semiconductor, and oxide clusters, which are a new form of materials of fundamental interest and technological importance. There are four key steps to develop these materials: controlled preparation of size and shape selected nanoparticles, control of the self-assembly process to produce large well-ordered NCSs, structural characterization, and modeling the dynamic behavior of the system. Indeed, understanding and optimizing the structures of the NCSs is an important step towards a systematic exploration of the nature of patterned superstructures assembled from such building units. This will further lead to formulation and implementation of methods for designing and controlling such novel assembled materials and their operational characteristics.

Self-assembled arrays involve self-organization of size selected nanoclusters encapsulated in protective compact organic coatings into monolayers, thin films, and superlattices. A key step in this process is the fabrication of size and shape controlled NCAs that have the potential to grow to a size large enough for technological applications. Colloidal chemistry, or soft chemistry, has played a powerful role in this process. Self-organization of nanoparticles is a new route to the synthesis of superlattice materials-solid and periodic arrays built using them as building blocks [8-12]. This is achieved by preparing size and shape selected nanocrystals using colloid chemistry and then using self assembly as a means of joining them together (Fig. 3.1) [13].

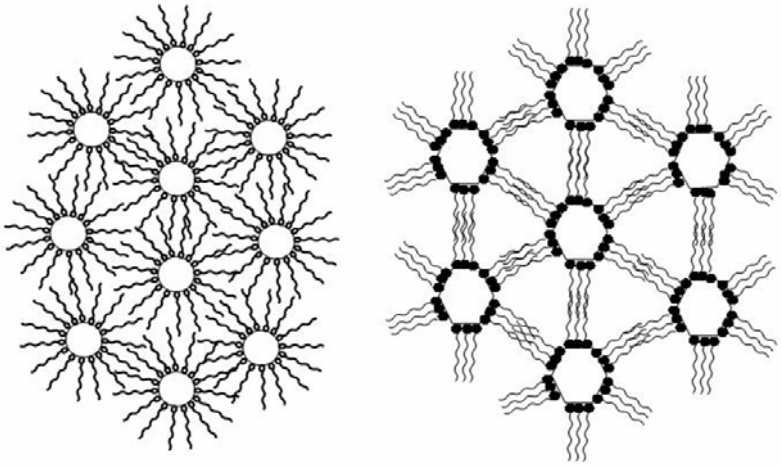

(a) (b)

Figure 3.1 *Schematic showing self assembled passivated nanocrystal superlattices of spherical (a) and faceted (b) particles.*

The macroscopic properties of the NCSs is determined not only by the properties of each individual particle but also by the coupling/interaction between nanocrystals interconnected and isolated by a monolayer of thin organic molecules. By changing the length of the molecular chains, quantum transitions and insulator-to-conductor transitions could be introduced. NCSs are characterized by the unprecedented size uniformity, translational and even orientational order.

Although there are numerous techniques for preparing metal clusters, most of the current research on self-assembled metal particles is concentrated on Au [8,14,15], Ag

[12,16,17], and Ag_2S [18,19]. Particles that can be self-assembled are usually smaller than 10 nm in size. It is in this size range that many exciting and unusual physical properties are enhanced. The nanocrystal thin films reported here are formed primarily on a solid substrate via the self-assembly of nanocrystals.

Directed self-assembly of nanoparticles opens new avenues of technology through controlled fabrication of these nanoscopic materials. Ligand-stabilized colloidal nanoparticles are ideally suited for hierarchical self-assembly, because the nanoparticle's core dictates optical, electronic, or magnetic properties, whereas the surface-bound ligands define the particle's interactions with its surroundings. Periodicity is one of nature's fundamental beauties. Ordering at the atomic scale produces energy bands that determine the electrical and optical properties of crystalline materials. On the other hand, lack of symmetry can lead to distinctly different properties that are unique to noncrystalline materials [20]. Moreover, the ability to assemble into well defined two and three dimensional spatial configurations leads to the development of a general procedure for the fabrication of "quantum" crystals. Fabrication of such nanocrystals would, for example, lead to production of optical gratings [21, 22], optical filters [23], antireflective surface coating [24, 25], selective solar absorbers [26], and data storage and microelectronic devices [27]. Therefore the development of highly ordered nanoscale and microscopic structures has drawn much attention, and a great deal of work has been done on the development of different alternatives for organizing materials with high degree of accuracy, reproducibility, and efficiency.

Several approaches have been adopted in order to obtain 2D and 3D self assembled nanostructures. Synthesis of inorganic-organic superlattices have been obtained by using a multilayer cast film [28]. Highly monodisperse nanoparticles synthesized in nonpolar organic solvents have been shown to self-assemble into ordered structures during solvent evaporation on suitable substrates [8, 29, 30]. However, these nanoparticle assemblies generally lack long-range ordering. Other methods for nanoparticle assembly depends on their immobilization onto the surface of self-assembled monolayers [30a, 31], surface-modified polymers [32] by covalent attachment,

electrophoretic assembly onto suitable substrates [33, 34], or immobilization of nanoparticles at the air-water interface by using electrostatic interactions between nanoparticles and oppositely charged Langmuir monolayers [30a, 35]. Recently, extensive studies have been performed on optical and electronic [36-38] properties of 2D superlattices of metal nanoparticles, and it has been proposed that the structure [37], interparticle spacing [38], and periodicity [39] of 2D super lattices greatly affect their properties. The degree of ordering in the superlattice correlates with core size dispersity. The polydispersity in particle size prevents fabrication of such well-defined two or three-dimensional structures. Hence, external forces are used to induce formation of ordered monolayers made of such particles. For example, electrodeposition [40] and Langmuir-Blodgett [41] techniques favor the formation of submonolayers. The Langmuir-Blodgett (LB) technique is a potential way to assemble the nanoparticles with well-defined structure and thickness controlled at the molecular level. It has shown great potential in the synthesis and assembly of nanocrystals. Sastry and coworkers have developed a simple protocol for hydrophobization of nanoparticles, their organization at the air-water interface and their subsequent transfer to solid support in order to obtain closed packed structures [42]. So far, metal, metal oxide, and semiconductor nanocrystals have been shown to self-assemble into ordered structures upon evaporation of the solvent on a solid substrate or at the air-water interface [8, 10, 19, 43]. However, the resulting morphologies and the degree of ordering achieved vary significantly. Most of the nanocrystal superlattices reported so far have ordered domain sizes less than a few hundred nanometers. Spatial disorder can induce undesirable change in the electronic and optical properties of the nanocrystal network [44]. Experimentally, periodicity with long-range ordering is hard to achieve not only because of the intrinsic particle size distribution but also because of the dewetting of the solvent during the self-assembly process. Korgel and Fitzmaurice suggested that the polarity of the solvent affects its wetting properties and subsequently influences the aggregation of nanocrystals on the surface [45]. Ohara et al. and Gelbart et al. have also examined the mechanism of solvent dewetting in annular ring structures formed by drying diluted metal colloids on a solid substrate [46].

Periodic packing of nanocrystals is different from the 3D packing of atoms in several aspects. First, to an excellent approximation atoms are spherical, while nanoparticles can be faceted polyhedra, thus the 3D packing of particles can be critically affected by their shape and size. Second, the atom size is fixed, but the size of nanoparticles can vary slightly, although their size distribution can be very narrow. Finally, atomic bonding occurs between outershell (valence) electrons to form ionic, covalent, metallic bonds or mixtures of these. In most cases the interatomic distance is fixed, while the bonding between nanoparticles is generated by surfactant molecules whose length is controllable, thus the ratio of particle size to inter particle distance is adjustable. This is a parameter likely to determine the 3D packing of the nanoparticles and the control over interparticle interactions, giving rise to novel tunable structural, optical and transport properties.

This chapter describes the role of solvents, surfactants and surface pressure in the formation of 2D superlattice of gold nanocrystals. Specifically, we show that the morphology of the domain structures in gold nanocrystal arrays is determined by a competition between the 2D superlattice formation and solvent evaporation. By controlling the spreading and subsequent evaporation process of the solvent, long-range-ordered nanocrystal superlattices can be prepared routinely, with domain size of several microns. The monolayer present on the surface of water reduces its surface tension, which in turn considerably reduces the rate of spreading of nanoparticles and subsequent evaporation rate of the solvent as compared to that on the surface of pure water. Two different surfactants, one anionic (stearic acid, StA) and other cationic (octadecylamine, ODA), have been used to form the monolayer. Rate of evaporation of the solvent is another factor by which the range of ordering rate can be tuned. For this purpose, a polar (chloroform) and a nonpolar (benzene) organic solvent with different rates of evaporation have been used for dispersing nanoparticles. We observe that by varying the surface pressure, it is also possible to manipulate nanoparticle assembly at different length scales.

3.2 Synthesis and Characterization

3.2.1 Synthesis of ODA-capped gold nanoparticles

Gold nanoparticles were synthesized by sodium borohydride reduction of 10^{-4} M aqueous solution of chloroauric acid, that results in a clear ruby red coloured gold nanoparticles solution of pH 9 [47]. Particle size when measured was found to be 9 ± 1.5 nm [47]. Vigorous shaking of these aqueous gold nanoparticles with 10^{-3} M ODA solution in chloroform resulted in the rapid phase transfer of these gold nanoparticles from aqueous phase into chloroform phase, which could be clearly seen from the appearance of red color in the originally colourless chloroform phase. Figure 3.2 shows the steps for the formation of hydrophobized gold nanoparticles (Au-ODA). The chloroform phase was separated from the aqueous phase and was dried using rotavapor to form a powder of the hyrophobized gold nanoparticles. This powder was washed several times with ethanol to remove uncoordinated ODA molecules [48].

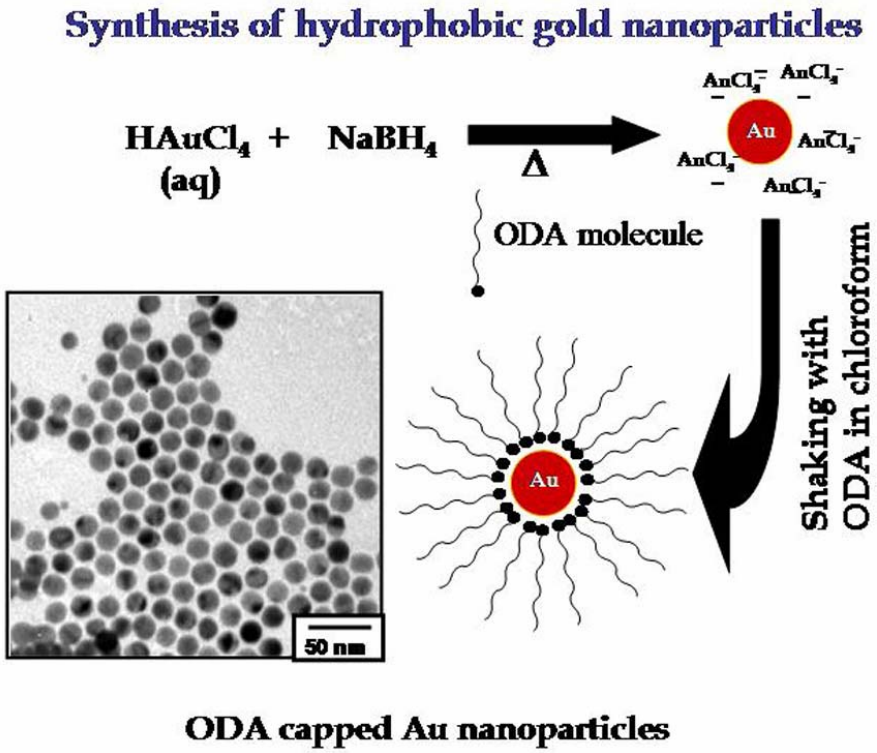

Figure 3.2 Schematic *showing the synthesis of hydrophobized gold nanoparticles and a TEM micrograph showing the hydrophobized gold nanoparticles.*

3.2.2 Organization of hydrophobized gold nanoparticles at the air-water interface

3.2.2.1 In the absence of monolayer

Thin multilayered films of hydrophobized gold nanoparticles were formed using Nima model 611 LB trough equipped with a Wilhelmy plate as the surface-pressure sensor and pure deionized water as the subphase. The solution of hydrophobized gold nanoparticles was prepared in chloroform and benzene at a concentration of 1 mg/mL. This solution was spread slowly onto the water surface in a drop wise fashion using a Hamilton micro liter syringe and was allowed to stand for at least 20 min for solvent evaporation prior to compression. The film was then compressed by a barrier moving at a speed of 20 cm^2/min. Particle monolayers were deposited onto carbon-coated copper grids by lifting the substrates vertically under controlled surface pressures.

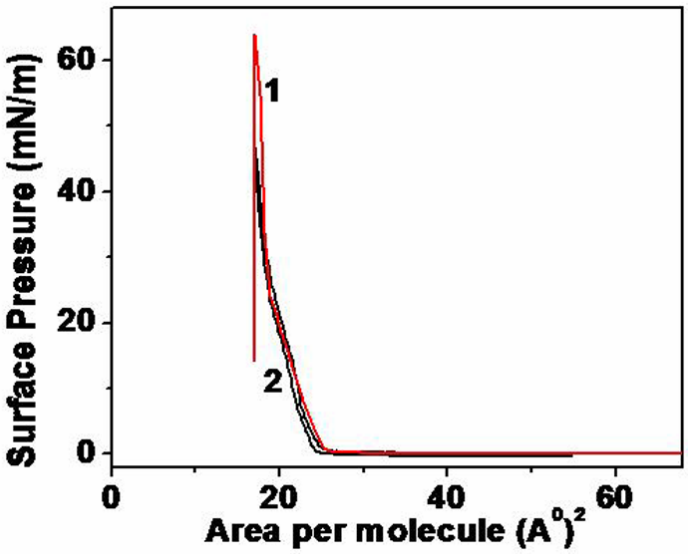

Figure 3.3 *π–A isotherms recorded during one compression and expansion cycle of StA (curve1) and ODA (curve 2) Langmuir monolayer on surface of pure deionized water at pH 7.1*

3.2.2.2 In the presence of monolayer

Stearic acid (StA) and octadecylamine (ODA) were used as a choice of anionic and cationic lipids for the formation of the monolayer on the water subphase. For the formation of monolayer, 75 µl of (1 mg/ml) solution of ODA in chloroform was spread slowly onto the water surface at pH 7.1 in a drop wise fashion with the barrier set at a

maximum area of 580 cm^2. After spontaneous spreading on the sub phase, the film was allowed to stand for at least 20 min for solvent evaporation prior to isotherm measurements and between compression cycles. The monolayer thus formed was compressed to three different pressures of 5 mN/m, 15 mN/m and 20 mN/m respectively by using the barrier at a rate of 20 cm^2/min. These pressures represent the gas, liquid and solid phase of the StA and ODA monolayer on aqueous subphase. The pressure-area (π-A) isotherm of StA and ODA on pure ionized water as subphase is shown in Fig 3.3.

Upon reaching the target value, the surface pressure was maintained at that value by the adjustment of the barrier, thereafter 50 µl of the 1 mg/ml mixture of hydrophobized gold nanoparticles in chloroform/benzene was spread on the monolayer in the compressed state. The same procedure was repeated for formation of StA monolayer.

3.2.3 Brewster Angle Microscopy

The BAM images shown in Fig. 3.4 exhibit the morphological information of StA monolayer at different points of the π-A isotherm shown in Fig 3.3 (curve 1), corresponding to the gas, liquid and liquid condensed zones.

As seen in the Fig 3.4A, when the occupied area of molecule is large, no light is reflected from the air-water interface and a dark image is observed, which is identified to be gas phase. Upon monolayer compression, bright zones of low contrast appear and the brightness and area of these zones increase gradually, indicating the increasing density of the monolayer and the formation of liquid phase. The bright zones tend to form domains with distinct boundaries between gas and water phase. The gas/liquid coexistence phase persists before the lift off point of isotherm. As shown in Fig. 3.4B, upon further compression, the gas-phase zone becomes less visible and the various liquid phase domains form a pattern, this has been reported in the literature for the monolayers of fatty acids [49]. The contrast between the mosaic domains decreases when the surface pressure is increased further (Fig. 3.4C) and a uniform morphology is approached after passing the phase transition. The uniform phase image is identified to be the solid phase of the StA monolayer. The BAM images of ODA show a slightly different morphology. The

coexisting gas and liquid phases were observed before the lift off point of the isotherm as in the case of StA monolayer.

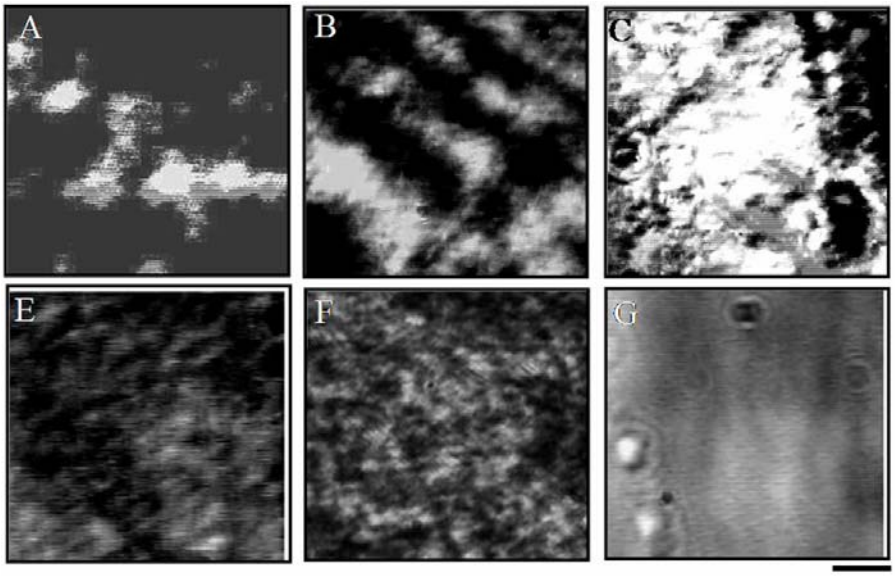

Figure 3.4 *BAM images of pure StA (A-C) and pure ODA (E-G) monolayer on air – water interface at room temperature. The figures correspond to the BAM images at barrier pressure corresponding to gas, liquid and condensed liquid phase respectively. The scale bar corresponds to a length of 80 μm.*

3.2.4 The spreading behaviour of the hydrophobized gold nanoparticles on the monolayer

The spreading behavior of Au-ODA in solvent on the monolayer protected water surface was studied at room temperature by varying the surface pressure and also by using two different solvents, such as Chloroform and Benzene. (Video recording of the spreading behaviour is available in the attached CD). Fig. 3.5A-B shows the photographs of the domain of Au-ODA nanoparticles in chloroform on StA/ODA at surface pressure of 5 mN/m and 10 mN/m respectively. In the case of Au-ODA in chloroform on StA/ODA monolayer, it was observed that at surface pressure of 5 mN/m, a drop of Au-ODA-chloroform solution onto the monolayer spreads fast and then contracts to form an irregular shaped film on the surface within a time of 1-3 sec, resembling the phenomenon of viscous fingering. As we increase the pressure to 10 mN/m, the spreading area of the drop when added onto the monolayer reduces and there is formation of both irregularly

shaped domains as well as some circular domains. Fig 3.5 C-D shows the domain of Au-ODA nanoparticles at surface pressure of 15 mN/m, in chloroform on StA and ODA monolayer respectively.

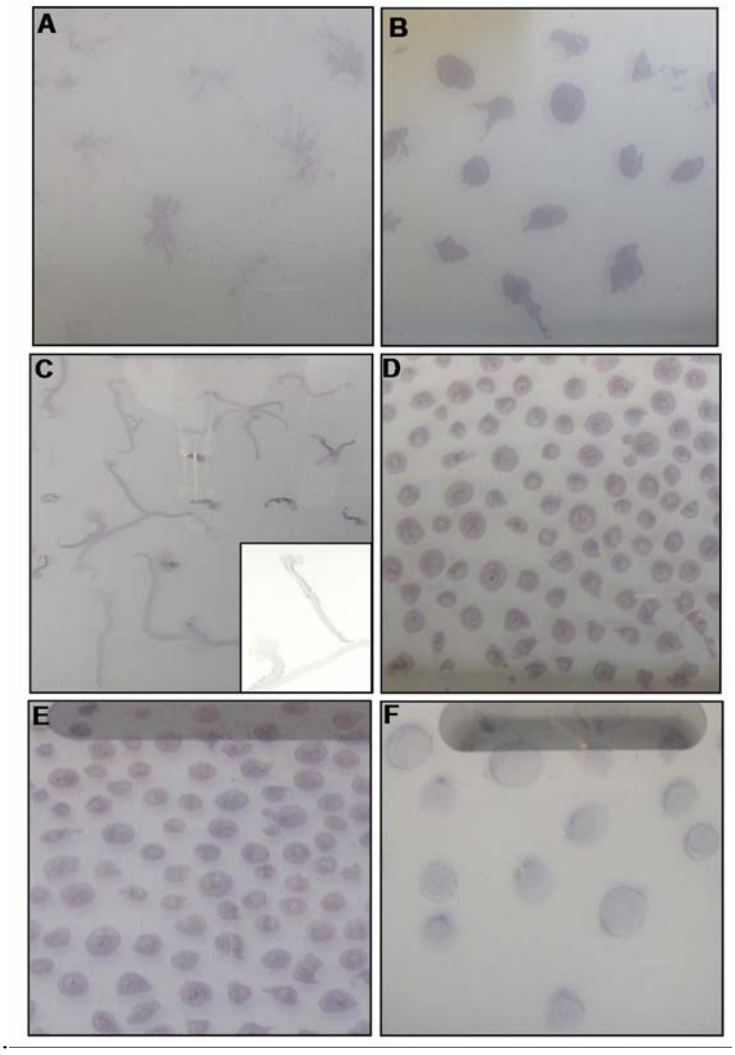

Figure 3.5 *(A) and (B) shows the optical images of microscopic domains of gold nanoparticles formed after spreading Au-ODA in chloroform on StA/ ODA monolayer at surface pressures 5 mN/m and 10 mN/m respectively. (C) and (D) are the photographs after spreading Au-ODA in chloroform at surface pressures 15 mN/m, on StA and ODA monolayer respectively. (E) and (F) show the photographs of microscopic domains of gold nanoparticles formed after spreading Au-ODA in benzene at surface pressures 15 mN/m, on StA and ODA monolayer respectively.*

It is evident from the images that the structure of the domains on StA and ODA monolayers are different in nature. In case of StA monolayer they are thin and stretched, with a clear outer dark line and thin inner areas (inset of Fig 3.5C), whereas in the case of

ODA monolayer, the domains are larger in size, circular with an outer line of contact. The structures are different due to difference in spreading nature of chloroform on StA and ODA monolayers because of the difference in the interaction of the hydrophobized gold particles with the surfactant monolayer.

In the case of Au-ODA in chloroform on StA monolayer, it was observed that as the compression pressure is increased to 15 mN/m from lower pressures, the drop does not spread at all, but contracts in size sitting on the monolayer and then after a gap of 2-3 sec, it starts to move fast in a jet-like motion onto the surface, leaving a trail of nanoparticle film behind and then stops when the spreading solution is over. On further increasing the pressure to 20 mN/m we found that the drop does not spread, it just sits for some time and then travels all over the monolayer as it evaporates very slowly leaving a thick circular area behind which exhibits a multilayer characterat. This may be due to the fact that in the solid phase of the monolayer, the surfactant molecules have lesser gaps between and free space for thus the interaction of Au-ODA in solvent with the aqueous subphase and the monolayer is less.

In the case of Au-ODA in chloroform on ODA monolayer, the spreading and evaporation behavior of the drop at 5 mN/m and 10 mN/m is the same as in the case of StA monolayer however at the pressure of 15 mN/m the drop wets the surface and then the solvent slowly evaporates over a time of 3-4 sec, leaving behind a thin circular domain which resembles the coffee stain pattern. At 20 mN/m, the drop when poured, does not spread on the monolayer surface (no wetting and dewetting), but slowly evaporates leaving multilayers behind. These domains are of the same size and shapes for all the drops put on to the surface as shown in Fig. 3.5D. It is well known that the evaporation of sessile drops can proceed either through constant contact area and decreasing contact angle or by constant contact angle and decreasing contact area [50]. The case of Au-ODA on the ODA monolayer, the drop seems to maintain a constant area

We also studied the spreading of Au-ODA in a nonpolar solvent, benzene which has slower evaporation rate (as compared to chloroform), on StA and ODA monolayers. The drop of solution when poured on the monolayer wets the surface at low pressures,

contracts into irregular shapes and evaporates fast. As we increase the surface pressure, the rate of spreading and evaporation reduces. Fig. 3.5E and F show the photographs of the domain of Au-ODA nanoparticles in benzene, at surface pressure 15 mN/m, on the StA and ODA monolayer respectively. In both the cases, the structure of domains are same in nature, which indicates that the spreading behavior and rate of evaporation in case of benzene as a solvent does not depend on the nature of monolayer. The TEM studies presented in next section agrees with our observation. These films on the monolayers range from pink to purple in color for the monolayer and multilayer structures, respectively.

3.2.5 Transmission Electron Microscopy

A range of different monolayer patterns was observed after evaporation of solvent in the gold colloid at different pressures in the presence and absence of the monolayer. The formation of nanoparticle networks is supported by direct and visual characterization (TEM measurements). Fig. 3.6A and B show the TEM images of drop-coated samples of Au-ODA in chloroform and Au-ODA in benzene on carbon coated copper grids respectively. From the TEM images it is clearly seen that though the particles are arranged in a hexagonal assembly only in case of benzene as a solvent but there is lack of long range ordering.

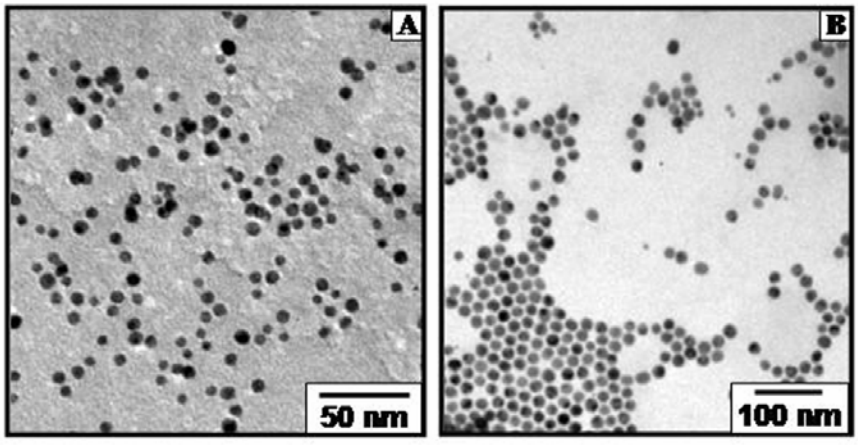

Figure 3.6 *(A) and (B) Representative TEM images of drop coated film of Au-ODA in chloroform and benzene respectively.*

Fig. 3.7A, B and C, D show the TEM images at different magnification of Au-ODA in chloroform on StA monolayer and on ODA monolayer respectively. From the TEM images it is clearly seen that in both the cases (on StA and ODA monolayers) the monolayer domains are large. A range of different monolayer patterns were observed in the case of Au-ODA in chloroform from the StA and ODA monolayers. When we changed the monolayer from StA to ODA, the patterned morphology changed from the domain having thick outer multilayers, (Figure 3.7, B) to uniform large domain (Figures 3.7 C,D).

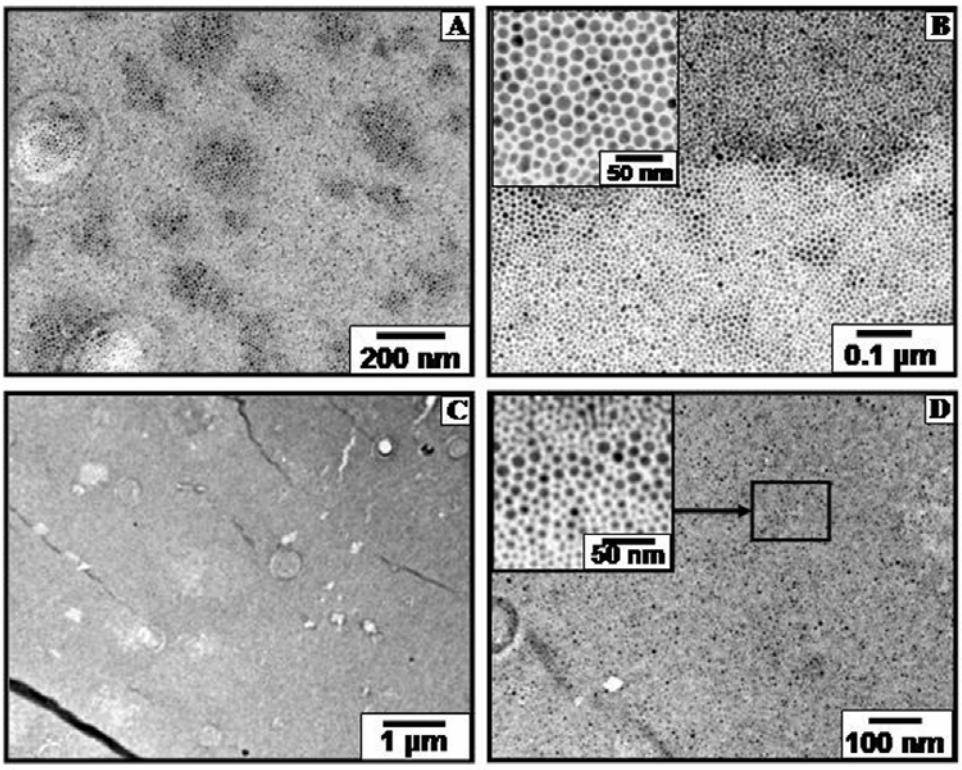

Figure 3.7 *(A) and (B) Representative TEM images at different magnifications, of Au-ODA nanoparticles in chloroform on StA monolayer at surface pressure 15 mN/m. (C) and (D) show the different magnified TEM images of Au-ODA nanoparticles in chloroform on ODA monolayer at surface pressure 15 mN/m. Inset of B and D show the TEM images at higher magnification.*

As explained earlier the gold nanoparticles are capped with ODA molecules, therefore in the case of ODA monolayer, the interaction between particles and monolayer may be driving the particles towards the surface of the drop and then these crystallites dry to form long range ordering with no multilayers. Whereas in the case of StA monolayer

the interaction between the particles and monolayer is expected to pull the particles in and the nanocrystals are pinned to the monolayer. The domains thus formed depend on the nanocrystal and monolayer interaction. Comparing the TEM images of Au-ODA nanoparticles on StA and ODA monolayers, it is clear that the lipid molecules (StA and ODA) play a crucial role along with other parametrs in forming well-ordered arrays of gold nanoparticles. The interactions between ODA-capped Au nanoparticles and lipid molecules present in the monolayers are responsible for the formation of thermodynamically stable well-ordered assembly at the air-water interface by balancing steric repulsion interaction and strong hydrophobic interactions between the hydrophobic part of the lipid molecules present in the monolayer and on gold nanoparticles.

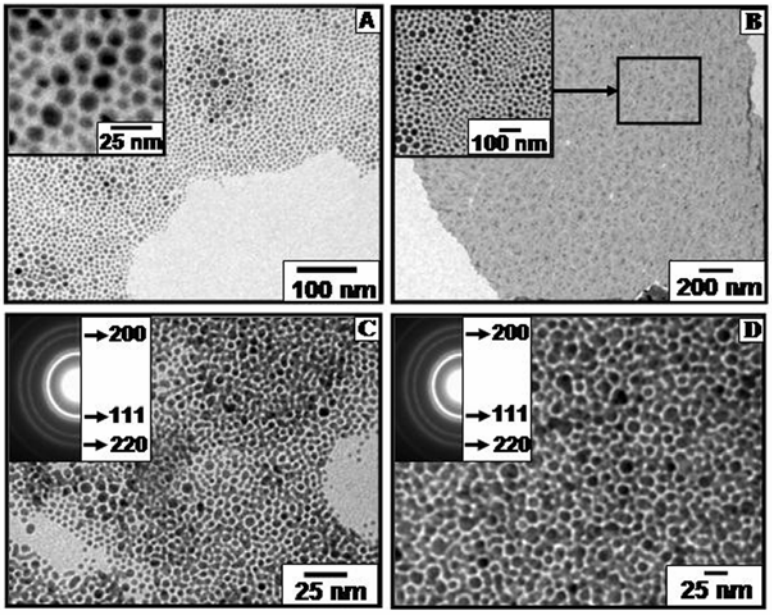

Figure 3.8 *Representative TEM images of Au-ODA nanoparticles in chloroform on StA and ODA monolayer (A-B) at surface pressures 5 mN/m respectively. Inset of Figs. 3.8 A and B show the TEM images at higher magnification. (C-D) at surface pressures 20 mN/m respectively. Inset of C and D show SAED pattern from the gold nanoparticles* .

In order to know whether the surface pressure plays a role in the assembly of nanoparticles, we carried out the same experiment with Au-ODA in chloroform at different surface pressure on StA and ODA monolayers. Fig. 3.8A and B show the TEM images of Au-ODA in chloroform on StA and ODA monolayers, respectively, at surface pressure of 5 mN/m. From the TEM pictures it is clear that at low pressures we see more

number of isolated domains. Therefore the external force i.e. higher pressure induces the formation of compact monolayer with large-scale assembly. Fig. 3.8C and D show the TEM images of Au-ODA in chloroform spread on StA and ODA monolayers, respectively, at higher surface pressure, 20 mN/m. From the TEM images it is evident that when the surface pressure is further increased to 20 mN/m, the order of monolayer is disrupted and the particles tend to fuse together. Inset of the Fig. 3.8C and D shows the selected area electron diffraction pattern which could be indexed to fcc gold lattice structure. Therefore from the TEM images it is confirmed that the transition from incomplete coverage of the surface at low surface pressure to almost complete coverage, eventually leading to fused interlinked superstructures of the monolayer occurs at sufficiently high pressure. With increasing surface pressure, the surface tension decreases and hence the interaction between ODA-capped Au nanoparticles and monolayer increases, and as a result the rate of evaporation of chloroform solvent slows down which helps to get long range ordering in the liquid phase of the system.

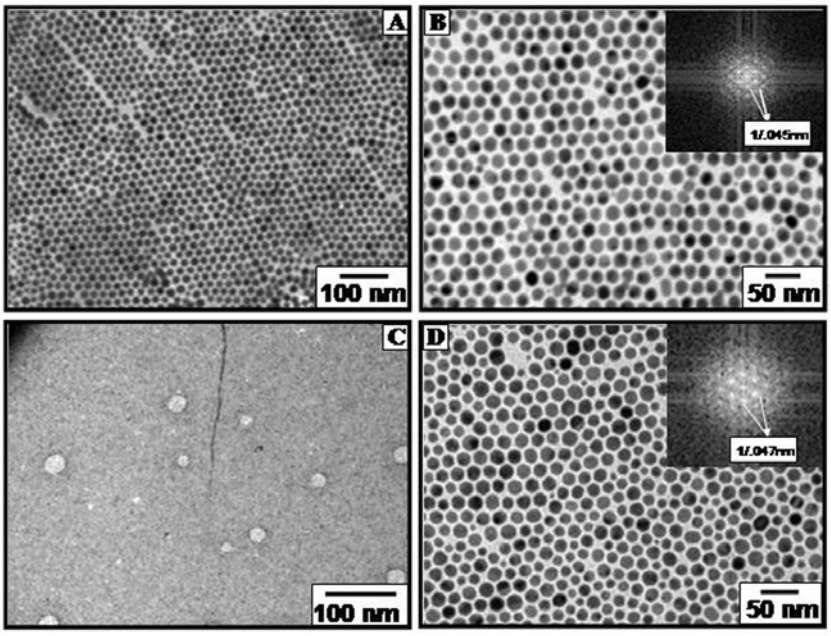

Figure 3.9 *Different magnified TEM images of Au-ODA nanoparticles in benzene (A) and (B) on StA monolayer at surface pressure of 15 mN/m. (C) and (D) on ODA monolayer at surface pressure of 15 mN/m. Inset of the Figs (B) and (D) show the FFT of the arrangement showing hexagonal close packing with the first, second and third-order reflexes.*

In order to understand the role of rate of evaporation of the solvent, similar experiments were carried out by spreading the Au-ODA nanoparticles in benzene on the StA and ODA monolayers. Fig. 3.9A and B show the lower and higher magnification TEM images respectively of the ODA capped gold nanoparticles spread onto the StA monolayer at the surface pressure of 15 mN/m whereas Fig. 3.9 (C and D) represent the different magnification TEM images of Au-ODA in benzene on ODA monolayers. From the TEM images it is clear that small gaps (cracks) are present in the ordered assembly of nanoparticles in the presence of StA monolayer. The interaction of ODA capped gold nanoparticles with the StA and ODA present in the monolayers are different in this case also as mentioned above and it is reflective in the range of ordering displayed by the fast Fourier transform (FFT), shown in the inset of Fig 3.9 (B and D) respectively.

These FFT profiles clearly show an ordering up to the third order and the 6-fold symmetry of the structure respectively in the presence of StA and ODA monolayers. This indicates that the Au nanoparticles crystallize into a hexagonal close-packed lattice [40]. Interparticle spacing is found in both the cases to be 21-22 Å, which agrees with the single molecular length of ODA.

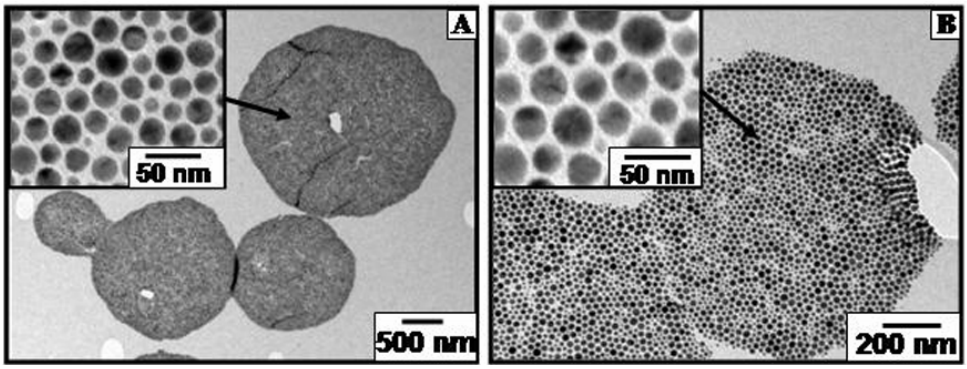

Figure 3.10 *(A) and (B) Representative TEM images of Au-ODA nanoparticles in benzene on StA and ODA monolayer at surface pressures 5 mN/m respectively. Inset A and B show the high magnification images of the area marked by arrow shown in the main figures.*

As is in the case of chloroform, the role of surface pressure in the assembly of nanoparticles with benzene being the solvent of dispersion was also studied. Fig. 3.10A and B show the TEM images of Au-ODA in benzene spread onto StA and ODA monolayers at 5 mN/m surface pressures. Comparing the TEM images at pressure 5

mN/m and 15 mN/m surface pressures (Fig. 3.9), it is clear that in case of benzene as solvent, the surface pressure is again an important factor in controlling the extent of monolayer formation but not for the long range ordering of particles. It can be clearly seen that at both the surface pressure (5 and 15 mN/m) close-packed superlattices are formed without the appearance of particle aggregation.

However at higher pressures, a transition from monolayer coverage of the surface to multiple layers of highly ordered nanoparticles is observed. Figs. 3.11A and B show the TEM images of Au-ODA in benzene spreading on StA and ODA monolayers at surface pressure 20 mN/m. The structure of this bilayer formed in 3.11 A is different from the structures reported earlier [29, 51], in which the second-layer nanocrystals sit on the two-fold saddle sites between the first-layer particles, forming either line or ring structures. These structures were attributed to packing arrangements of nanocrystal facets. However, in our highly ordered bilayers, the second-layer particles position themselves almost exclusively on the three-fold sites of the monolayer underneath much like hard sphere packing. Three-fold sites are more favorable and stable and hence we are able to achieve a perfect formation of well-ordered bilayers on increasing the surface pressure. 3.11B shows second-layer nanocrystals sitting on the three-fold saddle sites but there are occasional presences of the second-layer nanocrystals sitting on the two fold saddle site (explained later in the text).

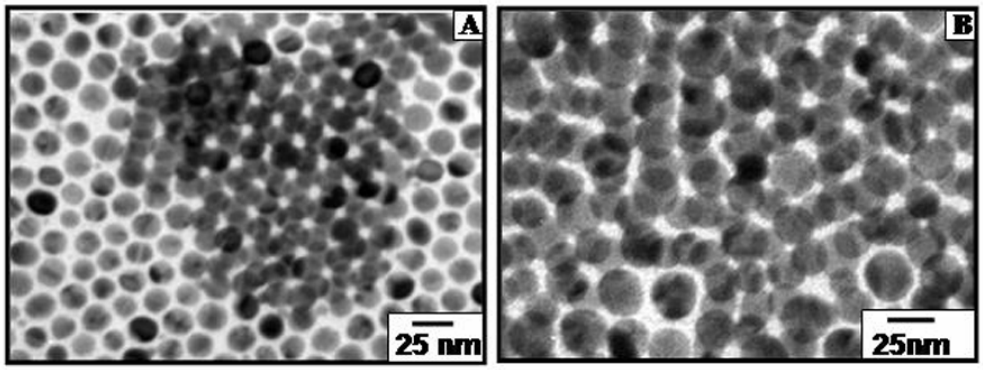

Figure 3.11 *(A) and (B) Representative TEM images of Au-ODA nanoparticles in benzene on StA and ODA monolayer at surface pressures 20 mN/m respectively.*

3.3 Analysis of nanocrystal super lattice

3.3.1 Spreading behaviour

The unusual spreading behavior of the ODA capped gold nanoparticles when spread onto the StA monolayer can possibly be attributed to the following reason. The pressure area isotherm of StA on water sub phase (Fig 3.3, curve1) shows that at a barrier pressure of 15 mN/m, the monolayer is in the liquid state and thus there will be small gaps in between the molecules of the monolayer on the water surface. We believe that the Au-ODA capped gold nanoparticles being positively charged, get attracted to the carboxylic head group of the StA through a columbic attractive interaction through the gaps in the monolayer. In addition to this, chloroform continues to evaporate from the surface at a rapid rate (evaporation rate 11.2 w.r.t. butyl acetate=1) thus imposing a pressure onto the particles to spread faster in between the gaps of the monolayer. The monolayer of stearic acid on water subphase at this pressure is in the form of domains (BAM studies). It has been observed that the jet-like motion of the drop onto the StA monolayer has a time lag of around 2-3 seconds which suggests that the rapid movement of the suspended ODA capped gold nanoparticles to bind to the StA monolayer is triggered by a critical size of the chloroform drop onto the surface. It is also seen from the TEM analysis that the trail left by the moving drop has high concentration of the nanoparticles towards the periphery while towards the center of the trail the particle density is far less. This further suggests that the ODA capped gold nanoparticles prefer to bind to the StA monolayer to stabilize themselves by electrostatic interaction and thus the particle density towards the periphery is more. It is worth noting that in a similar case with ODA capped nanoparticles in benzene with all other condition being same, we do not observe a similar phenomenon. Thus, it suggests that for the jet-like action of the drop, the wetting of the monolayer within the solvent drop and the rate of evaporation of the solvent have a significant role to play. In case of chloroform, the rate of evaporation is significantly high compared to that of benzene (evaporation rate 2.8 w.r.t. butyl acetate=1) and thus the solvent evaporates faster than the rate of particles wetting the surface whereas in case of benzene,

the particles within the solvent drop get enough time to wet the monolayer within the domain of the drop, causing them to settle down to form a superlattice like structure.

In case of Au-ODA nanoparticles in chloroform on the ODA monolayer, the particles just wet the surface as the surface tension of the subphase is reduced but there is no affinity of the particles and the monolayer, as the head group of the monolayer and the capping of the particles is of the same nature. This results into the spreading of the droplet on the ODA molecule may be due to interdigitization of the hydrophobic chains , and the eventual slow evaporation of chloroform solvent facilitates the rearrangement of the nanoparticles in long-range order assembly.

3.3.2 Spontaneous segregation

In the case of solution of gold nanoparticles in chloroform and benzene, it is noticed that besides the range of ordering in the monolayer, the bimodal distributed gold particles also show some tendency to form ordered structures by a process involving spontaneous size segregation [52]. It is clearly seen that gold nanocrystals of different, well defined sizes organize themselves spontaneously into complex, ordered two-dimensional array that are structurally related to both colloidal crystals and alloys between metals of different atomic radii. We observe three types of organization in the case of chloroform as a solvent : first, size-segregated regions, each containing hexagonal-close-packed monodisperse particles (Fig. 3.12A); second, a structure in which particles of two different sizes occupy random positions in a pseudohexagonal lattice (Fig. 3.12B); and third, (Fig. 3.12C) a structure in which smaller particles have partially sintered, and formed a semi-continuous network around the larger particles.

Fig. 3.12A shows an organization of an approximately bimodal ensemble of particles for which $R_B/R_A \approx 0.47$, where R_A and R_B are the radii of the nanoparticles. The particles show a distinct tendency to phase-separate into domains of small and large spheres, each domain exhibiting two-dimensional hexagonal packing. This observation is in agreement with the work of Murray and Sanders [53]. In contrast, if R_B and R_A are very similar, as shown in Fig. 3.12B for $R_B/R_A < 0.87$, the structure formed approximates

to an intimate random alloy. The latter observation is in accordance with the 15% Hume-Rothery rule for simple alloy theory [54].

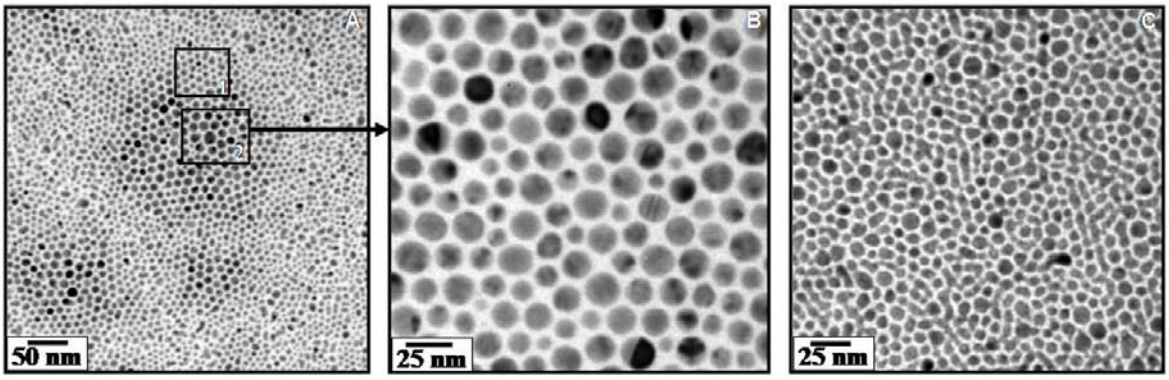

Figure 3.12 *(A-C): (A) TEM micrograph of phase separated A+B mixture of Au nanoparticles in chloroform. (B) 'Random alloy' of Au nanoparticles in chloroform. (C) Bimodal Au nanoparticles at higher pressure, smaller particles have partially sintered and form a semi-continuous network around the larger particles*

A third kind of arrangement, Fig. 3.12C is seen in the case of increased pressure condition. This phenomenon can be attributed to the fact that the smaller particles have fused together as it may be energetically favourable for the smaller Au particles to minimize their surface energy [43e] by sintering under higher barrier pressure. The micrograph shows an ordered bimodal raft wherein the 13±1 nm diameter particles are still intact, whereas the 9±1 nm particles have spread. The smaller particles have effectively connected to form a semi-continuous network in which the regular isolated ODA-capped larger particles are embedded. The reason for the decreased stability of smaller particles as compared to the larger ones may be related to their structure also, an area which can be taken up for study later on. The coexistence of several types of spatially discrete monodisperse and bidisperse rafts, as repeatedly found in the TEM is highly likely for entropy-driven crystallization [55] of a system in which the solution contains a small number of different, but well defined, particle sizes [53]. A further contributing factor is the strong dependence of sintering rate on particle radius. All other conditions (such as temperature, ambient humidity) being equal, the smaller particles are expected to sinter at a higher relative rate [56]. This raises the possibility that the size-dependence of particle stability might be exploited for nanopatterning. The observations

described here indicate the possibility of manipulating the composition and structure of nanoscale materials by simply adjusting the size ratios and relative proportions of their constituents (for example, metallic, magnetic or semiconducting particles).

The contact angle of the films of ODA and StA of glass substrate showed that they both are slightly hydrophobic in nature but as a measure of oleophobicity the ODA films had faster instant spreading compared to StA films, which showed a contact angle of 20° with chloroform carrying ODA capped nanoparticles.

3.3.3 Defect structures in nanocrystal supperlattices (NCSs)

It is well known that defects and dislocations are created in solid materials to accommodate local strain and deformation. Structural characterization of solid-state materials is usually concentrated on the analysis of defects and interfaces. A defect structure is a deviation from the ordered structure, and a full understanding of the periodic structure is the basis of analyzing defects.

3.3.3.1 Stacking faults

Twins and stacking faults are important microstructures in deformation of materials. These types of planar defects are also observed in NCSs, as shown in Fig. 3.13 (B-D). The dodecahedron Au nanoparticles are neatly arranged in the hcp ordered packing and the Fourier transformation of the packing arrangement clearly indicated the same (Fig. 3.9). It has been shown earlier that the slow evaporation results in a long range ordering as in the case of benzene as a solvent. But the hcp ordering of the Au nanoparticles do clearly show the stacking faults as indicated in Fig. 3.13 (B-C). The formations of these planar defects are due to the shift in the particle sites to modulate the interparticle distance. This modulation is limited to only one row of nanoparticles but still preserves the face-to-face packing. Nanoparticle packing is a fascinating subject in which surprises occur. Many a times there are translational as well as orientational shifts if there is face selective binding of the capping agents. In our case, no orientational rotations leading to defects is possible as the nanoparticles are fully capped with the ODA molecules. The particles being dodecahedral and bound with five (111) faces, there is no

preferential binding of the capping agents thus eliminating any rotation of the faces for efficient packing.

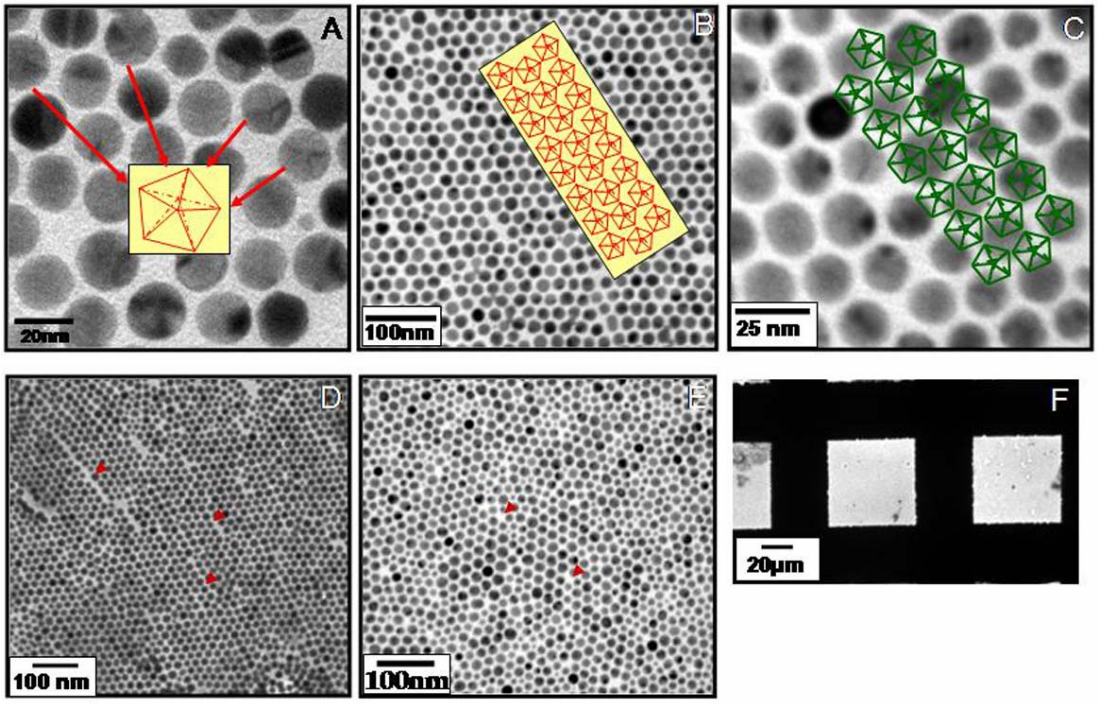

Figure 3.13 *(A) The Dodecahedron gold nanoparticle showing the (111) faces (B-C) TEM image of an hcp Au NCS with stacking fault planar defects, where the models for the stacking fault defects are given, in case of Au on StA and ODA monolayer respectively. (D-E) TEM image of an hcp Au NCS on StA monolayer having crack defects and on ODA monolayer having point defect (marked by arrow). (F) The grid showing the extent of monolayer formation in the presence of lipid monolayer. All the images are for the Au-ODA nanoparticles in benzene.*

3.3.3.2 Cracks and Point defects

As described earlier, the as-synthesized nanoparticles are dispersed in solvent, this solution is used to form a monolayer on the LB trough and during the spreading process size selection occurs according to mass. NCSs are formed by vertical lifting on the monolayer formed under different pressure conditions. The diffusion of the nanocrystals on the subphase is possibly driven by hydraulic forces as drying takes place. Thus, wetting problem, viscosity, and limiting concentration of the nanocrystals determine the types of defects and their density. The TEM image shown in Fig. 3.13 D clearly illustrates the “microcracks” created in the packing of a monolayer of Au nanocrystals, which are likely to be the result of wet-drying processes. Point defects are also frequently

observed in NCSs. Cracks are apparent in the case of StA monolayer, (Figure 3.13 D) and point defects in the case of ODA monolayer, (Figure 3.14 E) when Au-ODA in benzene is spread on to the preformed monolayers.

3.3.3.3 Dynamic diffraction in NCS imaging

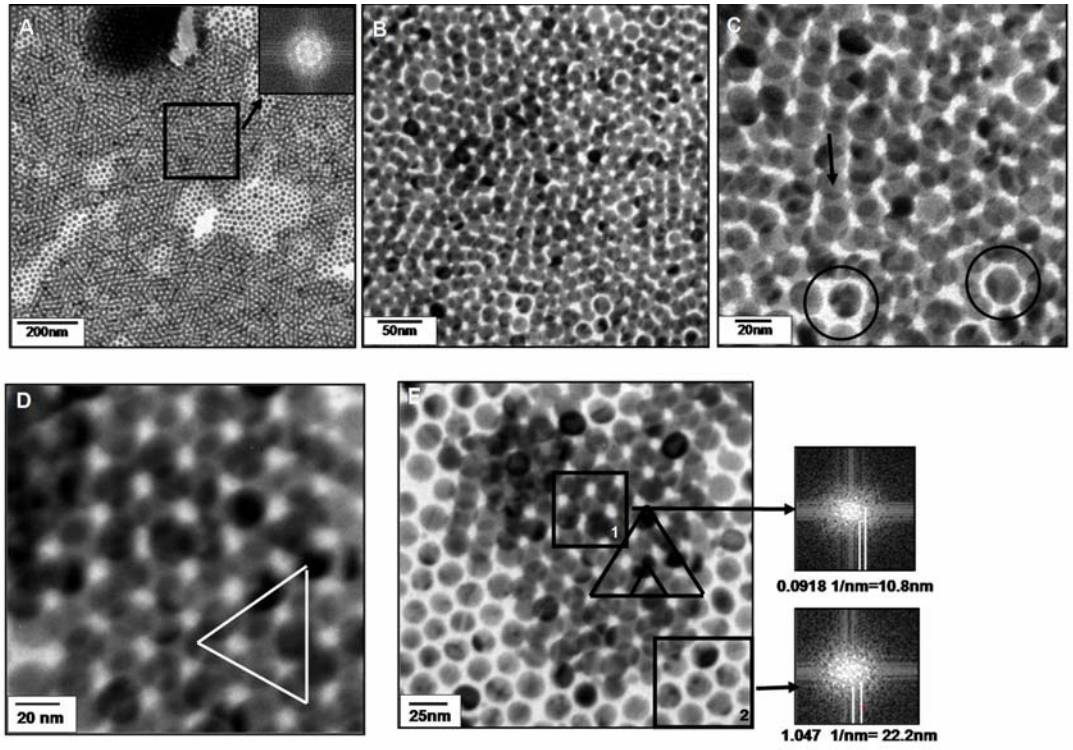

Figure 3.14 *(A-C) Bright field micrograph of a bilayer structure of Au NCPs on ODA monolayer showing double layer structures at different magnifications (C) shows the ordered straight chains of Au clusters (in projection , marked by arrows) and isolated and connected rings in a bilayer structure. The circle drawn is only included to aid the eye. (D-E) Bright field micrograph of a bilayer structure of Au NCPs on StA monolayer showing double layer structures at different magnifications The FFTs from the area marked 1 and 2 of E are also shown.*

It is well known that electron diffraction is dominated by dynamic scattering, leading to the extensive development of multiple scattering theory for electron diffraction [57] for specimens thicker than 2±3 nm. In NCS analysis, dynamic scattering is also inevitable although the number of stacked layers is low. Fig. 3.14 A-E shows a bright-field TEM image of an Au NCS. The particle size is seen at the places in the specimen where the number of stacked layers is likely to be one or two. However, in the region with multilayer stacking, fringes considerably smaller than the interparticle distance are

observed. A Fourier transform of this image is given in the inset of Fig 3.14A and also for region 1 and 2 of Fig. 3.14E. The FFT of region 2 reveals the presence of the second-order diffraction spots from the NCS. The interference of these beams with the central transmitted beam or the beams located at the opposite side in the pattern could give rise to fringes with spacings less than the actual distance between the particles. It is apparent by the distance measured using Digital Micrograph where the single layer gives the particle to particle distance to be 22.2 nm (Fig 3.14E, region 2), and 10.8 nm from the region 1 (Fig. 3.14E) showing double layer.

3.3.3.4 Slip planes

Figure 3.14 shows self-ordered structures commonly observed when the rafts contain more than one layer. It is obvious that in case of formation of double and triple monolayers for Au-ODA in benzene on preformed ODA and StA monolayers, the second-layer particles position themselves almost exclusively on the three-fold sites of the monolayer underneath much like hard sphere packing. The three-fold sites are more favorable and stable and hence, we are able to achieve a perfect formation of well-ordered bilayers on increasing the surface pressure. Schematic in Fig 3.15A shows the formation of multilayer in the absence of any defects in the structure. In addition to the perfect double layer arrangement, TEM images Fig. 3.14B (at most places) and 3.14 (D, E) , we do notice that in case of Au nanoparticles in benzene on the ODA monolayer there are combination of the stacking fault and slip plane.

We noticed chain arrangements of nanoparticles, which appear as straight lines in projection in Fig 3.14C (indicated by arrow). A schematic representation of these structures is shown in Figure 3.15B. Interestingly, these chainlike arrangements can be generated only if the second layer of particles occupy the 2-fold saddle site between two particles in the first layer rather than 3-fold hollow sites created where three basal plane particles meet. The domains of chains that can be observed are then just a consequence of filling the energetically equivalent saddle sites. These chain structures can be considered as a simple rigid body shift of an upper hexagonal raft of clusters with respect to a basal raft. The preferred stabilization of the 2-fold saddle over the 3-fold hollow site is

surprising. In fact, it would be expected that occupancy of the 2-fold saddle positions should be less energetically favorable than that of a 3-fold hollow position as the stabilization energy of the lattice depended *only* on a balance between polarizability interactions of particles and short-range repulsive interactions. This may be due to the presence of a strong short-range electrostatic dipolar repulsive component to the energy where, the 3-fold sites is unfavorable compared with 2-fold sites as was observered earlier [58].

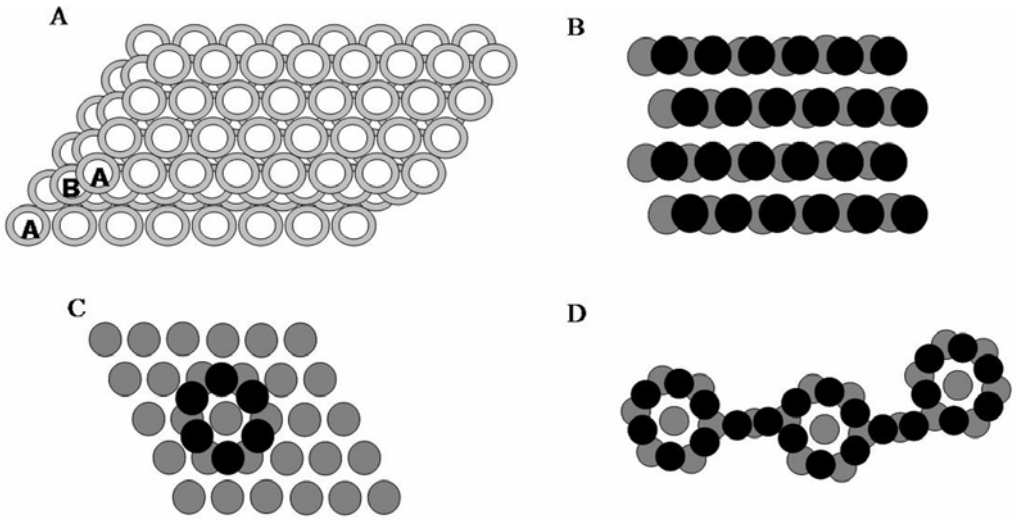

Figure 3.15 *(A) Schematic of the double layer structure arrangement showing hcp arrangement. (B) Schematic diagram illustrating how domains of projected chains can be generated by second layerclusters occupying the 2-fold saddle sites on the basal raft of particles. (C-D) Schematic diagram illustrating how a single ring feature can be formed by filling 2-fold saddle sites(D) Generation of ring structures, such as those in Figure 3.14 C, by rotating an upper hexagonal raft of clusters by 30° with respect to the lower raft resulting in formation of a Moiré pattern.*

In addition to the chain like structures there are few ring structures, such as those shown in Figure 3.14C as commonly observed feature in these bilayer agglomerates. Single ring structures of about 20 nm external diameter are observed, indicated by dark cicles in Figure 3.14C. Figure 3.15C and D shows schematically how these features can arise. The rings are simply closed chain structures where once more, the second layer particles preferentially occupy 2-fold hollow sites, but this time in an ABCABC sequence. These features can be reproduced by a notional 30° rigid-body rotation of a second layer of clusters with respect to a basal plane, as shown in schematic of Figure

3.15C-D. This leads to isolated ring structures of the correct dimensions. Thus, the ring structures observed are probably again a consequence of the balance between electrostatic repulsion of the surface dipoles present on the Au clusters and dispersion interactions. Ring structures were also observed with thiol-capped gold clusters obtained by reaction of the C_8 quaternary ammonium preparation with excess C_{10} thiol. In view of the large surface dipole of gold alkanethiolates [58b], this behavior can be understood on the basis of the electrostatic arguments presented above.

This interruption of placement of the second layer of the Au nanoparticles on the three fold site can also be due to the slip of the particles and it results in the occurrence of Moiré patterns Fig 3.14C. Moiré pattern presents itself in electron diffraction patterns, and it is generated by the stacking of two crystals oriented in different directions. Moiré patterns are also observed in NCSs, in which two assembled layers are stacked rotated at an angle to each other. For a (111) packed layer stacked on the other layer rotated by 30°, a "donut" ring contrast is produced around the rotation center in the image (Figure 3.14 C and schematic 3.14 G). This was observed in Au NCSs [58a].

3.4 Conclusion

We conclude that in the absence of the monolayer on the water sub phase, the liquid drop spreads fast into a very thin film and evaporates before the long range ordering or super lattice formation. Only when the interactions between particles are strong enough and they will get time to assemble, the perfect monolayer is formed. To maintain a arrangement of nanoparticles the evaporation rate of the solvent must be slow. In analogy to molecular crystallization, it is reasonable to propose that better super lattices, larger and with fewer defects, are obtained when they form slowly. Once formed, these super lattices may be tough enough not to be perturbed when we change the pressure conditions. Klabunde and co-workers [59] stated that adding a low volatile additive slows the evaporation rate on the substrate surface. In our case, we have shown that keeping all other parameters constant and varying the pressure can change the evaporation rate and leads to the formation of long range ordering and subsequently to super lattices.

One can see that the thin films without the monolayer offer rather random or short-range distribution of the particles. In sharp contrast, it can be clearly seen that rather close-packed ordered arrangements are formed without the appearance of particle aggregation (defects are relatively rare) in the presence of the monolayer on the surface of water wherein the hydrocarbon bed won't allow the solvent drop to be stretched immediately. It should also be noted that the deposition pressure along with monolayer presence and the solvent type appears to be an important factor in controlling the long range ordering. With a dependence on pressure and evaporation rate, the ordered domain sizes are routinely greater than several microns in size.

References:

(1) Wales, D. J. *Science* **1996**, *271*, 925. All the review articles in the February 16 issue of Science, 1996.

(2) Kastner, M. A. *Phys. Today* **1993**, *46(1)*, 24.

(3) Brus, L. *Appl. Phys. A* **1991**, *53*, 465. Alivisatos, A. P. *Science* **1996**, *271*, 933.

(4) Lewis, L. N. *Chem. Rev*. **1993**, *93*, 2693.

(5) Freer, R. *Nanoceramics*, Institute of Materials, London **1993**.

(6) Awschalom, D. D.; DiVincenzo, D. P. *Phys. Today* **1995**, *48*, 43. Shi, J.; Gider, S.; Babcock, K.; Awschalom, D. D. *Science* **1996**, *271*, 937.

(7) Smyth, J. F. *Science* **1992**, *258*, 414.

(8) Whetten, R. L.; Khoury, J. T.; Alvarez, M. M.; Murthy, S.; Vezmar, I.; Wang, Z. L.; Cleveland, C. C.; Luedtke, W. D.; Landman, U. *Adv. Mater*. **1996**, *8*, 428.

(9) Braun, P. V.; Osenar, P.; Stupp, S. I. *Nature* **1996**, *380*, 325.

(10) Weller, H. *Angew. Chem. Int. Ed. Engl*. **1996**, *35*, 1079.

(11) Whetten, R. L.; Khoury, J. T.; Alvarez, M. M.; Murthy, S.; Vezmar, I.; Wang, Z. L.; Cleveland, C. C.; Luedtke, W. D.; Landman, U. *Chemical Physics of Fullerenes 5 and 10 Years Later (Ed: W. Andreoni), Kluwer, Dordrecht, The Netherlands* **1996**, p. 475.

(12) Harfenist, S. A.; Wang, Z. L.; Alvarez, M. M.; Vezmar, I.; Whetten, R. L. *J. Phys. Chem.* **1996**, *100*, 13 904.

(13) Nuzzo, R. G.; Allara, D. L.; *J. Am. Chem. Soc.* **1983**, *105*, 4481.

(14) Dorogi, J.; Gomez, J.; Osifchin, R.; Andres, R. P.; Refenberger, R. *Phys.Rev. B* **1995**, *52*, 9071.

(15) Leff, D. V.; Ohara, P. C.; Heath, J. R.; Gelbart, W. M. *J. Phys. Chem.* **1995**, *99*, 7036.

(16) Harfenist, S.A.; Wang, Z. L.; Alvarez, M. M.; Vezmar, I.; Whetten, R. L. *Adv. Mater.* **1997**, *9*, 817.

(17) Heath, J. R.; Knobler, C. M.; Leff, D. V. *J. Phys. Chem. B.* **1997**, *101*, 189.

(18) Motte, L.; Billoudet, F.; Lacaze, E.; Pileni, M.-P. *Adv. Mater.* **1996**, *8*, 1018.

(19) Motte, L.; Billoudet, F.; Lacaze, E.; Douin, J.; Pileni, M.-P. J. *Phys. Chem. B.* **1997**, *101*, 138.

(20) Pye, L. D.; La Course, W. C.; Stevens, H. J. *The Physics of noncrystalline solids*; Taylor & Francis: Washington, DC, **1992**.

(21) Xia, Y.; Kim, E.; Mrksich, M.; Whitesides, G. M. *Chem. Mater.***1996**, *8*, 601.

(22) Kumar, A.; Whitesides, G. M. *Science* **1994**, *263*, 60.

(23) Asher, S. A. U. S. Patents 4,627,689 and 4,632,517.

(24) Yoldas, B. E.; Partlow, D. P. *Appl. Opt.* **1984**, *23*, 1418.

(25) Hinz, P.; Dislich, H. *J. Non-Cryst. Solids* **1986**, *82*, 411.

(26) Hahn, R. E.; Seraphin, B. O. In *Physics of Thin Film*, Academic: New York, 1978.

(27) Kastner, M. A. *Phys. Today* **1993**, 24.

(28) Kimizuka, N.; Kunitake, T. *Ad*V. *Mater.* **1996**, *8*, 89.

(29) Wang, Z. L. *Adv. Mater*. **1998**, *10*, 13.

(30) (a) Sastry, M. *Handbook of Surfaces and Interfaces of Materials.Volume 3*: *Nanostructured Materials, Micelles, and Colloids*; Nalwa, H., Ed.; Academic Press: SanDiego, **2001**; Chapter 2, p 87 and references therein. (b) Brown, L. O.; Hutchison, J. E. *J. Phys. Chem. B* **2001**, *105*, 8911. (c) Pileni, M. P. *J. Phys. Chem. B* **2001**, *105*, 3358. (d) He, S.; Yao, J.; Jiang, P.; Shi, D.; Zhang, H.; Xie, S.; Pang, S.; Gao, H. *Langmuir* **2001**, *17*, 1571. (e) Sun, S.; Murray, C. B.; Weller, D.; Folks, L.; Moser, A. *Science* **2000**, *287*, 1989. (f) Pileni, M. -P. *New J. Chem.* **1998**, 693. (g) Murray, C. B.; Kagan, C. R.; Bawendi, M. G. *Science* **1995**, *270*, 1335. (h) Osifchin, R. G.; Andres, R. P.; Henderson, J. I.; Kubiak, C. P.; Dominey, R. N. *Nanotechnology* **1996**, *7*, 412.

(31) (a) Hutter, E.; Fendler, J. H.; Roy, D. *J. Phys. Chem. B* **2001**, *105*, 11159. (b) Nakanishi, T.; Ohtani, B.; Uosaki, K. *J. Phys. Chem. B* **1998**, *102*, 1571. (c) Chan, E. W. L.; Yu, L. *Langmuir* **2002**, *18*, 311. (d) Jiang, P.; Liu, Z. F.; Cai, S. M. *Langmuir* **2002**, *18*, 4495. (e) Okamoto, T.; Yamaguchi, I. *J. Phys. Chem. B* **2003**, *107*, 10321. (f) He, H. X.; Zhang, H.; Li, Q. G.; Zhu, T.; Li, S. F. Y.; Liu, Z. F. *Langmuir* **2000**, *16*, 3846.

(32) (a) Hao, E.; Lian, T. *Chem. Mater.* **2000**, *12*, 3392. (b) Malynych, S.; Luzinov, I.; Chumanov, G. *J. Phys. Chem.B* **2002**, *106*, 1280. (c) Sun, S.; Anders, S.; Hamann, H. F.; Thiele, J. -U.; Baglin, J. E. E.; Thomson, T.; Fullerton, E. E.; Murray, C. B.; Terris, B. D. *J. Am. Chem. Soc.* **2002**, *124*, 2884. (d) Tanaka, H.; Mitsuishi, M.; Miyashita, T. *Langmuir* **2003**, *19*, 3103. (e) Gole, A.; Sainkar, S. R.; Sastry, M. *Chem. Mater.* **2000**, *12*, 1234. (f) Mayya, K. S.; Sastry, M. *Langmuir* **1999**, *15*, 1902.

(33) Trau, M.; Saville, D. A.; Aksay, I. A. *Science* **1996**, *272*, 706.

(34) (a) Li, H. X.; Lin, M. Z.; Hou, J. G. *J. Cryst. Growth* **2000**, *212*, 222. (b) Teranishi, T.; Hosoe, M.; Tanaka, T.; Miyake, M.*J. Phys. Chem.B* **1999**, *103*, 3818. (c) Chandrasekharan, N.; Kamat, P. V. *Nano Lett.* **2001**, *1*, 67

(35) (a) Sastry, M.; Rao, M.; Ganesh, K. N. *Acc. Chem. Res.* **2002**, *35*, 847. (b) Sastry, M. In *Colloids and Colloid Assemblies*; Caruso, F., Ed.; Wiley-VCH: Weinheim, **2004**; Chapter 12, p 369.

(36) Andres, R. P.; Bein, T.; Dorogi, M.; Feng, S.; Henderson, J. I.; Kubiak,C. P.; Mahoney, W.; Osifchin, R. G.; Reifenberger, R. *Science* **1996**, *272*, 1323.

(37) Kim, S.H.; Medeiros-Ribeiro, G.; Ohlberg, D. A. A.; Williams, R. S.; Heath, J. R. *J. Phys. Chem. B* **1999**, *103*, 10341.

(38) Beverly, K. C.; Sampaio, J. F.; Heath, J. R. *J. Phys. Chem. B* **2002**, *106*, 2131.

(39) Kim, B.; Tripp, S. L.; Wei, A. *J. Am. Chem. Soc.* **2001**, *123*, 7955.

(40) Giersig, M.; Mulvaney, P. *Langmuir* **1993**, *9*, 3408.

(41) Fendler, J. H.; Meldrum, F. C. *Ad*V. *Mater.* **1995**, *7*, 607.

(42) (a) Sastry, M.; Patil, V.; Mayya,K. S.; Paranjape, D. V.; Singh, P.; Sainkar, S. R. *Thin Solid Films*, **1998**, *324*, 239. (b) Sastry, M.; Gole, A.; Patil, V. *Thin Solid Films*, **2001**, *384*, 125. (c) Damle, C.; Gole, A.; Sastry, M. *J. Mater.Chem.* **2000**,*10*,1389. (d) Swami, A.; Kumar, A.; Selvakannan, PR.; Mandal, S.; Sastry, M. *J. Colloid Int. Sci*. **2003**, *260,* 367.

(43) (a) Motte, L.; Billoudet, F.; Pileni, M. P. *J. Phys. Chem.* **1995**, *99*, 16425. (b) Kiely, C. J.; Fink, J.; Brust, M.; Bethell, D.; Schiffrin, D. J. *Nature* **1998**, *396*, 444.

(44) Remacle, F.; Collier, C. P.; Markovich, G.; Heath, J. R.; Banin, U.; Levine, R. D. *J. Phys. Chem.* **1998**, *102*, 7727.

(45) Korgel, B. A.; Fitzmaurice, D. *Phys. Re*V. *Lett.* **1998**, *80*, 3531.

(46) Ohara, P. C.; Gelbart, W. M. *Langmuir* **1998**, *14*, 3418.

(47) Patil, V.; Malvankar, R.B.; Sastry, M *Langmuir* **1999**,15, 8197.

(48) Sastry, M; Kumar, A; Mukherjee, P *Colloids Surf*., A **2001**, 181, 255.

(49) Overbeck, G. A.; Mobius, D. *J. Phys. Chem*. **1993**, 97, 7999. (b) Lee, Y.; Yang, Y.; Shen, Y. *J. Phys. Chem. B*, **2005** ,10, 4662.

(50) (a) Deegan, R. D.; Bakajin, O.; Dupont, T. F.; Huber, G.; Nagel, S. R.; Witten, T. A. *Nature* **1997**, *389*, 827 ,(b) Picknett, R. G.; Bexon, R. *J. Colloid Interface Sci.* **1997**, *61*, 336(c) Hu, H.; Larson, R. G. *J. Phys. Chem. B* **2002**, *106*, 1334.

(51) Korgel, B. A.; Fullam, S.; Connolly, S.; Fitzmaurice, D. *J. Phys.Chem.* **1998**, *102*, 8379. (b) Fink, J.; Kiely, C. J.; Bethell, D.; Schiffrin, D. J. *Chem. Mater.***1998**, *10*, 922. (c) Zanchet, D.; Moreno, M. S.; Ugarte, D. *Phys. Re*V. *Lett.* **1999**, *82*, 5277.

(52) (a) Ohara, P. C.; Leff, D. V., Heath; J. R Gelbart *Phys. Rev. Lett*. **1995** 75, 3466 (b) Murthy; Wang, Z. L; Whetten, R. L. *Phil. Mag. Lett*. **1997** 75, 321

(53) Murray, M. J. & Sanders, J. V. Close-packed structures of spheres of two different sizes II; the packing densities of likely arrangements. Phil. Mag. A 42, 721, **1980**.

(54) Hume-Rothery,W.; Smallman, R. E.; Haworth, C.W. The Structure of Metals and Alloys (Metals and Metallurgy Trust, London, **1969**.

(55) Eldridge, M. D.; Madden, P. A.; Frenkel, D. Entropy driven formation of a superlattice in a hardsphere binary mixture. *Nature* **1993**, *365*, 35 .

(56) Murray, C. B.; Kagan, C. R.; Bawendi, M. G. Self-organisation of CdSe nanocrystallites into 3-dimensional quantum dot superlattices. *Science,* **1995**, *270*, 1335.

(57) Wang, Z. L. Elastic and Inelastic Scattering in Electron Diffraction and Imaging, Plenum, New York **1995**.

(58) (a) Fink, J.; Kiely, C.J.; Bethell, D.; Schiffrin, D.J. *Chem. Mater.* **1998,** *10,* 922-926 (b)Seller, H.; Ulman, A.; Shnidman, Y.; Eilers, J. E. *J. Am. Chem.Soc.* **1993**, *115*, 9389.

(59) Lin, X. M.; Jaeger, H. M.; Sorensen, C. M.; Klabunde, K. J. *J. Phys. Chem. B* **2001**, *105,* 3353.

CHAPTER IV

Shape and Size Selective Separation of Gold Nanoparticles by Competitive Complexation at the Air-Water Interface

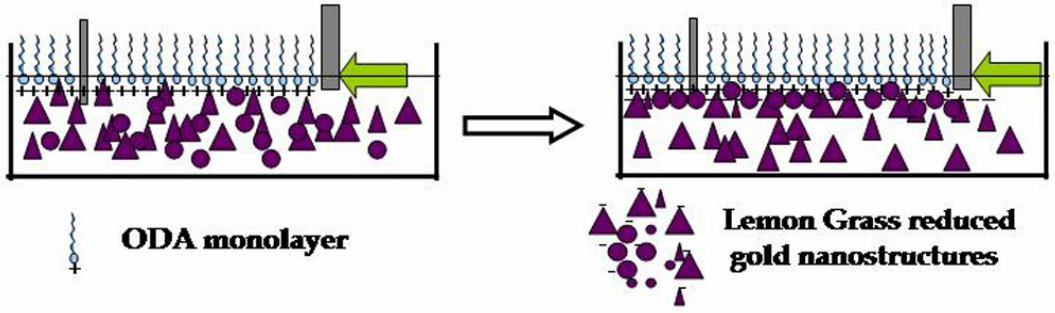

What I want to talk about is the problem of manipulating and controlling things on a small scale…… (Richard Feynman)

Electrostatic interactions are known to play a very important role in biological systems and chemical reactions. Among all the interactions that drive self assembly, the use of electrostatic interactions for multilayer formation is very attractive. In this chapter we present time-dependent study of preferential complexation of spherical gold nanoparticles over triangular gold nanoparticles to the octadecyl amine (ODA) monolayers at the air-water interface. These nanoparticles have a net negative charge on their surface due to the presence of biomolecules, facilitating electrostatic interaction with the positively charged ODA monolayer leading to the complexation process. We have demonstrated that extent of preferential complexation of the gold nanoparticles to the ODA monolayer is a function of charge on the particles and the relative mobility of the nanoclusters in the medium. The process has further been tested as a separation technique.

Part of the work presented in this chapter has been communicated:

1) Pasricha, R.; and Sastry, M. *J. Colloids Interface Sci.,* **2007** (communicated).

4.1 Introduction

Important advances in the area of nanoscience are instrumental in turning Feynman's prophesy that 'Miniaturization would play a key role in future technologies' into a reality [1]. The two major approaches currently being used for the generation of organized nanoscale assemblies are the "top-down" (or "engineering-down") and "bottom-up" ("engineering-up") methods. Top-down method is based on growing of patterned structures by suitable lithographic and ion-implantation techniques. Considering the rate of growth in miniaturization, physical limits will soon be reached on its extent possible using top down approach. It is thus clear that an alternative approach based on completely different principles would be required to overcome this barrier toward further miniaturization. Hence the bottom-up approach is the need of the time.

While the exotic properties of individual (non interacting) nanoparticles are well documented [2], in some specific applications, it might be required to organize them in thin film form with effective packaging by means of the bottom-up self-assembly methods. Some commercial application would require assembling the nanoparticles on suitable substrates and linking them in specific manner. The main challenge in this area is to develop protocols for the organization of crystalline arrays of nanoparticles wherein both the size and separation between the nanoparticles can be tailored. Flexibility in controlling the nanoarchitecture of the film affects the applications based on the collective properties of the organized particles [3].

The formation of thin films of nanoparticles, either in monolayer or multilayer form essentially consists of two main steps. The first step is the synthesis of the nanoparticles and, if necessary, modification of the surface of the colloidal particles by using capping agents. The process of surface modification may be used to not only stabilize the colloidal particles in solution, but also to self-assemble them on suitable substrates, which is the second step in the realization of nanoparticle thin films. Different approaches have been investigated for the organization of nanoparticles in thin film form. Some of the more prominent nanoparticle film formation methods include (a) self-assembly by simple solvent evaporation [4] (b) covalent attachment to suitably modified

surfaces [5] (c) using molecular recognition events for self assembly [6] and (d) organization at the air–water (using hydrophobized colloidal particles) [7] and water–organic solution interfaces [8] and thereafter formation of superlattice films by the Langmuir–Blodgett (LB) technique. In the present study we are primarily concentrating on using electrostatic interactions between charged colloidal particles and ionizable lipid molecules in film form for selective binding. The first report on the electrostatically driven layer-by-layer self-assembly of inorganic colloidal particles may be traced to the work of Iler et al. [9]. Iler and co-workers showed that oppositely charged glass and alumina particles could be electrostatically self-assembled in multilayer structures by alternatively immersing the substrate in the two colloidal solutions. However, true layer-by-layer growth was not fully established in this case [9]. Electrostatic interaction, which have long been known to play an important role in biological and chemical processes [10] have only recently been investigated for the growth of multilayer of polyelectrolytes [11] and nanoparticle–polyelectrolyte films [12] as well as micron-sized objects [13]. Many groups have now used electrostatically driven layer-by-layer assembly to realize assemblies containing proteins/ polyeletrolytes [14] and inorganic nanoparticles such as magnetite [15], SiO_2, TiO_2, and CeO_2 [16], alternating layers of positively charged gold and negatively charged silver particles [17] as well as quantum dots of CdSe [18]. Using electrostatic interaction, Sastry and coworkers have used two different techniques for the growth of thin nanoparticle films (a) electrostatic self-assembly at the air–water interface with charged Langmuir monolayers, and (b) electrostatically controlled diffusion into thermally evaporated fatty lipid films.

The air–water interface has long been recognized to be an excellent medium for the organization of inorganic cations using charged amphiphilic monolayers (Langmuir monolayer) [19]. The process of electrostatic assembly of charged colloidal particles at the air–water interface using ionizable Langmuir monolayers is illustrated in Figure 4.1. The figure shows the attractive electrostatic interaction between negatively charged colloidal particles and a positively charged octadecylamine (ODA) Langmuir monolayer and, thereby, the immobilizing nanoparticles at the air–water interface. This approach has

been extended to the organization of large inorganic anions [20] and biological macromolecules as well [21]. It is clear from the above that the electrostatic interaction between the ions/macromolecules in solution and charged lipid Langmuir monolayer drives the organization at the air–water interface. It has been shown by Sastry and coworkers that colloidal nanoparticles, which are charged (using surface- bound ionizable groups or due to synthesis conditions), can be electrostatically bound to charged Langmuir monolayer [22]. Moreover, the nanoparticle organizations can be transferred onto suitable substrates facilitating formation of thin films of organized nanostructures by the elegant LB technique [22], as illustrated in Scheme 4.1.

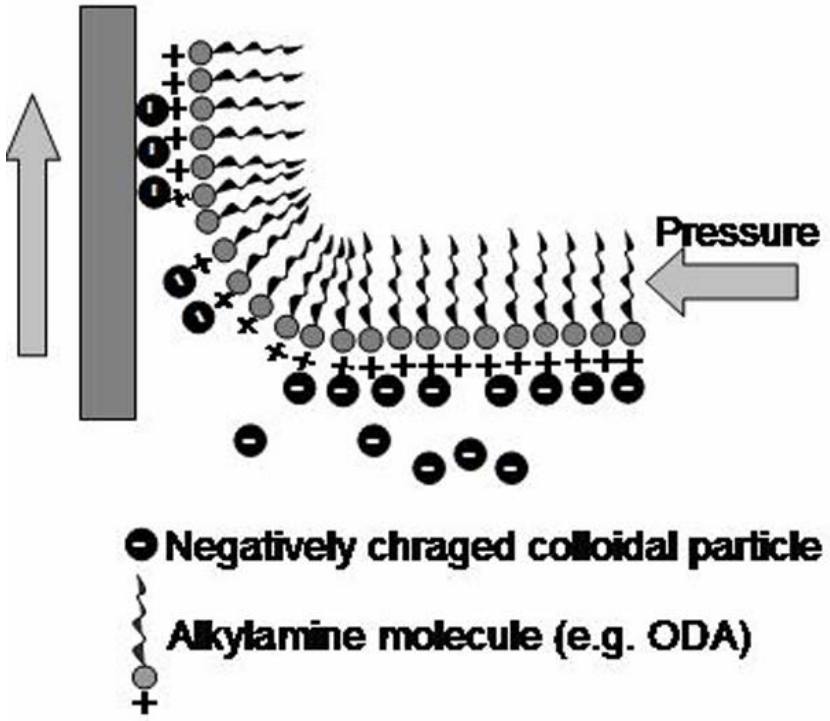

Scheme 4.1 *Schematic showing the electrostatic assembly of negatively charged colloidal particles at the air–water interface with cationic Langmuir monolayer (Not to scale.)*

In this chapter it has been demonstrated that in addition to deposition of reasonably compact, lamellar multilayer gold colloidal particle film, the electrostatic binding can be utilized for the separation of particles of different sizes/shapes by the competitive complexation process. These nanoclusters otherwise can not be separated effectively and the popular separation process e.g. Gel-electrophoresis or column

chromatography takes long time and are slow. The end result is low yield. The films of well separated nanoparticles can thereafter be deposited on variety of solid supports by the LB method. To the best of our knowledge, formation of metal cluster films using a separation technique has not been demonstrated until now and has many advantages over the chemical insertion route [23, 24]. The versatility of this method is that the density of clusters in the LB films can be controlled quite easily through variation of the colloidal solution pH which modulates simultaneously the charge on the functional groups in the film matrix as well as on the colloidal particle surface [22, 25, 26] and also by the size of the nanoclusters, which plays a critical role in the separation process of colloid solutions.

In the following work, we address the specific problem of electrostatically controlled complexation of lemon grass reduced triangular gold nanoparticles in Langmuir monolayer films in greater detail. We also demonstrate that compact, lamellar multilayer gold colloidal particle films can be transferred to solid supports by the LB method. These can be further used for specific applications as Near Infra-red (NIR) wavelength blockers in optical coatings for architectural applications [27]. It has been shown by Sastry and coworkers that films of the nanotriangles of varying thickness on glass substrates are efficient absorbers of Infra-red (IR) radiation in an application where the temperature in a compartment exposed to an infrared source was considerably reduced by the presence of the nanotriangle coating on a glass window [27].

The gold cluster complexation was found to increase as the cluster size decreased. More interestingly, in a competitive diffusion of large triangular (350 nm and 90 nm) and small spherical (75 nm) gold clusters, it was observed by UV-Vis absorption and TEM studies that the larger clusters were also incorporated despite their comparative lower mobility. The study thus indicates that the ionization of the amine groups on the monolayer is truly pH dependent and the binding of the gold nanoparticles to amine is strongly affected by the nanoscale curvature of the particles.

4.2 Synthesis and Characterization

4.2.1 Synthesis of spherical gold nanoparticles

In a typical experiment, 100 mL of 10^{-4} M aqueous solution of chloroauric acid was reduced using 0.01 g of sodium borohydride at room temperature, resulting in a ruby-red solution indicating the formation of gold nanoparticles [28a]. The gold nanoparticle solution obtained by this method was heated to remove the excess sodium borohydride.

4.2.2 Synthesis of triangular gold nanoparticles

The gold nanotriangles were synthesized using the protocol described by Sastry and coworkers [29]. In a typical experiment, 100 gm of thoroughly washed and finely cut leaves of lemon grass were boiled for 5 min in 500 mL of sterile deionized water. 8 mL of the broth thus formed was added to 100 mL of 10^{-3} M aqueous solution of chloroauric acid ($HAuCl_4$). The bioreduction of the $AuCl_4^-$ ions was monitored by time dependent UV-vis-NIR spectroscopy measurement of the mixture till the saturation of the reaction. The reaction was observed to saturate in 6 hours giving a brown red colored solution, which contains a mixture of triangular and spherical nanoparticles. This solution was centrifuged three times at 3000 rpm for 20 minutes, each followed by washing with deionized water. The pellet was finally redispersed in 5 mL of distilled water and was used for further experiments. The centrifugation and washing steps remove majority population of the small sized spherical particles and thus the pellet contains nearly 90% population of gold nanotriangles. The purified nanoparticle solution was used for further experimentation.

4.2.3 Synthesis of solution containing spherical and triangular gold nanoparticles

To study the role of particle size and shape in a competitive complexation process, we prepared a solution containing the lemon grass synthesized triangular and borohydride reduced (chemically synthesized) spherical gold particles by mixing varying volumes of the individual spherical and triangular gold nanoparticles. Two sets of solution were prepared by mixing 50 µl and 100 µl of spherical gold nanoparticles to 550µl solution of lemon grass reduced gold nanotriangles respectively. We would like to

mention here that the volume ratio of the individual solution used in this study is not to be confused with the actual nanoparticle concentration ratios. In fact, for the particle sizes reported earlier and assuming complete reduction of the salt solution, mixtures prepared would contain many more times small spherical nanoparticles particles per unit volume as compared to the larger gold triangular nanoparticles.

4.2.4 UV-vis-NIR spectroscopy

UV-vis-NIR spectroscopy measurements of the gold nanoparticle solution yielded an absorbance maximum centered at ca. 520 nm. Spherical gold nanoparticles of diameters less than 20 nm absorb in the visible region of the electromagnetic spectrum (at 520 nm) due to excitation of surface plasmon vibrations (also known as the surface plasmon resonance or SPR) in the particles [28]. Fig 4.1A; curve 1 shows the UV-vis spectrum of the spherical gold nanoparticles shown in TEM images in Fig 4.1B. The average size of the particle was measured to be 8 ±1 nm.

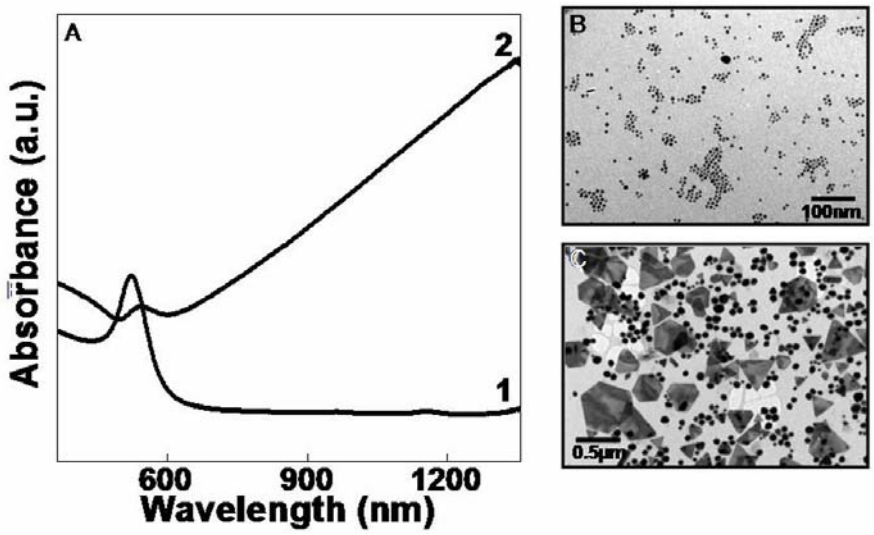

Figure 4.1 *(A) UV-Vis spectra of sodium borohydride reduced gold nanoparticles (curve 1) and Lemon grass reduced gold triangles (curve 2) (B) Representative TEM image of borohydride reduced gold nanoparticles (C) Representative TEM image of as prepared lemon grass reduced gold nanoparticles.*

UV-vis-NIR spectroscopy measurements of the solution containing gold nanotriangles yielded transverse and longitudinal peak with absorbance maximum centered at ca. 520 nm and 1300 nm respectively. It is well known that open aggregated

structures of gold nanoparticles and particles possessing an intrinsic anisotropy (for example, nanorods and nanotriangles) exhibit two prominent absorption bands, a low wavelength transverse absorption band (out-of-plane vibration band) and a longitudinal absorption band at longer wavelengths (in-plane plasmon vibrations) [30-32]. The longitudinal plasmon absorption band is a strong function of the aspect ratio of the nanoparticle [31]. Under certain conditions of anisotropy, the longitudinal component of the SPR for nanorods can extend into NIR region of the electromagnetic spectrum [31c]. Fig 4.1 A, curve 2 shows the UV-vis-NIR absorbance spectrum of triangular gold nanoparticles shown in TEM images in Fig 4.1C. The triangles had a bimodal distribution with 350 ± 10 nm and 90 ± 5 nm edge length, though there were a few bigger triangles. The spherical particles have an average size of 75 ± 3 nm.

4.2.5 HRTEM analysis

Figure 4.2A shows the HRTEM image of the spherical gold nanoparticle synthesized by borohydride reduction and Fig 4.2B shows the HRTEM image of triangular nanoparticles synthesized using lemon grass. It can be clearly seen that the spherical nanoparticle is multiple twinned. Figure 4.2B shows the HRTEM image of the edge of the triangular gold nanoparticles. The lattice spacing between the planes was found to be 2.36 Å which shows that the flat surface of the gold nanotriangles is highly {111} oriented.

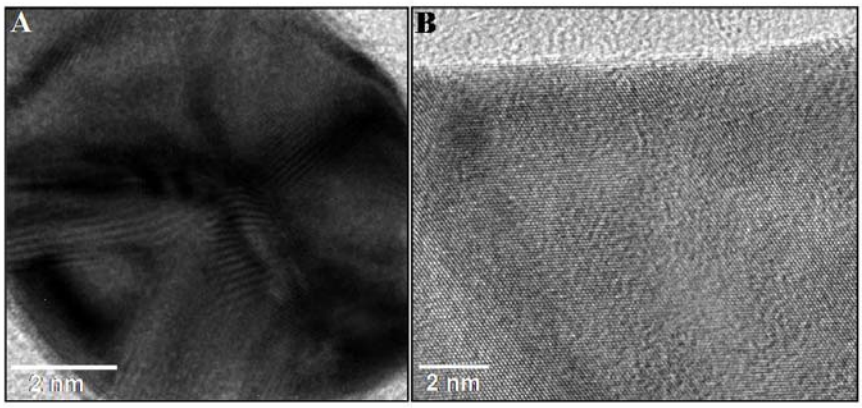

Figure 4.2 *HRTEM image of (A) spherical gold nanoparticles synthesized using borohydride reduction (B) gold nanotriangles showing the {111} plane of flat surface with lattice spacing of 2.36 Å, synthesized by lemon grass reduction .*

4.2.6 Zeta Potential and electrophoretic mobility

Classical capillary electrophoresis (consisting of light microscope with embedded scale, stopwatch) was used for the determination of electrophoretic mobility of the triangular gold nanoclusters. Capillary zone electrophoresis was carried out with a ZETA meter 3.0 from ZETA U.S. Electrophoretic determinations of zeta potential were carried out in phosphate buffer at pH 7.4. The calculation of zeta potential from the mobility is done for systems that fit the Smoluchowski model, i.e. particles larger than about 0.2 microns dispersed in electrolytes containing more that 10^{-3} M salt. The electrophoretic properties of colloidal gold nanoparticles serve as a measure for their size-based characterization [33].

The Agarose gel electrophoresis was also done in order to confirm the relative mobility of the triangular and spherical nanoparticles and also to determine the surface charge on them. 1 % Agarose gel was made in tris-acetate ethylene diamine tetra acetic acid (TAE) buffer (pH 7.4) and the gel was run in the same buffer at 50 Volts for 1 hour.

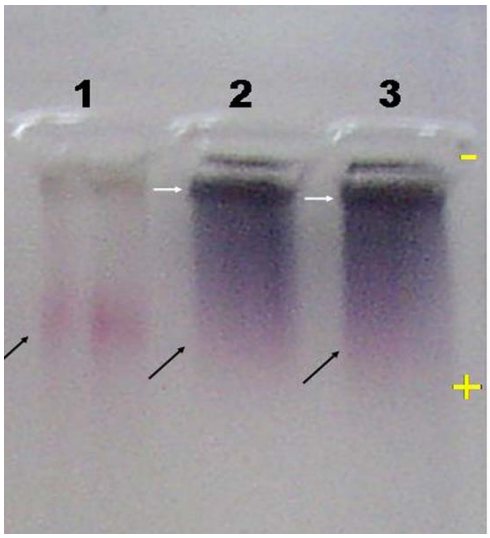

Figure 4.3 *Results of Gel Electrophoresis depicting the position of spherical (black arrow) and triangular (white arrow) nanoparticles under the influence of electric field.*

Gel electrophoresis and zeta potential measurements confirmed the negative charge on the gold particles as we see them moving towards the positive electrode under the influence of electric field. Figure 4.3 shows the result of the gel electrophoresis of

spherical and triangular gold nanoparticles. Well 1 was loaded with spherical nanoparticles while Well 2 and 3 were loaded with as prepared solution of lemon grass reduced gold nanoparticles containing both spherical and triangular nanoparticles. The black arrows indicate the position of ruby red colored spherical nanoparticles and the white arrows correspond to the position of triangular nanoparticle. It is clearly evident that owing to the larger size, the triangular nanoparticles have barely managed to enter the gel while the spherical particles are moving freely under the influence of the electric field.

4.3 Complexation of the gold clusters with the lipid monolayer

4.3.1 Langmuir-Blodgett studies

A 1 mg/mL concentrated ODA solution (75 µL) in chloroform was spread on a subphase of purified triangular gold nanoparticles prepared by 10 times dilution of the as-prepared nanoparticle solution (pH 6 after dilutions) in a Nima 611 Langmuir trough equipped with a Wilhelmy plate pressure sensor. To study the process of shape dependent preferential complexation, same process was repeated for (a) as prepared lemon grass reduced gold nanoparticle solution and (b) purified triangles mixed with chemically synthesized spherical gold nanoparticles. The solutions were simultaneously spread on the LB trough interfaced with a Brewster angle microscope for imaging of the monolayer as a function of time.

Pressure–area (π–A) isotherms were recorded at room temperature as a function of time after spreading the monolayer at a compression and expansion rate of 50 cm^2/min. Pressure-Area isotherm measurement was started 10 min after spreading of the ODA solution to allow the evaporation of the solvent. Kinetics of complexation of the gold nanoparticles with the ODA monolayer was also studied in the constant area mode (π -t), wherein the barriers were maintained at constant area of the trough and the pressure changes were monitored as a function of time after spreading the ODA monolayer. Figure 4.4 shows the π-A isotherm of the ODA monolayer spread on the water surface, which was taken as a reference.

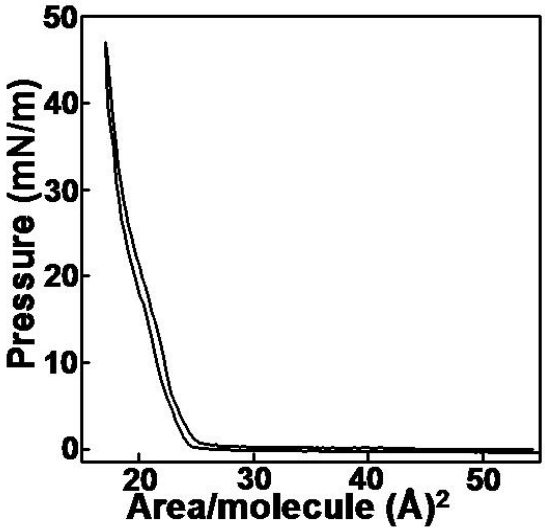

Figure 4.4 π *-A isotherm of the ODA Langmuir monolayer on the surface of pure water (pH 7.1) at 28 °C temperature*

The pH of the subphase containing purified triangles was found to be 6, at this pH the amine groups of ODA are expected to be partially protonated (pK_b of ODA is 10.6), thereby imparting a positive charge to the amine group in the monolayer. The electrophoretic mobility experiments clearly indicate that biomolecules capping the gold nanotriangles impart negative charge to the particles resulting in electrostatic complexation with the positively charged ODA molecule. Fig 4.5A shows the surface pressure Vs area of trough plot (Pressure - Area of molecule isotherm for the same is shown in the inset), measured on Langmuir trough for ODA monolayer on solution of gold nanoparticles recorded after 30 min, 60 min, 90 min, 5 h, 18 h and 26 h of spreading of the ODA monolayer on the surface of the triangular gold nanoparticles solution. The arrows in the isotherm indicate the compression and expansion cycles of the monolayer.

We notice an expansion of the ODA monolayer on the subphase containing gold nanoparticles with time when compared to the amine monolayer on millipore water (Fig 4.4) i.e. an increase in the area/molecule (as well as the increase in the take off area of the amine monolayer with time), which indicates complexation of the gold nanoparticles with the protonated amine head groups of the monolayer. Fig 4.5B shows the variation in takeoff value with time to emphasize the complexation process. The area per molecule after equilibration of nanoparticle density at the air-water interface was determined to be

26 Å (Fig 4.5A-26 h), which is considerably larger than the area per molecule for the uncomplexed ODA molecules 22 $Å^2$ (Fig 4.4) and the area per molecule (22.5 $Å^2$) at t=30 min (Fig 4.5A-30 min). The π-*A* isotherms after 26 hours of equilibration of the monolayer remain unchanged. A region of fairly large incompressibility is observed for the monolayers on the gold hydrosol, which is important for transfer of compact LB monolayers. We have also studied the variation in monolayer area with time at a surface pressure of 25 mN/m. A steady decrease in area is observed which was found to stabilize after a gap of five hours of compression of the monolayer. This time interval and surface pressure determine the optimum conditions for transfer of the gold nanoparticle-ODA films to solid substrates at fixed surface pressures.

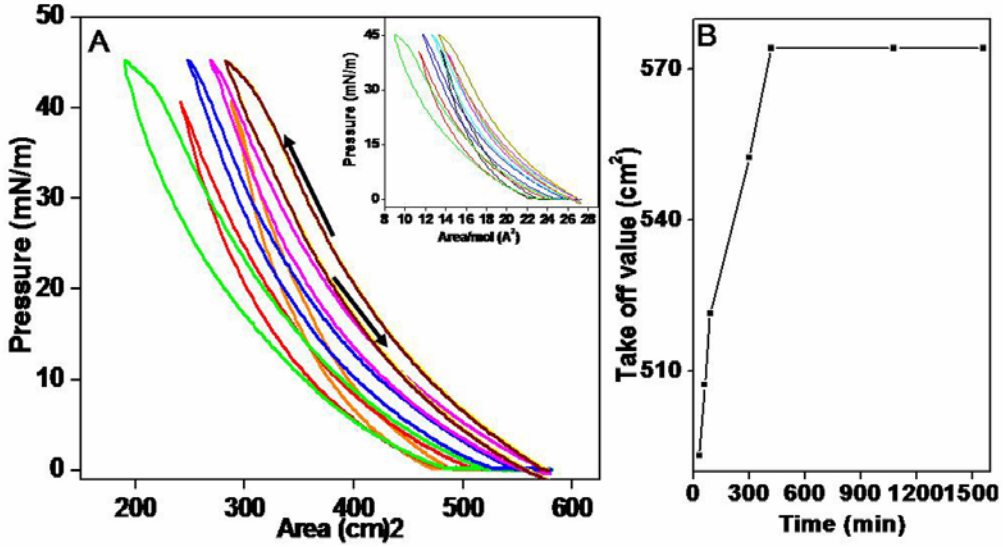

Figure 4.5 *(A) π-A isotherms recorded after the stabilization of the ODA Langmuir monolayer on the surface of lemon grass reduced gold nanoparticles as a function of time of spreading the monolayer: 30 min (orange), 60 min (red), 90 min (green), 5 h (blue), 18 h (pink) and 26 h (brown), Inset shows the π-A isotherm of the same in terms of Area/molecule ($Å^2$) (B) Plot of take off value with time.*

While the controlled assembly of gold nanoparticles at the air-water interface is interesting, formation of thin films of the nanoparticles would be important from the application point of view. The formation of superlattice films of the gold nanoparticle-ODA monolayer assembled at the air–water interface was effected using the LB technique at a surface pressure of 30 mN/m which falls in the solid phase of the π-A

isotherm of ODA on the gold clusters subphase. This is a simple (and versatile) technique wherein a solid support is slowly immersed in the Langmuir monolayer covered trough and withdrawn (Scheme 4.1) [19]. Each immersion cycle enables transfer of a bilayer of the Langmuir monolayer and in this fashion, films were picked up at different time intervals on copper grids for TEM measurements, quartz substrate for UV-vis-NIR measurements and finally on Si (silicon) (111) substrate for FTIR analysis. Prior to deposition of the gold nanoparticle-ODA LB films, the substrates were rendered hydrophobic by depositing a monolayer of lead arachidate. Under these circumstances, it was observed that the gold nanoparticle-ODA monolayer transfer occurred during both upward and downward strokes of the deposition cycle in the Y-type (head-to-head and tail-to-tail) configuration at close to unity transfer ratios for transfers of 46 monolayer (ML). The quality of the gold cluster LB films improves considerably if a hydrophobic substrate is used. Hence all results presented below are for substrates rendered hydrophobic by deposition of 1 ML of lead arachidate prior to transfer of the gold cluster LB film. It is also observed that the hysteresis in the π–A isotherms is not changing as a function of time, whereas the TEM and UV studies indicate the incorporation of the triangular nanoclusters with time in to the ODA monolayer. Hence it can be inferred that the particles are not reorganizing with time.

4.3.2 Brewster angle microscopy

In situ examination of complexation is carried out with the help of Brewster Angle Microscope (BAM), developed at NCL, coupled with 20x10 cm^2 Langmuir trough for real time plotting of the Pressure-Area isotherm. Brewster angle microscopy was primarily used to monitor the topographic variations in the ODA Langmuir monolayer as a function of complexation of gold nanoparticles to the monolayer. These images of the ODA-gold nanoparticle monolayer at the air-water interface were recorded as a function of time holding the barriers at constant and predetermined area. The instrument used did not permit measurement of intensities in the images and consequently, our analysis is purely qualitative. The images of pure ODA spread on the sub phase of Millipore water (pH 7) was taken as reference.

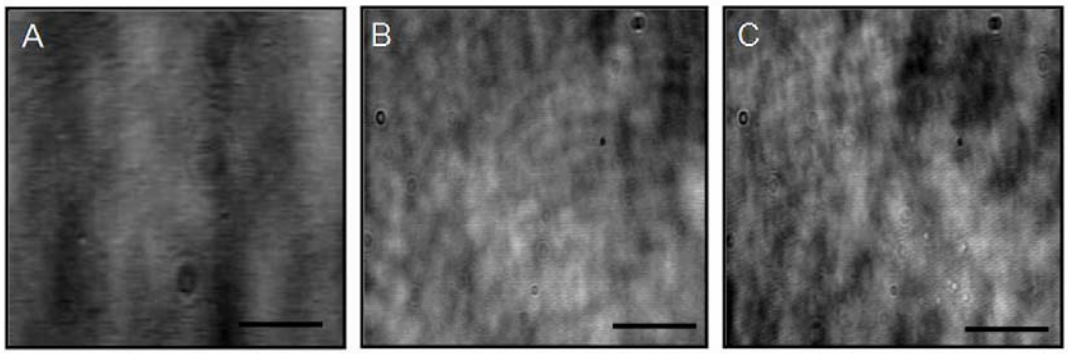

Figure 4.6 *Representative BAM images of the binding of gold nanotriangles with ODA at the air-water interface as a function of time of spreading of ODA monolayer on the purified lemon grass reduced gold solution. t= 0 min (A); (B) t = 60 min and (C) t = 120 min. Scale bar corresponds to 80 µm. The pressure was kept constant at 10 mN/m for all the measurements.*

BAM measurements were carried out on the ODA monolayer at different stages of complexation with gold nanoparticles. Fig 4.6(A-C) shows the time evolution of the ODA monolayer structures on the surface of the 10 times diluted gold nanoparticle solution (pH 6) as seen by BAM. These images were recorded at regular time intervals at fixed area. At t=0, only some small structures are seen which are similar to ODA monolayer. The dark regions correspond to the exposed gold nanoparticle solution and are regions that satisfy the Brewster angle criterion. Immediately after spreading the monolayer, significant contrast exists between the water surface and the ODA domains which appear as bright patches. It can be seen that after 60 min of ODA spreading (Figure 4.6B), the contrast between the exposed gold nanoparticle solution and the regions of ODA complexed with gold nanoparticles has increased. The bright domains also appear to be more continuous than those observed at time $t = 0$. In the BAM images at progressively higher times of complexation of ODA with gold nanoparticles, the same trend follows, with increase in the size of the bright coloured ODA-gold nanoparticle domains. The BAM images clearly indicate that as the gold nanoparticle density at the air-water interface increases, the surface becomes more rigid and dense. In principle, it is possible to treat the intensity variation in the BAM images in terms of Fresnel reflectivity equations to derive information on refractive index/thickness variation in the structures observed in the images. However, the instrument used in this study did not permit

quantification of the contrast in the images, and consequently, BAM has been used only qualitatively to understand the nature of domains formed by complexation of ODA with gold nanoparticles.

4.3.3 FTIR measurement

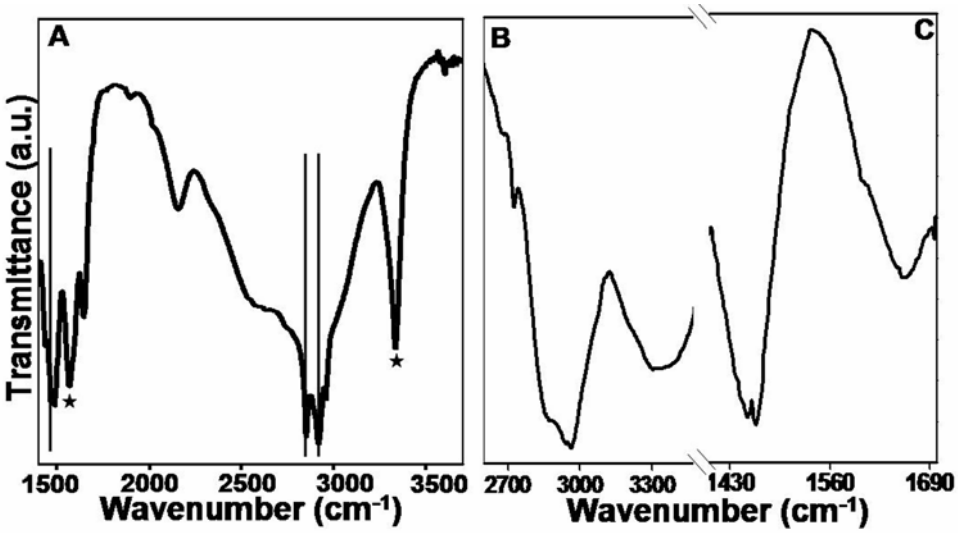

Figure 4.7 *FTIR spectra recorded from (A) Pure ODA and 30-ML ODA bound gold nanoparticle LB film on a Si (111) wafer in two different spectral windows: (B) 2350–3800 cm^{-1} and (C) 1300–1800 cm^{-1}. See text for details.*

FTIR measurement was done to understand the functional group/groups involved in the complexation of the gold nanoparticles with the ODA monolayer. Fig 4.7 shows the FTIR spectra of the pure ODA recorded with KBr pellet (Fig 4.7A) and of a 30 ML gold nanoparticle LB film grown on a hydrophobized Si (111) wafer (Fig 4.7 B,C). The spectra for the film of gold nanoparticles bound to ODA is shown in the regions 2350–3800 cm^{-1} and 1300–1800 cm^{-1} (Fig 4.7B and C), respectively.

The peaks obtained at 3370 cm^{-1} and 1565 cm^{-1} in the case of pure ODA can be attributed to N-H stretching and bending vibrations mode (indicated by star), respectively. The broadening of peaks centered at 3370 cm^{-1}, in Fig 4.7B can be due to the octadecylamine molecules binding with the gold nanoparticle surface. In addition to this there can be an O-H stretching mode due to the fact that the gold clusters might be carrying water around them while binding with ODA monolayer which results in this

broadening. The unbound hydroxyl group strongly absorbs in this range and these bands are only observed in high dilution [35a].

Peaks at 2920 cm^{-1} and 2850 cm^{-1} in Fig 4.7A are indicative of the methylene asymmetric and symmetric vibration modes respectively. Another peak at 1460 cm^{-1} is due to methylene scissoring mode. The methylene asymmetric and symmetric vibration modes in Fig 4.7B are not very prominent, however on careful examination we do notice the splitting of the peak into symmetric and asymmetric modes which is indicative of the ordering of the alkyl chains. This implies that the hydrocarbon chains of ODA capping the gold nanoparticles are closely packed without a significant density of defect in the chains [34]. In the lower spectral region Fig 4.7C, the splitting of the feature at 1460 cm^{-1} is a sensitive indicator of the crystalline packing of hydrocarbon chains [35b]. The fact that this feature is present with splitting indicates that the chains, though close packed are in a crystalline environment. This feature is not seen in the case of spherical particles as a consequence of the curvature of surface of the nanoparticles [36]. The feature at 1640 cm^{-1} is indicative of the shift of the N–H bending vibrational mode arising from the ODA molecules bound to the gold nanoparticle surface. Such effects and shifts of spectral features when compared to the features of the unbound fatty amine molecule are not surprising in the proximity of metal surfaces to the bonds involved with the fatty amine molecule [37].

4.3.4 UV-vis-NIR spectroscopy

The growth of the LB films of the ODA bound gold nanotriangles was followed using UV-vis-NIR spectroscopy measurements. The measurements were performed on LB films of the gold cluster-ODA films of varying thickness transferred onto hydrophobized quartz substrates. Optical absorption spectroscopy is an excellent tool for following the process of LB film formation of gold nanoparticles due to the strong surface plasmon resonance exhibited by gold nanoparticles. Fig 4.1A shows the optical absorption spectra recorded for solution of pure triangles and pure spherical nanoclusters. With change in shape of the nanoparticles there is a distinct difference in the optical absorption spectra, there is a prominent longitudinal peak at 1300 nm in addition to the

transverse peak at 520 nm. This appearance of two prominent absorption bands is an intrinsic property of anisotropic structures [29-31]. It is germane to this investigation as the optical absorption signatures of the nanoparticle solution is quite distinct and can therefore be used to identify the size and shape of the clusters during complexation with the amine films.

Fig 4.8A show the optical absorption spectra recorded as a function of the number of monolayers of gold nanoparticle-ODA in the LB films on hydrophobized quartz substrates at a subphase pH of 6. The surface plasmon resonance occurs at 520 nm and 1300 nm in all the films, and a monotonic growth in the resonance intensity is observed as the film thickness increases. Fig 4.8B shows the plot of the variation in the ratio of longitudinal to transverse surface plasmon absorption maximum with film thickness. The increase in the intensity of the peaks for the transverse and longitudinal plasmon is indicative of layer by layer growth of the gold cluster film in a lamellar fashion [22a, j] by the LB technique. The increase in the longitudinal/transverse ratio values with increase in the number of layers is indicative of the fact that with time in addition to the spherical particles the number of bigger triangular nanoparticles is also increasing in the ODA monolayer resulting in building of longitudinal peak. The inset of Fig 4.8B shows the variation in the intensity of the surface plasmon resonance with film thickness. The curve was found to be non-linear and a number of reasons could contribute to this disparity. We believe this difference is due to changes in the nature of the optical absorption spectrum as the nanoparticle density is built up in the LB film. Close proximity of gold nanoparticles in films is known to lead to broadening of the surface plasmon resonance [38]. The distinct shift in the maxima with increase in the number of dips clearly indicates the aggregation or cross linking of the particles [39-41]. TEM studies were done on the samples for clarification.

The optical properties of the films were found to remain unchanged on storage under ambient conditions for many weeks. No deterioration in the optical properties were found even after prolonged immersion of the gold cluster LB films in water, indicating strong binding of the clusters to the hydrophilic groups of the amine monolayer. Inset in

Fig 4.8B shows the photograph of 16 ML of triangular nanoclusters on to the quartz substrate transferred using LB technique.

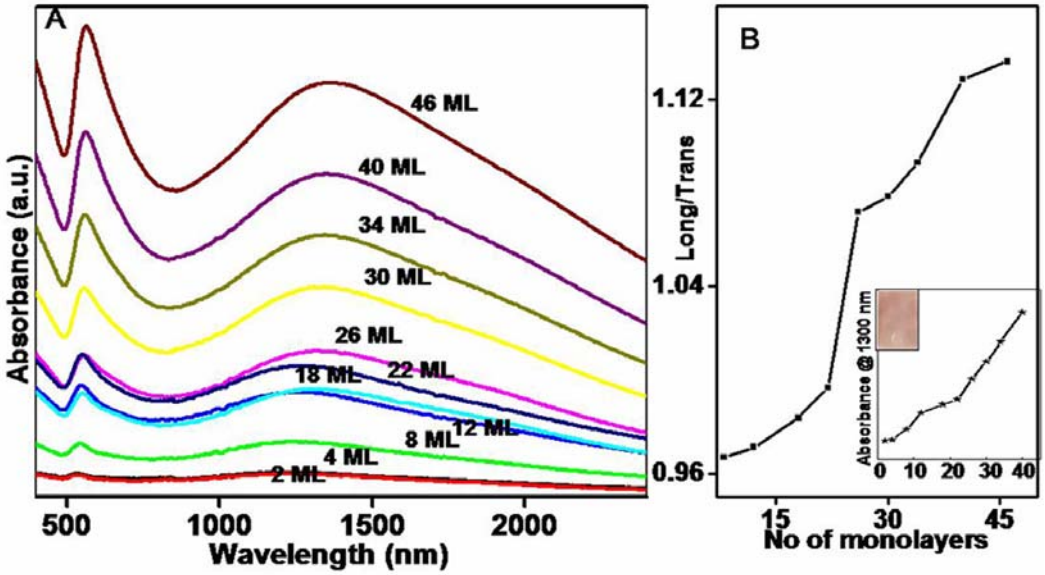

Figure 4.8 *(A) UV–Vis spectra recorded from ODA complexed gold nanoparticle LB films transferred onto quartz substrate at different thicknesses of the film, no. of ML are mentioned in the plot. (B) Plot of the longitudinal to transverse values for various film thickness ,inset shows the plot of intensity of the surface of plasmon resonance (at 1300 nm) plotted as a function of number of monolayer of ODA and gold nanoparticles LB films grown on quartz, transferred by LB technique.*

4.3.5 Transmission Electron Microscopy (TEM)

While the UV-vis-NIR and FTIR data provides an insight into the changes during a competitive complexation process of large and small gold colloidal particles with the ODA monolayer, TEM enables a direct estimation of the relative concentration of the colloidal particles in the film. TEM studies were performed to get the view of the complexation at different time intervals and with different solutions.

TEM measurements carried out for the chemically synthesized gold solution yielded a particle size of 8 ± 1 nm and for the gold solution prepared using lemon grass broth shows a bimodal distribution of triangles, ≈ 350 nm and 90 nm and spherical particles of ≈ 75 nm. TEM measurements clearly rule out the aggregation of gold particles with increase in number of dips. It can be seen that the particles are disperse and form assemblies of the gold nanoparticles where the individual particles are separated,

indicating the possibility of interconnection via some other bonding. The close packing can be explained as follows. At the interface, gold colloidal nanoparticles may come close to each other due to the screening effect that is provided by the positively charged Langmuir monolayer. Thereafter, it may be possible for hydrogen bonding to occur between the biomolecules covering the surface of the neighbouring gold nanoparticles leading to the formation of hydrogen bonded networks of the gold nanoparticles at the air–water interface. [42].

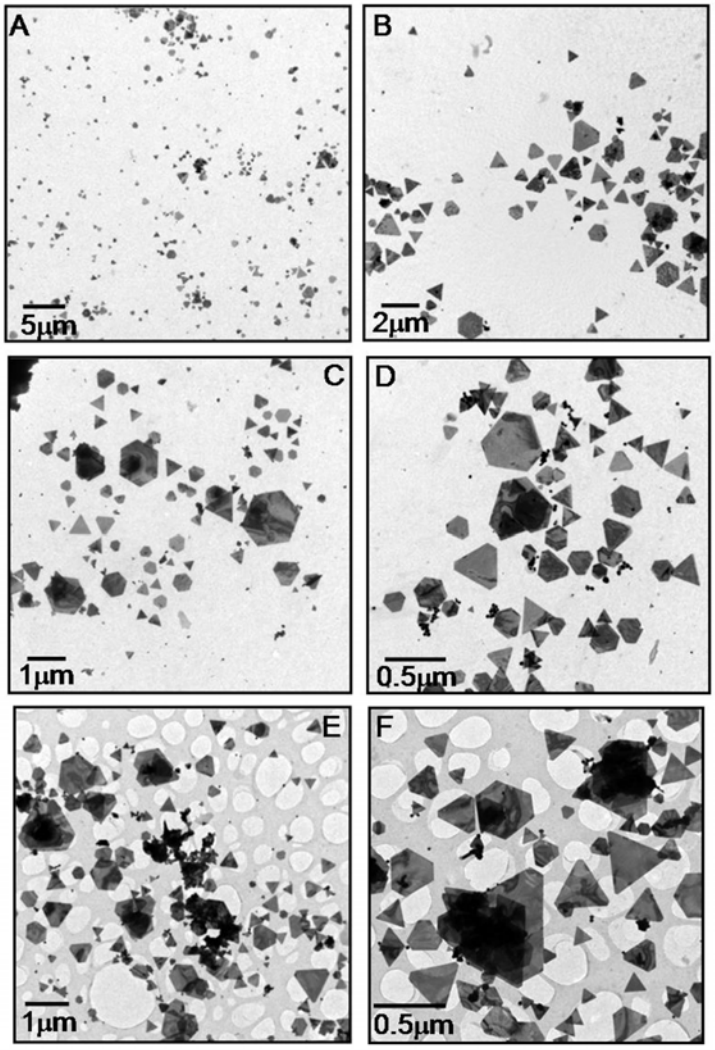

Figure 4.9 *Representative TEM images at different magnification of the binding of gold nanotriangles with ODA at the air-water interface as a function of time of spreading of ODA monolayer on the purified lemon grass reduced gold solution. t- 3 h (A, B) ;(C,D) t - 10 h and (E,F) t - 24 h.*

Fig. 4.9 (A-F) shows TEM micrographs recorded at different magnifications for a single monolayer of ODA film deposited on a carbon-coated electron microscope grid after complexation with the gold triangles at time interval of 3h (A,B), 10h (C,D) and 24 h (E,F). It is evident from the micrographs that the triangles are binding to the positively charged ODA monolayer and the population of the triangles steadily increases with time due to the higher number of triangles binding to the available fatty amine.

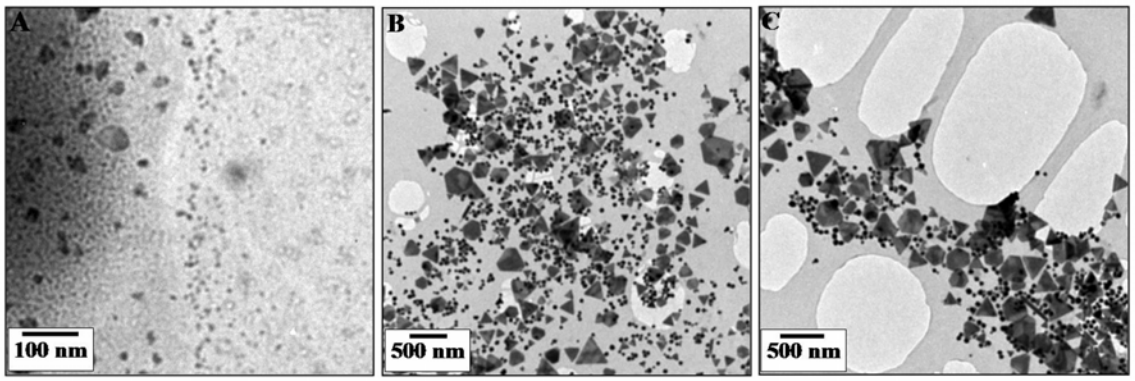

Figure 4.10 *Representative TEM images of the binding of gold nanoparticles with ODA at the air-water interface as a function of time of spreading of ODA monolayer on the as prepared solution of lemon grass reduced gold nanoparticles. (A) t- 1 h; (B) t - 9 h and (C) t - 24 h.*

As the triangles were binding with the ODA monolayer so instead of the purified solution we tried the complexation of the ODA monolayer with the as prepared, unpurified solution of lemon grass reduced gold. This solution contains almost equal proportion of triangular and spherical nanoparticles. It was observed that in the case of unpurified solution the film comprises of a mixture of both spherical and triangular gold particles. Fig 4.10A, B and C shows the micrographs at the time interval of 1h, 9h and 24 h respectively. From the micrographs taken at various regions of the grid a plot of the particle size distribution (PSD) was determined and it is evident that initially at t = 1h, we find only spherical particles coming to the surface and as the time increases more and more triangles are binding with the fatty amine monolayer. At any given time there is many times the number of spherical particles per triangle. The PSD clearly shows that 7.5 nm clusters occur six times more frequently than the triangular gold clusters on an

average and this ratio decreases slightly with time. Therefore, we can infer that the cluster population in the films obtained from complexation of the ODA film with the mixture is rightly dominated by the *small gold particles*. However, if one considers that the ratio of the surface areas of the triangular to the spherical particles is ca. 8.4, the 6 fold excess of the smaller clusters still leave the mixed distribution dominated by the larger clusters in phenomena where surface effects are important. The thickness of the triangular nanoparticles was obtained from the AFM studies done on the same, Fig 4.11.

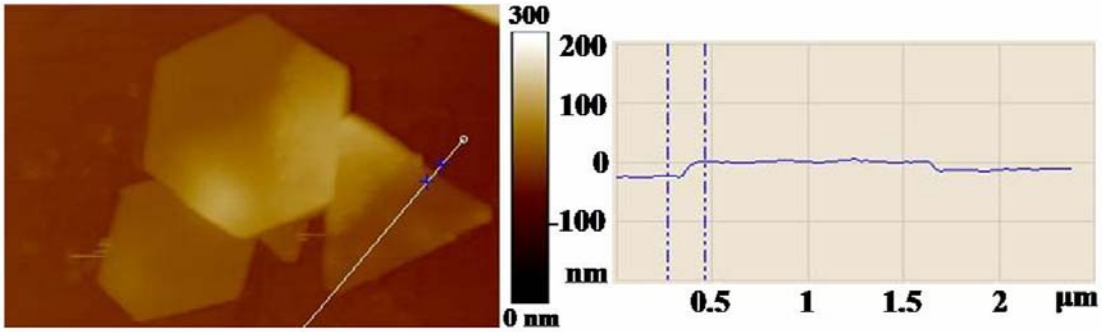

Figure 4.11 *AFM image of the gold nanotriangles where the right panel shows the line profile of the triangle with the thickness of 24.8 nm.*

This clearly explains why the UV-vis-NIR (which yield the surface plasmon excitations) and the FTIR (which yield information on the packing of the hydrocarbon chains coordinated to the particle surface) measurements showed that the large gold particles dominates the complexation process even though the concentration of the small gold particles in solution is greater than that of the large gold particles. This process may be further rationalized in terms of the energy required to distort the packing of the hydrocarbon chains in the ODA monolayer. It is clear that the hydrocarbon sheath surrounding the colloidal particle surface will be required to be much more distorted around the smaller colloidal particles due to the curvature effect and thus would be energetically less favorable than when coordinated to the large gold particles. Sastry and coworkers had earlier also seen a similar behavior in the study of the competitive diffusion of spherical silver and gold colloidal particles in ODA films [43]

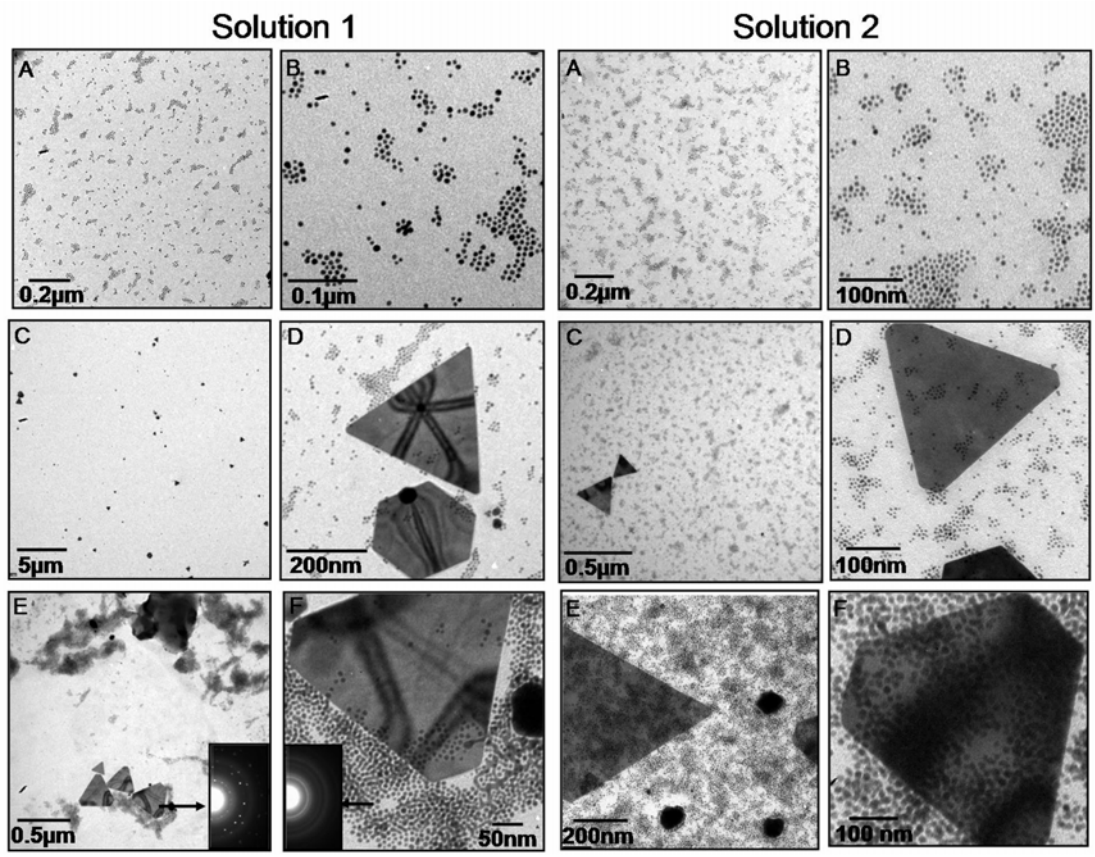

Figure 4.12 *Representative TEM images at different magnification of solution 1(the time dependent binding of the hydrosol containing 50 µl of spherical nanoparticles) and 2 (the time dependent binding of the solution containing 100 µl of spherical nanoparticles) (A,B) t- 1 h;(C,D) t - 6 h and (E,F) t - 24 h.*

From the kinetics of complexation it is evident that the spherical particles are binding to ODA monolayer much faster than the bigger triangular nanoparticles so the complexation can be used as a tool of separation of spherical and triangular gold nanoclusters from the mixture. To further emphasize this point we used a mixture of purified triangles and sodium borohydride reduced gold nanoparticles in different concentration. In the first case, 50 µL of borohydride reduced gold spherical particles were added to the 550 µL of purified solution of the lemon grass reduced triangles. Fig 4.12, titled Solution 1 shows the micrographs of complexation of gold particles with amine monolayer after 1h (A,B), 6h (C,D) and 24h (E,F) respectively. On increasing the concentration of spherical nanoparticles to 100 µl, Fig 4.12 (A-F), titled Solution 2, we

clearly notice that the number of spherical particles coming to the surface is far more in number over a given period in time as compared to the 50 μL addition of spherical gold nanoparticles. From the TEM studies it is evident that the spherical particles are binding much more frequently than the triangles as the ratio of spherical/triangles are very high. As seen from the TEM micrographs few (one or two) triangular particles are also incorporated in with spherical particles in first 30 min. The inset in the Fig 4.12 E and F under Solution 1 shows the SAED pattern from two regions indicated by the arrow in the images. The SAED pattern in E is from a collective region of triangles and spherical particles. The spots indicative of the crystalline structure [32] of the nanotriangles as well as the rings of polycrystalline spherical particles are clearly seen. SAED pattern in F is from a collection of spherical particles only and is showing the polycrystalline nature of the gold nanoparticles.

This can be explained from a purely electrostatics point of view. The higher number of amine molecule charged pairs due to the larger surface area of bigger gold cluster makes the incorporation energetically favorable. Another contribution to the energetics of cluster complexation arises from the packing of the amine hydrocarbon chains on the triangular gold clusters leads to larger volumes available to the terminal groups of the amine molecules and, consequently, weaker van der Waals interaction between the chains. In other words, the presence of smaller size clusters distorts the packing of the hydrocarbon chains of the amine films to a larger extent than the larger clusters with their smaller surface curvature as is also seen from the FTIR data.

4.3.6 pH dependent complexation

To control the complexation of the gold nanoparticles with amine monolayer, a pH dependent study was carried out. ODA molecules were dispersed on the surface of the colloidal solution held at different pH values and complexation of the gold nanoparticles with the ODA Langmuir monolayer was followed as a function of time of spreading the monolayer. This is conveniently done by measuring the π–*A* isotherms.

The earlier experimentation was at pH 6 (acidic) and a further study with pH 12 (basic) was taken up. At pH = 6, both the amine ($-NH_3^+$, pK_b 10.5) and the coating on

gold clusters are expected to be fully ionized, leading to maximum attractive electrostatic interaction and a large increase in the Langmuir monolayer area with time (Fig 4.13 *A*). On the other hand at pH = 12, the amine functionality in the Langmuir monolayer is un-ionized and hence the electrostatic interaction between the gold nanoparticles and the ODA monolayer is considerably weaker than at pH 6. Almost negligible complexation occurs and the π–*A* isotherms are relatively unchanged with time (Fig 4.13 *B*). The black lines refer to the isotherms measured immediately after spreading the ODA monolayer (*t* = 15 min) and the red lines are the isotherms measured 26 hrs after spreading. It is clear that the area/ODA molecule increases with time for the Langmuir monolayer of gold nanoclusters solution at pH = 6 (Fig 4.13 *A*) and also that a slight expansion of the monolayer is observed when the colloidal solution subphase is at pH = 12 (Fig 4.13 *B*).

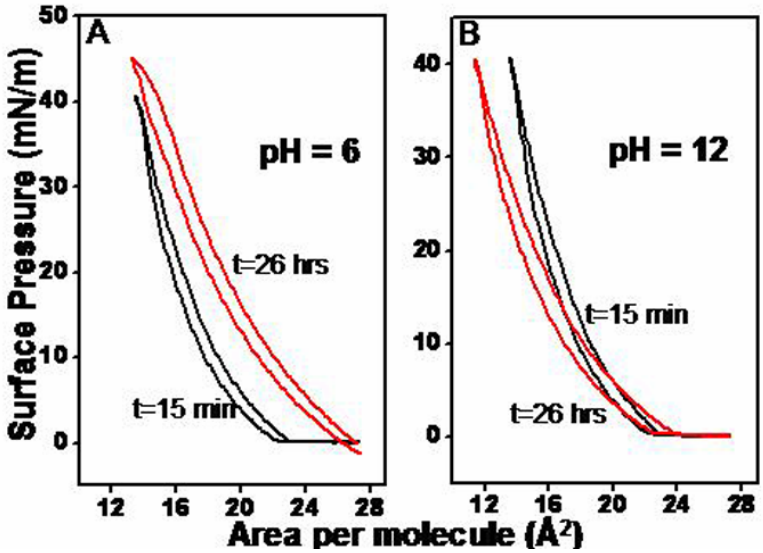

Figure 4.13 *π–A isotherms of ODA monolayer spread on lemon grass reduced gold nanoparticle solution (A) pH = 6 and (B) pH = 12, recorded as a function of time of spreading the monolayer*

Even though the nanoparticle-ODA interaction is negligible at pH 12, there was a slight change in colour of the monolayer at this pH. This indicates that a small percentage of gold nanoparticles do complex with the ODA monolayer under these conditions as well. At pH 12, the only possible interaction between the gold nanoparticle and the ODA monolayer would be hydrogen bonding and hydrophobic interaction. Serra et al. have shown that hydrogen bonding interaction does play a significant role in the complexation

and film formation of an ODA titanyl oxylate system [44]. They have shown that after the ODA monolayer is spread onto potassium titanyl oxylate, complexation and subsequent film transfer can be achieved. They attribute this film transfer to be due to hydrogen bonding interaction between the protonated amino group of stearylamine and TiO_2 surface hydroxyl groups [44]. It is clear from Fig 4.13 that electrostatic interactions play a crucial role in the complexation process. By simple variation of the colloidal solution pH, it is possible to modulate the electrostatic interaction between the colloidal particles and the Langmuir monolayer and thus vary the nanoparticle concentration at the air–water interface. This has earlier been demonstrated for a number of other colloidal particle systems such as gold [22a, d] and CdS quantum dots [22f] .

4.4 Proposed size and shape dependant separation technique

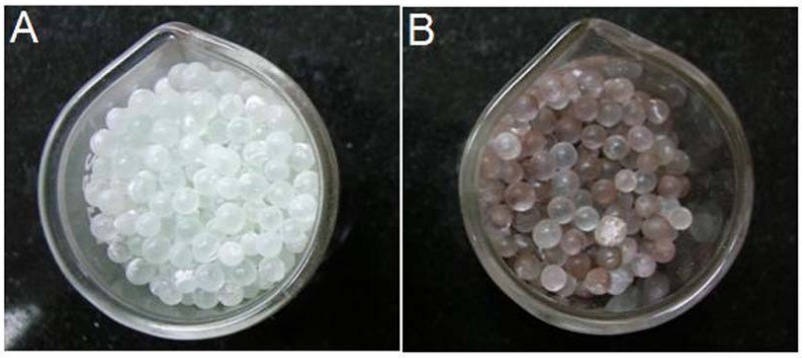

Figure 4.14 *Photograph of (A) ODA coated glass beads. (B) ODA coated glass beads exposed to as prepared lemon grass reduced gold nanoparticles.*

The complexation process explained and demonstrated in previous sections was tested as a separation technique by exposing the hydrosol of as prepared lemon grass reduced gold nanoclusters which contains approximately equal population of spherical as well as the triangular nanoparticles, to the ODA capped spherical glass beads. The ODA coated glass beads resulted in increase in the surface area available for complexation (Fig 4.14A). With the presence of increased surface area of spherical beads available for binding of nanoclusters we reduce the time needed for diffusion. These ODA coated glass beads were prepared by leaving the glass beads in 2 mg/ml solution of ODA in chloroform till the solvent evaporates. The triangular gold nanoparticles being heavy,

tend to settle down under gravity, and hence the set up was so planned as to enable the beads to be just covered with the hydrosol thus maximizing the binding and minimizing the loss due to settling.

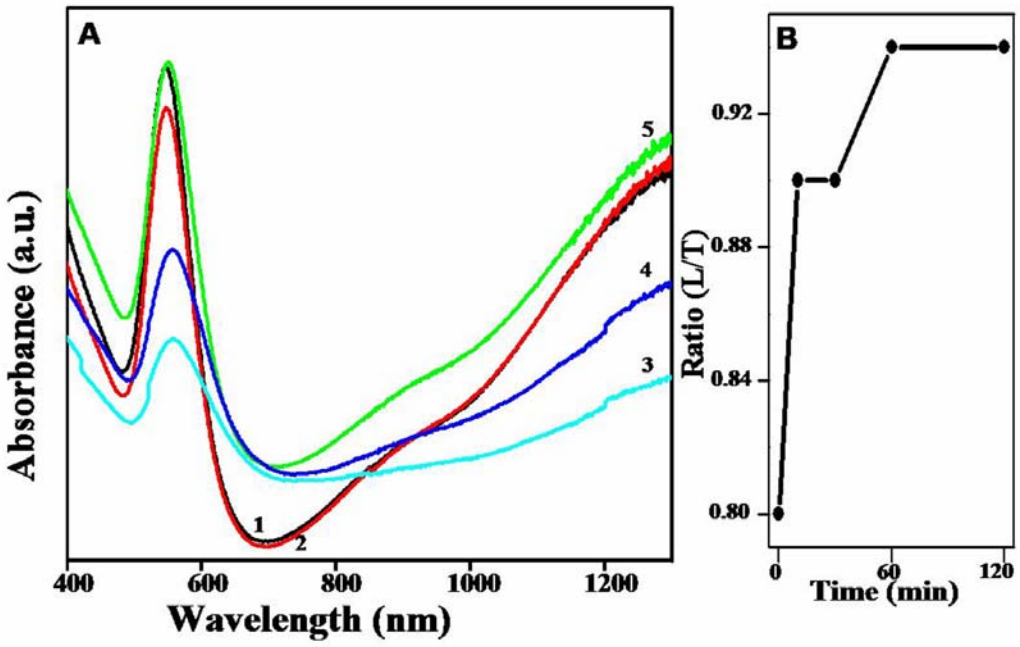

Figure 4.15 *(A) UV-vis-NIR spectra of the lemon grass reduced nanoparticles solution exposed to ODA capped glass beads at time 0 (curve 1), 10 min (curve 2), 30 min (curve 3), 1 hour (curve 4) and 2 hours (curve 5).*

The UV-vis-NIR readings of the solution were taken at regular time intervals to obtain the indirect spectroscopic signature of the competitive complexation process. It was observed that the UV-vis-NIR studies of the solution showed a decrease in the intensity of the peak at 520nm (corresponding predominantly due to the spherical nanoparticles) for the initial period of 30 min as compared to the control (Fig 4.15A). The ratio of the longitudinal to transverse (L/T) peaks shows an increase for the period of 10 min and then tends to become stable indicating that the complexation of the spherical nanoparticles is complete within a short span of 10 minutes (Fig 4.15 B). Thereafter the increase in the L/T ratio is indicative of the binding of triangular nanoparticles along with the spherical nanoparticles. The photographs in fig 4.14A shows the glass beads coated with the ODA on its surface while Fig 4.14B shows the ODA coated glass beads after

exposure to the as prepared solution of lemon grass reduced gold nanotriangles. The ruby red color of the glass beads in the figure 4.15B clearly shows the complexation of the spherical gold nanoclusters to the surface bound ODA as compared to the unexposed ODA capped glass beads. Thus, this shows that spherical gold nanoclusters are indeed getting bound to the ODA capped glass beads as is indicated from the UV-vis-NIR spectra obtained from the solution (Fig 4.15A). The technique can therefore be effectively used to separate the two types of the gold nanoclusters from a mixture on the basis of there mobility and shape.

4.5 Conclusion

In conclusion, it has been shown that colloidal gold particles can be incorporated in ODA films by simple spreading of the organic films on the colloidal solution. It is also possible that increasing surface curvature could lead to reduced electrostatic interaction via a purely geometrical effect. We would like to mention here that it was noted that the pH at which maximum cluster incorporation occurs for gold nanotriangles and spherical gold particles in ODA films was found to be 6. This indicates that in addition to the nanoscale curvature of the colloidal particle surface, the chemical nature of the colloidal particle also plays an important role in the ionization of the carboxylic acid groups. This aspect of the work has enormous scope for further study.

References

(1) Feynman, R. P., in a lecture delivered at the American Physical Society Meeting, **1959**.

(2) AliVisatos, A. P. *Science* **1996,** *271*, 933.

(3) Collier, C. P.; Saykally, R. J.; Shiang, J.J.; Henriches, S. E.; Heath, J. R. *Science,* **1997**, *277*, 1978.

(4) Brust, M.; Walker, M.; Bethell, D.; Schiffrin, D. J.; Whyman, R. *J. Chem. Soc., Chem. Commun*., **1994**, 801. (b) Vijaya Sarathy, K.; Raina, G.; Yadav, R. T.; Kulkarni, G. U.; Rao, C. N. R. *J. Phys. Chem. B*, **1997**, *101*, 9876. (c) Brinker, C. J., Lu, Y.; Sellinger, A.; Fan, H. *Adv. Mater*., **1999**, *11*, 579. (d) Wang, Z. L., *Adv. Mater*. **1998**, *10*, 13. (e) Connolly, S.; Fullam, S.; Korgel, B.; Fitzamurice, D. *J. Am. Chem. Soc* **1998**, *120*, 2969.

(5) (a) Colvin, V. L.; Goldstein, A. N.; AliVisatos, A. P. *J. Am. Chem. Soc*.,**1992**, *114*, 5221. (b) Chumanov, G.; Sokolov, K.; Gregory, B. W.; Cotton, T. M. *J. Phys. Chem*., **1995**, *99*, 9466. (c) Grabar, K. C.; Smith, P. C.; Musick, M. D.; DaVis, J. A.; Walter, D. G.; Jackson, M. A.; Guthrie, A. P.; Natan, M. J. *J. Am. Chem. Soc*., **1996**, *118*, 1148. (d) Bandyopadhyay, K.; Patil, V.; Vijayamohanan, K.; Sastry, M. *Langmuir*, **1997**, *13*, 5244. (e) Garcia, M. E.; Baker, L. A.; Crooks, R. M. *Anal. Chem*., **1999**, *71*, 256. (f) Sarathy, K. V.; Thomas, J. P.; Kulkarni, G. U.; Rao, C. N. R. *J. Phys. Chem. B*, **1999**, *103*, 399.

(6) Li, M.; Wong, K. K. W.; Mann, S. *Chem. Mater*., **1999**, *11*, 23.

(7) (a) Fendler, J. H.; Meldrum, F. *Adv. Mater*., **1995**, *7*, 607 and references therein. (b) Sastry, M.; Patil, V.; Mayya, K. S.; Paranjape, D. V.; Singh, P.; Sainkar, S. R. *Thin Solid Films*, **1998**, *324*, 239. (c) Sastry, M.; Ramakrishnan, V.; Pattarkine, M.; Gole, A.; Ganesh, K.N. *Langmuir,* **2000,** *16*, 9142 .

(8) Mayya, K. S. ; Sastry, M. *Langmuir*, **1999**, *15*, 1902.

(9) Iler, R. K. *J. Colloid Interface Sci*. **1966**, *21*, 569.

(10) Honig, B. ; Nicholls, A. *Science*, **1995**, *268*, 1144.

(11) Taguchi, Y.; Kimura, R.; Azumi, R.; Tachibana, H.; Koshizaki, N.; Shimomura, M.; Momozawa, N.; Sakai, H.; Abe, M.; Matsumoto, M. *Langmuir*, **1998**, *14*, 6550. (b) Lvov, Y.; Ariga, K.; Ichinose, I.; Kunitake, T. *J. Am. Chem. Soc.*, **1995**, *117*, 6117.

(12) (c) Caruso, F.; Lichtenfeld, H.; Giersig, M.; Mohwald, H. *J. Am. Chem. Soc.*, **1998**, *120*, 8523.

(13) Tien, J.; Terfort, A.; Whitesides, G. M., *Langmuir*, **1997**, *13*, 5349.

(14) Caruso, F; Niikura, K.; Furlong, D.N.; Okahata. Y. *Langmuir* **1997**, *13*, , 3427.

(15) Mamedov, A.; Ostrander, J.; Aliev, F.; Kotov, N. A. *Langmuir* **2000**, *16,* 3941.

(16) Lvov, Y.; Ariga, K.; Onda, M.; Ichinose, I.; Kunitake, T. *Langmuir* **1997**, *13*, 6195..

(17) Kumar, A.; Mandale, A.B.; Sastry, M. *Langmuir* **2000**, *16*, 6921 .

(18) Cassagneau, T.; Mallouk, T.E.; Fendler, J.H. *J. Am. Chem. Soc*. **1998**, *120*, 7848.

(19) Ulman, A., *An Introduction to Ultrathin Organic Films: From Langmuir–Blodgett to Self-Assembly*, Academic Press, San Diego, CA, **1991**.

(20) Ganguly, P.; Paranjape, D. V. ; Sastry, M., *J. Am. Chem. Soc.*, **1993**, *115*, 793. (b) Ganguly, P.; Paranjape, D. V.; Patil, K. R.; Sastry, M.; Rondelez, F., *Langmuir* **1997**, *13*, 5440. (c) Clemente-Leon, M.; Mingotaud, C.; Agricole, B.; Gomez-Garcia, C. J.; Coronado, E.; Delhaes, P., *Angew. Chem. Int. Ed. Engl.* **1997**, *36*, 1114.

(21) Riccio, A.; Lanzi, M.; Antolini, F.; De Nitti, C.; Tavani, C.; Nicolini, C., *Langmuir*, **1996**, *12*, 1545. (b) Raedler, U.; Heiz, C.; Luigi, P. ; Tampe, R., *Langmuir* **1998**, *14*, 6620.

(22) (a)Mayya, K. S.; Patil, V.; Sastry, M., *Langmuir* **1997**, *13*, 2575. (b) Sastry, M.; Mayya, K. S.; Patil, V.; Paranjape, D. V.; Hegde, S. G., *J. Phys. Chem. B* **1997**, *101*, 4954. (c) Mayya, K. S.; Sastry, M., *J. Phys. Chem. B* **1997**, *101*, 9790. (d) Mayya, K. S.; Patil, V.; Sastry, M., *J. Chem. Soc., Faraday Trans*. **1997**, *93*, 3377. (e) Mayya, K. S. Sastry, M., *Langmuir* **1998**, *14*, 74. (f) Mayya, K. S.; Patil, V.; Kumar, M.; Sastry, M., *Thin Solid Films* **1998**, *312*, 308. (g) Patil, V.; Sastry, M., *Langmuir* **1998**, *14*, 2707. (h) Sastry, M.; Mayya, K. S.; Patil, V., *Langmuir* **1998**, *14*, 5921. (i) Lala, N.; Chittiboyina, A. G.; Chavan, S. P.; Sastry, M., Paper presented at the 5th International Symposium on Bio- Organic Chemistry, Pune, 30 January–4 February

2000. (j) Tian , Y.; Wu, C.; Fendler, J. H. *J. Phys. Chem.* **1994**, *98*, 4913. (k) Zhao, X. K.; Xu, S.; Fendler, J. H. *J. Phys. Chem.* **1990**, *94*, 2573.

(23) Pan, Z.; Liu, J.; Peng, X.; Li, T.; Wu, Z.; Zhu, Z. *Langmuir* **1996**, *12*, 851.

(24) (a) Urquhart, R. S.; Furlong, D. N.; Gegenbach, T.; Geddes, N. J.; Grieser, F. *Langmuir* **1995**, *11*, 1127. (b) Urquhart, R. S.; Hoffmann, C. L.; Furlong, D. N.; Geddes, N. J.; Rabolt, J. F.; Grieser, F. *J. Phys. Chem.* **1995**, *99*, 15987.

(25) (a) Leloup, J.; Maire, P.; Ruadel-Teixier, A.; Barraud, A. *J. Chim. Phys. (Paris)* **1985**, *82*, 695. (b) Leloup, J.; Ruadel-Teixier, A.; Barraud, A. *Thin Solid Films* **1992**, *210/211*, 407.

(26) Mayya K. S.; Sastry, M. *J. Nano. Res.* 2, **2000**,183.

(27) Shankar, S; Rai, A; Ahmad, A; Sastry, M *Chem. Mater.* **2005**, *17,* 566.

(28) (a)Patil, V.; Malvankar, R. B.; Sastry, M. *Langmuir* **1999**, *15*, 8197. (b) Alvarez, M. M.; Khoury, J. T.; Schaaf, T. G.; Shafigullin, M. N.; Vezmar, I.; Whetten, R. L. *J. Phys. Chem. B* **1997**, *101*, 3706. (c) Henglein, A. *J. Phys. Chem.* **1993**, *97*, 5457 (b) Mulvaney, P. *Langmuir* **1996**, *12*, 788

(29) Rai, A; Singh, A; Ahmad, A; Sastry M. *Langmuir* **2006**, *22,* 737

(30) Shipway, A. N.; Lahav, M.; Gabai, R.; Willner, I. *Langmuir* **2000**, *16*, 8789.

(31) Kelly, K. L.; Coronado, E.; Zhao, L. L.; Schatz, G. C. *J. Phys.Chem. B* **2003**, *107*, 668-677. (b) El-Sayed, M. A. *Acc. Chem. Res.* **2001**, *34*, 257-264. (c) Link, S.; Mohamed, M. B.; El-Sayed, M. A. *J. Phys. Chem. B* **1999**, *103*, 3073

(32) Shankar, S. S.; Rai, A.; Ankamwar, B.; Singh, A.; Ahmad, A.; Sastry,M. *Nat. Mater.* **2004**, *3*, 482

(33) Schnabel, U; Fischer, C.H.; Kenndler, E . *J. Microcolumn Separations* **1997,** *529*, 534

(34) Hostetler, M. J; Stokes, J. J.; Murray, R. W. *Langmuir* **1996**, *12*, 3604.

(35) (a) *Introduction to specroscopy* **2001** pp 25,26. Pub. John Vondeling (b) Von Sydow, R.G. *J. Mol. Spectrosc*. **1961**, *7,* 116.

(36) Swami, A; Kumar,A; Selvakannan, PR ; Mandal, S; Sastry, M. *J. Colloid Interface Sci.* **2003***, 260,* 367.

(37) Daniel V. Leff, D. V.; Brandt, L.; Heath, J. R. *Langmuir* **1996**, *12,* 4723

(38) Blatchford, C. G.; Campbell, J. R.; Creighton, J. A. *Surf. Sci.* **1982**, *120*, 435. (b) Taleb, A.; Petit, C.; Pileni, M. P. *J. Phys. Chem. B* **1998**, *102*, 2214.

(39) Kreibig, U; Genzel, L; Surf. Sci. **1985**, *156* ,678.

(40) Weisbecker, C. S; Merritt, M. V; Whitesides, G. M *Langmuir* **1996**, *12*, 3763.

(41) Gole, A; Ganpule, C; Pasricha, R; Sastry, M. *J. Nanosci. Nanotechnol*. **2002** ,*2*1, 47.

(42) Mayya, K. M; Jain, N; Gole, A; Langevin, D; Sastry, M. *J. Colloid Interface Sci.* **2004** *270* 133

(43) Patil, V.; Sastry, M. *Langmuir* **1997**, *13*, 5511.

(44) Serra, A.; Genga, A.; Manno, D.; Micocci, G.; Siciliano, T.; Tepore, A.; Tafuro, R.; Valli, L. *Langmuir* **2003**, *19*, 3486.

CHAPTER V

Transmetallation Reaction between Silver Nanoparticles and Chloroaurate Ions: Means to build anisotropic nanostructures

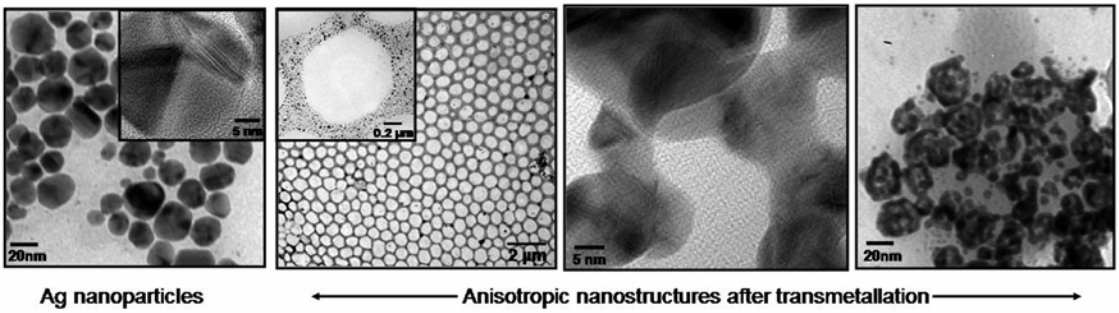

Creativity requires the courage to let go of certainties. (Erich Fromm)

The transmetallation reaction between a sacrificial nanoparticle and more noble metal ions in solution has emerged as a novel method for creating unique hollow and bimetallic nanostructures. We have tried to show that transmetallation reactions between nanoparticles constrained into a close-packed structure and appropriate metal ions could lead to a new strategy for metallic cross-linking of nanoparticles, generation of coatings with promising optoelectronic behavior and structures with electrical behavior. In this report, we investigate the possibility of carrying out the transmetallation reaction between close packed silver nanoparticles and gold ions at air-water interface and at liquid-liquid interface. The transmetallation reaction may be modulated (a) by the insertion of an electrostatic barrier in the form of an ionizable lipid monolayer between the silver nanoparticles and the aqueous gold ions that impacts the gold nanoparticle assembly and (b) by introducing halide ions during transmetallation.

Part of the work presented in this chapter has been published:

Pasricha, R.; Swami, A.; Sastry, M. *J. Phys. Chem. B*, 2005, *109*, 19620

5.1 Introduction

The synthesis, deposition and subsequent patterning of thin films of metal nanoparticles is of great interest because of their potential for application as building blocks in nanodevices [1]**.** It is well known that metal nanoparticles possess unique optical, chemical, magnetic and electrical properties, which are different from the properties in their bulk states [2]**.** Apart from variation in parameters such as size, shape and dielectric constant of the dispersing medium, these properties can also be controlled though their ordered or patterned assembly on suitable substrates [3]. This is because the parameters that influence the collective behavior of assembled nanostructures can now be manipulated by chemists with a high degree of control thus providing new initiative to research on cluster-engineered materials. To date, several techniques have been reported for fabricating patterned arrays of nanoparticles on solid surfaces that include spin coating [4]**,** photolithography [5], soft lithography [6], microcontact printing [7] etc. The Langmuir-Blodgett (LB) technique is a versatile method, which has been extensively used for generating ordered monolayer arrays of metallic [8], semiconducting [9], and polymer nanoparticles [10] and their thin film formation.

One variant of the LB technique involves spreading a colloidal suspension of hydrophobic nanoparticles on water, allowing the solvent to evaporate and subsequently transferring the nanoparticle array that forms on the water surface to solid substrates. However, the role of the air-water interface in the above-mentioned cases is relatively passive, since it is utilized merely to organize nanoparticles. An exciting option is to design experiments wherein the air-water interface is dynamic and permits reactions involving nanoparticles. Progress in this direction was made by Chen and coworkers [11] who showed that two-dimensional gold nanoparticle networks could be cross-linked by bifunctional bridging linkers such as TBBT (4,4'-thiobenzenethiol) through hydrogen bonding at the air-water interface. Sastry and coworkers have shown how the symmetry-breaking nature of the air-water interface can be exploited to build anisotropic nanostructures by carrying out the reduction of precursor metal ions preferentially at the interface [12]**.** This has been achieved either by constraining the precursor metal ions

[12a] or the reducing agent [12b, c] to the air-water interface thus confining the reduction of metal ions strictly to the interface.

As mentioned above in addition to nanoparticle size and composition, the shape of the nanoparticles also play an important role in modulating their electronic, optical [2a,13] and catalytic properties [14]. As a consequence, there is considerable current interest in developing synthesis methods to control the shape of nanoparticles. In so far as noble metal nanoparticles such as gold, silver and semiconductor nanoparticles are concerned, plethora of solution based experimental procedures have been developed for shape modulation [2a, 15, 16,17(a-c)].

In a series of elegant reports, research groups led by Xia [17] and Bai [18] have investigated the possibility of using the transmetallation reaction to modulate the structure of aqueous nanoparticles. Galvanic exchange reaction between sacrificial nanoparticles (which act as a template) and other suitable metal ions often results in the formation of hollow nanostructures [17,18] with interesting application potential. Xia and co-workers have studied in detail the mechanistic aspects of the transmetallation reaction between sacrificial Ag nanospheres/nanocubes and Au ions [17]. They observe that the plasmon absorption band of the metal nanostructures following the replacement reaction can be tuned in the range 500 – 1200 nm by simple variation of the experimental conditions [17]. Using Co nanoparticles as sacrificial templates, Bai and co-workers have shown that transmetallation reaction with Au and Pt ions results in the formation of hollow Pt nanospheres [18a] and rod-like Au-Pt alloy nanoparticles [18b] with excellent catalytic properties.

An interesting possibility that has not been addressed so far is to study transmetallation reactions involving nanoparticles assembled on suitable surfaces/interfaces with appropriate metal ions. An important motivation for such a study is the possibility of interconnecting close-packed nanoparticles assembled on surface/interfaces through transmetallation reactions leading to electrically conducting structures over large length-scales. That this is indeed a realizable goal is indicated by the rod-like structures observed by Bai *et al* in the transmetallation reaction of Co nanoparticles and Au/Pt ions; the rod-like structures were explained to arise due to interconnections formed during transmetallation of

linearly assembled Co nanoparticles in solution [18b]. In this context, the air-water interface can be an excellent candidate to follow in real time transmetallation reactions between hydrophobic nanoparticles assembled in close-packed structures on water and aqueous metal ions present in the subphase.

This chapter deals with the transmetallation reaction between silver nanoparticles and gold ions. Nanoparticles made of silver and gold have been the focus of research for many decades as a result of their intriguing optical properties [19]. Previous studies suggested that the SPR band of spherical silver or gold nanoparticles could only be slightly varied by changing their sizes in the range of 1 to 100 nm [20, 21]. In contrast, the SPR band could be tuned in the spectral region from visible to near-infrared by working with nanoparticles of other morphologies, structures [15a, 22] and compositions [13b].

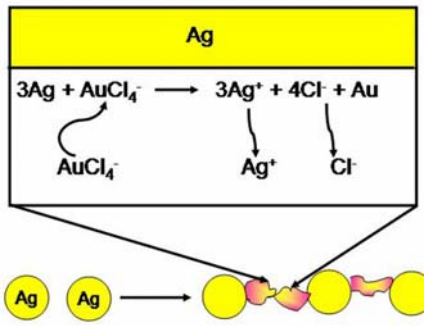

Scheme 5.1 *Illustration of the experimental procedure that generates interconnected bimetallic structures (not to scale)*

In the present work silver nanoparticles are used as sacrificial templates while the chloroaurate ions are chosen as metal ions for the transmetallation reaction. The standard reduction potential of $AuCl_4^-$ / Au redox pair (1.40 V vs. SHE respectively) is higher than that of Ag+ / Ag redox pair (0.80 V vs. SHE). Hence silver particles are immediately oxidized to silver ions when mixed with chloroauric acid ($HAuCl_4$) solution and chloroaurate get reduced immediately to gold [23]. In order to carry out the reaction at the air water interface, either silver nanoparticles or chloroaurate ions were to be hydrophobized. Sastry and co-workers have shown the methodology to hydrophobize the

silver nanoparticles [8d, 24] as well as chloroaurate ions [25]. Scheme 5.1. illustrates the transmetallation reaction.

5.2. Transmetallation at the air-water interface

Aqueous $AuCl_4^-$ in the subphase with hydrophobic Ag nanoparticles

5.2.1 Scheme of work:

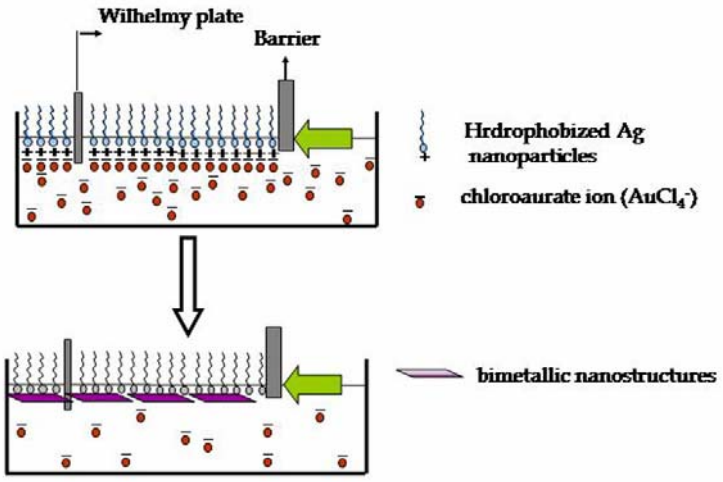

Scheme 5.2 *Schematic of the transmetallation reaction between chloroaurate ions and hydrophobized silver nanoparticles at the air- water interface. (Not to scale)*

In this section, we discuss the reaction of aqueous chloroaurate ions in the subphase with hydrophobic silver nanoparticles constrained at the air-water interface. Consumption of the sacrificial silver nanoparticles leads to the formation of gold nanostructures of interesting morphology at the air-water interface, Scheme 5.2. We noticed that the reaction of subphase chloroaurate ions with the silver nanoparticles is rapid and completes within 15 minutes of spreading the monolayer. In order to modulate the rate of reaction of subphase gold ions with the silver nanoparticles we decided to position a suitable barrier between the nanoparticles and the subphase. Since the reaction involves gold ions, an electrostatic barrier comprised of an ionizable lipid monolayer would be an excellent candidate. Keeping this in mind, we have carried out the transmetallation reaction between hydrophobic Ag nanoparticles and $AuCl_4^-$ ions in the subphase in the presence of a cationic (octadecylamine) and an anionic Langmuir

monolayer (stearic acid). We have tried to show that the transmetallation reaction and thereby the morphology of nanostructures formed at the air-water interface, can be modulated by placing an electrostatic barrier [in the form of Langmuir monolayers of octadecylamine (ODA, cationic) or stearic acid (StA, anionic)] between the hydrophobic silver nanoparticles and the aqueous chloroaurate ions in the subphase.

5.2.2 Synthesis and Characterization

5.2.2.1 Synthesis of hydrophobic silver nanoparticles

Silver nanoparticles capped with octadecylamine (ODA, CH_3-$(CH_2)_{17}$-NH_2 (Ag-ODA) were prepared by taking the tyrosine reduced silver [8d]. In a typical experiment, 10 mL of 10^{-3} M aqueous silver sulphate solution was taken along with 10 mL of 10^{-3} M aqueous solution of tyrosine and the solution was diluted to 100 mL with deionized water. To this solution 1 mL of 10^{-1} M solution of KOH was added and the mixture was allowed to boil until the colorless solution turned yellow, indicating the formation of silver nanoparticles. The pH of silver nanoparticles (25 mL) was adjusted to 5 by using dilute hydrochloric acid (HCl). This solution was taken in a separating funnel and added to 25 mL of 10^{-3} M solution of ODA in chloroform. Vigorous shaking of the mixture results in the quantitative transfer of silver nanoparticles from the aqueous to chloroform phase.

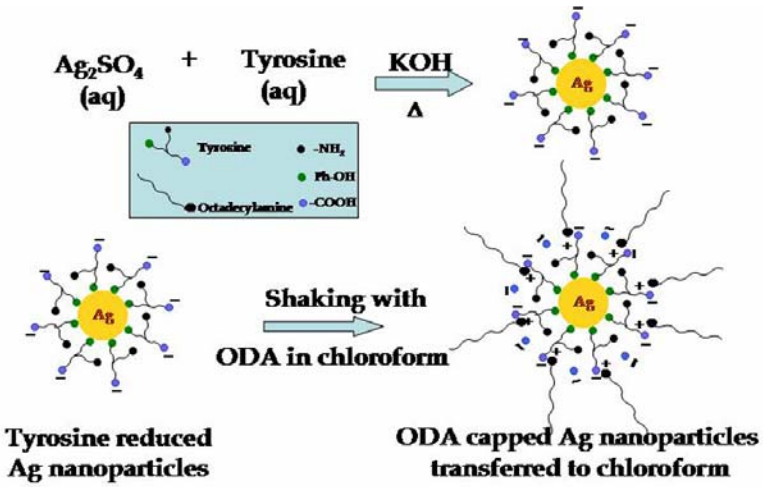

Scheme 5.3 Illustration *of synthesis and hydrophobization of Ag nanoparticles (Not to scale)*

After the completion of phase transfer, the organic phase was separated from the aqueous phase, rotavapped and washed three times with ethanol to remove uncoordinated ODA molecules (if any). The purified and dried powder of ODA-capped silver nanoparticles could be dispersed in a range of weakly polar/non-polar organic solvents, Scheme 5.3.

5.2.2.2 Transmetallation reaction

Transmetallation reaction between ODA-capped silver nanoparticles and aqueous chloroauric acid ($HAuCl_4$) was carried out at the air-water interface using a Nima model 611 LB trough equipped with a Wilhelmy plate as the surface-pressure sensor at room temperature. An aliquot of 100 μL of Ag-ODA nanoparticle solution in benzene at a concentration of 1 mg/mL was spread slowly on to the surface of 10^{-3} M aqueous $HAuCl_4$ subphase. At least 15 min was allowed for solvent evaporation and the monolayer was compressed to a surface pressure of 15 mN/m. At different time intervals of reaction of the ODA-capped silver nanoparticles with $AuCl_4^-$ ions in the subphase, the nanoparticle monolayers were transferred onto carbon-coated copper grids and quartz slides by the conventional LB method.

In presence of ionizable lipid monolayer

Langmuir monolayers of ODA/StA were formed by spreading 75 μL solution of ODA/StA in chloroform (1 mg/mL concentration) on the surface of 10^{-3} M aqueous $HAuCl_4$ subphase. At least 15 min was allowed for solvent evaporation and the monolayer was compressed to a surface pressure of 15 mN/m. 100 μL of Ag-ODA nanoparticle solution in benzene at a concentration of 1 mg/mL was then spread slowly onto the ODA/StA monolayers in a dropwise fashion followed by 15 min of solvent evaporation. At different times of reaction of the ODA-capped silver nanoparticles with $AuCl_4^-$ ions in the subphase, the nanoparticle monolayers were transferred onto carbon-coated copper grids for TEM measurements and quartz slides for UV-vis measurements by the conventional LB method. LB films of Ag-ODA were also formed by nanoparticle organization on deionized water as the subphase under the conditions mentioned above;

this serves as a point of reference and a control. The quartz substrates were hydrophobized prior to transfer of the nanoparticles by deposition of 3 monolayers of lead arachidate onto the substrates. It is known that metal salts of fatty acids (cadmium arachidate, lead arachidate etc.) form stable monolayers strongly bound to substrates with oxide layers and hydrophobization of the support resulted in significantly better transfer ratios of the nanoparticle monolayers. For the LB films grown on different substrates, monolayer transfer was observed both during upward and downward strokes of the substrate at close to unity transfer ratio.

In the series of studies, it would be of interest to study the transmetallation reaction between LB films of Ag-ODA nanoparticles during immersion in $HAuCl_4$ solution. The transmetallation reaction between silver nanoparticles and gold ions was also carried out by first transferring a thick Ag-ODA LB film on quartz (20 ML(monolayer)) followed by immersion in the 10^{-3} M aqueous $HAuCl_4$ solution.

5.2.2.3 Ultraviolet-visible (UV-vis) spectroscopy

The transmetallation reaction between ODA-capped Ag nanoparticles and aqueous gold ions at the air-water interface (with and without the presence of lipid monolayer (ML)) and in $HAuCl_4$ solution (using Ag-ODA film) was monitored by measuring the UV-vis absorption spectra of LB films of the nanoparticles on quartz substrates at different intervals of reaction.

A 20 ML LB film of the silver nanoparticles was transferred from the water subphase onto a quartz substrate and the UV-vis absorption spectrum obtained from this film is shown in Fig. 5.1A (curve 1). A strong absorption band centered at ca. 470 nm is observed from the multilayer Ag-ODA film. This absorption is characteristic of excitation of surface plasmon vibrations in the silver nanoparticles and is responsible for the yellow color exhibited by these films (inset of Fig. 5.1B, slide ‘a’). Well-dispersed silver nanoparticles in water normally show absorption at ca. 420 nm. The red shift in this absorption band in LB films of the nanoparticles indicates assembly of the nanoparticles [26] or anisotropic nanostructures [27] and also the fact that the dielectric properties of the film are significantly different from water. Such shifts have been observed earlier by

Sastry and coworkers [26, 27]. The inference that the particles are in an assembled, close-packed configuration is consistent with the TEM results of monolayer of the Ag-ODA nanoparticles assembled on water (presented later).

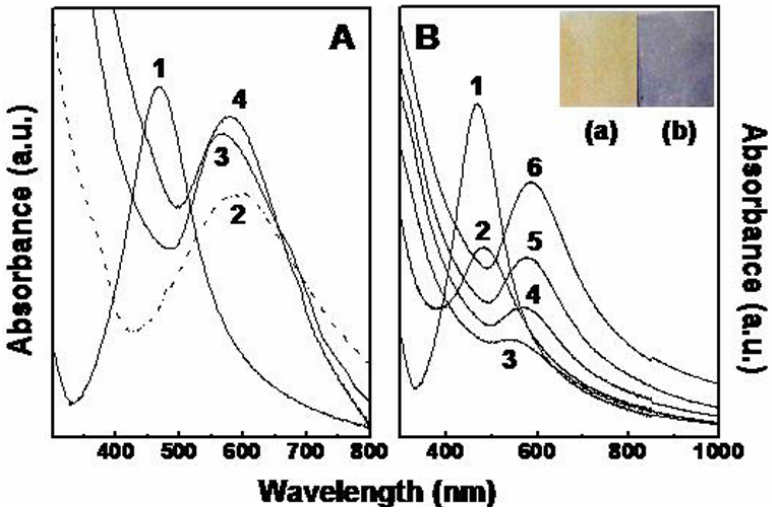

Figure 5.1 *UV-vis absorption spectra recorded from 20 ML of Ag-ODA films lifted by LB technique: (A) curve 1 – on pure water as the subphase; curve 2- after 1 h of reaction of the nanoparticles with 10^{-3} M $HAuCl_4$ solution in the subphase; curves 3,4 - after 1 h of transmetallation reaction on the surface of 10^{-3} aqueous $HAuCl_4$ in presence of StA and ODA monolayers respectively (B) curve 1 – on pure water as the subphase (same as curve 1 in Fig.1A); curves 2-6 – deposited from pure water as the subphase after immersion in 10^{-3} M aqueous $HAuCl_4$ solution for t = 10 min, 1 h, 4h, 12 h and 48 h respectively. The inset in the figure shows photographs of Ag-ODA LB film deposited from pure water as the subphase before (a) and after (b) transmetallation reaction by immersion in 10^{-3} M $HAuCl_4$ for 1 h. The pictures correspond to curves 1 and 6 in the figure respectively.*

The main evidence that the transmetallation reaction has taken place is from the optical properties provided by the UV-vis spectrum, Fig. 1A, curve 2, 3 and 4.

UV-vis absorption spectrum recorded from a Ag-ODA nanoparticle film after 1 h of reaction with aqueous $AuCl_4^-$ ions is shown in curve 2, Fig. 5.1A. The surface plasmon band characteristic of silver nanoparticles (curve 1) is completely damped and is now replaced by an absorption band centered at 588 nm (curve 2). The latter absorption band is a clear indication of the formation of gold nanoparticles by the reduction of subphase $AuCl_4^-$ ions by the silver nanoparticles.

Curve 3, Fig. 5.1A, shows the UV-vis absorption spectrum Ag-ODA nanoparticle film transferred after 1 h of reaction with aqueous $AuCl_4^-$ ions in the presence of a StA

Langmuir monolayer barrier clearly shows a strong absorption band at 578 nm that is also characteristic of gold nanoparticles.

The spectrum recorded from a 20 ML Ag-ODA nanoparticle film transferred after 1 h of reaction with aqueous $AuCl_4^-$ ions in the presence of an ODA Langmuir monolayer barrier is shown as curve 4 in Fig. 5.1A. Complete disappearance of the silver surface plasmon band at 470 nm and appearance of a strong plasmon absorption at 570 nm indicates completion of the transmetallation reaction

The surface plasmon absorption in spherical, non-interacting gold nanoparticles occurs at ca. 520 nm in water. The shift to longer wavelengths observed in the LB films of the silver nanoparticles post transmetallation is similar to that observed by Xia and co-workers in their study of transmetallation of silver nanocubes by gold ions [17]. The red shift in the gold surface plasmon band was explained as arising due to the formation of a thin shell of gold around the sacrificial silver nanocube core and under certain experimental conditions, could extend into the near infrared region of the electromagnetic spectrum [17]. We believe the red shift in the surface plasmon band of gold observed in this experiment may also be explained on the basis of formation of shells of gold around the spherical silver core, evidence for which will be provided in subsequent TEM studies.

We notice that the optical properties of the nanoparticles formed by transmetallation reaction in the presence of StA (Fig. 5.1A, curve 3) and ODA (Fig. 5.1A, curve 4) are rather similar in spite of the fact that the structure of the assemblies as seen using TEM is so different (result presented later). This may be due to the fact that the assembly of the nanoparticles (honey-comb in the case of StA and no regular assembly of ODA barriers) does not play a crucial role in determining the optical properties of the film. In other words, inter-particle interaction via plasmon coupling is negligible and to a large extent, the film properties are determined by the plasmon frequency of the Ag-core-Au-shell bimetallic nanoparticle structure.

The UV-vis absorption spectra recorded from a 20 ML LB film of Ag-ODA nanoparticles measured as a function of time of immersion in 10^{-3} M $HAuCl_4$ solution is shown in Fig.5.1B. It is observed that as the transmetallation reaction proceeds, there is a

progressive decrease in the intensity of the silver plasmon band at 470 nm (curve 2, 10 min of reaction) which is then followed by the appearance of a separate and distinct absorption band from metallic gold nanoparticles at ca. 560 nm after 1 h of reaction (curve 3). Further immersion in the chloroaurate ion solution leads to an increase in the gold plasmon band intensity and small shift in the peak position to 570 nm (curves 4-6). The reaction is complete after nearly 48 h of reaction and is much slower than the transmetallation reaction between the silver nanoparticles and gold ions at the air-water interface. We believe that this difference in reaction rates is due to the fact that the infusion rate of gold ions and effusion of Ag^{+} ions arising from the transmetallation reaction would be much smaller in the case of the LB films of the hydrophobic silver nanoparticles during immersion in chloroauric acid solution. Such a constraint does not occur at the air-water interface where the silver nanoparticles fully access the subphase gold ions with no barrier to metal ion diffusion. The color of this film turned from yellow (inset of Fig 5.1B, a) to a deep blue on completion of reaction with gold ions (inset of Fig 5.1B, b). The blue color indicates the interparticle surface plasmon coupling in a monolayer of gold nanoparticles [26].

5.2.2.4 Transmission Electron Microscopy (TEM)

Ag-ODA nanoparticles LB films were deposited before and after transmetallation reaction at the air-water interface onto carbon-coated copper grids for TEM measurements. Selected Area Electron Diffraction (SAED) patterns were recorded from ensembles of particles under conditions of operating voltage of 120 kV, camera length of 80 cm and with insertion of a 120 μm field limiting aperture.

Fig. 5.2(A,B) show low and high magnification TEM images of a 1 monolayer (ML) LB film of hydrophobic silver nanoparticles (Ag-ODA) transferred from deionized water as the subphase at a surface pressure of 15 mN/m. It is observed from these images that the hydrophobic silver nanoparticles assemble into large two-dimensional domains of hexagonally close packed, nanoparticles on the surface of water. An analysis of the particles in these and other similar images yielded an average nanoparticle size of 20 ± 6 nm.

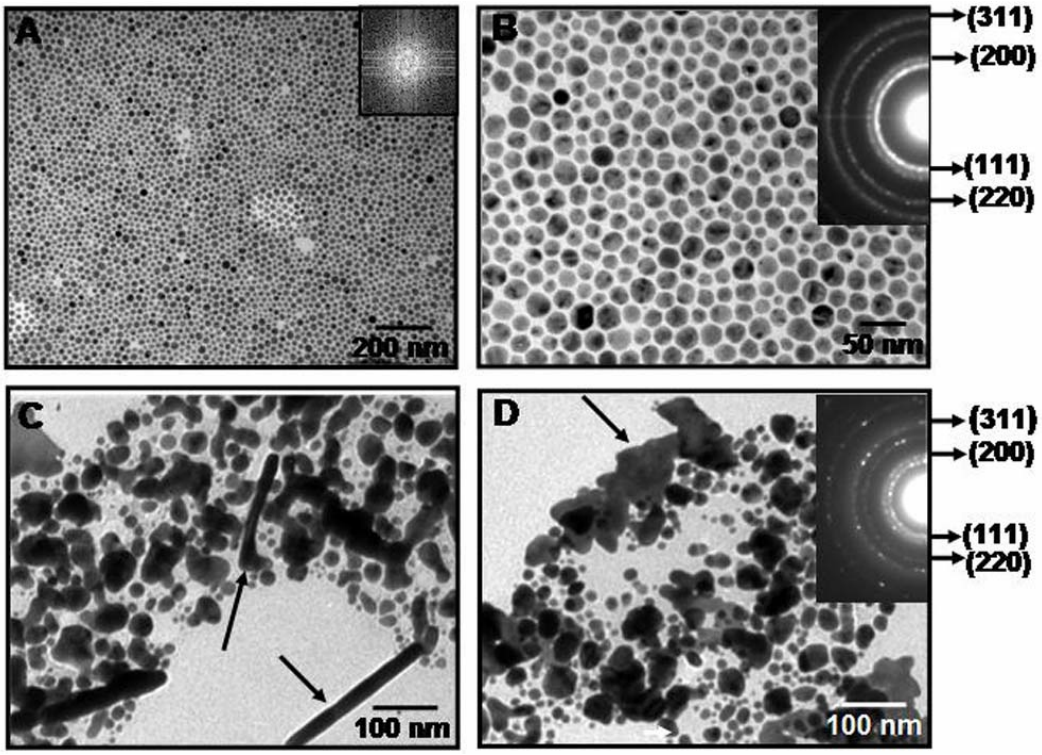

Figure 5.2 *(A,B) Representative low and high magnification TEM images of one monolayer of ODA-capped silver nanoparticles assembled on deionized water and (C,D) on 10^{-3} M $HAuCl_4$ solution after 1 h of transmetallation reaction with subphase $AuCl_4^-$ ions. The insets in A shows the FFT of the arrangement of Ag-ODA nanoparticles on deionized water. Inset of B and D correspond to SAED patterns recorded from the nanoparticles in the main part of the respective figures.*

Inset of Fig 5.2A shows the FFT of the arrangement of hydrophobized silver nanoparticles on the subphase of deionized water. The FFT shows the first and second order rings portraying long range hcp arrangement of the particle on the subphase. The silver nanoparticles are spherical in nature and often show contrast characteristic of multiply twinned particles (MTPs, Fig. 5.2B). The selected area electron diffraction (SAED) pattern recorded from the silver nanoparticles is shown as an inset in Fig. 5.2B. The diffraction rings indicate that the particles are polycrystalline and could be indexed on the basis of the face centered cubic (fcc) structure of silver.

Fig. 5.2(C,D) correspond to representative TEM images of the Ag-ODA nanoparticle Langmuir monolayer recorded 1 h after reaction with the aqueous 10^{-3}M $HAuCl_4$ subphase. It is seen that the morphology of the particles has changed

dramatically; the original close-packed spherical nanoparticulate structure (Fig. 5.2A,B) is now replaced by irregularly shaped particles that show no ordered packing. Clearly, the transmetallation reaction has taken place and the irregular structures arise due to consumption of silver nanoparticles by the reduced gold ions. Occasionally, rod-like and triangular structures similar to those observed by Sastry and coworkers in an earlier study on 4-hexadecylaniline mediated reduction of gold ions [12b] are seen in the film after transmetallation (structures identified by arrows in Fig.5.2C,D). The SAED pattern recorded from the monolayer after the transmetallation reaction is shown as an inset in Fig. 5.2D. The diffraction rings indicate that the particles are polycrystalline and could be indexed on the basis of the fcc structure of gold. As the crystallography of gold and silver is almost identical and we rely on the UV-vis data presented above as an indicator that the transmetallation reaction has occurred and that gold has been deposited on the silver structures.

The reaction of subphase chloroaurate ions with the silver nanoparticles at the air-water interface in the absence of the lipid monolayer is rapid and is complete within 15 minutes of spreading the monolayer.

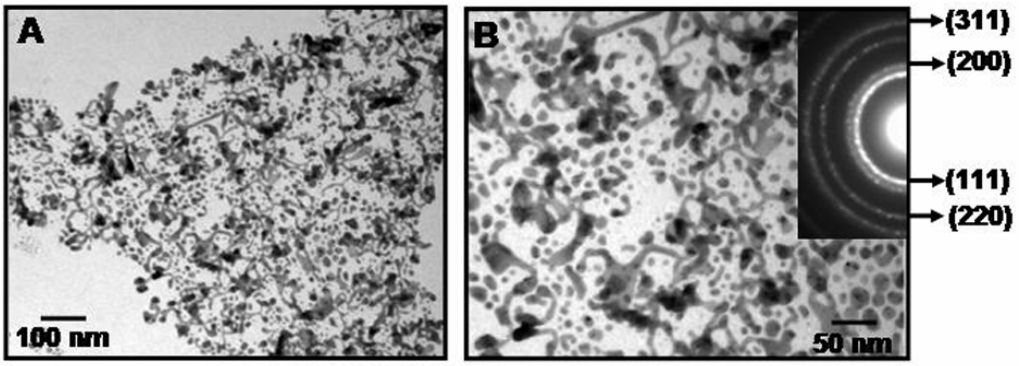

Figure 5.3 *Representative TEM images in (A,B) correspond to ODA-capped silver nanoparticles assembled onto the ODA Langmuir monolayer on the surface of 10^{-3} M $HAuCl_4$ recorded after 1 h of reaction at different magnifications. The inset in B corresponds to SAED patterns recorded from the nanoparticles in the main part of the figures.*

The rate of reaction of subphase gold ions with the silver nanoparticles may be modulated by positioning a suitable barrier between the nanoparticles and the subphase. Since the reaction involves gold ions, an electrostatic barrier comprised of an ionizable

lipid monolayer would be an excellent candidate. With this in mind, we have carried out the transmetallation reaction between hydrophobic Ag nanoparticles and $AuCl_4^-$ ions in the subphase in the presence of a cationic (octadecylamine) and an anionic Langmuir monolayer (stearic acid). One would expect that the presence of the cationic ODA monolayer would result in an increase in the $AuCl_4^-$ counterion concentration at the air-water interface and thus, enhance the rate of reaction of the silver nanoparticles with the gold ions. On the other hand, anionic StA would lead to a reduction of $AuCl_4^-$ co-ion concentration at the air-water interface and slow down the reaction. Fig. 5.3**(**A,B**)** show representative TEM images recorded from the hydrophobic Ag nanoparticle Langmuir monolayer after 1 h of reaction in the presence of an ODA barrier monolayer. The transmetallation reaction in this experiment leads to the formation of a large percentage of elongated and twisted worm-like nanostructures. Clearly, the ODA Langmuir monolayer does not impede the reaction between the gold ions and hydrophobic silver nanoparticles and to a large extent, it rather appears to promote the formation of high aspect ratio nanoparticles most likely due to metallic cross-linking due to the transmetallation reaction. The selected area electron diffraction (SAED) pattern recorded from the monolayer after the transmetallation reaction is shown as an inset in Fig.5.3B; the diffraction rings could be indexed on the basis of the fcc structure of gold subject to the caveat mentioned earlier.

As seen earlier in the UV-vis absorption spectrum **(**curve 4 in Fig. 5.1A**),** **c**omplete disappearance of the silver surface plasmon band at 470 nm and appearance of a strong plasmon absorption at 570 nm indicates completion of the transmetallation reaction and we can say that the elongated structures seen in the TEM images (Fig. 5.3A**,**B**)** are due to metallic gold. Attempts were made to follow the kinetics of reaction in this experiment. These experiments (TEM measurements of the silver nanoparticle monolayer at times smaller than 10 minutes) did not show significant differences in the nanoparticle structure at reaction times ~ 10 minutes.

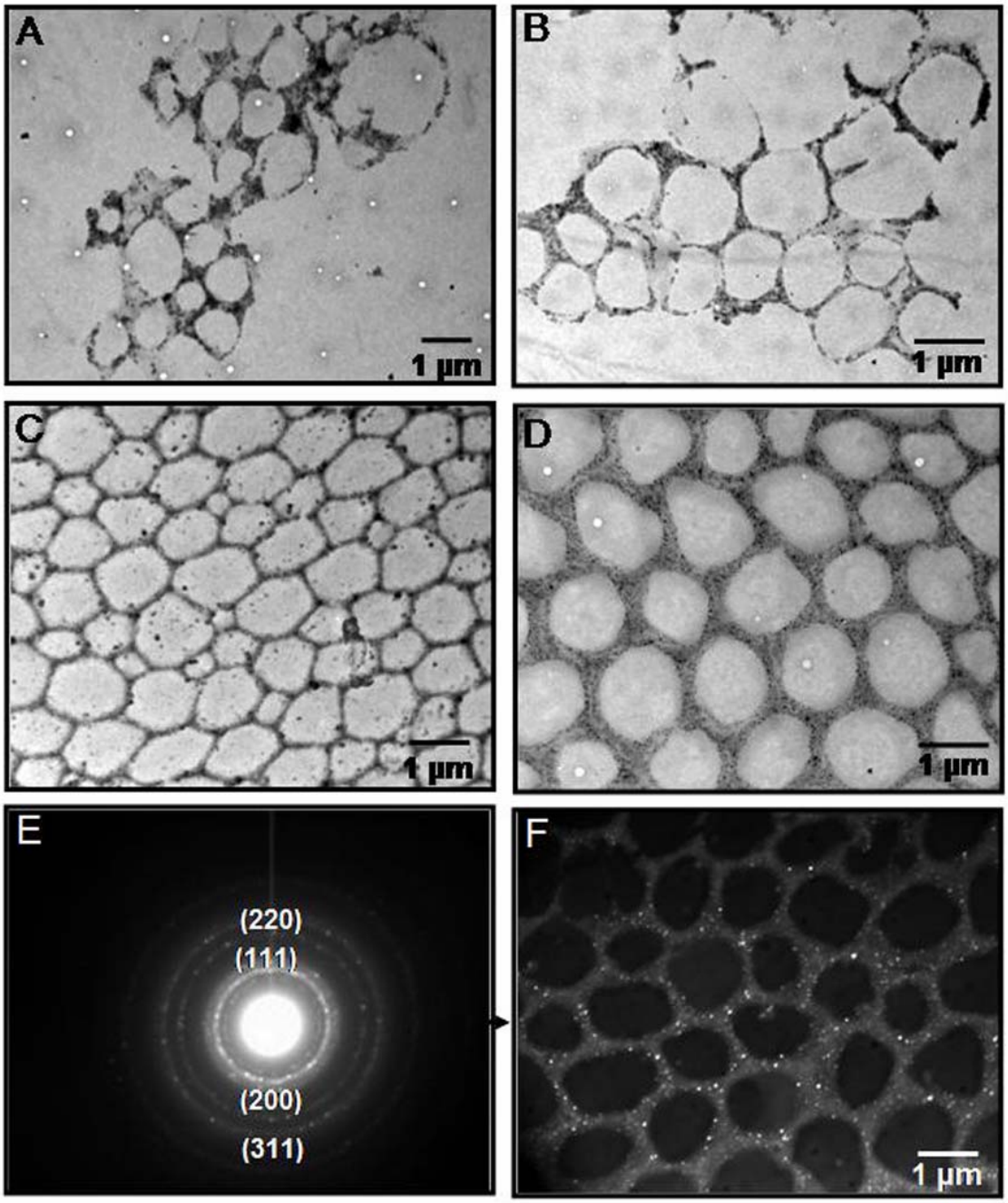

Figure 5.4 *Representative TEM pictures of Ag-ODA nanoparticles as a function of time of reaction with 10^{-3} M subphase $AuCl_4^-$ ions in the presence of StA as a barrier; A-D : times of reaction t = 15 min, 1 h, 2 h and 3 h respectively. (E) correspond to SAED patterns recorded from the nanoparticles in figure D. (F) Dark field TEM images recorded by selecting the electrons scattered to (111) angular range showing that the particles forming the walls of honeycomb are polycrystalline.*

The reaction between subphase gold ions and Ag-ODA nanoparticles in the presence of the anionic Langmuir monolayer, stearic acid, resulted in the formation of structures that were significantly different than those obtained with and without ODA as a barrier. Due to slowing down of the reaction for the electrostatic reasons discussed above, the kinetics of reaction could also be followed. Fig. 5.4A-D show representative TEM images recorded from the Ag-ODA nanoparticles after 15 min, 1 h, 2 h and 3 h of reaction respectively with 10^{-3} M aqueous $HAuCl_4$ in the subphase in the presence of StA as a barrier. It is observed that at the beginning of the reaction, the particles assemble into rudimentary open, ring-like structures (Fig. 5.4A,B) which then close up to form honey-comb like nanoparticle patterns towards the completion of the reaction (Fig. 5.4C,D). The low and high magnification images of the Ag-ODA nanoparticles after 3 h of reaction with $AuCl_4^-$ subphase illustrate this point better. The honeycomb-like patterns are seen to be composed of nanoparticles of dimensions 10 – 18 nm along the periphery while the gaps in the structures are devoid of nanoparticles. The assembly of nanoparticles along the periphery of the honeycomb pattern is truly long-range and extends well upto 80-100 μm in length.

Unlike in the previous cases (reaction of Ag-ODA nanoparticles directly with subphase gold ions and in the presence of ODA Langmuir monolayer), elongated, coiled structures are not seen in this case. The only evidence that the transmetallation reaction has taken place is from the optical properties of a 20 ML LB film of these Ag-ODA nanoparticles (curve 3, Fig. 5.1A). The SAED pattern recorded from the reacted gold nanoparticles in the presence of StA is shown in Fig. 5.4E. The ring pattern suggests that the particles are polycrystalline and they could be indexed on the basis of the fcc structure of gold/silver. The dark field image of the honeycomb arrangement of the particles taken by selecting the electrons scattered to (111) plane is shown in Fig. 5.4F. The image reinforces the polycrystalline nature of the particles as we see that only a part of the particles is bright in the selected angular range.

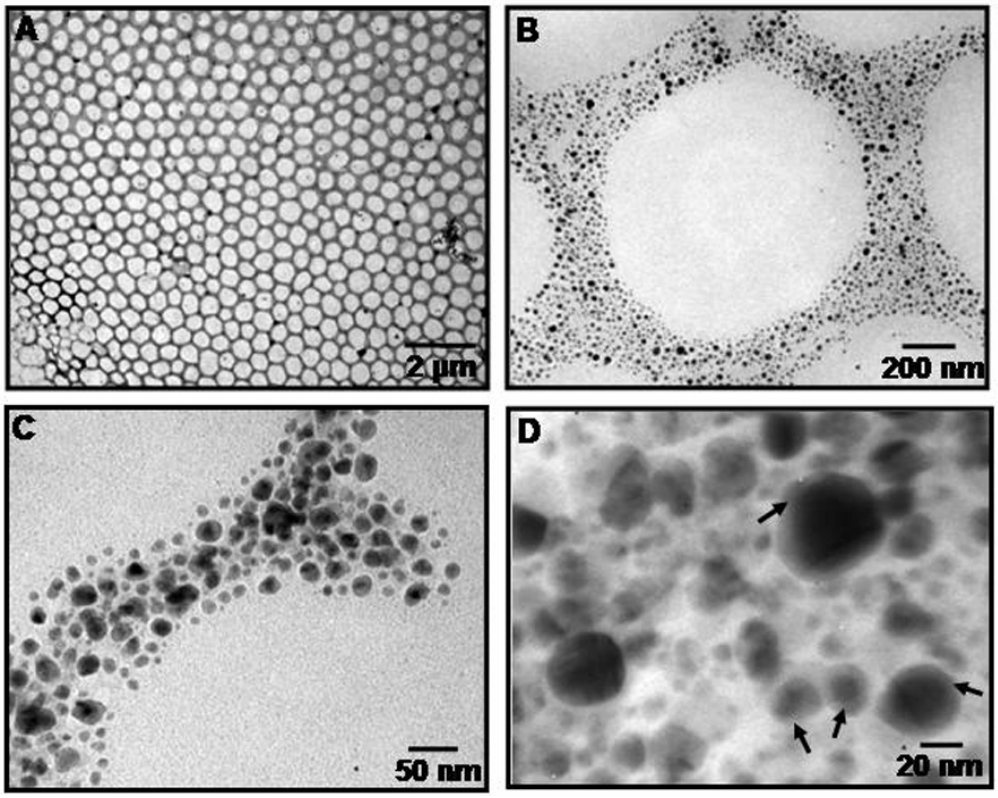

Figure 5.5 *(A-B) Representative TEM images at low and high magnification recorded from Ag-ODA nanoparticles after 3 h of reaction with subphase 10^{-3} M $AuCl_4^-$ ions in the presence of the StA barrier. (C-D) Representative TEM images at low and high magnification of the walls of the honeycomb structure.*

Fig 5.5(A-D) shows the images of the perfect honeycomb formed in the presence of the StA monolayer at different magnifications. It is clearly seen that the walls are made up of bimetallic structures formed as a result of the transmetallation reaction. Fig 5.5D clearly shows the formation of core-shell like structures also in the walls of the honeycomb (indicated by arrows) after the galvanic exchange reaction.

There could be a number of reasons for the honeycomb structures formed. One is that the transmetallation reaction leads to assembly into such structure while the second possibility is that there is a separation of the Ag-ODA and StA phases; the transmetallation reaction then proceeds along the Ag-ODA rich phases (which in this case, is the honeycomb pattern). Yet another possibility is that the transmetallation reaction itself drives the phase separation.

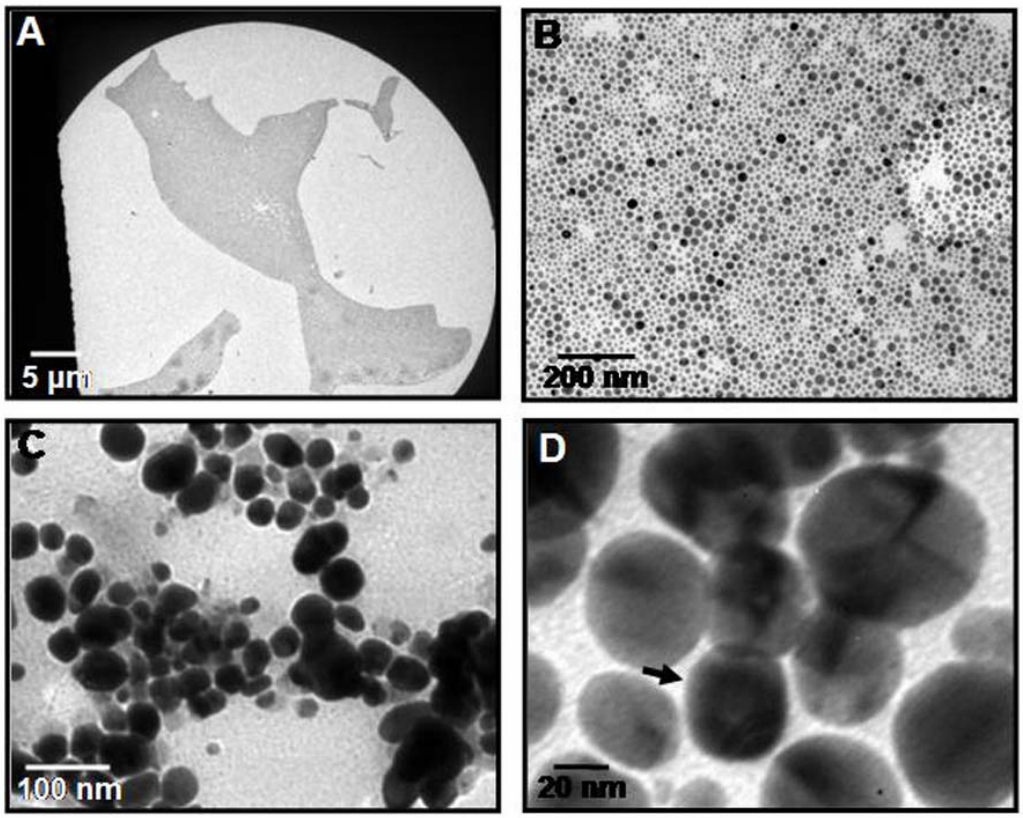

Figure 5.6 *(A, B) Representative TEM images at different magnifications of one ML of Ag-ODA recorded 1 h after spreading the ML on the surface of pure distilled water (pH adjusted to 3 by dil. HCl) in the presence of StA. (C, D) Representative TEM images of Ag-ODA nanoparticles after reaction with aqueous 10^{-3}M chloroaurate ions by immersion of a 20 ML Ag-ODA LB film in gold ion solution for 48 h and thereafter dissolved in chloroform.*

In order to test this hypothesis, Ag-ODA nanoparticles were spread on the surface of deionized water held at pH 3.4 (pH close to that of the 10^{-3} M $HAuCl_4$ solution, pH adjusted using dil. HCl) in the presence of StA and then lifted onto a TEM grid. Fig. 5.6A,B shows the representative TEM images from this monolayer. It is clear that there is no evidence for a honeycomb structured assembly of the silver nanoparticles and in most respects, the images resemble those recorded from the nanoparticles spread directly onto water (Fig. 5.2A,B). This control indicates that the honeycomb assembly of the nanoparticles is driven by the transmetallation reaction between the silver nanoparticles and the subphase $AuCl_4^-$ ions. The fact that the particles in the honeycomb structures are not interconnected (Fig. 5.5C and D) suggest that the transmetallation reaction forces the separation of the StA and Ag-ODA phases into the lovely honeycomb pattern observed.

Transmetallation of Ag-ODA films

20 ML (monolayer) Ag-ODA LB film after 48 h of immersion in chloroauric acid solution was dissolved in chloroform and the nanoparticles were imaged by TEM (Fig.5.6C,D). It is observed that the particles are well separated from one another and that the particles are bigger (average size ~ 50 nm) than the as-prepared silver nanoparticles (20 ± 6 nm). This may be attributed to the fact that the AgCl formed after the transmetallation reaction is not able to leach out fully due to the entrapment in the lipid monolayer and stays in the form of solid AgCl. We do not observe any interconnection between the nanoparticles possibly because during immersion of the Ag-ODA LB film in the chloroauric acid solution, the film swells and leads to considerable separation between the silver nanoparticles. Transmetallation thereafter may not be capable of interlinking the nanoparticles and they merely grow in size.

We note that the UV-vis absorption curves recorded from the LB films after transmetallation reaction (Fig. 5.1A, B) shows the absorbance at ca. 580 nm indicative of the formation of gold nanostructures. Usually it is observed that the transmetallation reaction between silver nanoparticles and gold ions either in aqueous [17,18] or organic [28] medium leads to the formation of hollow gold nanostructures. However in the present study the UV-vis spectroscopy results (Fig. 5.1A, B) indicate the formation of either pure solid gold nanostructures or bimetallic nanostructures (gold coated silver cores) [29]. TEM results support the UV-vis spectroscopy data showing the presence of both solid gold (Fig.5.2D, 5.3B, Fig.5.4D) and bimetallic, Au-Ag (Fig.5.5D and Fig. 5.6D, particles indicated by arrows) nanostructures. While the exact reasons for this difference are not understood at this moment, we believe the ODA capping layer surrounding the sacrificial silver nanoparticles may be playing an important role. The ODA monolayer could act as a barrier towards the infusion of $AuCl_4^-$ ions and the effusion of Ag^+ ions during the transmetallation reaction thereby limiting the reaction to the stage where only a thin shell of gold is formed around the silver core. It is known that a gold shell of 3-5 atomic layers is sufficient to damp the surface plasmon vibrations of

the underlying silver core completely [2b,c] and could thus explain the UV-vis spectroscopy trends observed.

We note that in these experiments, the transmetallation reaction between the silver nanoparticle surface and aqueous gold ions takes place even though a hydrophobic sheath of ODA molecules surrounds the particles and in some of the examples, an additional barrier to ion transport in the form of ODA and StA monolayers is present. The galvanic exchange reaction between dodecylthiolate-monolayer protected Ag clusters and gold ions leading to the formation Ag-Au bimetallic nanoparticles has been reported previously by Murray and coworkers [30]. Taken together with the findings of this study, it is clear that the transmetallation reaction can proceed even in the presence of a barrier to ion transport, reasons for which need to be elucidated.

The silver ions formed as a consequence of the transmetallation reaction are expected to dissolve in the subphase. However, the concentration of the Ag^+ ions was found to be below the detection limits of atomic absorption spectroscopy.

5.2.2.5 Current-voltage (I-V) measurements

The TEM images shown in Fig. 5.3(A, B) indicate the formation of elongated and coiled nanostructures most likely due to metallic cross-linking of the sacrificial silver nanoparticles after the transmetallation reaction in the presence of ODA monolayer; the formation of these interlinked structures was further confirmed by electrical transport measurements.

The silver nanoparticle film as well as the bimetallic film obtained by transmetallation reaction were deposited onto quartz substrates by vertical lifting and were allowed to dry. After thorough drying, the nanoparticles films were used for I-V measurements. Electrodes of 1 mm width were painted at the opposite ends of the nanoparticulate films using conducting silver paste as thick pads to ensure proper electrical contact. The separation between the electrodes was 10 mm. The I-V characteristics were measured in the sweep mode at a voltage increment of 5 V in the range of –40 to + 40 V.

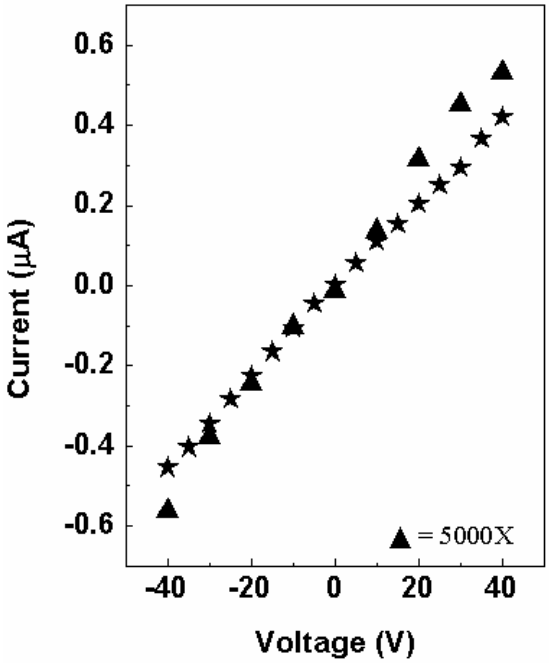

Figure 5.7 *I-V characteristics of 60 ML of LB film of silver nanoparticles deposited by vertical lifting on quartz substrate before (triangles) and after (stars) transmetallation reaction. The current values in the plot obtained before transmetallation reaction (triangles) have been multiplied by a factor of 5000 to bring the values on the same scale as the recorded from the film after transmetallation (stars).*

Fig. 5.7 shows the current vs voltage (I-V) plots of 60 ML LB film of silver nanoparticles before (triangles) and after (stars) the transmetallation reaction. The I-V plot is fairly linear in both the cases, however the resistance of the film after the transmetallation reaction reduces by an order of 5 x 10^3 (the current values recorded for the LB film before transmetallation have been multiplied by a factor of 5000 in this plot). The significant drop in the film resistance after transmetallation is a clear indication of the formation of elongated structures leading to electrical interlinking of the silver nanoparticles observed in the TEM images (Fig. 5.3A, B). The I-V measurements were carried out after thorough drying of the films in a dehumidified atmosphere at different sweep rates and different voltage increments. We did not observe a detectable difference in the I-V plots under these different experimental conditions and believe, therefore contributions due to water etc. to the electrical conduction may be ruled out.

Thinking about the possibility of van der Waals or physical interaction between the particles, conductivity measurements were also done for the LB films deposited after transmetallation reaction in the presence of StA monolayer. However, increase in the conductivity of the film was negligible and nowhere comparable to that obtained in case of transmetallation in presence of the ODA monolayer**.**

5.2.2.6 Conclusion

We have shown that facile transmetallation reaction between hydrophobic silver nanoparticles and aqueous chloroaurate ions can be carried out at the air-water interface. Such reactions with nanoparticles assembled into close-packed structures at interfaces could lead to metallic cross-linking of the nanoparticles and synthesis of extended nanoparticulate structures as shown. In the presence of suitable electrostatic barriers, the assembly of the nanoparticles after transmetallation reaction leads to interesting honeycomb-like superstructures. The possibility of connecting nanoparticles in close proximity via electrical contacts shows potential for generation of conducting electrodes with nanoparticles as building blocks and in the design of optical coatings and chemical/biological sensor.

5.3 Transmetallation at Liquid-liquid interface

5.3.1 Introduction

Films of close-packed metal nanoparticles can be achieved via self-assembly of metal nanoparticles from organic media onto solid supports [31]. However, the formation of dense films of metal nanoparticles from aqueous nanoparticle dispersions is often difficult to obtain [32]. Previous reports have shown that the surface coverage of gold nanoparticles adsorbed from aqueous solution onto substrates is less than about 30% [32b, 33]. A common approach to increase the nanoparticle loading on surfaces includes using additional linker molecules to bind extra nanoparticles to the surface [32a, 33a, 34]. Recent efforts toward controlling the physical and chemical properties of nanostructured materials through molecular-level design have generated enormous interest in thin films comprised of organically encapsulated metal nanoparticles. In several reports, it has been

shown that the optical and electronic properties of such films can be tuned by varying the size of the metal nanoparticles [35]. An interesting application of metal nanoparticle/organic films is their use as chemiresistor-type [36] gas sensors. As a first example, Wohltjen and Snow [36b] reported that films from octanethiol-stabilized Au nanoparticles respond with a fast, reversible, and very sensitive increase of their resistance when exposed to vapors of toluene or tetrachloroethylene (TCE). Meanwhile, other reports have appeared showing that the selectivity of such sensors can be tuned by introducing chemical functionality into the organic shell encapsulating the nanoparticles [36a, c-d].

Nanoparticles containing two metals (bimetallic nanoparticles) are also of great interest since they can exhibit catalytic [37], electronic [38], and optical properties [39] distinct from those of corresponding monometal nanoparticles [40]. Unsupported bimetallic nanoparticles have been prepared by reductive deposition of one metal onto a nanoparticle of another metal [41], simultaneous reduction of salts of two different metals (with or without protecting ligands being present) [42], and laser-induced melting [43]. Depending on the preparation method, either alloy or layered (core-shell) nanoparticles can be synthesized [41-43]. Galvanic reactions between metal nanoparticles and a salt of a more noble metal are another route to alter the nanoparticle's metallic composition.

In the following section, we demonstrate that close packing of metal nanoparticles may be achieved by a simple reaction without using linkers where tyrosine-reduced silver nanoparticles were stirred with dodecylamine in chloroform. The silver nanoparticles form a film at the liquid- liquid interface which on further analysis shows closely packed silver nanoparticles in the form of a monolayer. Thereafter, a transmetallation reaction was carried out on the film of silver nanoparticles at the interface with aqueous gold ions resulting in a bimetallic film, which showed profuse interconnections. The goal of our present study was also to investigate systematically how the particle arrangement, composition, I-V characteristics, and vapor-sensing properties of silver nanoparticle films vary with transmetallation. The nanoparticle films were prepared via layer-by-layer self-assembly and various characterizations were done which include the structure and

chemical composition analysis of the films. The application of these bimetallic films in vapor sensing was also pursued where the films showed excellent sensitivity to the ammonia vapors.

5.3.2 Synthesis and Characterization

5.3.2.1 Synthesis and phase transfer of Tyrosine-reduced silver nanoparticles

Silver nanoparticles were prepared as by tyrosine reduction [8d] as described in section 5.2.2. For the phase transfer of Ag nanoparticles, 50 mL of an aqueous dispersion of silver nanoparticles were taken along with 50 mL of 10^{-3} M solution of dodecylamine (DDA, CH_3-$(CH_2)_{11}$-NH_2) in chloroform in a Teflon beaker. Vigorous shaking of the mixture results in the formation of thin film of silver nanoparticles at the liquid-liquid interface, scheme 5.4; this is seen as a formation of a silver color band covering the aqueous phase from all sides. The colorless chloroform phase is seen separately, Fig 5.8A. Unlike octadecylamine, which was used to phase transfer the tyrosine reduced silver from aqueous to organic phase by forming the reverse micelles as described in the previous section, here we observe that the dodecylamine capped silver nanoparticles get assembled at the interface. This may be because of the alkaline pH 10 of the solution, due to addition of KOH. The amine group is not fully protonated at this pH to form a strong electrostatic bond with the silver nanoparticles and result formation of an assembly at the interface.

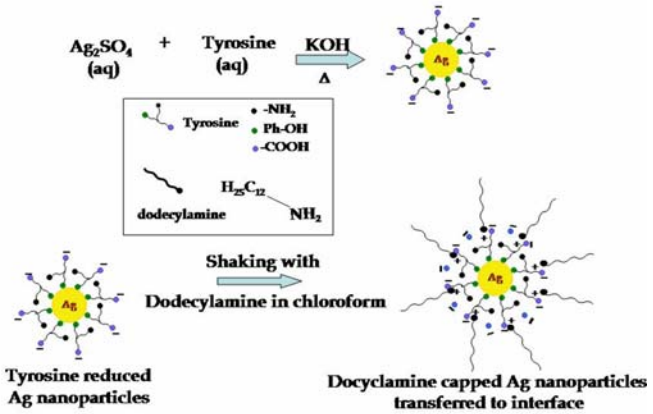

Scheme 5.4 *Schematic of synthesis and hydrophobization of Ag nanoparticles.(Not to scale)*

The same experiment was done using a glass beaker and it was observed that this leads to the formation of a film of Ag nanoparticles at the liquid-liquid interface but the film surrounds the organic phase and not the aqueous phase in this case, Fig 5.8B. The behavior can be explained in terms of glass surface (silicon) having a net negative charge, as the surface of native silicon is hydrophilic consisting of SiO_2 and Si-OH group and thus leading to electrostatic attraction with the positive charges Ag silver nanoparticles whereas the Teflon surface is hydrophobic and the silver film does not come in contact with the organic part and stays in the aqueous region only. The experiment was also repeated using dodecylamine in toluene phase in a teflon beaker, Fig 5.8C.

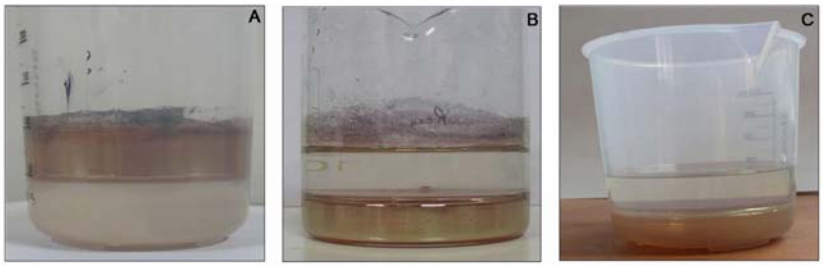

Figure 5.8 *(A) Picture showing silver film at the liquid-liquid interface using dodecylamine in chloroform in Teflon beaker. (B) Picture showing silver film at the liquid-liquid interface using dodecylamine in chloroform in glass beaker. (C) Picture showing the silver film at the liquid-liquid interface using dodecylamine in toluene in Teflon beaker.*

5.3.2.2 Transmetallation reaction

Hydrophobic Ag nanoparticles with aqueous $AuCl_4^-$ at liquid-liquid interface

The clear aqueous solution was drained carefully from the top of the film formed at the interface of chloroform and aqueous phase. Thereafter the transmetallation reaction between exposed film of silver nanoparticles and aqueous chloroauric acid ($HAuCl_4$) was carried out by injecting 5 ml of 10^{-3} M $HAuCl_4$ so that its effective ion concentration is 10^{-4}M in the entire solution, Scheme 5.5. After five minutes of injection, the nanoparticle monolayers were transferred onto carbon-coated copper grids for TEM measurements and quartz slides for UV-vis measurement by vertical lifting. The quartz substrates were rendered hydrophobic prior to transfer of the nanoparticles by deposition of 3 ML of lead arachidate onto the substrates.

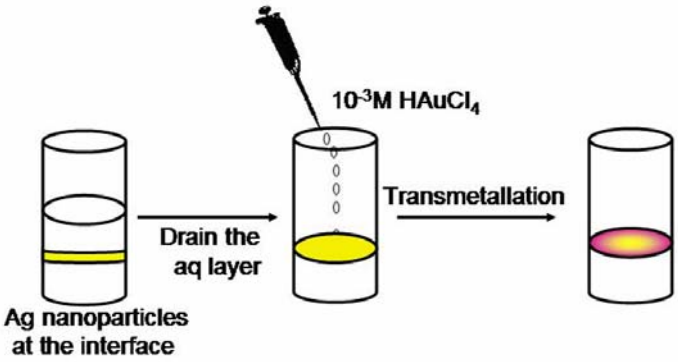

Scheme 5.5 *Illustration of the transmetallation reaction between chloroaurate ions and hydrophobized silver nanoparticles at the liquid-liquid interface (Not to scale)*

5.3.2.3 Ultraviolet visible (UV-vis) spectroscopy

The optical properties of the tyrosine-reduced silver nanoparticles, the Ag film at liquid-liquid interface and the Au-Ag film after transmetallation at the liquid-liquid interface were studied to ascertain the reduction of gold ions by the sacrificial silver nanoparticles. Fig 5.9 shows the UV-vis spectra recorded from aqueous solutions of tyrosine-reduced silver nanoparticles (curve 1), 10 ML of the silver film formed at the liquid-liquid interface (curve 2) and 10 ML of the Ag-Au bimetallic film formed at the liquid-liquid interface after the transmetallation reaction after the addition of the chloroaurate ions (curve 3). The strong absorption at ca. 415 nm in curve 1 is the characteristic of silver nanoparticles and clearly indicates the formation of silver nanoparticles. This absorption arises due to excitation of surface plasmon in the silver nanoparticles [8d]. The broad absorption band at 620 nm in curve 2 is due to the coupling of the surface plasmon in the close packed structure of silver nanoparticles in the film at the interface. Well-dispersed silver nanoparticles in water normally show absorption at ca. 400 nm, however the red shift in the absorption band of silver film in curve 2 indicates assembly of the silver nanoparticles at the liquid-liquid interface [26]. The absorption band at around 640 nm in curve 3 after the transmetallation reaction is due to the formation of gold and silver interlinked structures [29].

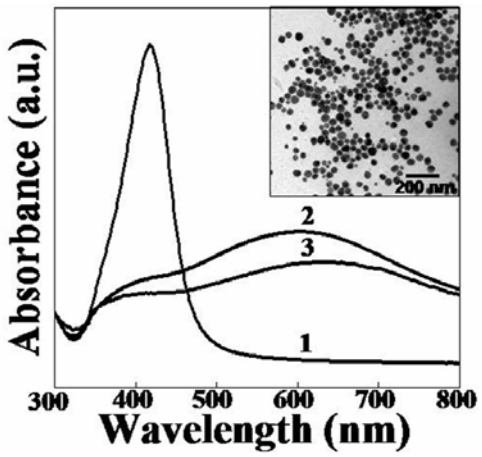

Figure 5.9 *UV-vis absorption spectra of the tyrosine-reduced silver nanoparticles in aqueous medium curve1. Curve 2 corresponds to the spectra of silver nanoparticles film formed at the interface using dodecylamine in chloroform while curve 3 shows spectra of Ag-Au bimetallic film after transmetallation reaction. The inset shows the tyrosine-reduced silver nanoparticles in aqueous medium.*

The inset in Fig 5.9 shows the TEM micrograph of the tyrosine-reduced silver nanoparticles and it can be clearly observed that the nanoparticles which are well separated from each other with little evidence for aggregation. The silver film formed at the interface showed a reddish tint, which is found in case of aggregated silver nanoparticle solution wherein the surface plasmon shows a red shift as oppose to the characteristic absorption at 420 nm [44]. This result is in agreement with the UV-vis spectra which show an absorbance at 620 nm (Fig 5.9 curve 2).

5.3.2.4 Transmission Electron Microscopy (TEM)

TEM measurements of Ag nanoparticles films deposited before and after transmetallation reaction at the liquid-liquid interface were performed by picking up the film by vertical dipping of the 400 mesh carbon-coated copper grids. Fig 5.10A shows the TEM micrograph of the tyrosine-reduced silver nanoparticle film at the liquid-liquid interface. When aqueous solution of tyrosine-reduced silver nanoparticles is stirred with the dodecylamine solution in chloroform, the particles assemble in a close knit fashion at the liquid-liquid interface. The image emphasizes the length of film that can be deposited on the substrate. We do see some crack pattern in the film which develops on the

evaporation of the solvent, due to the adhesion of the film to the substrate. The TEM image reveals that the silver nanoparticles are confined in a two dimensional fashion at the interface forming a densely packed assembly. Fig 5.10(A-B) shows low magnification image of the same film, which shows that the film is continuous up to 35μm length and is, made up of densely packed silver nanoparticles, having no significant packing arrangement [5.10B]. Fig 5.10C shows a magnified image, which clearly reveals that the silver nanoparticles are spherical and poly disperse in nature with most of the particles showing contrast characteristic of multiply twinned particles (MTPs). It is worth noticing that the silver particles at the interface are densely packed but not aggregated. This may be due to the hydrophobic sheath of dodecylamine molecule on the nanoparticles. The interparticle separation between the particles can be calculated using the digital micrograph software and it is found to be 2.6 ± 0.5 nm. The size of the Ag particles in the film at the interface is 30 ± 2 nm.

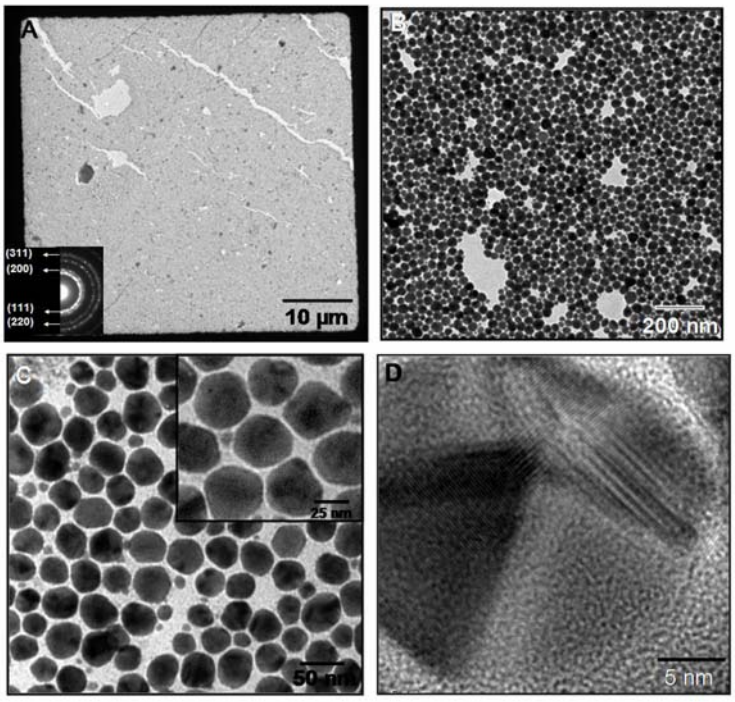

Figure 5.10 *TEM micrograph at different magnifications, of the silver nanoparticle film at the interface in an aqueous-dodecylamine in chloroform biphasic system (A). Low magnification image (B) the dense arrangement of the silver nanoparticles in the film. (C) High magnification of silver nanoparticles. (D) A HRTEM image of a single tyrosine reduced dodecahedron silver nanoparticle. The inset in (A) shows the SAED pattern from the silver nanoparticles*

The selected area electron diffraction (SAED) pattern recorded from the silver nanoparticles is shown as an inset in Fig. 5.10A. It can be easily concluded from the SAED pattern that the silver nanoparticles are polycrystalline in nature with "d" values matching the face centered cubic (fcc) structure of silver and shows the Braggs reflection corresponding to (111), (200), (220) and (311) hkl planes. The diffraction of the single particle could not be done as the probe size is bigger than the particle. Fig 5.10D show the HRTEM image of one of the Ag-ODA particles. It can be clearly seen that the particle is dodecahedron. We can see the presence of the {111} planes, emphasizing the twining.

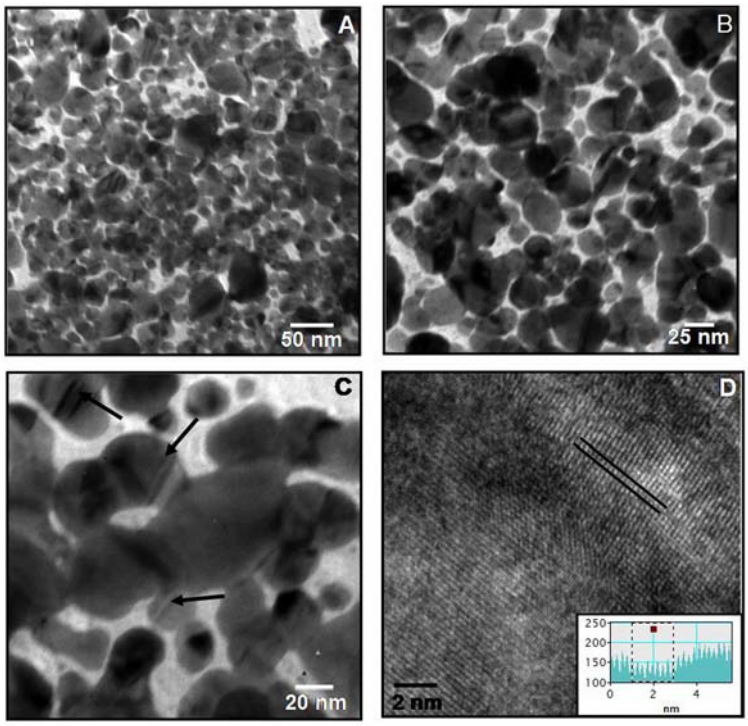

Figure 5.11 *TEM micrograph at different magnifications of Ag-Au bimetallic nanoparticles film formed at the liquid-liquid interface. (A-B) A low and high magnification image showing the extent of interconnections. (C) Micrograph of Ag-Au bimetallic nanoparticles film showing the Moiré fringes and strain patterns in the thin interconnections (indicated by arrows). (D) A HRTEM image of the interconnections showing the lattice, which can be measured to 0.234 nm, inset shows the profile of the region indicated in the image.*

Fig. 5.11A-D correspond to representative TEM images of the film ten minutes after reaction with the aqueous $HAuCl_4$, which was injected at the interface, on the already formed silver film at two different magnifications. It is seen that the morphology

of the particles changes dramatically. The original close-packed spherical silver nanoparticulate structure (Fig. 5.10A) is now replaced by highly irregular interlinked structures. Fig 5.11 shows interconnected structures at different magnifications. Clearly, the transmetallation reaction has taken place and the irregular interlinked structures have risen due to the reduction of the gold from its ionic form at the expense of silver nanoparticles. From the presence of strain pattern on some structures and Moiré fringes (due to overlapping of two ribbon like structures) at some places in Fig 5.11C, it can be inferred that these structures are not very thick. Fig 5.11D shows the HRTEM image of one of the interconnected structures. From the profile in the inset of the region marked in the image, one can measure the lattice distance to be 0.234 nm, corresponding to [111] plane of silver or gold.

The TEM results are in accordance with the UV-vis spectra obtained from the Ag-Au bimetallic film (fig 5.9, Curve 3), which showed no silver peak at around 420nm but showed an absorbance at around 640nm. Usually the spherical gold nanoparticles show an absorbance at around 520nm; however, here the interlinking of the particles results into the red shift of the longitudinal plasmon due to incorporation of some extent of asymmetry. Thus, we obtain a peak at around 640 nm.

5.3.2.5 XPS measurements

XPS measurements of tyrosine reduced Ag nanoparticles assembled at the interface before and after transmetallation cast in the form of films onto Si (111) substrate by vertical lifting (30 ML thickness) were carried out to confirm the reduction of gold from its ionic form. The general scan and the C 1s, O 1s, Ag 3d, and Au 4f core level spectra were recorded with un-monochromatized Mg Kα radiation (photon energy) 1253.6 eV at a pass energy of 50 eV and electron take off angle (angle between electron emission direction and surface plane) of 60°. The overall resolution of measurement is thus 1 eV for the XPS measurements. The core level spectra were background-corrected using the Shirley algorithm [45], and the chemically distinct species were resolved using a nonlinear least squares procedure. The core level binding energies (BEs) were aligned with respect to the C1s binding energy (BE) of 285 eV.

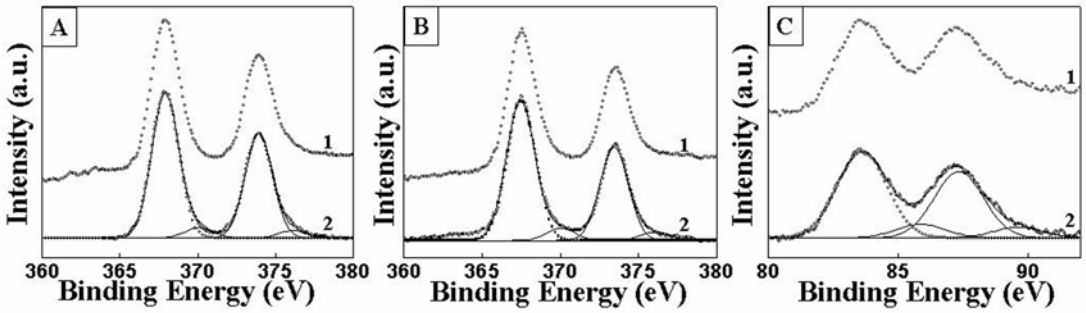

Figure 5.12 *(A) Ag 3d core level spectra from the sliver film has been shown with the spin orbit component. Curve 1 shows the raw data with charge correction while curve 2 shows the baseline and charge corrected data. (B) Silver (Ag 3d) core level spectra from Ag-Au bimetallic film has been shown with the spin orbit component. Curve 1 shows the raw data with charge correction while curve 2 shows the baseline and charge corrected data. (C) Gold (Au 4f) core level spectra from Ag-Au bimetallic film has been shown with the spin orbit component. Curve 1 shows the raw data with charge correction while curve 2 shows the baseline and charge corrected data.*

Fig 5.12 shows the spectra of the core levels of silver film as well as the Ag-Au bimetallic film to observe the composition of the films. Fig 5.12A shows the Ag 3d core level spectrum recorded from the silver film which could be decomposed into two chemically distinct species with Ag $3d_{5/2}$ and BEs of 368 and 370.2 eV that are assigned to metallic silver (Ag^0) and unreduced silver ions (Ag+), respectively, indicating that a small percentage of unreduced silver ions are present. Fig 5.12B shows the Ag 3d core level spectrum recorded from the film deposited after transmetallation reaction has taken place and here as well we obtain similar result where in the spectra can be resolved into two distinct peaks which correspond to the binding energies of 368 and 370.2 eV as obtained in case of the silver film. The slope of the background data is more in the case of Ag 3d curve recorded from Au-Ag bimetallic film as compared to the pure silver film, indicating the reduction of gold on the surface of silver nanoparticles. The TEM rules out the formation of core shell nanoparticles and thus, we can infer from the data that we are getting essentially Ag-Au bimetallic nanostructures [46]. Fig 5.12C shows the Au4f core level spectrum recorded from the film that can be deconvoluted into two spin–orbit pairs (splitting 3.7 eV). Two chemically distinct Au $4f_{7/2}$ components are observed at 83.8 and 86 eV binding energies. The lower BE component is attributed to binding energy from Au^0 metal in the film while the high BE component arises from unreduced Au^{3+} ions in

the film [47] indicating that a small fraction of the $AuCl_4^-$ ions remain in the solution. Thus, the XPS study reveals the presence on silver as well as gold in the film after the transmetallation reaction suggesting that not all the silver is consumed in the reaction and we have silver in the Ag^0 and gold in Au^0 state. Thus, what we achieve by this reaction is the silver nanoparticles interlinked by gold atoms which are reduced on the surface of the existing silver nanoparticles.

5.3.2.6 I-V Measurements

5.3.2.6.1 Experimental details

All the electrical measurements were done using quartz as solid substrate. 10 layers of the Ag film from the interface was deposited on the substrate and used as control for baseline resistance/conductance measurement. Thick pads of silver paste was painted and allowed to dry for use as electrodes for all the measurement. In order to avoid any contribution from moisture, the film was properly dried under an IR lamp prior to use, all the measurements were redone in desiccators in a moisture free environment and the results were compared for consistency.

For the time dependent electrical conductivity measurements in a controlled environment, a closed glass vessel was used with an inlet and outlet for all the vapors. A program written in Test Point was used for these time dependent conductivity measurements to estimate the response time of the film towards the vapor in question.

The silver film as well as the bimetallic nanoparticle films were deposited onto quartz substrate by vertical lifting and were allowed to dry. The I-V characteristics were measured in the sweep mode in the range of –20 to 20 V in step of 1 V.

5.3.2.6.2 Electrical measurement

The formation of elongated and coiled interlinked nanostructures after the transmetallation reaction was further confirmed by I-V measurements. We believe that if the nanoparticles are interlinked, the conductivity of the film should increase which indeed is the case here. Fig.5.13 shows the current vs. voltage (I-V) plots of a film of silver nanoparticles before (curve 1) and after (curve 2) the transmetallation reaction. It can be seen from curve 1 that film of silver nanoparticles showed ohmic behavior with a

resistance of 334 MΩ, which is very high for metallic nanoparticles. However, when the image showing the nanoparticle film is recollected (Fig. 5.10C), the high resistance value for the film seems obvious. The image clearly shows gaps between the aggregates of silver nanoparticles and thus the conduction across the nanoparticles is by the process of electron tunneling, which is a strong function of the distance between the particles [48]. Thus, the silver nanoparticle film shows a very high value of resistance. The I-V characteristics clearly show a drop in the resistance of the film after the transmetallation reaction, which was found to be more than five orders of magnitude. The resistance of the film of silver particles was 334 MΩ whereas the resistance of the Ag-Au bimetallic film was found to be 7.4 kΩ. Thus, by the transmetallation reaction, we are able to interconnect the preordered closely packed silver nanoparticle films to obtain a reasonably conducting Ag-Au bimetallic film.

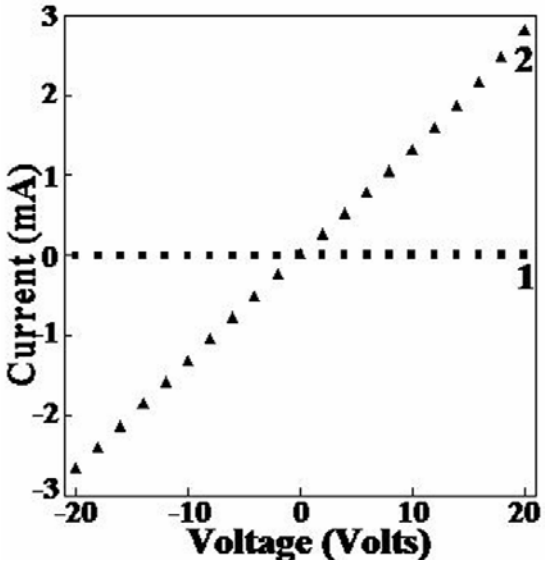

Figure 5.13 *I-V characteristics of silver film and Ag-Au bimetallic film. Curve 1 corresponds to the conductivity of the silver film while curve 2 shows the conductivity profile of the Ag-Au bimetallic nanoparticles film.*

5.3.2.6.3 Temperature dependent conductivity measurement

Studies were done to investigate the temperature dependent changes in the silver-gold bimetallic films. Fig 5.14 shows a plot of the temperature dependent resistance change of the silver and the silver-gold bimetallic films lifted from the liquid-liquid

interface. Fig 5.14A shows the ln resistance (natural log) vs 1/T in Kelvin plot of the silver film at fixed voltage of 100 volts. It is clearly evident from the nature of the curve that the resistance of the silver film decreases with increasing temperature showing negative temperature coefficient of resistance which is indicative of the semiconductor like behavior of the film. The measurement clearly indicated that the silver nanoparticles behave like a semiconductor with activation energy required for electron conduction. Arrhenius-type activated tunneling model was used to describe the electron conduction through the film where the activation energy could be calculated from the equation

$$\sigma(\delta,T) = \sigma_0 (e^{-\beta\delta}).e^{-E_A / k_B.T}$$

where β is the electron tunneling coefficient in $Å^{-1}$, δ the average interparticle distance, E_A the activation energy and $\sigma_0 e^{-\beta\delta}$ the conductivity at $k_BT >> E_A$ [49].

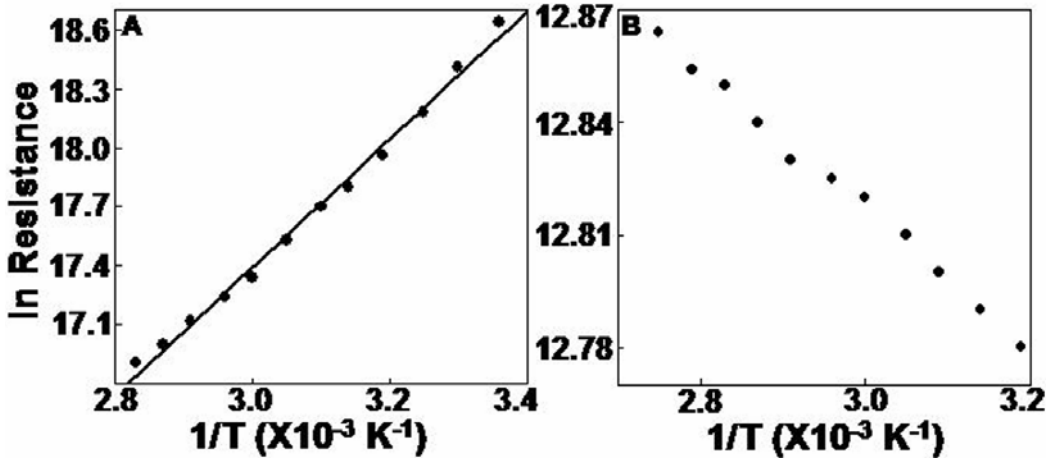

Figure 5.14 *ln resistance vs 1/T plot for the (A) silver film and (B) for the silver-gold bimetallic film lifted from the liquid-liquid interface.*

The straight line fit to the data points gave the slope and the activation energy calculated was found to be 280 meV. The high value of the activation energy for the silver film could be attributed to the energy needed for the electrons to hop between the particles. However, when the sacrificial silver film at the liquid-liquid interface reacts with chloroaurate ions, transmetallation reaction takes place which results in the formation of interconnected structures facilitating electrical interlinking of the silver nanoparticles. This can be confirmed from the "ln resistance vs 1/T" plot in fig 5.14B for

the silver-gold bimetallic film which shows a decrease in the conductivity of the film with increasing temperature i.e. positive temperature coefficient of resistance which is characteristics of the metallic behavior. Besides, as indicated by the TEM images in the Fig 5.11A-C, we observe that the transmetallation reaction tends to fuse the silver nanoparticles together by bridging between isolated particles causing increase in the conductivity of the film.

5.3.2.6.4 Ammonia sensing

A conceptually different approach has been exploited to study the ability of these films to sense chemical vapors in terms of the electrical resistance to examine the electronic communication behavior between the immobilized gold nanoparticles. The electrical resistance change at lower gas concentrations largely depends on particle-to-particle separation and provides a sensitive method of transducing the analyte-induced changes in the detector films. For example by this method resistance changes in a given exposure period could be readily determined for a much lower gas concentration than those required to produce significant optical absorption spectral changes. Resistance measurements also have the advantage of requiring only low-cost and low-power electronic components that are easily multiplexed, and are compatible with portable device configurations due to the low-profile design of the sensor.

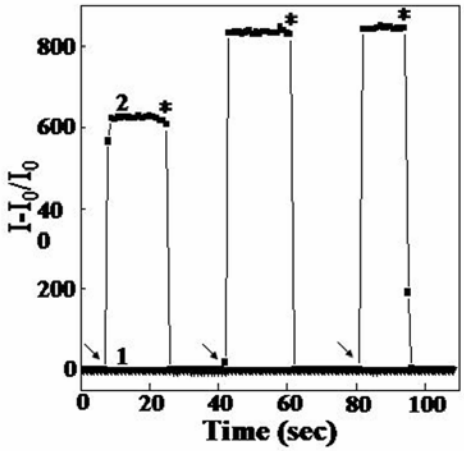

Figure 5.15 *Normalized current vs. time plot showing conductivity change on exposure to ammonia vapors. Curve 1 shows the conductivity of the silver film while curve 2 shows the conductivity of the Ag-Au bimetallic film on exposure to the ammonia vapors.*

The silver nanoparticles film as well as Ag-Au bimetallic film deposited on quartz substrate was challenged with ammonia vapor environment to analyze its sensing capability. For all the sensing experiments, current measurements were done at constant voltage of 20 V. The electrical measurement for sensing purpose was done in a controlled environment using a closed beaker with an inlet and outlet for ammonia vapors. Fig 5.15 shows the normalized current vs. times plot of the film on exposure to the ammonia vapors. It can be seen from the nature of the Curve 2 that the Ag-Au bimetallic film shows nearly three orders of magnitude increase in the conductivity on exposure to the ammonia vapors. The arrow indicates the point of exposure of the film to the ammonia vapor while the star (*****) shows the point of removal of the gas. We see a rapid increase in the conductivity of the film as soon as it is exposed to the ammonia vapors and the conductivity falls back to original level as soon as the gas is removed. This confirms that the ammonia molecules are weakly physisorbed on the surface of the nanoparticles. In contrast to this, the silver film control did not show much sensitivity to the vapors (Curve 1). The electronic conduction across such discontinuous metal nanoparticles film has been explained on the basis of the electron tunneling across a potential barrier [48], which is a strong function of the interparticle spacing [49], bias voltage and the micro-environment around the particles [50]. It has been shown in the previous studies that the presence of an electron donor group on the surface of the particles reduces the work function [51] of the film and thus facilitates the electron conduction. Ammonia molecule has a nitrogen-atom with a lone pair of electrons and thus acts as the electron donor group and thus, theoretically, the conductivity of the bimetallic film should increase on exposure to the ammonia vapor. The obtained experimental results corroborate well with the information where we obtain increased electron conduction across the film in the presence of ammonia vapors in the environment. We also observed that 90% of the total response of the Ag-Au bimetallic film came within 5 seconds of exposure to the gas, which suggests that the film is highly sensitive to the ammonia vapors. The exposure cycle was repeated for 3 cycles and it was seen that the result was consistent suggesting that the film has a good efficiency for reuse.

5.3.2.7 Conclusion

The electrical and sensor properties of films composed of silver nanoparticles (Ag-NPs) and the bimetallic film which has been synthesized by the core metal galvanic exchange reaction of dodecylamine monolayer-protected metal (Ag) clusters with the more noble metal (Au) were compared to investigate how these properties depend on the morphology of the particles. The optical properties reflect bimetallic cluster formation by shifts in the surface plasmon resonance absorbance. The transmetallation reaction of chloroaurate ions with the sacrificial silver nanoparticles greatly improves the conductivity and the electron transfer ability of the film. Additionally, the electronic and gas sensing properties of the formed films can be exploited to utilize the films for the detection of NH_3 vapors by monitoring the resistance change on exposure. The sensitivity of the films is dependent on the extent of interconnections. With the rapid developments in nanoparticle preparation, surface modification, and assembly, the emergence of novel applications of these and other nanoparticle-related films are likely to impact the areas of sensing, catalysis, and optoelectronics.

5.4 Transmetallation and halide ions

5.4.1 Introduction

Taking the study further, we intend to draw attention to the possible crucial role of halide ions, that have so far not been given due emphasis, during the transmetallation reaction for the growth of anisotropic nanostructures. We observe that the presence of halide ions in solution during $AuCl_4^-$ ion reduction by silver nanoparticles critically affects the morphology of the nanostructures thus formed.

One important class of anisotropic nanostructure are the ones with hollow interiors. Nanostructures with hollow interiors are useful in many areas [52]. For example, they can serve as extremely small containers for encapsulation process that has been extensively explored in applications related to catalysis, drug delivery, and protection of environment-sensitive materials such as enzymes [53]. When used as fillers in making composite materials, hollow structures also offer some advantages over their solid counterparts as a result of their relatively low densities [54]. Hollow nanostructures

of noble metals are particularly interesting to synthesize and investigate because they exhibit plasmonic properties completely different from those of solid nanoparticles [55]. Recent studies by Halas and co-workers, for example, suggest that the plasmon peak of spherical gold nanoshells could be conveniently tuned to cover the spectral regime from 600 to 1200 nm, whereas it is difficult to shift the plasmon peak of spherical gold (or silver) nanoparticles by more than 20 nm [56]. Hollow spheres of various materials have been extensively investigated in the literature but most materials that have been processed into hollow spheres are ceramic or polymeric materials [57, 58]. These materials are amorphous and thus form conformal coatings on spherical templates. More recently, several effective methods have been demonstrated to coat particulate templates with metal shells [56]. More recently, Xia and coworkers have demonstrated transmetallation as an effective method for the synthesis of hollow structures. They had conducted the temperature at higher temperature. At room temperature when the same experiment was conducted, it resulted in the synthesis of hollow shells but the walls were thick and irregular. This may be due to the presence of Cl^- ions which have an affinity to the (111) face of the Ag/Au nanoparticles.

We have shown in the following study that the addition of halide ions at the room temperature can result in the synthesis of bimetallic hollow shells after the transmetallation reaction with thin walls. To investigate the effect of halide ions on the structures formed during the transmetallation reaction between the gold ions and the silver nanoparticles, we carried out the same reaction in the solution phase in the presence of KCl, KBr and KI. We found drastic changes in the morphologies of the hollow structures synthesized as a result of the reaction. The presence of the Br^- ions gave a shift in the UV-vis spectra also from 540 nm to 800 nm. The presence of I^- ions causes aggregation. Bromide and iodide ions are known to be capable of replacing chemisorbed Cl^- ions from the gold surface [59] and thus can potentially control the growth of the nanonuclei. Surface chemistry of the reduced bimetallic nanostructures was analyzed by XPS and spot EDAX measurements. From the characterizations carried out

we have tried to explain the effect of halide ions on the changes of the morphologies of the nanostructures and the shift in the UV-vis absorption.

The role of halide ions is not unique to the transmetallation reaction investigated here, but has been recently gaining importance in the crystal growth mechanism in few other systems too [60]. Pileni's group have demonstrated that though the presence of halide ions do not affect the structure of the micellar template, drastic changes in the shape of the copper nanoparticles formed in their presence could be observed [60a-f]. In their study, while NaCl addition was observed to promote rod like structures and NaBr promoted the formation of cubic copper nanoparticles, NaF was not observed to impart any specific shape, though presence of small cubes have been claimed [60a, e]. Similarly, importance of the Cl^- on the structure of the nanoparticles formed has also been claimed by Roberts et. al. and Xia et. al. in their reports on the synthesis of copper [60g] and silver nanoparticles [60h] respectively. The role of halide ions seems so prominent that they are able to impart morphological distortions even in an aqueous solution of preformed Ag nanoparticles to a small extent. We can say that the halide ions serve as chemical agents to induce morphological changes to well formed gold nanoparticles [61].

5.4.2 Experimental procedure

Silver nanoparticles (synthesized by the method mentioned in section 5.2.2) were mixed with aqueous solution of 10^{-4} M chloroauric acid. On mixing silver nanoparticles were oxidized by the chloroaurate ions to form hollow gold nanoparticles. The reaction between the silver nanoparticles and chloroaurate ions is

$$3Ag + HAuCl_4 \rightarrow Au + 3AgCl\downarrow + HCl$$

as reported by Xia and co-workers [17f]. According to the reaction stoichiometry, three silver atoms are required to reduce one Au^{3+} to one Au atom. Thus the concentration of chloroaurate ions required to oxidize all silver atoms to silver ions should be one-third of silver nanoparticles concentration. In the present case, the exact concentration of silver nanoparticles is difficult to measure, but 10^{-3} M silver ions were used in the synthesis of silver nanoparticles. Approximately the concentration of the silver nanoparticles would be slightly higher than 10^{-4} M. Hence the required concentration of chloroaurate ions to

oxidize all silver atoms in the nanoparticles would be ranging from $3x10^{-5}$ to $5x10^{-5}$M. The concentration of gold ion used in the reaction will not be consuming the silver nanoparticles fully so there will be traces of left in the final formed nanostructures.

5.4.3 Synthesis and Characterization

5.4.3.1 Synthesis of hollow shell nanoparticles in the presence of halide ions

To study the effect of the halide ions on the morphology of gold nanoshells, silver nanoparticles synthesized by the above–mentioned methods and 10^{-4} M chloroauric acid in aqueous was mixed together in the presence of 10^{-4}M KCl/ KBr/ KI. On mixing, silver nanoparticles were oxidized by the chloroaurate ions to form hollow gold nanoparticles. In almost all cases, the solution rapidly changed color. The color of the solution formed varied in all cases. It changed from yellow to red on addition of KCl, to greenish blue on addition of KBr and to grayish purple on addition of KI, Fig 5.28B.

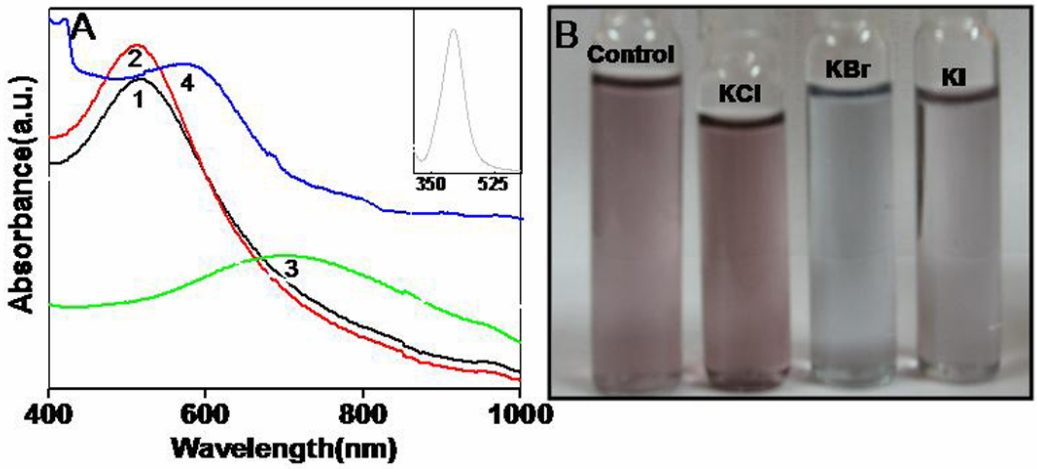

Figure 5.28 *(A) UV-vis absorption spectra recorded from solution after transmetallation reaction between 10^{-4} M $HAuCl_4$ and Ag nanoparticles (curve1) Control, no halide ions (curve2) in presence of 10^{-4} M KCl (curve3) in presence of 10^{-4} M KBr and (curve4) in presence of 10^{-4} M KI. (B) Photograph showing the colour of the solution after reaction control, in presence KCl, KBr and KI respectively . Inset is the UV-vis spectra of pure silver nanoparticles. The x axis corresponds to wavelength in nm and y axis to absorbance.*

5.4.3.2 UV-visible spectroscopy

We first followed the replacement reaction between $HAuCl_4$ and silver nanoparticles using the UV-vis spectroscopic method. It is well-known that their aqueous suspensions exhibit strong plasmon resonance peaks at ~420 and ~530 nm, respectively.

Figure 5.28A (curve1) shows the absorption spectra when an aqueous solution of silver nanoparticles (with a mean size of ≈ 30 nm) was reacted with $HAuCl_4$ at room temperature. The plasmon peak (~422 nm) of silver nanoparticles (inset of Fig 5.28A) decreases as the reaction proceeded. This peak disappeared after few minutes, as the reaction was very fast, indicating the complete consumption of all silver templates. At the same time, a new absorption peak evolved with increasing intensity at 540 nm. Upon addition of different halide ions during the transmetallation reaction between the gold ions and silver nanoparticles, it was observed that the Ag surface plasmon resonance band is reduced in intensity and new distinct bands appeared on addition of halide ions. Fig. 5.28A curve 2 shows the new absorption band at ~550 nm in presence of chloride ions, at ~ 730 nm in presence of bromide ions, curve 3 and at ~ 590 nm in presence of iodide ions, curve4. These solutions were allowed to react for 24 h at room temperature and then UV-vis spectroscopy and TEM analysis were pursued to characterize the gold nanoparticles formed in each of these solutions.

5.4.3.3 TEM analysis

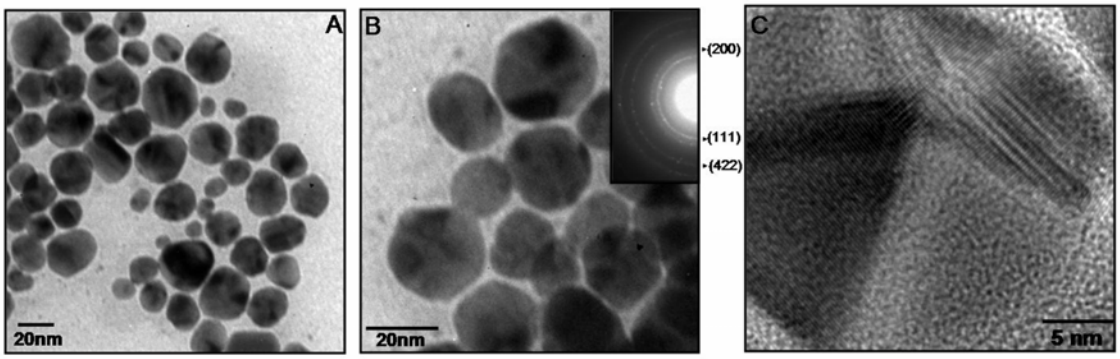

Figure 5.29 *(A,B) Representative TEM images of the silver nanoparticles at different magnifications. (C) HRTEM image of one of the silver nanoparticle, sowing the lattice spacing of 0.234 nm, corresponding to (111) plane of Ag. Inset of B shows the SAED pattern obtained from Ag nanoparticles.*

The final nanostructures obtained from the transmetallation reaction were characterized using Transmission electron microscopy. Fig 5.29 shows a TEM image at different magnifications, of the silver nanoparticles that were used as templates for the reaction. These nanoparticles exhibited a range of different morphologies, with an

average size of ~30 nm. The central portions of these particles were darker than their edges due to different thickness of silver along the path of electron beam. Thinner regions (edges) were less effective in scattering electrons. The inset shows the SAED pattern obtained from the silver particles. All diffraction rings could be indexed to face center-cubic silver with a lattice constant of ~4.08 Å. Figure 5.29C shows the HRTEM image of one of the silver particles. The particle is dodecahedral in shape, with the {111} faces.

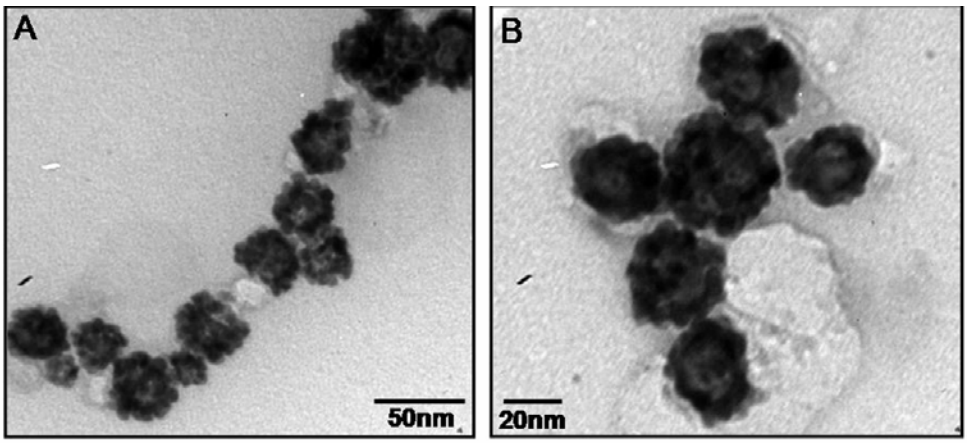

Figure 5.30 (A-B) *Representative TEM images, at different magnifications of drop coated solution on Cu grid after the transmetallation reaction between silver nanoparticles and 10^{-4} M aqueous $HAuCl_4$.*

Fig. 5.30 gives a TEM image of these silver nanoparticles after they have completely reacted with the aqueous $HAuCl_4$ solution. In this case, the center portion of each particle was lighter than its edge, indicating the formation of a shell-type nanostructure. It should be noted that the morphology of these gold nanoshells are slightly different from the silver templates with them having uneven edges, but the surfaces of these gold nanoshells are essentially free of defects such as pinholes. These gold nanoshells were also strong enough to survive the capillary forces involved in solvent evaporation process.

Figure 5.31 gives a TEM image of silver nanoparticles after they have completely reacted with the aqueous $HAuCl_4$ solution in the presence of halide ions. It can be seen that in the presence of Cl^- ions Fig 5.31 (A-B) the morphology of the resultant gold shells

is almost similar to the structure which were obtained in the absence of halide ions, Fig 5.31 (A-B).

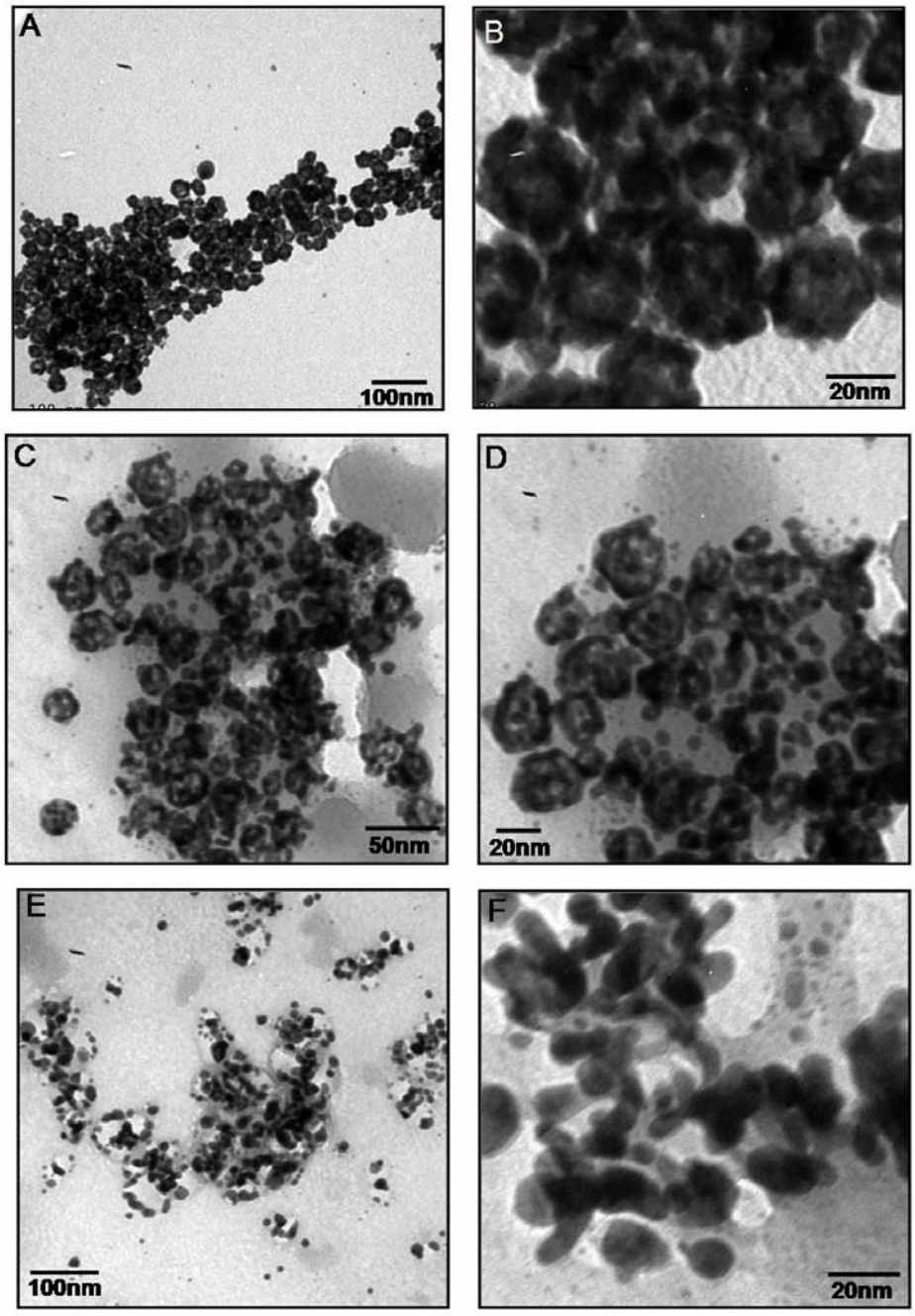

Figure 5.31 (A-E) *Representative TEM images, at different magnifications of drop coated solution on Cu grid after the transmetallation reaction between silver nanoparticles and 10^{-4} M aqueous $HAuCl_4$, in presence of (A-B) KCl, (C-D) KBr and (E-F) KI respectively.*

Fig 5.31 (C-D) shows the images of the nanoshells formed in the presence of Br^- ions, at different magnifications. These nanoshells are different from the shells formed in the presence of Cl^- ions. Fig 5.31 (E-F) shows the image of the structures formed when the transmetallation reaction was performed in the presence of I^- ions. We see only aggregated structures. The TEM images are in agreement with the UV-vis readings obtained from the samples.

5.4.4 Study of growth of gold nanoparticles in presence of halide ions

Figure 5.28 shows the UV-vis-NIR spectra of transmetallation reaction between Ag nanoparticles and gold ions at room temperature (27° C) in the absence (curve 1, Fig 5.28) and presence of different potassium halides (Au : KX, 1 : 1, X= Cl, Br, I). There is a shift in the peak when the reaction was performed in the presence of halide ions as shown earlier. From the UV-vis (fig 5.28, curve 2) and the TEM images we can infer the following. On carrying the reaction in the presence of KCl we notice that the size and shape of the gold nanoshells formed in the absence (Figure 5.30) and presence of KCl (Figure 5.31A,B) are essentially similar and thus in agreement with the UV-vis-NIR results. But we do notice that the size is slightly larger (from ~30 nm to ~35 nm) and the number of the nanoshells formed has increased in the presence of KCl. We can infer that KCl enhances the reaction.

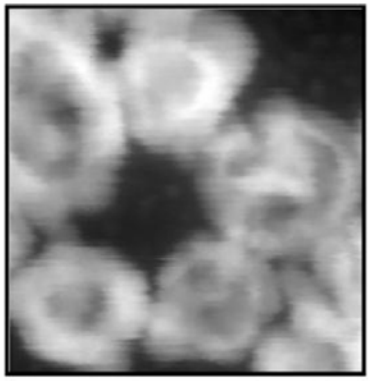

Figure 5.32 *STEM images of the nanoshell formed after the transmetallation reaction between sacrificial Ag nanoparticles and 10^{-4} M $HAuCl_4$ in presence of 10^{-4}M KBr.*

The presence of KBr during the reaction medium results in a large red-shift of the absorbance peak (Figure 5.28, curve 3). The TEM image of the gold nanoshells formed in

the presence of KBr (Figure 5.31C,D) shows that the gold nanoshells are indeed different than those obtained in the control experiment (Figure 5.30, absence of halide ions) and in the presence of KCl. These have thinner walls and there is distinct absence of the (111) faces, only walls are present. This indicates that the formation of gold nanoshells with thinner walls is being favored in this condition. The red shift in the UV-vis spectra with the variation in the shell thickness is in agreement with the results earlier shown by Halas and coworkers [56].

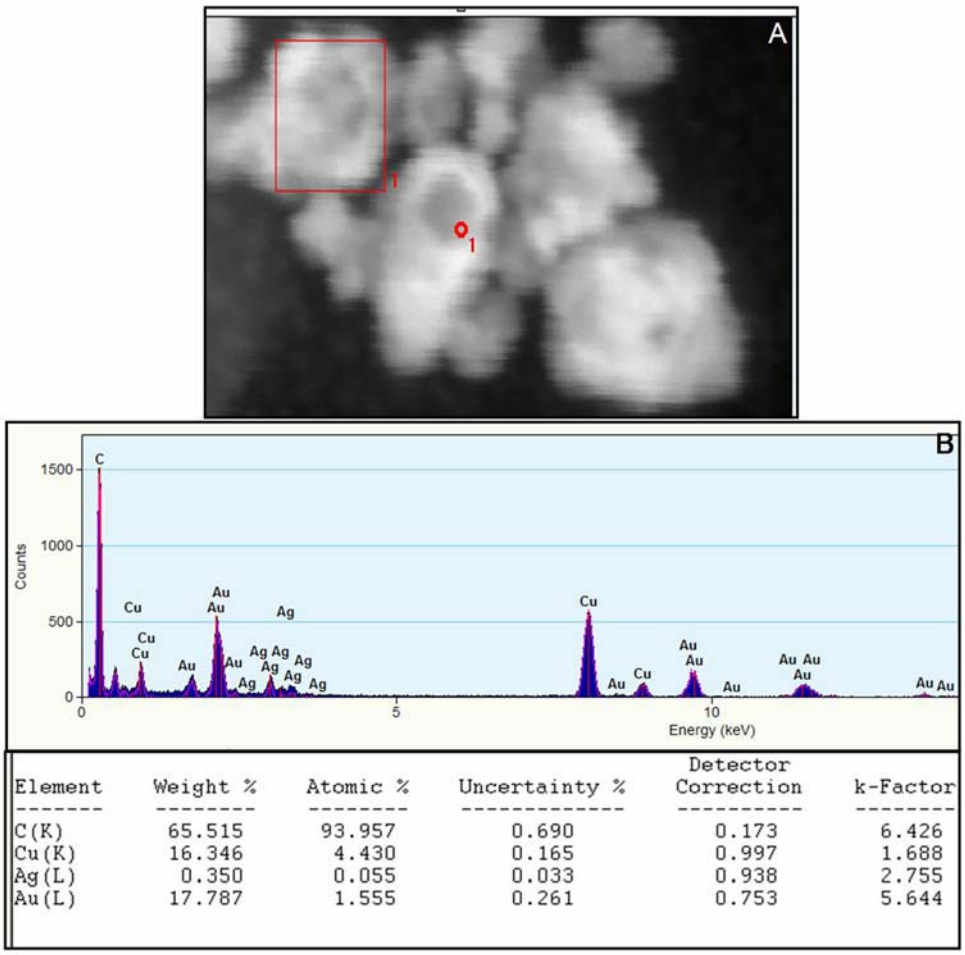

Element	Weight %	Atomic %	Uncertainty %	Detector Correction	k-Factor
C(K)	65.515	93.957	0.690	0.173	6.426
Cu(K)	16.346	4.430	0.165	0.997	1.688
Ag(L)	0.350	0.055	0.033	0.938	2.755
Au(L)	17.787	1.555	0.261	0.753	5.644

Figure 5.33 *(A) STEM images and the (B) Spot EDAX measurement with data for one of the nanoshell formed after the transmetallation reaction between sacrificial Ag nanoparticles and 10^{-4} M $HAuCl_4$ in presence of 10^{-4}M KBr.*

The STEM scan of the shells shows the prominent deposition of thin layer gold on the walls of the shell, Fig 5.32. The image is taken using the HAADF detector. The spot EDAX measurement done on one of the shells shows the presence of Ag and Au, but does not shows the presence of Br. Fig 5.33 shows STEM of one of the shells and the results of the spot EDAX measurements performed on the region marked. However when the area consisting of the collection of shells was selected, we do get a signal for Br, indicating that though Br is present but is not directly forming any metal complex. Fig 5.34 shows the spot EDAX analysis conducted of the region marked in red and the corresponding quantified data.

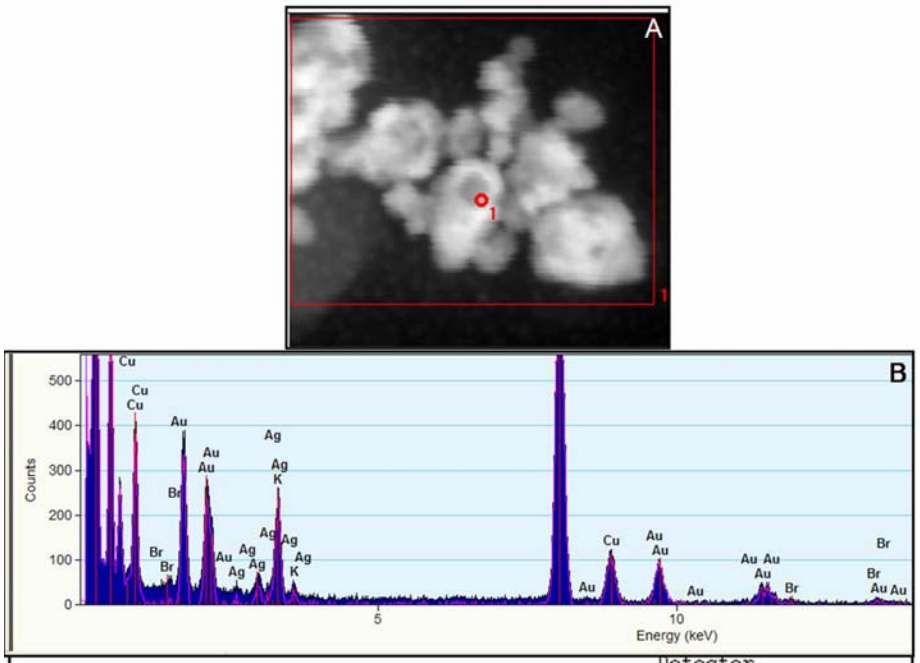

Element	Weight %	Atomic %	Uncertainty %	Detector Correction	k-Factor
C(K)	79.795	93.040	0.525	0.173	6.426
O(K)	4.545	3.979	0.069	0.514	2.014
K(K)	1.093	0.391	0.023	0.966	1.139
Cu(K)	10.161	2.239	0.083	0.997	1.688
Br(K)	0.115	0.020	0.010	1.000	2.563
Ag(L)	0.414	0.053	0.018	0.938	2.755
Au(L)	3.873	0.275	0.077	0.753	5.644

Figure 5.34 *(A) STEM images and the (B) Spot EDAX measurement with data for the cluster of nanoshells formed after the transmetallation reaction between sacrificial Ag nanoparticles and 10^{-4} M $HAuCl_4$ in presence of 10^{-4} M KBr.*

There is a marked difference in the STEM images in the Fig 5.32 and the ones shown in fig 5.33 and Fig 5.34. The ones in Fig 5.34 look elongated. This is due to the fact that for the collection of the X-rays from the sample for the EDAX measurements, the sample is tilted at an angle of 20°.

The synthesis of gold nanoparticles in the presence of KI leads to a significant or complete suppression of formation of gold nanoshells, (Fig 5.31 (E, F). The gold nanostructures formed in the presence of KI are almost all aggregated and shows no noticeable shape, again consistent with the UV-vis spectrum recorded from this sample that shows just a red in the absorption band centered at 590 nm (Figure 5.28A, curve 4). In addition to this there is another peak centered at 410 nm, which might be due to the formation of Au-metal complex [61a]. The aggregation of the particles was earlier also observed by Cheng et. al. in their study of the effect of aqueous KI solution on the morphology of spherical citrate reduced gold nanoparticles solution (synthesized under boiling conditions) [61b].

A chemical analysis of the gold nanoshells synthesized in the absence and presence of different halide ions was carried out using XPS to further confirm the presence and effect of halide ions in the structures synthesized during the reaction. The solution was centrifuged prior to casting in thin film form for XPS analysis on Si substrate. While a extremely weak Cl 2p signal was recorded from the gold nanotriangles synthesized in the absence of halide ions and clearly is due to Cl^- ions produced during reduction of aqueous $AuCl_4^-$ ions, a stronger Cl 2p signal was obtained from the nanoparticles synthesized in the presence of KCl [Fig.5.36A]. The additional Cl^- coverage of the gold nanoshells in this experiment thus seems to play crucial role in promoting nanoshells formation (Fig. 5.32 (A, B)). Br 3d and I 3d signals were observed in the gold nanoshells prepared in the presence of KBr and KI respectively (Fig. 5.36B and C). The low intensity of the 2p core level of Cl and 3d core level of Br species can be attributed to its low photoemission cross-section. The 3d core level of I is reasonably strong.

These results are consistent with the gold nanoparticle morphology variation observed in the TEM images; the presence of Br^- and I^- ions changes the morphology and optical properties significantly relative to the control particles.

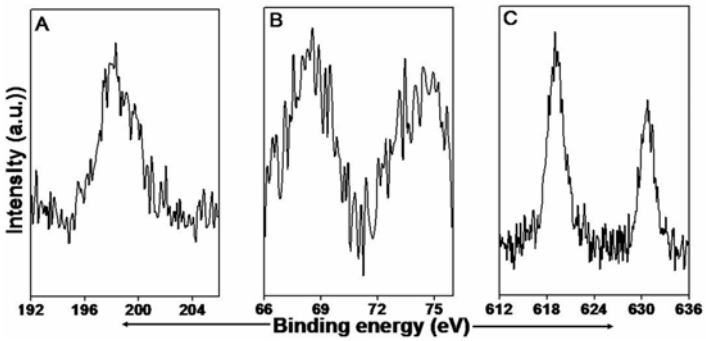

Figure 5.36 *XPS spectra of (A) Cl 2p, (B) Br 3d and (C) I 3d core levels from gold nanoshells synthesized in presence of KCl, KBr and KI respectively at room temperature.*

From the morphology of the structure formed in the presence of the halide ions, namely Cl^-, Br^-, and I^- and the previous studies done on reduction of gold ions by biological and chemical means in the presence of halide ions [62] we can infer that, the presence of Cl^- ions during the reduction results in the formation shells with thick, irregular and serrated walls. This may be due to the well known fact that the Cl^-, $Br^-$and I^- ions very efficiently chemisorb on the surface of gold and that bromide and iodide ions are capable of replacing chloride ions from the surface of gold [59]. This effect of different halide ions on the morphology of gold nanostructures reduced by the galvanic exchange process may possibly be rationalized as follows.

Cl^-, Br^- and I^- ions have the ability to chemisorb on the Au surface, forming Au-X bonds with force constants in the order I > Br > Cl [59, 63]. During the reduction and subsequent growth of the gold by Ag nanoparticles, the presence of Cl^- ions (due to the KCl and also due to the Cl^- in $HAuCl_4$), facilitates the formation nanoshells with thick walls. The ability of Br^- and I^- ions to compete with gold-surface bound Cl^- ions in complexing with the surface of gold could be because of their comparative ligating ability. This could also be the reason why molecules bearing functional groups that have better polarizability (thiols, phosphines,etc.) and charge transfer ability are able to interact with the surface of the gold nanoparticles as compared with molecules bearing

other functional groups viz. alcohols [64]. That the Cl^-, $Br^-$and I^- ions are present on the gold nanoparticles formed in their presence is clearly indicated in the XPS measurements (Figure 5.36) and by the EDAX studies.

The structure of the adlayers of Cl^-, Br^- and I^- ions on the Au surface has been well characterized [65]. It is reported that all the three halides form an incommensurate adlayer on gold (no lateral registry). Among these halides, Cl^- and Br^- ions form a hexagonal-close-packed adlayer of which the Cl^- adlayer is better aligned with the underlying Au (111) lattice plane. During the formation of the gold shells, due to the presence of the layer of Cl^- ions the (111) face of the shell is almost intact. Whereas the replacement of adsorbed Cl^- ions by the Br^- from the (111) face of the formed nanoshell makes it vulnerable to the replacement reaction and the shell wall becomes thin.

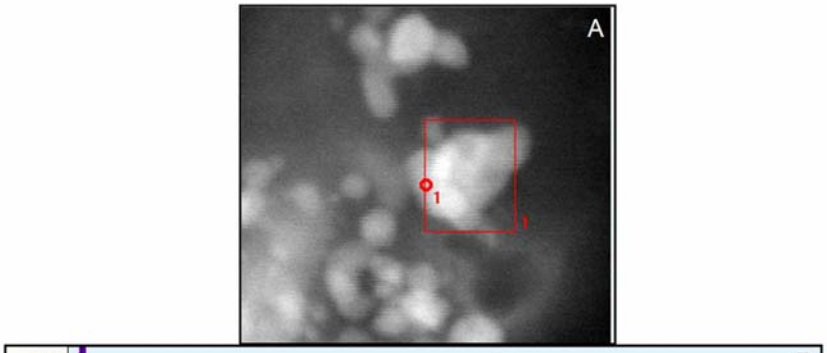

Element	Weight %	Atomic %	Uncertainty %	Detector Correction	k-Factor
C(K)	78.797	96.013	0.325	0.173	6.426
O(K)	0.631	0.577	0.017	0.514	2.014
Cu(K)	10.473	2.412	0.050	0.997	1.688
Ag(L)	1.586	0.215	0.012	0.938	2.755
I(L)	3.642	0.420	0.029	0.908	3.304
Au(L)	4.869	0.361	0.030	0.753	5.644

Figure 5.37 *(A) STEM images and the (B) spot EDAX measurement with quantified data for a single elongated structure formed after the transmetallation reaction between sacrificial Ag nanoparticles and 10^{-4} M $HAuCl_4$ in presence of 10^{-4} M KI.*

The aggregated structures observed in presence of I^- ions can be attributed to the increased covalency of the Au–I bond [63, 66] leading to lower surface charge and consequent instability of the gold nanoparticles unlike in the case of Br^- ions which has an intermediate mismatch [61] and also since they do not have as strong affinity as I^- ions to replace the surface bound Cl^- ions [59, 63] a complete aggregation of gold nanostructures is not observed. The adsorption of iodide during the transmetallation reaction is further confirmed by the spot EDAX done on one of the elongated structures formed after the transmetallation reaction, Fig. 5.37. The single shell shows the presence of Ag, Au and I also as listed in the quantified data.

During the consumption of the sacrificial Ag nanoparticles by the gold ions, we see favorism towards the formation of Au-X bond as compared to Ag-X bonds. Stronger metal-halide bonds for gold compared with silver are also seen for the related bulk-phase complexes [67]. These differences are consistent with the smaller $d^{I0} \rightarrow d^9s$ electron promotion energy for Au(1) vs. Ag(1) and suggest that the gold-halide bonds are more covalent than their silver counterparts [67a]. The similar behavior observed for the metal-halide surface bonds therefore strongly suggests that the gold surface also engenders greater coordinate covalency than silver for the halide chemisorption bond. Such covalency effects are also manifested in the observed differences in the dependence of the force constants in the surface and bulk-phase environments on the nature of the halide by Gao and Weaver [59]. They deduced that while the force constant (f_{M-x}) values for the bulk-phase A(1) and especially Au(1) complexes decreases monotonically from chloride to iodide, those for the surface Ag-X bonds appear to be roughly independent of the halide and for surface Au-X bonds instead increase substantially from chloride to iodide .This can be understood, at, in terms of the differing importance of ionic and covalent interactions. It can be inferred from their findings that $f_{Au-1} > f_{Au-Cl}$, whereas the two effects appear to be roughly balanced for halide bonding on the silver surface, so that $f_{Ag-I} \sim f_{Ag-C1}$.

5.4.5 Conclusions

In summary, we have highlighted the crucial role of halide ions on the evolution of the different morphologies of gold nanostructures during transmetallation reaction in solution between the Ag nanoparticles and gold ions. Cl^- ions are known to form an ordered layer on the (111) lattice plane of gold and thus have a greater probability of passivating (111) face. Further the Br^- and I^- ions can replace the adsorbed Cl^- ions. Based on these arguments it has been demonstrated that Br^- and I^- ions, having better ability to bind with gold surface. Thus the presence of Br^- favors the formation of thin shells in solution which are not possible in the presence of other halide ions and the presence of I^- ions promotes the formation of interconnected structures.

References

(1) (a) Sastry, M. "Colloids and Colloid Assemblies: Synthesis, Modification, Organization and Utilization of Colloid Particles Ed. Caruso, F. Wiley-VCH, Berlin Chapter 12, **2003**, 369. (b) Sastry, M. Handbook of Surfaces and Interfaces of Materials, Ed. Nalwa, H.S. Nanostructured Materials, Micelles and Colloids, Academic Press Volume 3, Chapter 2, **2001**, 87. (c) Fendler, J. H. *Nanoparticles and Nanostructured Films: Preparation, Characterization and Applications*; Wiley-VCH: Weinheim, **1998**. (d) Rotello, V. *Nanoparticles: Building Blocks for Nanotechnology*; Kluwer Academic/Plenum Publishers: New York, **2004**. (e) Horiuchi, S.; Sarwar, M. I.; Nakao, Y. *Adv. Mater.* **2000**, *12*, 1507. (f) Horiuchi, S.; Fujita, T.; Hayakawa, T.; Nakao, Y. *Langmuir* **2003**, *7*, 2963.

(2) (a) El-sayed, M. A. *Acc. Chem. Res.* **2001** *34*, 257. (b) Henglein, A. *J. Phys. Chem.* **1993**, *97*, 8457. (c) Henglein, A. *Chem. Rev.* **1989**, *89*, 1861. (d) Alivisatos, A. P. *J. Phys. Chem.* **1996**, *100*, 13226. (e) Schmid, G. *Clusters and Colloids: From Theory to Application*; VCH: Weinheim, **1994**. (f) Perenboom, J. A. A. J.; Wyder, P.; Meier, P. *Phys. Rep.* **1981**, *78*, 173. (g) Hughes, A. E.; Jain, S. C.; *Adv. Phys.* **1979**, *28*, 717.

(3) (a) Andres, R. P.; Bein, T.; Dorogi, M.; Feng, S.; Henderson, J. I.; Kubiak, C. P.; Mahoney, W.; Osifchin, R. G.; Reifenberger, R. *Science* **1996**, *272*, 1323. (b) Kim, S.H.; Medeiros-Ribeiro, G.; Ohlberg, D. A. A.; Williams, R. S.; Heath, J. R. *J. Phys. Chem. B* **1999**, *103*, 10341. (c) Beverly, K. C.; Sampaio, J. F.; Heath, J. R. *J. Phys. Chem. B* **2002**, *106*, 2131. (d) Kim, B.; Tripp, S. L.; Wei, A. *J. Am. Chem. Soc.* **2001**, *123*, 7955.

(4) (a) Xia, D.; Biswas, A.; LI, D.; Brueck, S. R. J. *Adv. Mater*. **2004**, *16*, 1427. (b) Xia, D.; Brueck, S. R. J. *Nano Lett.* **2004**, *4*, 1295.

(5) (a) Lee, K.; Pan, F.; Carroll, G. T.; Turro, N. J.; Koberstein, J. T. *Langmuir* **2004,** *20,* 1812. (b) Horiuchi, S.; Fujita, T.; Hayakawa, T.; Nakao, Y. *Adv. Mater.* **2003**, *15*, 1449.

(6) (a) Xia,Y.; Whitesides, G. M. *Angew. Chem. Int. Ed*. **1998**, *37*, 550. (b) Gorman, C. B.; Beibuyck, H. A.; Whitesides, G. M. *Chem. Mater.* **1995**, *7*, 526. (c) Zhao, X. M.; Xia, Y.; Whitesides, G. M. *J. Mater. Chem*. **1997**, *7*, 1069.

(7) Santhanam V.; Andres, R. P. *Nano Lett*., **2004**, 4, 41.

(8) (a) Sastry, M.; Patil, V.; Mayya, K.S.; Paranjape, D.V.; Singh, P.; Sainkar, S.R. *Thin Solid Films* **1998**, *324*, 239. (b) Perez, H.; Lisboa de Sousa, R.M.; Pradeau, J.P.; Albouy, P.A. *Chem. Mater*. **2001**, *13*, 1512. (c) Swami, A.; Kumar, A.; Selvakannan, PR.; Mandal, S.; Sastry, M. *J. Colloid Int. Sci.* **2003**, *260*, 367. (d) Selvakannan, PR.; Swami, A.; Srisathiyanarayanan, D.; Shirude, P. S.; Pasricha, R.; Mandale, A. B.; Sastry, M. *Langmuir* **2004**, *20*, 7829. (e) Wang, W.; Chen, X.; Efrima, S. *J. Phys. Chem. B* **1999**, *103,* 7238. (f) Heath, J. R.; Knobler, C. M.; Leff, D. V. *J. Phys. Chem. B* **1997**,*101*, 189. (g) Burghard, M.; Philipp, G.; Roth, S.; von Klitzing, K.; Pugin, R.; Schmid, G. *Adv. Mater.* **1998**, *10*, 842. (h) Bourgoin, J. F.; Kergueris, C.; Lefevre, E.; Palacin, S. *Thin Solid Films* **1998**, *327*, 515. (i) Chen, X. Y.; Li, J. R.; Jiang, L. *Nanotech.* **2000**, *11*, 108. (j) Brust, M.; Stuhr-Hansen, N.; Nørgaard, K.; Christensen, J. B.; Nielsen, L. K.; Bjørnholm, T. *Nano Lett.* **2001**, *1*, 189. (k) Brown, J. J.; Porter, J. A.; Daghlian, C. P.; Gibson, U. J. *Langmuir* **2001**, (l) Huang, S.; Minami, K.; Sakaue, H.; Shingubara, S.; Takahagi, T. *Langmuir* **2004**, *20*, 2274.

(9) (a) Kotov, N. A.; Meldrum, F. C.; Wu, C.; Fendler, J. H. *J. Phys. Chem.* **1994**, *98,* 2735. (b) Tian, Y.; Fendler, J.H. *Chem. Mater.* **1996**, *8,* 969. (c) Damle, C.; Gole, A.; Sastry, M. *J. Mater.Chem.* **2000**, *10*, 1389.

(10) (a) Lennox, R. B.; Goren, M. *Nano Lett*. **2001**, *1*, 735. (b) Seo, Y. S.; Kim, K.S.; Galambos, A.; Lammertink, R. G. H.; Vancso, G. J.; Sokolov, J.; Rafailovich, M. *Nano Lett*. **2004**, *4*, 483. (c) Yoo, S.; Sohn, B. H.; Zin, W. C.; Jung, J. C. *Langmuir* **2004**, *20*, 10734.

(11) (a) Chen, S. *Adv. Mater*. **2000**, *12*, 186. (b) Chen, S. *Langmuir* **2001**, *17*, 2878.

(12) (a) Swami, A.; Kasture, M.; Pasricha, R.; Sastry, M. *J. Mater.Chem.* **2004**, *14*, 709. (b) Swami**,** A.; Kumar, A.; Selvakannan, PR.; Mandal, S.; Pasricha, R.; Sastry, M.

Chem. Mater. **2003**, *15*, 17. (c) D'Costa, M.; Pasricha, R.; Sastry, M. *J. Mater. Chem.* **2004**, 14, 2696.

(13) (a) Victor F. P.; Krishnan, K.M.; Alivisatos. A. P. *Science* **2001**, *291*,2115. (b) Sun, Y.; Xia**,** Y. *Analyst* **2003**, *128,* 686. (c) El-sayed, M.A. *Acc. Chem. Res.* **2004,** *37*, 326.

(14) (a) Schmid, G. M. *Chem. Rev* **1992**, *92*, 1709. (b) Le Bars, J.; Specht, U.; Bradley, J. S.; Blackmond, D. G. *Langmuir* **1999**, *15*, 7621. (c) Li, Y.; Hong, X. M.; Collard, D. M.; El-Sayed, M. A. *Org. Lett*. **2000,** *2*, 2385. (d) Li, Y.; El-Sayed, M. A. *J. Phys. Chem. B* **2001,** *105*, 8938. (e) Dai, J.; Bruening, M. L. *Nano Lett.* **2002,** *2,* 497. (f) Yoo, J. W.; Hathcock, D.; El-Sayed, M. A. *J. Phys. Chem. A* **2002**, *106*, 2049.

(15) (a) Esumi, K.; Matsuhisa, K.; Torigoe, K. *Langmuir* **1995**, *11*, 3285. (b) Kameo, A.; Suzuki, A.; Torigoe, K.; Esumi, K. *J. Colloid Int. Sci.* **2001**, *241*, 289. (c) Leontidis, E.; Kleitou, K.; Kyprianidou-Leodidou, T.; Bekiari, V.; Lianos, P. *Langmuir* **2002**, *18*, 3659. (d) Brown, K. R.; Walter, D. C.; Natan, M. J. *Chem. Mater.* **2000**, *12*, 306. (e) Jana, N. R.; Gearheart, L.; Murphy, C. J. *J. Phys. Chem. B* **2001**, *105*, 4065. (f) Zhou, Y.; Wang, C. Y.; Zhu, Y. R.; Chen, Z. Y. *Chem. Mater.* **1999**, *11*, 2310. (g) Malikova, N.; Pastoriza-Santos, I.; Scheirhorn, M.; Kotov, N. A.; Liz-Marzan, L. M. *Langmuir* **2002**, *18*, 3694. (h) Zhu, Z.; Liu, S.; Palchik, O.; Koltypin, Y.; Gedanken, A. *Langmuir* **2000**, *16*, 6396.

(16) (a) Chung, S.-W.; Markovich, G.; Heath, J. R. *J. Phys. Chem. B* **1998**, *102*, 6685. (b) Jana, N. R.; Gearhart, L.;. Murphy, C. J. *Chem. Comm*. **2001**, 617.

(17) (a) Sun, Y.; Mayers, B.; Herricks, T.; Xia, Y. *Nano Lett*. **2003**, *3*, 955. (b) Sun, Y.; Xia, Y. *Adv. Mater*. **2002**, *14*, 833. (c) Sun, Y.; Xia, Y. *Science* **2002**, *298*, 2176. (d) Sun, Y.; Xia, Y. *Adv. Mater*. **2003**, *15*, 695. (e) Sun, Y.; Mayers, B. T.; Xia, Y. *Nano Lett*. **2002**, *2*, 481. (f) Sun, Y.; Mayers, B.; Xia, Y. *Adv. Mater*. **2003**, *15*, 641. (g) Sun, Y.; Xia, Y. *J. Am. Chem. Soc*. **2004**, *126*, 3892.

(18) (a) Liang, H.; Zhang, H.; Hu, J.; Guo, Y.; Wan, L.; Bai, C. A*ngew.Chem.Int.Ed.Engl.* **2004**, *43*, 1540. (b) Liang, H. P.; Guo, Y.G.; Zhang, H. M.; Hu, J.S.; Wan, L.J.; Bai, C. L. *Chem. Commun*. **2004**, 1496.

(19) (*a*) Templeton, A.C.; Wuelfing, W. P.; Murray, R. W. *Acc. Chem.Res.*, **2000**, *33*, 27; (*b*) Bönnemann, H.; Hormes, J.; Kreibig, U. in *Handbook of Surface and Interfaces of Materials*, ed. H. S. Nalwa, Academic Press, San Diego, **2001**, **vol. 3**, pp. 1–87; (*c*) El- Sayed, M.A. *Acc. Chem. Res.*, **2001**, *34*, 257.

(20) Kreibig, U.; Genzel, L. *Surf. Sci.*, **1985**, *156*, 678.

(21) (*a*) Henglein, A.; Giersig, M. *J. Phys. Chem. B*, **1999**, *103*, 9533; (*b*) M. M. Alvarez, M. M.; Khoury, J. T.; Schaaff, T. G.; Shafigullin, M. N.; Vezmar, I.; Whetten, R. L. *J. Phys. Chem. B*, **1997**, *101*, 3706; (*c*) Hodak, J. H.; Henglein, A.; Hartland, G. V. *Pure Appl. Chem.*, ***2000***, *72*, 189.

(22) (*a*) Link, S.; Mohamed, M. B.;. El-Sayed, M. A. *J. Phys. Chem. B*, **1999**, *103*, 3073; (*b*) Jana, N. R.; Gearheart, L.; Obare, S. O.; Murphy, C. J. *Langmuir*, **2002**, *18*, 922; (*c*) Murphy, C. J. *Science*, **2002**, *298*, 2139; (*d*) Murphy, C. J.; Jana, N. R. *Adv. Mater.*, **2002**, *14*, 80; (*e*) Oldenburg, S. J.; Averitt, R. D.; Westcott, S. L.; Halas, N. J. *Chem. Phys. Lett.*, **1998,** *288*, 243

(23) Atkins, P. W.; de Paula, J. Physical Chemistry, Seventh Edition, Oxford University Press. Data section page number 1092.

(24) Kumar, A.; Joshi, H. M.; Pasricha, R.; Mandale, A. B.; Sastry, M. *J. Colloid Interface Sci*., **2003**, *264*, 396.

(25) Swami, A.; Kasture, M.; Pasricha, R.; Sastry, M. *J. Mater. Chem*., **2004**, *14*, 709.

(26) (a) Sastry, M.; Patil, V.; Sainkar, S. R. *J. Phys. Chem. B.* **1998**, *102*, 1404. (b) Swami, A.; Selvakannan, PR.; Pasricha, R.; Sastry, M. *J. Phys. Chem. B.* **2004**, *108*, 19269. (c) Zhao, L.; Kelly, K. L.; Schatz G. C. *J. Phys. Chem. B* **2003**, *107,* 7343. (d) Haynes, C. L.; McFarland, A. D.; Zhao, L.; Van Duyne, R.P.; Schatz, G. C. *J. Phys. Chem. B* **2003**, *107,* 7337. (e) Bouhelier, A.; Bachelot, R.; Im, J.S.; Wiederrecht, G.P.; Lerondel, G.; Kostcheev, S.; Royer, P. *J. Phys. Chem. B* **2005**, *109,* 3195.

(27) (a) Hao, E.; Kelly, K. L.; Hupp, J. T.; Schatz, G. C.*J. Am. Chem. Soc***. 2002**, *124*, 15182. (b) Kelly, K. L.; Coronado, E.; Zhao, L.L.; Schatz, G. C.; *J. Phys. Chem. B* **2003**, *107,* 668. (c) Hao, E..; Bailey, R.C.; Schatz, G.C.; Hupp, J.T.; Li S. *Nano Lett*,

2004, *4*, 327. (d) Me´traux, G. S.; Cao, Y. C.; Jin, R.; Mirkin, C. A. *Nano Lett*. **2003**, *3*, 519.

(28) Selvakannan, PR.; Sastry, M. *Chem Commun.* **2005**, 1684.

(29) Link, S.; Wang, Z. I.; El-Sayed, M. A. *J. Phys. Chem. B* **1999**, *103*, 3529.

(30) Shon, Y.-S.; Dawson, G. B.; Porter, M.; Murray, R. W. *Langmuir* **2002**, *18,* 3880.

(31) (a) Whetten, R. L.; Khoury, J. T.; Alvarez, M. M.; Murthy, S.; Vezmar, I.; Wang, Z. L.; Stephens, P. W.; Cleveland, C. L.; Luedtke, W. D.; Landman U. *Adv. Mater.* **1996**, *8*, 428. (b) Murry, C. B.; Kagan, C. R. *Annu. Rev. Mater. Sci.* **2000**, *30*, 545. (c) Brust, M.; Kiely, C. *J. Colloids Surf. A* **2002**, *202*, 175.

(32) (a) Musick, M. D.; Keating, C. D.; Keefe, M.; Natan, M. *J. Chem. Mater.* **1997**, *9*, 1499. (b) Schmitt, J.; Decher, G.; Dressick, W. J.; Brandow, S. L.; Geer, R. E.; Shashidhar, R.; Calvert, J. M. *Adv. Mater.* **1997**, *9*, 61. (c) Ji, T.; Lirtsman, V. G.; Avny, Y.; Davidov, D. *Adv. Mater.* **2001**, *13*, 1253.

(33) (a)Musick, M. D.; Keating, C. D.; Lyon, L. A.; Botsko, S. L.; Pena, D. J.; Holliway, W. D.; McEvoy, T. M.; Natan, M. *J. Chem. Mater.* **2000**, *12*, 2869. (b) Ung, T.; Liz-Marzan, L. M.; Mulvaney, P. *J. Phys. Chem. B* **2001**, *105*, 3441.

(34) Wuelfing, W. P.; Zamborini, F. P.; Templeton, A. C.; Wen, X.; Yoon, H.; Murray, R. W. *Chem. Mater.* **2001**, *139*, 87.

(35) (a) Snow, A. W.; Wohltjen, H. *Chem. Mater.* **1998**, *10*, 947. (b) Doty, R. C.; Yu, H.; Shih, C. K.; Korgel, B. A. *J. Phys. Chem. B* **2001**, *105*, 8291.

(36) (a) Foos, E.E.;Snow, A.W.; Twigg, M.E.; Ancona, M.G. *Chem. Mater.* **2002**, *14*, 2401 (b) Wohltjen, H.; Snow, A. W. *Anal. Chem.* **1998**, *70*, 2856. (c) Zhang, H.-L.; Evans, S. D.; Henderson, J. R.; Miles, R. E.; Shen,T.- H. *Nanotechnology* **2002**, *13*, 439. (d) Evans, S. D.; Johnson, S. R.; Cheng, Y. L.; Shen, T. *J. Mater. Chem*. **2000**, *10*, 183. (e) Krasteva, N.; Besnard, I.; Guse, B.; Bauer, R. E.; Muellen, K.; Yasuda, A.; Vossmeyer, T. *Nanoletters* **2002**, *2*, 551. (f) Vossmeyer, T.; Guse, B.; Besnard, I.; Bauer, R. E.; Muellen, K.; Yasuda, A. *Adv. Mater.* **2002**, *14*, 238.

(37) (a) Mizukoshi, Y.; Fujimoto, T.; Nagata, Y.; Oshima, R.; Maeda, Y. *J. Phys. Chem B ,* **2000**, *104*, 6028. (b) Schmid, G.; West, H.; Mehles, H.; Lehnert, A. *Inorg. Chem.*

1997, *36*, 891.(c) Nashner, M. S.; Frenkel, A. I.; Adler, D. L.; Shapley, J. R.; Nuzzo, R. G. *J. Am. Chem. Soc.* **1997**, *119*, 7760. (d) Schmidt, T. J.; Noeske, M.; Gasteiger, H. A.; Behm, R. J.; Britz, P.; Brijoux, W.; Bo¨nnemann, H. *Langmuir* **1997**, *13*, 2591.

(38) Harikumar, K. R.; Ghosh, S.; Rao, C. N. R. *J. Phys. Chem.A* **1997**, *101*, 536.

(39) (a) Michaelis, M.; Henglein, A.; Mulvaney, P. *J. Phys. Chem.* **1994**, *98*, 6212. (b) Mulvaney, P.; Giersig, M.; Henglein, A. *J. Phys. Chem.* **1993**, *97*, 7061 (c) Henglein, A.; Brancewicz, C. *Chem. Mater.* 1997, *9*, 2164.

(40) (a) Brust, M.; Walker, M.; Bethell, D.; Schiffrin, D. J.; Whyman, R. *J. Chem. Soc.,Chem. Comm*. **1994,** 801 (b) Brust, M.; Fink, J.; Bethell, D.; Schiffrin, D. J.; Kiely, C. J.*J. Chem. Soc., Chem.Comm*. **1995**,1655. (c) Brust, M.; Bethell, D.; Schiffrin, D. J.; Kiely, C.J. *Adv. Mater*. **1995**, *7*, 795

(41) (a) Mandal, S.; Selvakannan, P.R.; Pasricha, R.; Sastry, M. *J. Am. Chem.Soc.* **2003**, *125*, 8440 (b) Bala, T.; Bhame, S. D. ;. Joy, P. A..; Prasad, B. L. V.; Sastry.M.*J . Mater. Chem*. **2004**, *14*, 2941 (c) Rivas, L.; Sanchez-Cortes, S.; Garcia-Ramos, J. V.; Morcillo, G. *Langmuir* **2000**, *16*, 9722. (D) Freeman, R. G.; Hommer, M. B.; Grabar, K. C.; Jackson, M. A.; Natan, M. J. *J. Phys. Chem.* **1996**, *100*, 718.

(42) (a) Hostetler, M. J.; Zhong, C.-J.; Yen, B. K. H.; Anderegg, J.; Gross,S. M.; Evans, N. D.; Porter, M.; Murray, R. W. *J. Am. Chem. Soc.* **1998**, *120*, 9396. (b) Sandhyarani, N.; Pradeep, T. *Chem. Mater.* **2000**, *12*, 1755.(c) Han, S. W.; Kim, Y.; Kim, K. *J. Colloid Interface Sci.* **1998**, *208*, 272.(d) Schmid, G. *Clusters and Colloids*; VCH: Weinheim, **1994**.

(43) Chen, Y.-H.; Yeh, C.-S. *Chem. Comm.* **2001**, 371.

(44) (a) Mayya, K.S.; Sastry, M. *Langmuir* **1999**, *15*, 1902. (b) Taleb, A.; Petit, C., Pileni, M.P. *J. Phys. Chem. B* **1998**, *102*, 2214.

(45) D. A. Shirley, *Phys. Rev. B.*, **1972**, 5, 4709

(46) Tunc, I; Suzer,S; Correa-Duarte,M.A.; Liz-Marza´n,L.M., *J. Phys. Chem. B,* **2005**, *109,* 7597

(47) Leff, D. V.; Brandt, L. ; Heath, J. R. *Langmuir* **1996**, *12*, 4723.

(48) Hill, R.M. *Proc. Roy. Soc. A*, **1969**, *309*, 377.

(49) (a) Wuelfing, W.P.; Murray, R.W. *J. Phys. Chem. B* **2002**, *106*, 3139. (b) Wessels, J.M.; Nothofer, H.G.; Ford, W.E.; Wrochem, F.V.; Scholz, F.; Vossmeyer, T.; Schroedter, A.; Weller, H.; Yasuda, A. *J. Am. Chem. Soc.* **2004**, *126*, 3349.

(50) De Renzi, V.; Rousseau, R.; Marchetto, D.; Biagi, R.; Scandolo, S.; del Pennino, U. *Phys. Rev. Lett.* **2005**, *95*, 46804

(51) Asscher, M.; Rosenzweig, Z. *J. Vac. Sci. Technol. A* **1991**, *9*, 1913

(52) (a) Caruso, F. *Ad*V. *Mater.* **2001**, *13*, 11. (b) Sauer, M.; Streich, D.; Meier, W. *Ad*V. *Mater.* **2001**, *13*, 1649. (c) Bergbreiter, D. E. *Angew. Chem., Int. Ed. Engl.* **1999**, *38*, 2870. (d) *Hollow and Solid Spheres and Microspheres: Science and Technology Associated with Their Fabrication and Application*; Wilcox, D. L., Sr.; Berg, M.; Bernat, T.; Kelleman, D.; Cochran Jr., J. K.; Eds.; MRS Proceedings Vol. 372; Materials Research Society: Pittsburgh, PA, **1994.** (e) Wooley, K. L. *Chem. Eur. J.* **1997**, *3*, 1397.

(53) (a) Mathlowitz, E.; Jacob, J. S.; Jong, Y. S.; Carino, G. P.; Chickering, D. E.; Chaturvedl, P.; Santos, C. A.; Vijayaraghavan, K.; Montgomery, S.; Bassett, M.; Morrell, C. *Nature* **1997**, *386*, 410. (b) Huang, H.; Remsen, E. E.; Kowalewski, T.; Wooley, K. L. *J. Am. Chem.Soc.* **1999**, *121*, 3805. (c) Gill, I.; Ballesteros, A. *J. Am. Chem. Soc.***1998**, *120*, 8587.

(54) Ohmori, M.; Matijevic, E. *J. Coll. Interface Sci.* **1992**, *150*, 594.

(55) (a) Sarkar, D.; Halas, N. J. *Phys. Re*V. *E* **1997**, *56*, 1102. (b) Neeves, A. E.; Birnboim, M. H. *J. Opt. Soc. Am. B* **1989**, *6*, 787.

(56) (a) Jackson, J. B.; Halas, N. J. *J. Phys. Chem. B* **2001**, *105*, 2473. (b) Westcott, S. L.; Oldenburg, S. J.; Lee, T. R.; Halas, N. J. *Chem. Phys. Lett.* **1999**, *300*, 651.

(57) (a) Philipse, A. P.; van Bruggen, M. P. B.; Pathmananoharan, C. *Langmuir* **1994,** *10*, 92. (b) Chang, S. Y.; Liu, L.; Asher, S. A. *J. Am. Chem. Soc.* **1994**, *116*, 6739. (c) Giersig, M.; Ung, T.; Liz- Marza´n, L. M.; Mulvaney, P. *Ad*V. *Mater.* **1997***, 9*, 570. (d) Yao, H.; Takada, Y.; Kitamura, N. *Langmuir* **1998***, 14*, 595. (e) Ung, T.; Liz-Marza´n, L. M.; Mulvaney, P. *Langmuir* **1998**, *14*, 3740.

(58) (a) Caruso, R. A.; Antonietti, M. *Chem. Mater.* **2001**, *13*, 3272. (b) Zhong, Z.; Yin, Y.; Gates, B.; Xia, Y. *Ad*V. *Mater.* **2000**, *12*, 206. (c) Caruso, F.; Lichtenfeld, H.; Giersig, M.; Mo¨hwald, H. *J. Am. Chem. Soc.* **1998**, *120*, 8523. (d) Caruso, F.; Caruso, R. A.; Mo¨hwald, H. *Science* **1998**, *282*, 1111. (e) Marinakos, S. M.; Novak, J. P.; Brousseau III, L. C.; House, A. B.; Edeki, E. M.; Feldhaus, J. C.; Feldheim, D. L. *J. Am. Chem. Soc.* **1999**, *121*, 8518. (f) Fleming, M. S.; Mandal, T. K.; Walt, D. R. *Chem. Mater.* **2001**, *13*, 2210.

(59) Gao, P. Weaver, M. J. *J. Phys. Chem.*, **1986**, *90*, 4057.

(60) (a) Pileni, M. -P. *Nat. Mater.* **2003**, *2*, 145. b) Filankembo, A.; Pileni M. P. *Appl. Surf. Sci.* **2000**, *164*, 260. c) Filankembo, A.; Pileni M. P. *J. Phys. Chem. B* **2000**,*104*, 5865. d) Pileni M. P. *Langmuir* **2001,** *17,* 7476 e) Pileni M. P. *C. R. Chimie* **2003**, *6*, 965. f) Filankembo, A.; Giorgio, S.; Lisiecki, I.; Pileni M. P. *J. Phys. Chem. B* **2003,** *107,* 7492. g) Kitchens, C. L.; McLeod, M. C.; Roberts C. B. *Langmuir* **2005,** *21,* 5166. h) Im, S. H.; Lee, Y. T.; Wiley, B.; Xia Y. *Angew. Chem., Int. Ed. Engl.* **2005**, *44*, 2154.

(61) (a) K. George Thomas, J. Zajicek, and Prashant V. Kamat *Langmuir* **2002,** *18,* 3722 (b) Cheng, W.; Dong, S.; Wang, E. *Angew. Chem. Int. Ed.*, **2003**, *42*, 449.

(62) (a) Rai, A.; Singh, A.; Ahmad, A.; Sastry, M. *Langmuir* **2006,** *22,* 736-741 (b)Shankar, S. S.; Bhargava, S.; Sastry, M. *J. Nanosci. Nanotech.* **2005**, *5*, 1721.

(63) Wasileski S. A.; Weaver, M. J. *J. Phys. Chem. B*, **2002**, *106*, 4782.

(64) Zhang, P.; Sham, T. K. *Phys. Rev. Lett.*, **2003**, *90*, 245502. b) Prasad, B. L. V.; Stoeva, S. I.; Sorensen, C. M.; Klabunde, K. J. *Chem. Mater.*, **2003**, 15, 935.

(65) Magnussen, O. M.; Ocko, B. M.; Adzic R. R.; Wang. J. X. *Phys. Rev.*, *B* **1995**, *51*, 5510. b) Magnussen, O. M.; Ocko, B. M.; Wang J. X.; Adzic, R. R. *J. Phys.Chem.*, **1996**, *100*, 5500. c) Ocko B. M.; Watson, G. M.; Wang, J. *J. Phys. Chem.*, **1994**, *98*, 897. d) Gao, X.; Weaver, M. J. *J. Phys. Chem.*, **1993**, *97*, 8685.

(66) Cheng, W.; Dong, S.; Wang, E. *Angew. Chem. Int. Ed.*, **2003**, *42*, 449.

(67) (a) Bowmaker, *G.* A.; Whiting, R. *Aust. J. Chem.* **1976,** *29,* 1907. (b) Breitinger, D.; Leuchtenstern, H. *Z. Noturforsch.* **1974**, *29b,* 1974.

CHAPTER VI

Synthesis of catalytically active Porous Platinum Nanoparticles

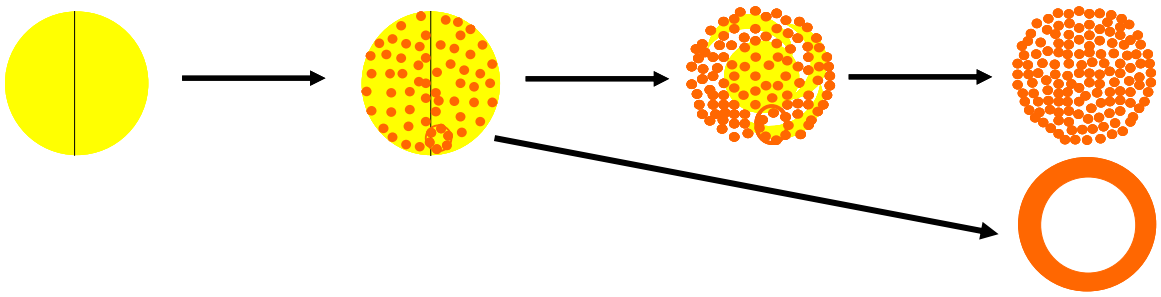

This chapter focuses on the synthesis of porous platinum nanoparticles at the air-water interface. Transmetallation reaction between the hydrophobized Ni nanoparticles and subphase chloroplatinate ions resulted in the formation of porous pt nanoparticles. Porous Pt nanoparticles synthesize by the method, displayed excellent catalytic activity.

Part of the work presented in this chapter has been communicated:

1) Pasricha, R.; Bala, T.; Biradar,A.; Umbarkar, ;Sastry, M., *Small*, **2007** (communicated).

6.1 Introduction

Development of protocols for the synthesis of metal nanoparticles of variable size and shape constitutes an area of research of considerable topical interest. Exciting application of metal nanoparticles in electronics [1], magnetic memories [2], biolabeling / biosensors [3], and catalysis [4] has to a large extent motivated researchers to synthesize them employing different methodologies. There are a number of methods available in the literature for synthesis of noble metal nanoparticles of different shapes other than spheres such as rods, triangles, wires and cubes [5].

In the previous chapter we have discussed the galvanic exchange reaction between hydrophobic silver nanoparticles assembled and constrained at the air-water interface and gold ions in the subphase. This resulted in the synthesis of elongated gold nanostructures. The reduced gold (Au) appears to cross-link the sacrificial hydrophobized silver nanoparticles constrained at the interface. This transmetallation reaction could be modulated by the insertion of an electrostatic barrier in the form of an ionizable lipid monolayer between the silver nanoparticles and the aqueous gold ions that impacts the gold nanoparticle assembly. Transmetallation between nanoparticles constrained into a close-packed structure and appropriate metal ions leads to a new strategy and interesting morphologies with promising application. This motivated us to carry out the same reaction at liquid-liquid interface. In the same series, to obtain different morphologies we had thereafter carried out the galvanic exchange between gold ions and silver nanoparticles by arresting the gold ions using different surfactants at the interface on the aqueous subphase containing silver nanoparticles.

By synthesizing nanoparticles of different shapes, their surface plasmon resonant absorption can be shifted anywhere from visible to the near infrared region depending upon the extent of anisotropy introduced in the shape [5]. The shape of the nanoparticles not only affects its optical properties but also, it influences the surface reactivities. Shape dependent surface reactivity is reflected in their catalytic activities. The activity of a catalyst depends upon the face exposed for adsorption of the reactants. In heterogeneous catalysis it was observed that gas molecules display differential adsorption on different

faces of the catalyst. Thus metal nanoparticles of different shapes covering different faces can be good candidates for molecule specific catalysis [6]. Size and shape are not the only two variables to tune the properties of nanomaterials; the presence of "holes and pores" in nanomaterials proves to be an additional variable to tune their properties. Introducing holes and pores in a nanomaterial reduces its density much faster than its strength, hence providing advantages like enhanced surface area, saving of material and cost reduction.

Nature provides plenty of examples of these kinds of porous materials and one such example is bone. Its open, porous structure not only provides spaces for capillaries and tissues to pass through, but also reduces its density, thereby making it lighter in weight [7]. The possibility of encapsulating drug molecules in the voids of porous and hollow nanomaterials and releasing them at the desired places can find applications in targeted drug delivery systems in future [8]. For a given volume, hollow and porous nanoparticles provide higher surface area than their solid counterparts with less amount of material [9]. While the synthesis of porous and hollow nanoparticles of polymer [10] and metal oxides [11] are well documented, synthesis of hollow and porous metal nanoparticles is relatively less explored. Hollow metal nanoparticles occupy an important position in the current scenario mainly due to their optical and catalytic properties. Xia and co-workers have demonstrated that the surface plasmon resonance sensitivity towards the environmental changes is higher in the case of hollow metal nanoparticles than their solid counterparts [12]. Halas and coworkers demonstrated the synthesis of gold nanoshells of different thickness on a silica core and found that their optical properties are a function of relative thickness of the shell against its core diameter [13]. Recently Sastry and coworkers have shown the synthesis of porous gold nanostructures in a controlled manner and its application in cell imaging [14]. The absorption in the NIR region by gold nanoshells makes them attractive therapeutic agents against cancer [15]. Gold nanoparticles can be easily conjugated with biomolecules like DNA and proteins. Sastry and coworkers have reviewed the interactions between them in a recent account [16]. Thus, the tunable optical properties and biocompatibility makes gold nanoshells

viable for both biological imaging and therapeutic applications [17]. Application of noble metal nanoparticles in catalysis has predictably centered around Pt and Pd nanoparticles [18,19] because of their ability to catalyze various organic reactions namely olefin hydrogenation [18,20], carbon-carbon coupling including the Heck and Suzuki reactions [21]. Currently there is significant interest in research areas focused on alternative energy sources that would accomplish future energy demands without pollution. One of the best alternatives to fossil fuels is fuel cell technology, which uses hydrogen and oxygen and generates water as a byproduct, thus promising to be a cleaner and cheaper energy sources. The main step in fuel cells is the generation of hydrogen, and platinum was found to be the best catalyst for the production of hydrogen from methane [22]. The cost of platinum is the only inhibiting factor but that can be overcome by using porous and hollow platinum nanoparticles, which require much less amount of platinum than their solid counterparts. These nanoshells have a very high surface area and low density, therefore the usage of catalytically active nanoparticles like platinum and palladium in large amounts can be avoided. Development of techniques to produce Pt catalysts with an increased surface area to achieve enhanced catalytic performance and utilization efficiency would make these processes economically viable. All these applications highlight the significance of hollow metal nanoparticles and synthesizing them with good control over the dimensions of holes and pores is an essential step towards further applications in this direction. The solution to this lies in a different morphology of nanomaterials: hollow metallic nanostructures and porous nanostructures because of their advantages of high specific surface and low density, which can save the raw materials and reduce the cost. They are expected to show enhanced catalytic activities compared to their solid counterparts [12, 23, 24]. There are two approaches followed to synthesize hollow metal nanoparticles. In one approach, preformed nanoparticles are deposited onto some colloidal templates to form core-shell type of nanostructures [25], followed by the removal of template resulting in the formation of hollow metal particles. Polymer latex particles and silica beads are the commonly used colloidal templates [26]. In the other approach, galvanic replacement of one metal nanoparticle species by the other metal ions

results in the formation of hollow nanoparticles that take on the morphology of the sacrificial partner. This type of galvanic replacement of one type of metal nanoparticles with suitable metal ions is called transmetallation reaction. Silver [27] and cobalt [28] nanoparticle are the commonly used sacrificial cores for such transmetallation reaction with gold and platinum ions. Recently Xia and co-workers have shown a simple and versatile route to the large-scale synthesis of gold nanostructures with well defined hollow interiors [27]. Based on this protocol, hollow structures of gold of different morphologies have been synthesized using different nanoscale templates like silver cubes, triangles etc [27b].

Mirkin and co-workers have also followed a similar strategy to form nanoframes using silver prisms as templates [27]. However, all the methods have the common disadvantage of formation of silver chloride during the reaction between silver nanoparticles with chloroaurate ions. This problem has been avoided by high temperature refluxing as demonstrated by Xia and coworkers. Wan and co-workers avoided this problem by using cobalt nanoparticles instead of silver nanoparticles as sacrificial templates due to the good solubility of the by-product cobalt chloride [28]. Recently Alivisatos and co-workers have shown the synthesis of hollow nanoparticles by the nanoscale Kirkendall effect [29]. Sastry et al. has demonstrated the synthesis of hollow Au and Pt nanoparticles by similar transmetallation reaction in the organic phase [30]. They have also shown the formation of hollow bimetallic Au/Ag nanoshells in aqueous medium with great control over the rate of the reaction [31]. Bai and coworkers have reported a facile method based on replacement reactions for large-scale synthesis of Pt hollow nanoparticles exploiting Co nanoparticles as sacrificial templates [32], the catalyst thus produced was effective in the reaction like oxidation of methanol. An understanding of the mechanism of hollow nanostructures formation via transmetallation reactions has been complicated by the fact that control over the rate of reaction, particularly at room temperature, is difficult to achieve [33].

With a focus on obtaining porous platinum nanoparticles which can be used as a potential catalytic material, we have tried the galvanic exchange between nickel

nanoparticles and platinum ions. The key idea of our method for synthesis of Pt porous nanoparticles is to exploit the replacement reaction between Ni nanoparticles and H_2PtCl_6. As the standard reduction potential of the $PtCl_6^{2-}$/Pt redox pair (0.735 V vs. the standard hydrogen electrode (SHE)) is much higher than that of the Ni^{2+}/Ni redox pair (-0.257 vs. SHE), Ni nanoparticles are immediately oxidized to Ni^{2+} ions when the aqueous Ni nanoparticles are allowed to react with H_2PtCl_6 solution. As this replacement reaction occurs rapidly, Pt atoms nucleate and grow as very small particles, initially organizing themselves at the periphery of the bigger nickel nanoparticle assuming a thin shell of Pt like appearance on the Ni nanoparticles. This shell initially has an incomplete porous structure because Ni^{2+} and $PtCl_6^{2-}$ continuously diffuse across the boundary until the Ni nanoparticles have been completely consumed. The expected galvanic exchange reaction between Ni nanoparticles with H_2PtCl_6 is given by the following equation:

$$2Ni + PtCl_6^{2-} \longrightarrow Pt + 2Ni^{2+} + 6Cl^-$$

In an attempt to find the mechanism we have tried to synthesize nano porous platinum by transmetallation in solution. The reaction was completed within ten minutes of addition of H_2PtCl_6 into the Ni solution. Catalytic activity shown by this system for hydrogenation of nitrobenzene to aniline was very encouraging. However from the morphologies of the products, it was not possible to deduce the mechanism. Furthermore, and there also were Pt nanoparticles synthesized in solution in addition to the porous platinum nanoparticles. Thus, in an attempt to have a controlled reaction and to have an idea regarding the mechanism of the reaction, we have performed the reaction at the air-water interface. The constrained environment at the interface can slow the rate of the transmetallation. Consequently what we obtained is a genuine strategy for the preparation of two-dimensional arrangement of highly catalytically active porous platinum nanoparticles in thin films by an elegant and simple transmetallation reaction. The air water interface has earlier been used for the synthesis of silver/gold core shell nanoparticles by diffusion limited aggregation (DLA) by thermoaccelerated electroless plating by Dong et al [34], where the plating temperature was a crucial vehicle. To the

best of our knowledge, the air-water has never been used for the synthesis of a highly active Pt catalyst at room temperature.

6.2 Synthesis and Characterization

6.2.1 Synthesis and phase transfer of Ni nanoparticles

The detailed synthesis of aqueous Ni nanoparticles has been described earlier by Sastry and coworkers [35]. In a typical experiment, 100 ml aqueous solution containing 1×10^{-3} M $Ni(NO_3)_2$ and 5×10^{-4} M oleic acid in methanol was added with 0.045 gm of $NaBH_4$ and stirred for ≈10 min. The colour of the solution immediately turned black, scheme 6.1, step1. 25 ml of this aqueous Ni nanoparticle solution was then taken in a conical flask along with 25 ml of 1×10^{-3} StA (stearic acid) in toluene. While the biphasic mixture was stirred, 0.25 gm of NaCl was directly added to the mixture and the stirring was continued for ≈10 – 12 h. At the end of the process, the organic phase turned black, indicating the phase transfer, scheme 6.1, step2. The organic layer was separated from the colorless aqueous layer using a separating funnel. The organic layer was again stirred with 25 ml of aqueous Ni nanoparticles solution and the process was repeated many times till the organic phase saturates with Ni nanoparticles. This saturated organic layer was then dried by evaporating the solvent using rota-vapour. The dried sample was washed with ethanol thrice to remove any uncoordinated StA. The dried mass was weighed and dissolved in chloroform keeping the overall concentration at 1 mg/ml.

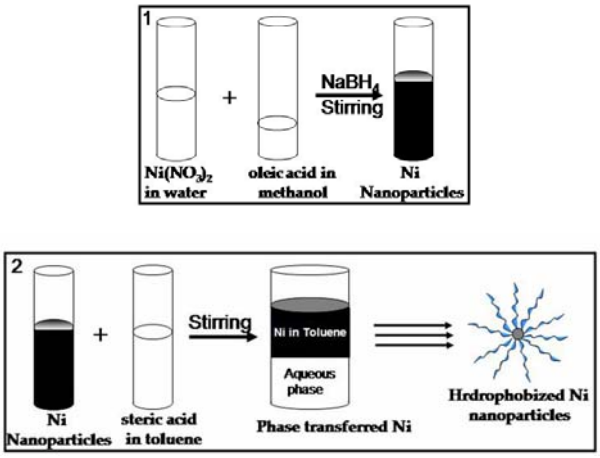

Scheme 6.1 *Schematic (not to scale) showing preparation of hydrophobic Ni nanoparticles. Step 1: Preparation of Ni nanoparticles. Step2: Phase transfer of Ni nanoparticles in organic phase toluene using StA.*

6.2.2 UV-vis spectroscopy

Figure 6.1 shows the UV-vis spectra recorded from the oleic acid capped Ni nanoparticles in aqueous solution (Curve 1) and Ni nanoparticles after phase transfer by StA in toluene (Curve 2). Both the spectra depict a typical monotonous increase in absorbance [36], which matches well with the reported UV-Vis spectrum of Ni nanoparticles [36]. Curve 3 in Figure 6.1 evidences the UV-Vis spectra recorded from the aqueous part after the completion of phase transfer. The absence of any absorbance clearly indicates the complete phase transfer of Ni nanoparticles to toluene in presence of StA.

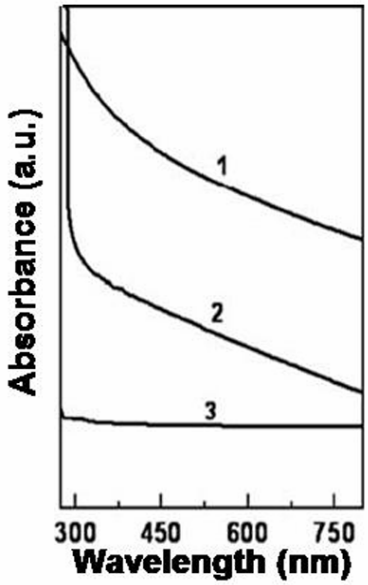

Figure 6.1 *UV-Vis spectra of Ni nanoparticles in aqueous (curve 1) and organic phase (curve 2).The UV-Vis spectrum of the aqueous phase after complete phase transfer is depicted as curve 3 which indicates a complete phase transfer of Ni nanoparticles from aqueous to organic medium.*

6.2.3 Fourier transform Infrared spectroscopy

The stability imparted to the Ni nanoparticles in aqueous medium originates from the capping of oleic acid on the surface of the Ni nanoparticles. The interaction of Ni nanoparticles with the organic molecules adsorbed on the surface can be proved from a careful FTIR study (Figure 6.2). *Curve 1* in Fig. 6.2 denotes the FTIR spectra for pure oleic acid which shows–COOH stretch at 1707 cm^{-1} and the C=C-H stretching vibration at 3004 cm^{-1} [37]. The carboxylic stretch shifts to 1561 cm^{-1} in aqueous Ni nanoparticles

capped only with oleic acid *(Curve 2)* and there is a complete disappearance of 3004 cm^{-1} peak. This observation leads to the hypothesis that probably oleic acid molecules are randomly oriented on the surface and the electron rich double bond interacts significantly with the nanoparticles. However, the carboxylic groups are also bound to the surface thereby showing a large shift in the value of its vibrational modes. The -COOH groups, which are exposed towards the solvent, are also bound to the Na^{+}, hence no free -COOH peak is observed. The oleic acid capped nanoparticles, when phase transferred to toluene using StA, display the retention of the peak at 1561 cm^{-1} along with the appearance of a peak at 1682 cm^{-1} *(Curve 4)*. The pure StA shows the –COOH band at 1701 cm^{-1} *(Curve 3)* and a shift to 1682 cm^{-1} *(Curve 4)* indicates its binding to the nanoparticle surface.

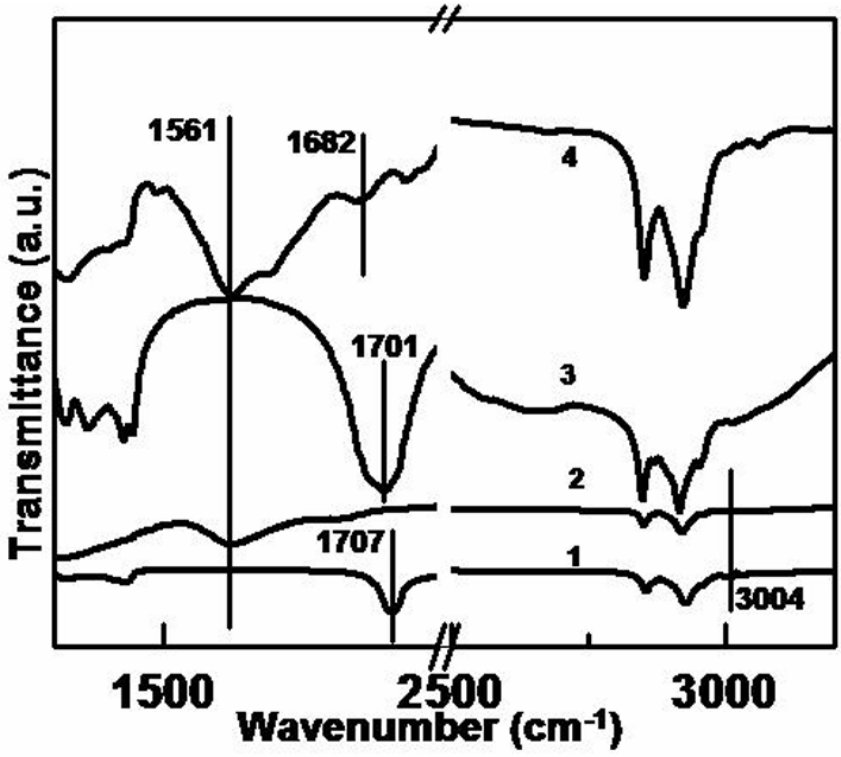

Figure 6.2 *The FTIR spectra of pure oleic acid (curve 1) and pristine oleic acid capped Ni nanoparticles (curve 2).The pure StA spectrum (curve 3) and Ni nanoparticles after phase transfer (curve 4) are also presented.*

A very careful observation reveals that there is a small hump at 3007 cm^{-1} *(Curve 4)* which can arise due to the detachment of the double bond of oleic acid from the surface of the Ni nanoparticles. This suggests that some of the bound oleic acid

molecules are probably exchanged with StA molecules imparting a hydrophobic nature to the surface of nanoparticles. The hydrocarbon chain is thus exposed to the solvent environment, bringing about the phase transfer. The pristine oleic acid capped Ni nanoparticles when stirred with only an organic solvent like toluene or cyclohexane in absence of StA, formed aggregates at the interface without any phase transfer to the organic medium. On the other hand in this case, StA could either be interacting with the –COOH group of oleic acid through hydrogen bonding or place exchanging some of the oleic acid molecules on the Ni surface and both the phenomena lead to exposure of the hydrophobic aliphatic chain of ligand acids to the organic solvent environment facilitating the phase transfer.

6.2.4 Assembly of hydrophobized Ni nanoparticles by the Langmuir-Blodgett technique

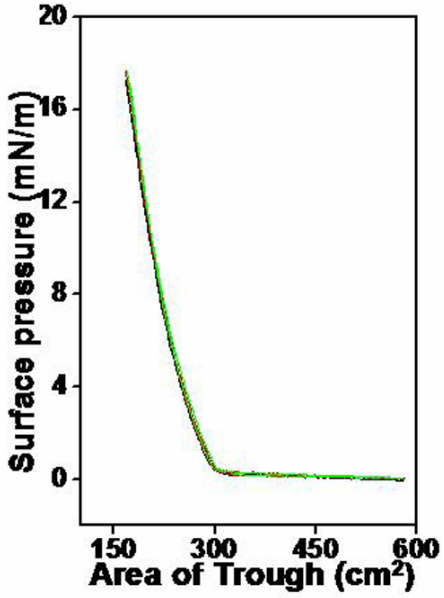

Figure 6.3 *The surface pressure-area isotherm recorded during compression and expansion cycle of hydrophobized Ni nanoparticles when spread on the subphase of distilled water. Isotherms were recorded 10 min (curve 1, black) and 15 min (curve 2, red) and 30 min (curve 3, green) after spreading the monolayer.*

The hydrophobized Ni nanoparticles capped with oleic acid and StA were weighed and dissolved in chloroform keeping the concentration as 1 mg/ml. A known volume of this solution was spread on the surface of double distilled water at pH 6.5. Figure 6.3 exemplifies the π-A isotherm recorded from the Langmuir monolayer at the

air/water interface. Surface pressure (π)- area (*A*) isotherms were measured at 25°C as a function of time of spreading the monolayer with the compression and expansion speed of 20 cm^2/min. A standard Wilhelmy plate was used for surface pressure sensing. An optimum surface pressure of 15 mN/m was selected as the pressure for deposition of the film onto various substrates for characterizations at deposition rate of 25 mm/min with a waiting time of 60 sec between the consecutive dips. This result combined with the fact that TEM images (vide infra) obtained from these assemblies do not show any multiple layer formation point to the presence of compact monolayer. It is observed that the monolayers formed are quite stable as indicated by the π-A isotherm with time presented in Figure 6.3. The isotherms show no shift and no significant change with time. No hysteresis is observed in the curve at t=10 min *(black)*, t=15 min cases *(red)* and t=30 min (*green*) cases.

6.2.5 Transmission Electron Microscopy

Fig. 6.4 A-D illustrates the transmission electron micrographs of drop coated and dried Ni nanoparticles from the aqueous solution on to the 400 mesh carbon coated copper grid. The micrographs (Figures 6.4A, B) show no apparent arrangement of the nanoparticles and the particle size analysis indicates a bimodal distribution with the average size in the range of 42±3 nm and 90±5 nm. The higher magnification image (Figure 6.4C) shows that many of the nickel nanoparticles have surface defects (indicated by arrow). Figure 1D shows the HRTEM image of one of the nickel nanoparticles. It can be seen from the micrograph that the particle is clearly polycrystalline, showing the presence of (111) and (200) planes of fcc Ni very near to the surface of the particle. This indicates that the Ni nanoparticles prepared by our synthetic method are polycrystalline and also proves the absence of any crystalline NiO_2 layers at the surface. The polycrystalline nature is further confirmed by the diffraction pattern (inset Fig. 6.4D) obtained by aligning the electron beam perpendicular to one of the spherical Ni nanoparticle. The diffraction displays a very diffuse and broad ring like pattern further confirming the polycrystalline nature of the Ni nanoparticles. The rings can be indexed to fcc structure of Ni [39].

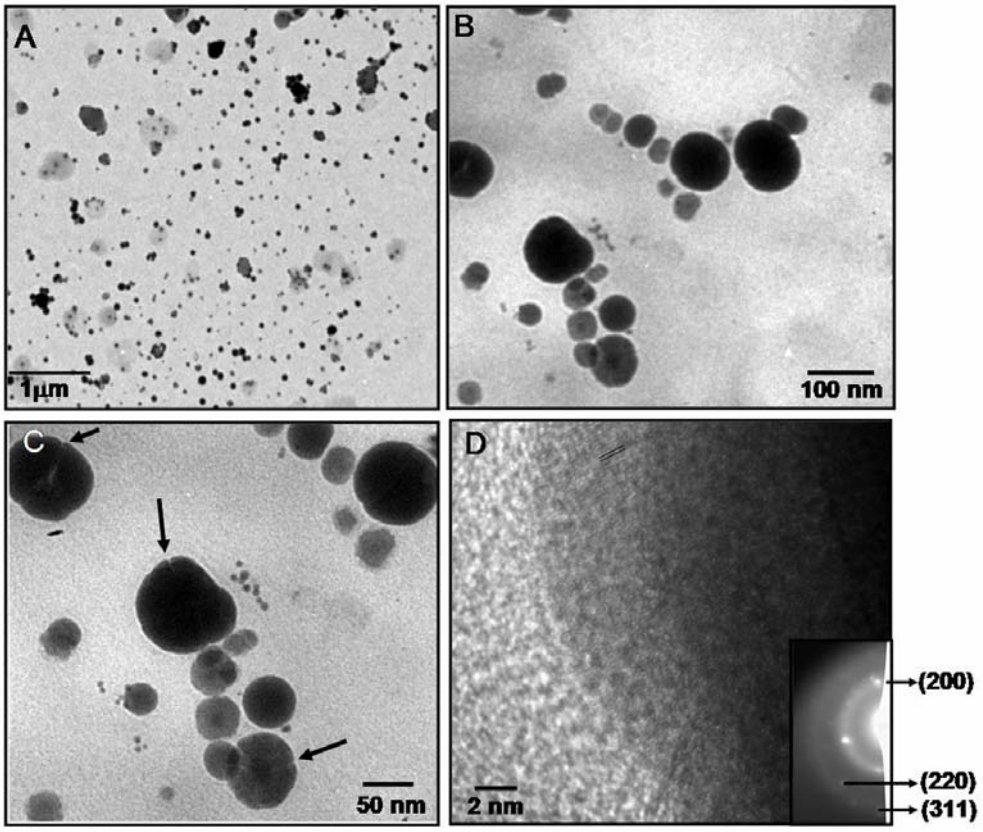

Figure 6.4 *(A) - (C) TEM images of oleic acid capped Ni nanoparticles in aqueous phase recorded at different magnifications. (D) HRTEM image of one of the nickel nanoparticle showing the lattice distance to be ≈ 0.124 nm, inset demonstrates the diffused ring pattern with (200), (220) and (311) hkl planes of fcc Ni. All the micrographs were recorded from the drop cast film from the aqueous phase.*

Figure 6.5A depict the TEM picture of the drop coated hydrophobized Ni nanoparticles. The aqueous Ni nanoparticles, when phase transferred to toluene containing StA, retain the bimodal distribution but lack any clear arrangement. In contrast, Figure 6.5B-F show the TEM images of the monolayer formed on LB trough. The film of 150 microlitre of hydrophobized Ni solution was compressed at 15 mN/m surface pressure and was transferred to the TEM grid by vertical dipping. The images show long range compact linear ensemble of the Ni nanoparticles at the air water interface.

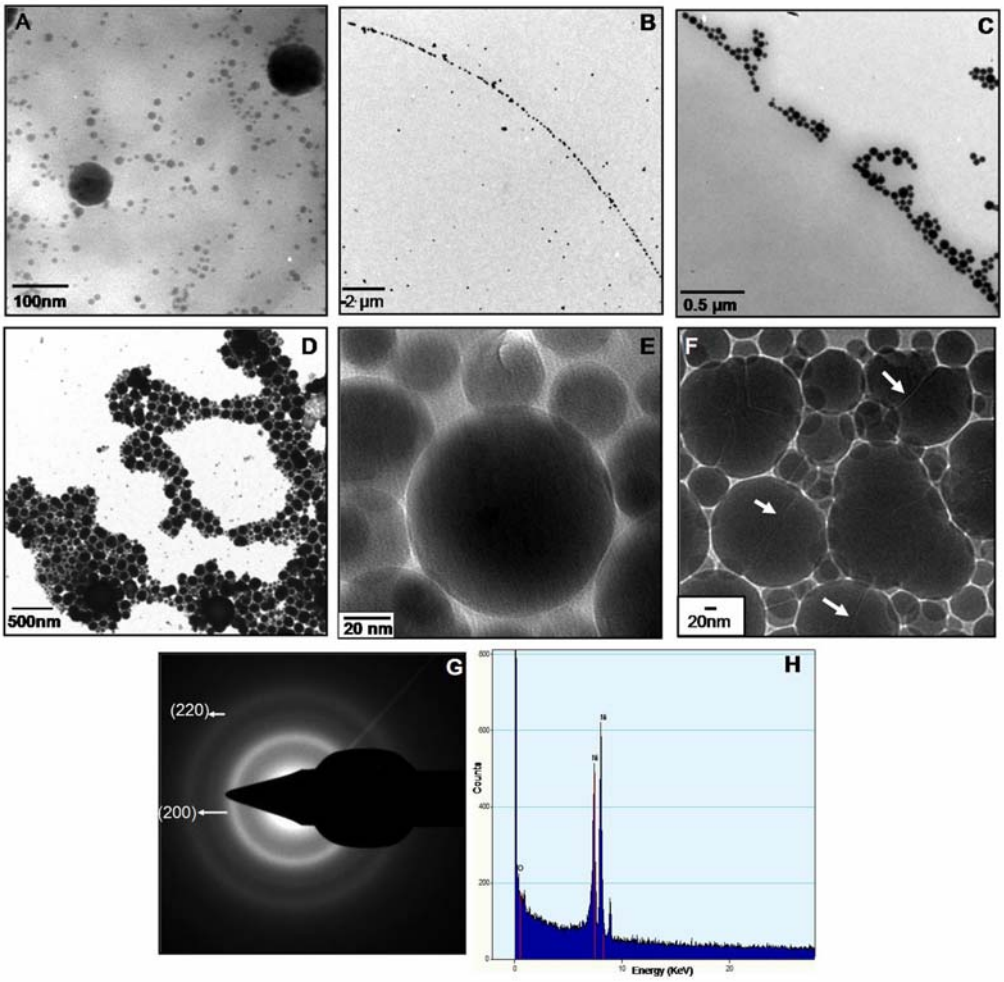

Figure 6.5 *Representative TEM images obtained (A) from drop coated solution of hrdrophobized Ni (B-F) when the Ni nanoparticles monolayer was transferred on to a TEM grid after compressing the monolayer to 15 mN/m surface pressure. The linear arrangement of the particles is visible at lower magnification (B–D) whereas the internal arrangement of the bigger and smaller particles is evidenced in (E-F). (E) shows a perfect hcp arrangement of the monolayer. The high resolution TEM image in (F) shows the Ni nanoparticles with defect sites (marked with arrows). The SAED pattern in (G) reveals diffused ring pattern of fcc Ni. (H) shows the EDAX measurement from one of the Ni particles.*

Most of the linear arrangements have internal assemblies of the Ni nanoparticles with bimodal size distribution. They form large two-dimensional hexagonally close packed domains as evident in Figure 6.5D. The void space in between the linear structures can be attributed to the presence of many components viz. the un-coordinated oleic acid or StA molecules in the Langmuir layer [35]. Nevertheless it is observed that

the monolayers formed are quite stable as documented by the π-*A* isotherm with time and shows no significant hysteresis. We clearly see the longer as well as smaller linear ensemble of Ni nanoparticles and the internal arrangement of the small and relatively bigger particles (Figure 6.5D-F). It is reported that for purely monodisperse particles regular hexagonal close-packed monolayer films are formed using Langmuir Blodgett technique. However, particles having well-defined bimodal size distributions can organize themselves into complex, ordered two-dimensional arrays. The magnified images (Figure 6.5E-F) clearly show the arrangement of the two kinds of particles in the assembly. The bigger particles (avg size ~90 nm) are surrounded by the smaller ones (average size ~42 nm) making the assembly more compact. From the particle size measurement and the theoretical calculation the radius ratio of the smaller to bigger particle is evaluated to be R_B/R_A = ~ 0.47 ($R_A > R_B$) which predicts an AB_2 type distribution when ensembled on Langmuir Blodgett trough. The TEM images reveal the expected structure showing a clear parallelism between the bimodal structures formed and those predicted either for atomic scale intermetallic alloys or for colloidal crystals based on the geometrical packing of hard spheres [40-41]. Figure 6.5F depicts the surface defects in the Ni particles arranged at the air water interface, indicated by the arrows.The SAED pattern is presented in the Figure 6.5G. The most intense ring in the SAED pattern can be matched with the (200) plane of fcc Ni (a= b= c= 3.523, space group= Fm3m, PCPDF # 040850). Figure 6.5H shows the EDAX pattern from one of the Ni nanoparticles, confirming the presence of only Ni.

6.3 Transmetallation reaction in aqueous solution

The transmetallation reaction between oleic acid capped nickel nanoparticles and chloroplatinic acid (H_2PtCl_6) was carried out in aqueous medium at room temperature. 100 ml of purified aqueous Ni nanoparticles were taken and to this 20 ml of 10^{-4} M of H_2PtCl_6 was added in a drop wise manner stirring the mixture continuously for the effective mixing of the two reactants, Scheme 6.2. This mixture was then stirred for 30 min continuously on the magnetic stirrer and at different time intervals of the

transmetallation reaction the solution was drop coated onto the grids for TEM analysis to study the changes occurring during the reaction.

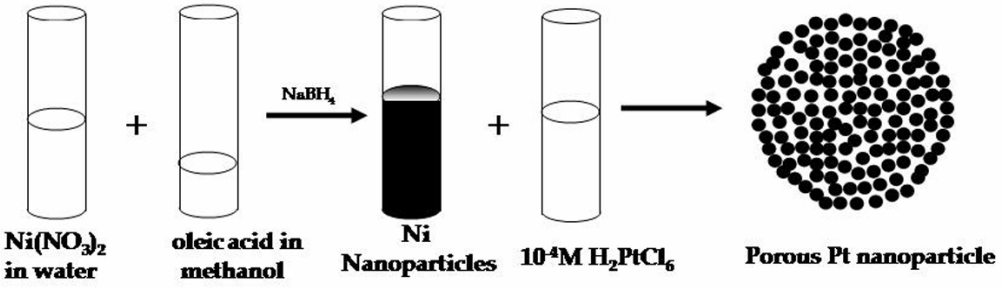

Scheme 6.2 *Schematic of the transmetallation reaction in aqueous phase (not to scale)*

6.3.1 Transmission Electron Microscopy

Morphological changes evolved during the transmetallation reaction

Fig. 6.6 A-D illustrate the transmission electron micrographs of the structures generated after transmetallation of Ni nanoparticles with H_2PtCl_6 in aqueous solution, drop coated on to the 400 mesh carbon coated copper grid. The images represent different regions of the drop coated grid after 30 min of the transmetallation with 10^{-4} M H_2PtCl_6 at room temperature in solution. It is evident from the micrographs that the galvanic exchange between platinum ion and sacrificial Ni particles is taking place that brings a morphological change on the surface of the Ni nanoparticles. Figure 6.6 A shows that the reduction of platinum particles is mainly concentrated around the Ni particles showing a tendency to generate core-shell structure. But Figure 6.6 B shows the platinum particles all over the region where there is no trace of Ni. Figure 6.6 C shows formation of porous platinum nanoparticles after consumption of Ni nanoparticles by the platinum ions, whereas Fig 6.6 D shows core shell structures. These porous Pt nanoparticles are actually an arrangement or aggregate of smaller Pt nanoparticles. It was found from the TEM micrographs that the centers of the porous arrangement of Pt nanoparticles are darker than the edges indicating a spherical structure. The average diameter of the porous structures was statistically calculated to be 42±3nm and 90±4nm, which is comparable to the size of nickel particles . It was found that in case of the core shell like structures the average diameters of the spheres have increased in size as compared to the initial size of

the sacrificial Ni nanoparticles by 2-3nm. This may be due to the deposition of platinum on the surface of Ni nanoparticles. The presence of multiple structures may be due to the fact that the different morphologies (core shell and porous nanoparticles) are at different stages of the reaction.

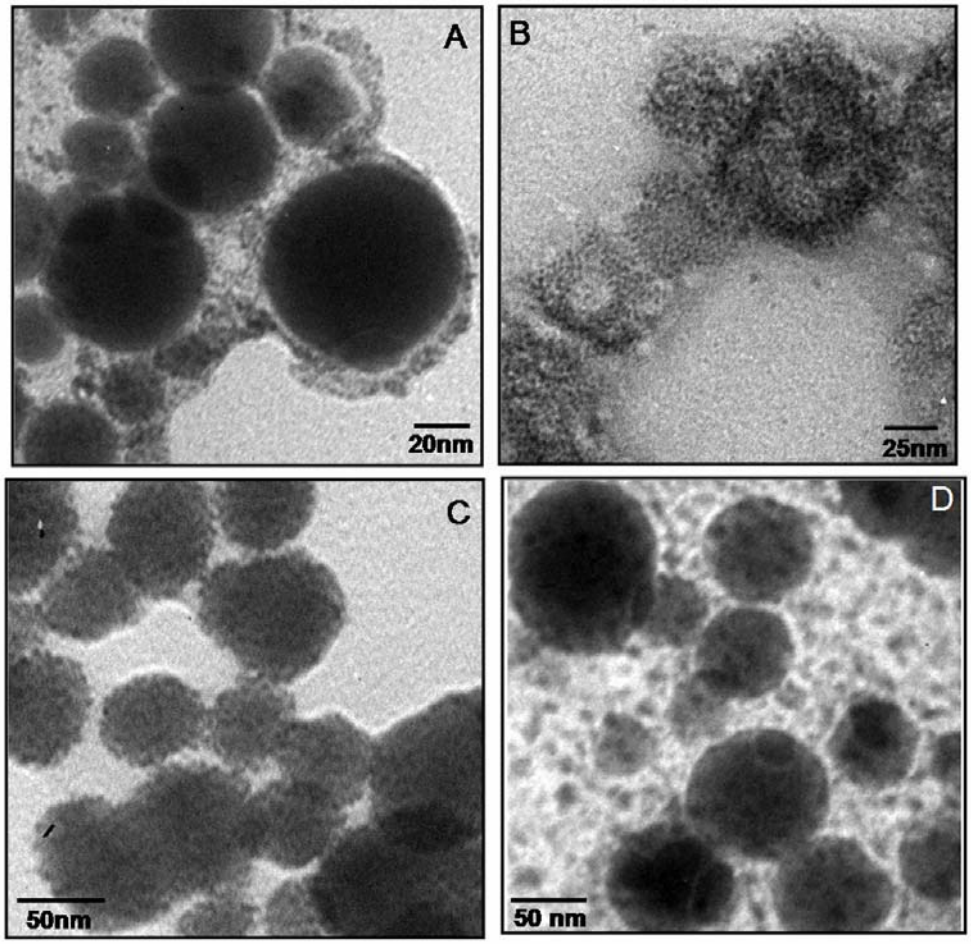

Figure 6.6 *Representative TEM images from four different regions of the carbon grid after the galvanic exchange reaction of aqueous Ni particles with aqueous 10 $^{-4}$ M H_2PtCl_6 at room temperature after t = 30 min. All the micrographs were recorded from the drop cast film from the aqueous solutions.*

The only problem area in the case of solution-based synthesis is that platinum nanoparticles are also formed in some places where Ni nanoparticles are not present (Figure 6.6 B). This may be due to the presence of dissolved $NaBH_4$ which is actually acting as reducing agent in this case. To avoid this uncontrolled reduction and in order to

know the mechanism of the galvanic exchange reaction we carried out the same reaction in constrained environment of the air-water interface. The beauty of conducting the reaction at the air water interface is that, the excess $NaBH_4$ (responsible for reduction of platinum in solution) is not phase transferred to the organic medium. Hence the system provides us with perfect controlled conditions where only Ni nanoparticles take part in the reaction responsible for the synthesis of the porous Pt nanoparticles, a rich candidate as a catalyst for hydrogenation reactions.

6.4 Transmetallation reaction at the air- water interface

The transmetallation reaction between hydrophobized nickel nanoparticles and aqueous chloroplatanic acid (H_2PtCl_6) was carried out at the air-water interface using a Nima model 611 LB trough (area 600 cm^2) equipped with a Wilhelmy plate as the surface-pressure sensor at room temperature. In a typical experiment, a Langmuir monolayer of hydrophobized Ni nanoparticles was formed by slowly spreading 150 μL solution of Ni nanoparticles capped by oleic acid and steric acid in chloroform (1 mg/mL concentration) on the surface of 10^{-4} M aqueous H_2PtCl_6 subphase in a drop wise fashion. At least 15 min was allowed for solvent evaporation, and the monolayer was compressed to a surface pressure of 15mN/m at a barrier speed of 20 cm^2/min. During the transmetallation reaction of the hydrophobized nickel nanoparticles with $PtCl_6^{2-}$ ions in the subphase, the nanoparticle monolayer were transferred onto carbon-coated copper grids at different time intervals by vertical dipping at a controlled surface pressure to 15 mN/m.

6.4.1 Transmission Electron Microscopy

Figure 6.7 (A-B) represents the TEM images recorded from the LB film lifted at t =10 min after initiation of the transmetallation reaction. The images show roughness on the surface as compared to the pristine oleic acid capped Ni nanoparticles and it is seen that the morphology of the particles has changed to some extent. The original smooth surface of Ni nanoparticles (Figure 6.5) is replaced by an assembly of very fine spherical Pt particles giving a rough look to surface. The Pt nanoparticles formed in the process are very small in size and roughly calculated to be 2-3 nm. From the images it is clearly seen

that the reaction at the air-water interface can provide a neat and controlled way of conducting the transmetallation reaction between sacrificial Ni and platinum ions, unlike in the case of transmetallation in solution. But the surface structure became clearly visible only under HRTEM, presented later in the study. Figure 6.7C corresponds to representative TEM images of the Langmuir monolayer lifted after 30 min of the start of the reaction. The TEM image shows that the formation of porous platinum nanoparticles is in progress.

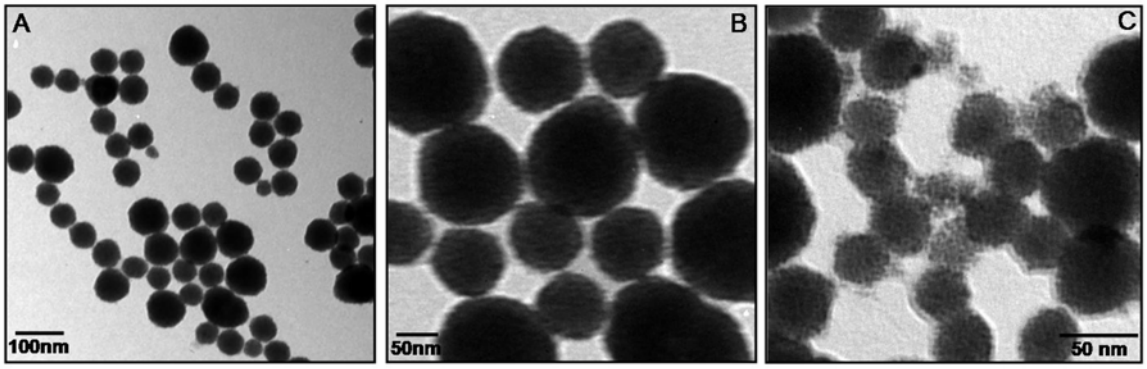

Figure 6.7 *Representative TEM image of one monolayer of hydrophobized Ni on aqueous 10^{-4} M H_2PtCl_6 at room temperature after (A)10 min of the start of the reaction. (B) A higher magnification image of the Ni nanoparticles. (C) After 30 min of the start of the transmetallation reaction. The grid was prepared by vertical dipping after compressing to 15mN/m*

Figure 6.8(A-D) corresponds to representative HRTEM image of the Langmuir monolayer lifted onto a grid by vertical dipping after regular interval of time during the transmetallation reaction between hydrophobized Ni nanoparticle monolayer with the aqueous 10^{-4} M H_2PtCl_6 in the subphase. The kinetics of the reaction was studied to perceive an idea regarding the mechanism of the reaction. The reaction was continued till the characterization showed that all the nickel was consumed. As can be seen, the structural details are more evident in the HRTEM images. At time t = 10 min, Fig 6.8A shows that the roughness that was mainly observed on the periphery under TEM is actually present all over the spherical structures indicating the reduction of platinum on to the surface of Ni nanoparticle. A hole-like feature is observed on every Ni nanoparticle and the concentration of Pt nanoparticles (indicated by white arrows) is more near the hole indicationg that probably this is the most active site through which the ions enter

into the sphere slowly after consuming the surface Ni atoms. The average size of smaller Pt nanoparticles was measured to be 2.2 ± 0.4 nm. In Figure 6.8A-C, these holes are clearly observed as black spots on the surfaces of the spherical nanoparticles (indicated by the arrows). A statistical analysis on many areas of the carbon-coated grid indicated that almost all the Ni spheres showed holes on their surfaces when viewed under TEM and STEM. The newly formed surface having holes represents the most active sites for further replacement reaction [38].

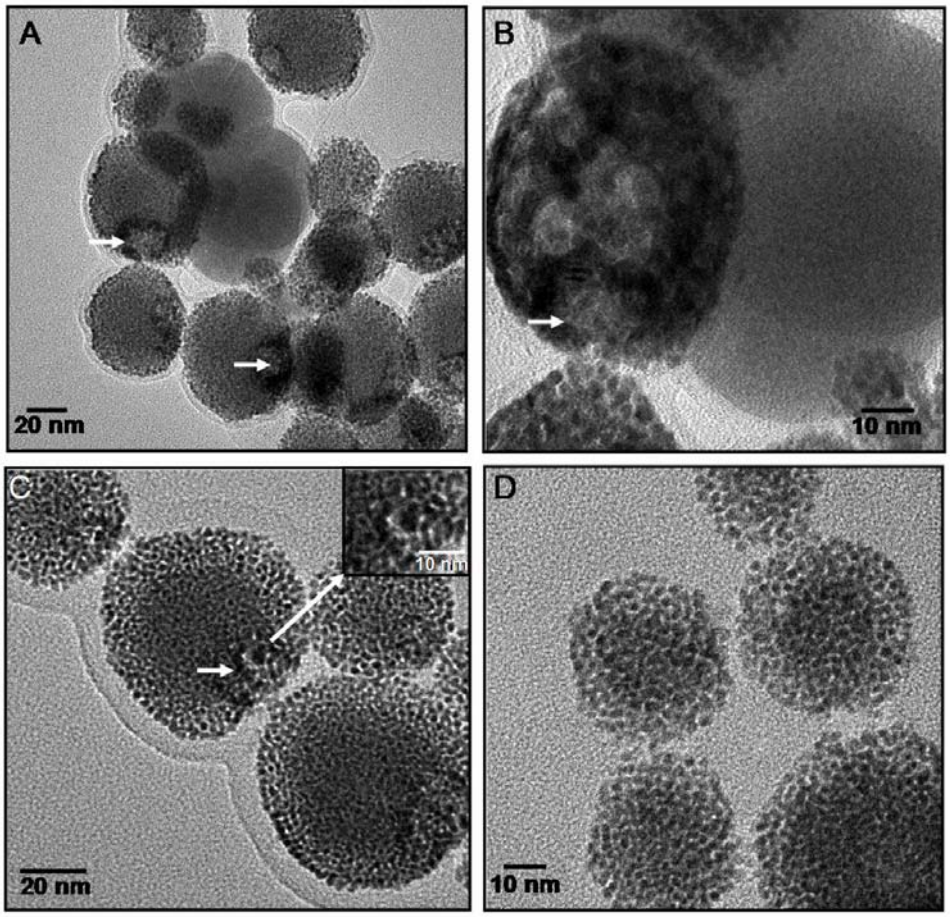

Figure 6.8 *HRTEM images taken from one monolayer thick sample of the film of hydrophobized Ni on 10^{-4} M H_2PtCl_6 after t =10 min (A, B), 30 min (C) and 45 min (D) of start of transmetallation reaction.*

The dimensions of each porous Pt nanoparticles exhibited no apparent change as compared to the diameter of Ni nanoparticles taken at the beginning of this reaction,

indicating that the outer layer of the Ni was being replaced by the small platinum nanoparticles in a thin shell like fashion. As the replacement reaction continues, the size of the holes becomes larger, (Figure 6.8C) which is evident in the grid obtained after t = 30 min. The coating of platinum gradually becomes thicker as more platinum atoms are generated from the replacement reaction. As the reaction continuous and the concentration of platinum increases, the size of each hole would start to shrink due to a combination of volume diffusion, surface diffusion, and/or dissolution and deposition [42] and eventually it disappears. At this stage, the shrinkage of the hole is dominated by a mass diffusion process thus producing a sphere with small Pt nanoparticles spread uniformly all over the spherical region [38 A]. The inset in Fig 6.8C gives the enlarged image of a hole, showing clearly the increase in the edge roughness of the hole. The formation of extruded structures towards the centre of the hole may be due to the mass diffusion process resulting in the shrinkage of the hole. As shown in Figure 6.8D, the opening on the surface of each sphere is negligible in area as compared to those shown in Figure 6.8A and ultimately they vanishes producing a porous sphere like structure comprising of small Pt nanoparticles (Figure 6.9A, B). The schematic depicting the possible approach of the platinum ion towards the defect sites and the plausible steps involved in the generation of porous Pt nanostructure is explained later (scheme 6.4).

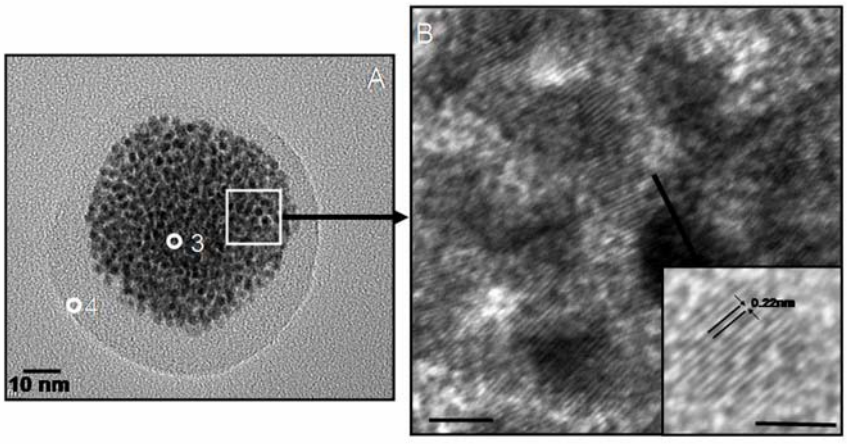

Figure 6.9 *HRTEM images taken from one monolayer thick sample of hydrophobized Ni on 10^{-4} M H_2PtCl_6 after t =45 min (A, B). (B is a HRTEM images of the region shown in A), it clearly shows the (111) planes of the Pt nanoparticles forming the porous nanoparticle. Both the scale bars in B are 2 nm.*

HRTEM images of the porous Pt nanoparticles, thus recorded after the completion of the transmetallation reaction are shown in Figure 6.9A and B. Figure 6.9 A depicts very clear complete porous Pt nanoparticles which results after 45 min of the reaction. The lighter shade surrounding the sphere is probably the organic capping of oleic acid and StA which is intact even after completion of the reaction. It was further analyzed by spot EDAX measurement and the results are presented later. A further magnified image shown in Figure 6.9B shows a group of Pt nanoparticles having the characteristic d-spacing value of fcc Pt crystals [43] and clearly revealing the crystal planes.

In yet another experiment when the concentration of the H_2PtCl_6 solution was increased, there appeared a void within each spherical nanoparticle resulting in the formation of nanoshells, as confirmed by the HRTEM image of one of the nanoshells, where the centre is lighter than the edges. Figure 6.10 shows the HRTEM image of the Ni-Pt nanoshell in one monolayer of vertically lifted Ni on 10^{-3} M of H_2PtCl_6 after 45 min of the reaction. It is worth noting that there are no holes on the surface of their nanoshells. Moreover, unlike the porous nanoparticles which are made up of small Pt nanoparticle, they are made up of platinum with not so rough surfaces. From the lattice measurement it is clearly indicated that the walls are made up of platinum showing the (111) lattice plane.

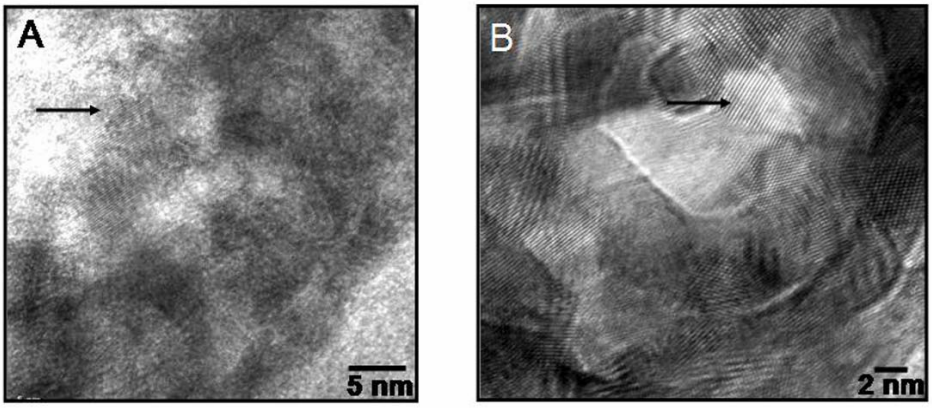

Figure 6.10 *(A) A nano Ni-Pt shell showing the presence of Ni in the centre (arrow marked) of the yet to be formed shell in one monolayer of vertically lifted Ni on 10^{-3}M of H_2PtCl_6 after 30 min of the reaction. (B) after 45 min of the reaction, perfectly formed shell of only Pt nanoparticles.*

The presence of Moiré fringes on the walls is an indication of presence of the lower wall of the nanoshell. The mean diameter of the shell was slightly increased as compared to that of the original nickel nanoparticles by measured using Gatan Micrograph software. This result indicated that the platinum atoms were deposited on the exterior surface of each nickel nanoparticles. The inner core of the shell is not empty in the initial stages of the reaction as indicated by the HRTEM images (black arrow, Figure 6.10A), and these lattices can be indexed to 0.20 nm, which corresponds to (111) hkl plane of Ni. As the reaction progresses the core is consumed and is also evident from the HRTEM image, which shows the formation of hollow Pt shell, Figure 6.10B, the lattice marked by arrow measuring 0.22 nm.

6.4.2 STEM studies.

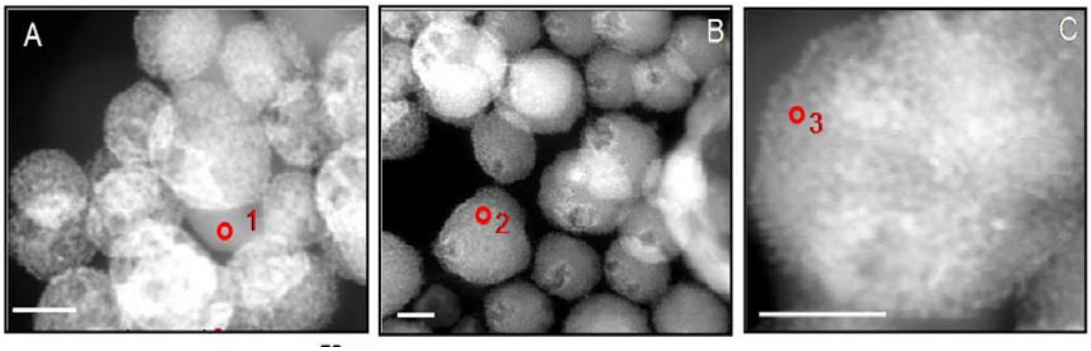

Figure 6.11 *(A)-(C) STEM images of the porous Ni-Pt and Pt nanoparticles after 10 min, 30 min and 45 min of the initiation of transmetallation reaction between hydrophobized Ni spread on aqueous 10^{-4} M H_2PtCl_6 subphase. The scale bar corresponds to 50 nm in all the images***.**

Figure 6.11(A-C) shows the STEM images of the nanoparticles taken at various stages of the reaction i.e. after t = 10 min (Figure 6.13A), t = 30 min (Figure 6.11B) and t = 45 min (Figure 6.11C). As STEM gives mainly the surface information, hence it serves as an excellent tool to characterize the change occurring on the surface of Ni nanoparticles as a result of the transmetallation reaction. Like the TEM images, STEM images also show the formation of hole on at least one site of each of the Ni nanoparticle in most of the cases. This is possibly because of the fact that when hydrophobized Ni nanoparticles are spread as a Langmuir monolayer on the subphase of platinum ion, the ion can access one particular side of Ni nanoparticles. It starts reacting at a site of surface

defect as also predicted by earlier reports [38]. Then it enters the spherical Ni slowly and consumes the entire particle forming porous nanostructures. The image in Figure 6.13A shows two kinds of surface morphologies, a smooth surfaced Ni and rough surfaced platinum. As explained in the case of HRTEM images, after about 30 in of the initiation of reaction, the holes on the surface seems to be bigger and there are structures extruding towards the inside of the sphere (fig 6.11B). Almost all the spherical nanoparticles at this stage have a open mouth like structure clearly visible. At the end of the reaction, i.e after approximately 45 min of the initiation of the reaction, we have a porous Pt nanoparticle without the presence of any hole on the surface (Fig 6.11C).

Basically the STEM images support the observation of TEM and also help to build up our hypothesis regarding the mechanism of the controlled transmetallation reaction at air-water interface.

6.4.3 EDAX studies

Compositional changes associated with the replacement reaction

Our proposition was also supported by a series of EDAX measurements, Fig 6.12A-B and 6.13A-B, shows the compositional change during the course of the reaction. Fig 6.12A represents the EDAX measurement spectrum corresponding to point 1 marked in Fig 6.11A, a place where a bare smooth Ni nanoparticle can be clearly observed. Likewise the spectrum displays strong peaks for only Ni. Fig 6.12B shows the spectrum corresponding to point 2 marked in the STEM image in Figure 6.11B. This can probably be considered as an intermediate stage of the transmetallation reaction where EDAX measurements also clearly shows the presence of both Ni and Pt elements. Figure 6.13A depicts the EDAX measurement from porous Pt nanoparticles (point 3, Figure 6.11C). This STEM image is recorded after 45 min of the initiation of the transmetallation reaction. The spectrum in Figure 6.13A demonstrates the peak of only Pt, indicating the completion of the reaction resulting in synthesis of porous Pt after consuming the sacrificial Ni nanoparticle.

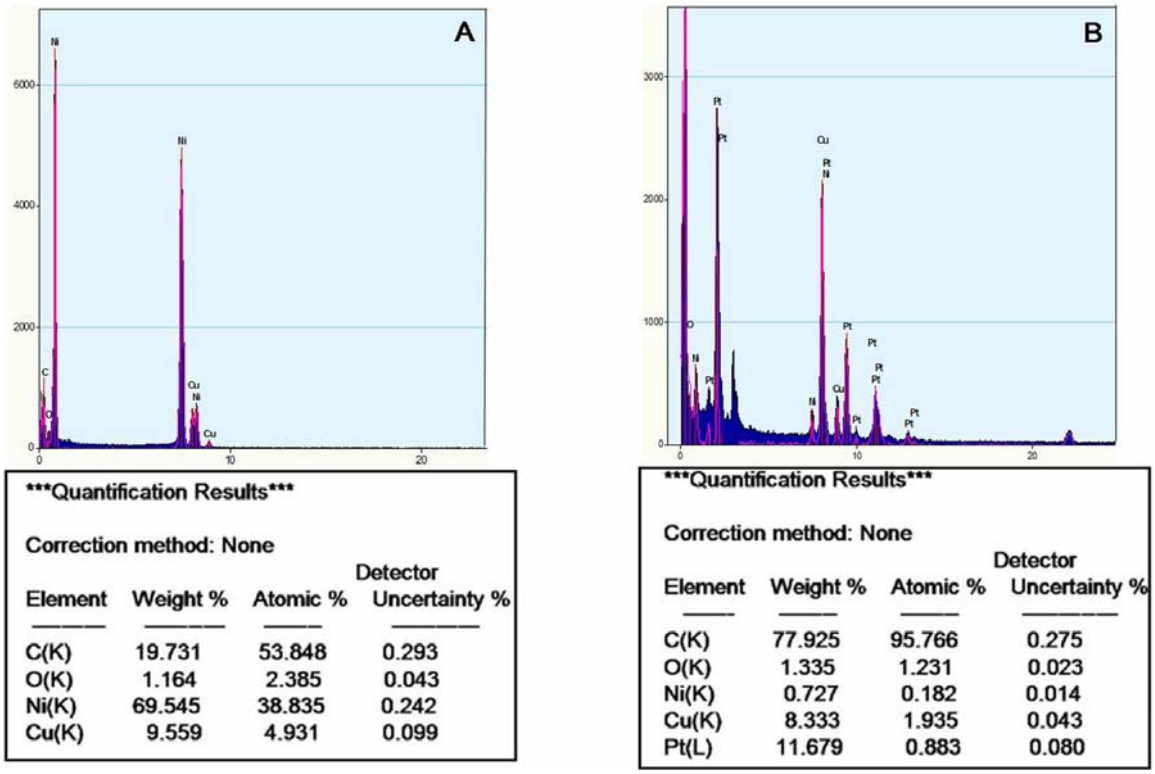

Figure 6.12 *(A) Spot EDAX spectrum of the pure Ni measured at point 1marked in Fig 6.11A. (B) spot EDAX spectrum measured at point 2 marked in Fig 6.11B, showing the presence of both Ni and Pt in one monolayer of hydrophobized Ni on aqueous 10^{-4} M H_2PtCl_6 subphase after 10 min of initiation of transmetallation reaction and their corresponding quantification results.*

The EDAX spectrum shown in Figure 6.13B was recorded from the lighter shaded structure surrounding the porous structure (Figure 6.9A). The elemental analysis here reveals that the layer contains only C and O. Thus it confirms the presence of the organic capping layer around the reduced porous Pt nanoparticles even after the completion of the transmetallation reaction, which becomes visible under the high resolution TEM. The presence of a peak of Cu in the EDAX is due to the fact that the samples were mounted on a Cu grid. All the readings were taken at a tilt angle of 20°, to ensure that almost all the x-rays reach the detector. A low background Beryllium holder was used for all the EDAX studies.

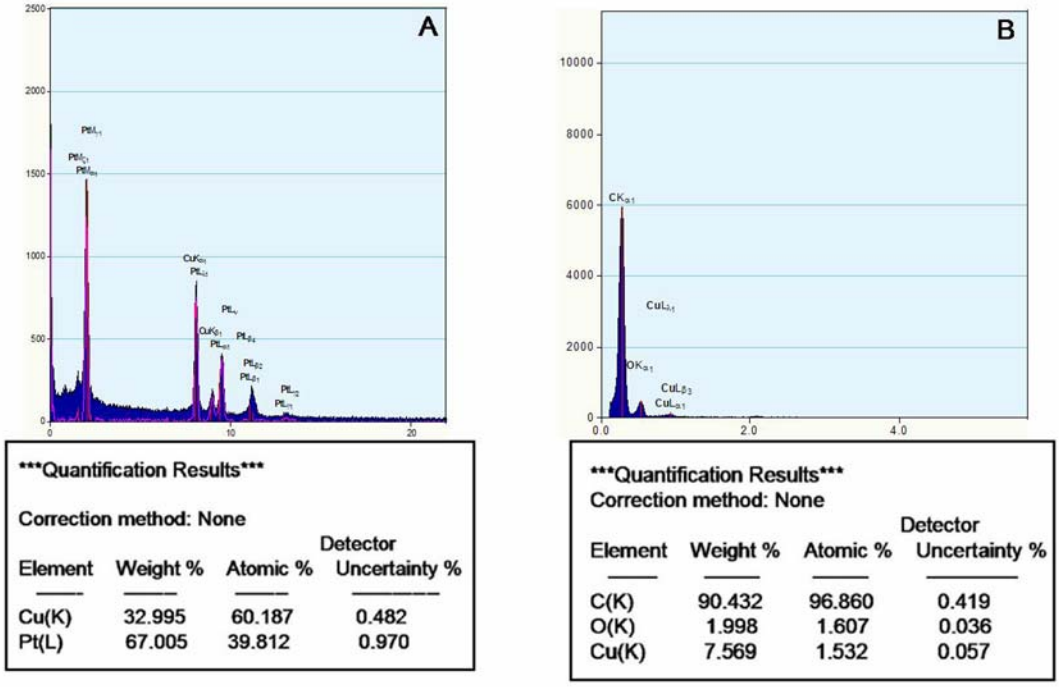

Quantification Results

Correction method: None

Element	Weight %	Atomic %	Detector Uncertainty %
Cu(K)	32.995	60.187	0.482
Pt(L)	67.005	39.812	0.970

Quantification Results

Correction method: None

Element	Weight %	Atomic %	Detector Uncertainty %
C(K)	90.432	96.860	0.419
O(K)	1.998	1.607	0.036
Cu(K)	7.569	1.532	0.057

Figure 6.13 *Spot EDAX (A) measured from point 3 in Fig 6.11C, showing only Pt after the transmetallation reaction between hydrophobized Ni monolayer of aqueous 10^{-4} M H_2PtCl_6 is over. (B) spot EDAX measured from point 4 marked in the Fig 6.9A, showing presence of only C and O in the outer coating their corresponding quantification details.*

6.5 The mechanism of reaction

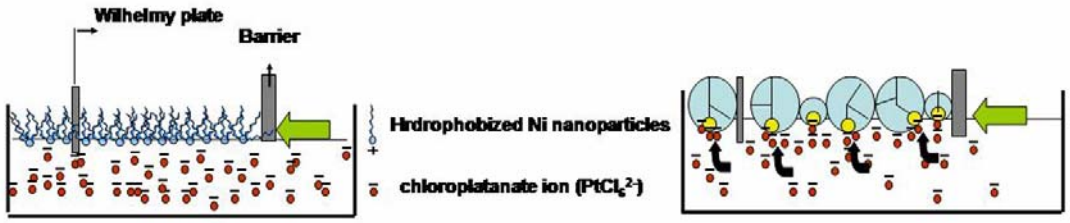

Scheme 6.3 *Schematic representation of the approach of platinum ions present in the subphase towards the Ni monolayer spread at the air-water interface (not to scale).*

With nickel nanoparticles as an example, the major steps involved in the galvanic replacement process that is performed at room temperature at the air water interface can be summarized as below. After the hydrophobized Ni monolayer has been spread on the 10^{-4}M H_2PtCl_6 subphase, the replacement reaction starts from the sites with relatively high surface energies (typical examples include steps, point defects, and stacking faults)

[38]. Scheme 6.3 shows the probable mode of reaction at the air water interface, where the defect sites facing the subphase are approached by the Pt ions from the subphase. Scheme 6.4 elucidates the various stages of the galvanic exchange reaction between sacrificial Ni nanoparticles and platinum ion during the formation of porous Pt nanoparticles. Once the reaction has started on the active site of each nanoparticle (A of Scheme 6.4 shows Ni with a surface defect, i.e the active site), the nickel will start to form Ni^{2+} and a hole is generated. The released electrons reduces Pt^{4+} into Pt atoms. The elemental platinum generated in the replacement reaction tends to deposit on the surface of each template because of a good matching between the crystalline structures (both nickel and platinum are face-centered cubic) and lattice constants (3.523 and 3.923 Å for nickel and platinum, respectively). The epitaxial deposition will lead to the formation of a thin, incomplete layer of platinum (B in Scheme 6.4), which can prevent the underlying nickel from reacting with H_2PtCl_6. As a result, the hole will continue to serve as an active site for subsequent reaction. At the same time, such an opening on the surface allows all the species (e.g., $PtCl_6^{2-}$, Ni^{2+}, Cl^-, and Pt) to continuously diffuse in and out of the hole. The dissolution of nickel transforms each nickel nanspheres into a structure characterized by a hollow interior, C of Scheme 6.4.

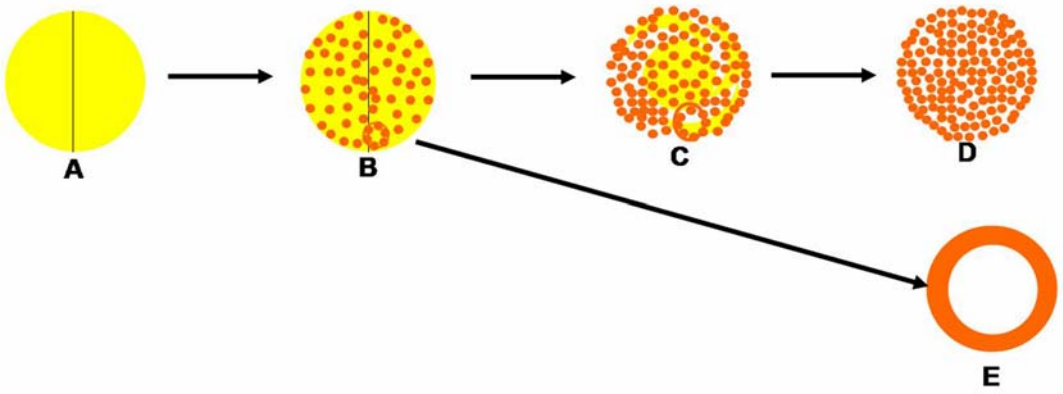

Scheme 6.4 *The schematic depicting the various stages of the galvanic exchange reaction between sacrificial Ni nanoparticles and platinum ions during the formation of porous Pt nanoparticles.*

The generated platinum atoms continue to grow on the outer surface of the template and gradually reduce the area of opening via various mass diffusion processes. When the

concentration of H_2PtCl_6 is high enough, the void size inside the template will be enlarged to its maximum size and the hole on its surface will disappear, leading to the formation of a porous spherical structure with uniform Pt nanoparticles, (D of Scheme 6.4). In yet another case, on increasing the concentration of the subphase Pt ions by 10 times, from 10^{-4} M to 10^{-3}M, we get a structure which resembles a hollow shell, (E of scheme in Scheme 6.4).

6.6 Catalytic activity

Hydrogenation of nitrobenzene to aniline

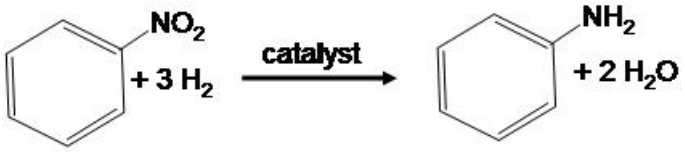

Nitrobenzene *Aniline*

The porous Pt nanoparticles could act as a catalyst for the hydrogenation of nitrobenzene to aniline. We evaluated their catalytic performance by studying the above mentioned reaction. The hydrogenation reactions were carried out in a 250 mL high-pressure stirred reactor supplied by Parr Instrument Company. The reactor was equipped with a heating arrangement, overhead stirrer, thermo-well, and pressure gauge as well as transducer, gas inlet, gas outlet, and sampling valve. The reactor has the provision to set temperatures and agitation speeds through controllers. In a typical hydrogenation reaction, a known amount of substrate was dissolved in solvent and the catalyst was charged into the reactor. The reactor was flushed thrice with nitrogen and then thrice with hydrogen. Hydrogen gas was introduced into the reactor to the desired pressure after setting the reaction temperature; the heater was put under slow stirring rate for uniform heat distribution. After attaining the desired temperature, the reaction was initiated by increasing the agitation speed to 550 rpm. The absorption of hydrogen gas due to reaction was monitored from the pressure drop in the reactor. The reaction was stopped when the gas absorption ceased. The reactor contents were cooled, and the liquid sample was analyzed on an Agilent 6890 Gas Chromatograph equipped with a HP-5 (5 % Dimethyl

polysiloxane, 60 m length, 0.25 mm internal diameter, 0.25 um film thickness) with flame ionization detector.

The concentration of the reactants used for the reaction were **Nitrobenzene** 2 g (0.0193 mol); **Catalyst** 10 mL (0.5 x 10^{-6} mol Pt); **Methnol** 50 ml; **H_2** pressure 400 psi; ***Ni** concentration 10^{-3}M.

*Reaction charge-

- Nitobenzene –2 gm
- Catalyst - 10 ml
- Methanol-50 ml
- RPM- 550 rpm

TOF = No of moles of aniline formed per mol of Pt in one hour.

The results in Table 6.1 clearly show remarkable increase in the catalytic activity of porous Pt compared to activity of pristine Ni nanoparticles for nitrobenzene hydrogenation to aniline. At a very low catalyst loading, very high turn over frequency (65041 h^{-1}) is obtained at 100 ºC and 400 psi hydrogen pressure.

	Catalyst	Time h	Temp ºC	Nitrobenzene Conversion, %	Aniline Selectivity, %	TOF,# h^{-1}
NHN-1	Ni*	3	100	30	100	10
NHN-2	Ni-Pt	0.5	100	100	100	65041
NHN-3	Ni-Pt	2	60	100	100	16260

Table 6.1 *Table showing the results of the nitrobenzene hydrogenation using Ni and porous Pt-Ni nanoparticles.*

In earlier cases Pt nanoparticles synthesized by borohydride reduction and immobilized on amine functionalized zeolite as well as Pt supported on carbon has been tested for hydrogenation at 100 ºC and 500 psi H_2 pressure by Sastry el al [44a]. The TOF obtained for nitrobenzene hydrogenation with our catalyst is almost four times that of Pt nanoparticles immobilized on zeolite (17538) or Pt/C (14837 h^{-1}), which clearly indicates

a very high catalytic activity of porous Pt nanoparticle prepared by transmetallation of nickle nanoparticles with aqueous platinum ions . In several other reports by various groups on the catalytic activity of Pt in hydrogenation reactions the activity reported has never been so effective. Bhaduri et al [44b] have used MCM-41 supported Pt-carbonyl cluster for hydrogenation of nitrobenzene at room temperature, at higher H_2 pressure (735 psi) and the TOF obtained is 42000 h^{-1}. Scelza et al [44c] have also carried out nitrobenzene hydrogenation using Pt (1 wt%) supported on purified activated carbon felt (ACF) at 25 ºC and atmospheric pressure of H_2, however the TOF obtained for hydrogenated notrobenzene is very low (~ 1170 h^{-1}) in this case. Yao et al have used carbon nanotubes supported Pt (1 and 3 %) for hydrogenation of nitrobenzene to aniline at ambient temperature and atmospheric pressure in alcohol solvent with TOF in the range of 570 - 860 h^{-1} [44 d]. This clearly indicates high catalytic activity of porous Pt nanoparticles prepared by transmetallation compared to Pt catalysts prepared by other methods reported in the literature. This may be because of the presence of higher effective surface area of the catalyst. The catalyst could be easily recovered from the reaction mixture and was further tested to find the recycling ability. In the second round, the catalyst was found to lose the activity.

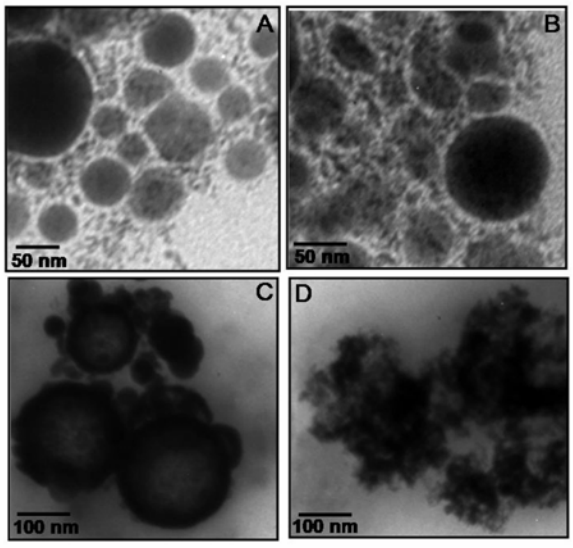

Figure 6.14 *Representative TEM images of the Pt nanoparticles (catalyst), before (A-B) and after (C-D) the hydrogenation reaction of nitrobenzene to aniline. All the micrographs were recorded from the drop cast film from the aqueous solutions after the transmetallation reaction.*

TEM was done to find out the changes in the morphologies responsible for the inactivity of the catalyst in the second cycle. Presented below are the TEM images (Figure 6.14) of the catalyst before (A-B) and after (C-D) the hydrogenation reaction. It is clear from the images that after the reaction of conversion of nitrobenzene to aniline, where the Pt nanoparticles were used as catalyst, there is a aggregation of the nanoparticles. This aggregation results in the reduction of the surface area which might be leading to the further inactivity of the catalyst.

6.6 Conclusion

In conclusion, we have shown a facile transmetallation reaction between hydrophobic nickel nanoparticles and aqueous platinum ions that led to the formation of porous Pt nanoparticles, which has shown excellent catalytic activity for hydrogenation reactions. These porous nanoparticles can be simply prepared at room temperature in a homogeneous solution with Ni nanoparticles as sacrificial templates. The method presented herein is cost effective. These porous Pt nanoparticles have a higher surface area and therefore exhibit enhanced catalytic performance. Thus these synthesized metallic hollow nanoparticles could be useful in industrial applications including catalytic nanoreactors. Same reaction when carried out at the air-water interface leads to nanoparticles assembled into linear structures and thereafter each of the spherical Ni nanoparticle initiates assembly of the small platinum nanoparticles giving rise to a structure like porous spheres. An attempt has been made to predict the plausible mechanism of the reaction based on the observations at every stage of the reaction. The rate of the reaction of subphase platinum ions with the hydrophobized nickel nanoparticles monolayer may further be modulated by positioning a suitable layer of organic molecule that can act as barrier between the nanoparticles and the subphase. Since the reaction involves platinum ions, an electrostatic barrier comprised of an ionizable lipid monolayer would be an excellent candidate and may generate new structures as obtained in the case of transmetallation reaction between gold and silver ions at air water interface [45].

References

(1) Schon, G.; Simon, U. *Colloid Polym. Sci.* **1995**, *273*, 202.

(2) Thomas, J. M. *Pure Appl. Chem.*, **1988**, *60*, 1517.

(3) Park, S. J.; Lazarides, A. A.; Mirkin, C. A.; Brazis, P. W.; Kannewurf ,C. R.; Letsinger, C. R. *Angew. Chem., Int. Ed.*, **2000**, *39*, 3845.

(4) Hirai, H.; Wakabayashi, H.; Komiyama, M. *Chem. Lett.*, **1983**, 1047.

(5) (a) Jin, R.; Cao, Y.; Mirkin, C. A.; Kelly, K. L.; Schatz G. C.; Zheng, J. G. *Science,* **2001***, 294*, 1901.(b) Shankar, S. S.; Rai, A.; Ankamwar, B.; Singh, A.; Ahmad, A.; Sastry, M. *Nat. Mater.,* **2004***, 3*, 482. (c) Jana, N. R.; Gearheart, L.; Murphy, C. J. *Adv. Mater.* **2001***, 13*, 1389. (d) Sun, Y.; Mayers, B.; Herricks, T.; Xia, Y. Nano Lett. 2003, 3, 955. (e) Caswell, K. K.; Bender, C. M.; Murphy, C. J. *Nano Lett., **2003**, 3*, 667. (f) Sun, Y.; Xia, Y. *Analyst,* **2003***, 128*, 686 (g) Maier, S. A., Brongersma, M. A.; Kik, P. G.; Meltzer, S., Requicha, A. A. G.; Atwater, H. A. *Adv.Mater***. 2001***, 13*, 1501. (h) Sun, Y.; Xia, Y. *Science,* **2002***, 298*, 2176.

(6) (a) Ahmadi, T. S.; Wang, Z. L.; Green, T. C.; Henglein, A.; El-sayed, M. A.; *Science*, **1996**, *272*, 1924.

(7) Philip Ball "*Made to Measure-New Materials for the 21st Century", Chapter 7*, Tunnel Vision, Porous Materials Princeton University Press, Princeton**, 1997**.

(8) (a) Lvov, Y.; Antipov, A. A.; Mamedov, A.; Mohwald, H.; Sukhorukov, G. B. *Nano Lett.* **2001**, *1*, 125. (b) Toprak, M.; Kim D. K.; Mikhailova1, M.; Zhang1, Y.; Jeong, Y. K.; Muhammed, M. *Mat.Res.Soc.Symp.Proc*. **2002**, *704*, W 6.29.1.

(9) S-Illia, G. J. A. A.; Sanchez, C.; Lebeau, B.; Patarin, *J. Chem. Rev.* **2002***, 102*, 4093.

(10) (a) Sun, L.; Crookes, R. M.; Chechik, V. *Chem. Comm.* **2001**, 359. (b) Marinakos, S. M.; Novak, J. P.; Brousseau, L. C.; House, A. B.; Edeki, E. M.; Feldhaus, J. C.; Feldheim, D. L. *J. Am. Chem. Soc*. **1999**, *121*, 8518.

(11) (a) Liang, Z.; Susha, A.; Caruso, F. *Chem. Mater.* **2003***, 15*, 3176. (b) Bansal, V.; Sanyal, A.; Rautaray, D.; Ahmad, A.; Sastry, M. *Adv. Mater.* **2005***, 17*, 889. (c) Caruso, F.; Caruso, R.A.; Mohwald, H. *Science* **1998***, 282*, 1111. (d) Zhong, Z.; Yin,

Y.; Gates, B.; Xia, Y. *Adv. Mater*. **2000**, *12*, 206. (e) Yin, Y.; Lu, Y.; Gates, B.; Xia, Y. *Chem. Mater.* **2001**, *13*, 1146.

(12) Sun, Y.; Xia, Y. *Anal. Chem*., **2002,** *74*, 5297.

(13) (a) Oldenburg, S. J.; Averitt, R. D.; Westcott, S. L.; Halas, N. *J. Chem. Phys. Lett*., **1998**, *288*, 243. (b) Halas, N. J. *The optical properties of nanoshells Optics and Photonics news*, **2002** August, 26.

(14) Shukla, S.; Priscilla, A.; Banerjee, M.; Bhonde, R.R.; Ghatak, J.; Satyam, P.V.; Sastry, M. *Chem. Mater*. **2005**, *17*, 5000.

(15) Hirsch, L. R.; Stafford, R. J.; Bankson, J. A.; Sershen, S. R.; Rivera, B.; Price, R. E.; Hazle, J. D.; Halas, N. J.; West, J. L. *Proc. Natl. Acad. Sci*. **2003**, *100,* 13549.

(16) Sastry, M.; Rao, M.; Ganesh, K.N. *Acc. Chem. Res*. **2002**, *35*, 847.

(17) (a) Brongersma, M. L. Nanoshells: *Nat. Mater*. **2003**, *2*, 296. (b) Chen, J.; Saeki, F.; Wiley, B. J.; Cang, H.; Cobb, M.J.; Li, Z-Y.; Au, L.; Zhang, H.; Kimmey, M. B.; Li, X.; Xia, Y. *Nano Lett*., **2005**, *5*, 473.

(18) Crooks, R. M.; Zhao, M.; Sun, L.; Chechik ,V.; Yeung, L. K. *Acc. Chem. Res.*, **2001**, *34*, 181.

(19) Alvarez, J.; Liu, J.; Kaifer, A. E.; *Chem. Commun.*, **2000**, 1151.

(20) (a) Zhao, M.; Crooks, R. M. *Angew. Chem., Int. Ed.* **1999**, *38*, 364.

(21) Reetz, M. T.; Westermann, E. *Angew. Chem., Int. Ed*. **2000**, *39*, 165. Li ,Y.; El-Sayed, M. A. *J. Phys. Chem. B* **2001**, *105*, 8938. (c) Reetz, M. T.; Lohmer, G. *Chem. Commun*. **1996**, 1921. (d) Reetz, M. T.; Lohmer, G.; Schwickardi, R. *Angew. Chem., Int. Ed*. **1998**, *37*, 481. (e) Klingelho ¨fer, S.; Heitz, W.; Greiner, A.; Oestreich, S.; Fo¨rster, S.; Antonietti, M. *J. Am. Chem. Soc*. **1997**, *119*, 10116.

(22) Bell, A. T. Science, **2003**, *299*, 1688. (b) Rolison, D. R. Science, **2003**, *299*, 1698.

(23) Jackson, J. B.; Halas, N. J.; *J. Phys. Chem. B*, **2001**, 105, 2743

(24) Kim, S-W. ; Kim, M.; Lee , W- Y. ; Hyeon, T. *J. Am. Chem. Soc.*, **2002**,*124*, 7642.

(25) Phadtare, S.; Kumar, A.; Vinod, V. P.; Dash, C. V; Palaskar, D. V.; Rao, M.; Shukla, P. G.; Sivaram, S.; Sastry, M. Chem. Mater. **2003**, *15*, 1944.

(26) (a) Lu, L.; Sun, G.; Xi, S.; Wang, H.; Zhang, H. A Langmuir **2003**, *19,* 3074. (b) Zhang, H.; Hussain, I.; Brust, M.; Cooper, A.I. Adv.Mater. **2004**, *16*, 27.

(27) (a) Sun, Y.; Mayers, B.; Xia, Y. Adv. Mater. **2003**, *15*, 641. (b) Metraux, G. S.; Cao, Y. C.; Jin, R.; Mirkin, C. A. Nano Lett. **2003**, *3*, 519.

(28) (a) Liang, H. -P.; Guo, Y. G.; Zhang, H. M.; Hu, J. -S.; Wan, L. -J.; Bai, C. -L. Chem. Commun. **200**4, 1496. (b) Liang, H. P.; Wan, L. J.; Bai, C. L.; Jiang, L. J. Phys. Chem. B **2005**, *109*, 7795.

(29) Yin, Y.; Rioux, R. M.; Erdonmez, C. K.; Hughes, S.; Somorjai, G. A.; Alivisatos, A. P. Science, **2004**, *304*, 711.

(30) Selvakannan, P. R.; Sastry, M. *Chem. Commun.* **2005**, 1684

(31) Shukla, S.; Priscilla, A.; Banerjee, M,; Bhonde, R.R.; Ghatak, J.; Satyam P.V.; Sastry, M.; *Chem. Mater.* **2005**, *17,* 5000

(32) Liang, H-P.; Zhang, H-M.; Hu,J-S.; Guo,Y-G.; Wan, L-J.; Bai, C-L.; *Angew. Chem. Int. Ed*. **2004**, *43*, 1540

(33) Sun, Y.; Xia, Y. *J. Am. Chem. Soc*. **2004**, *126*, 3892.

(34) Jin, Y.; Dong, S. *Angew. Chem. Int. Ed*. **2002**, *41*, No. 6

(35) Bala, T.; Joshi, B.; Iyer, N.; Sastry, M.; Prasad, B.L.V. *Journal of Nanoscience and Nanotechnology,* **2006**, *6*, 3736.

(36) Creighton, J.A.; Eadon, D.G. *J. Chem. Soc., Faraday Trans.* **1991**, *87*, 3881.

(37) N.W u, N.; Fu, L.; Su, M.; Aslam, M.; W ong, K.C.; Dravid, V.P. *NanoLett.* **2004***, 4*, 383.

(38) (a) Wang, Z.L.; Ahmad, T.S.; E1-Sayed, M.A. *Surface Science,* **1997**, *380,* 302 (b) Gai, P. L.; Harmer, M.A. *Nano Lett.,* **2002,** *2*, 771,

(39) PCPDF file no.04-0850 CAS no.7440-02-0, Space group Fm3m with cell parameter *a* = 0_3523 nm.

(40) Kiely, C.J.; Fink, J.; Zheng, J.G.; Brust, M.; Bethell, D.; Schiffrin, D.J.*Adv. Mater.* **200**0, *12*, 640.

(41) Kiely , C.J.; Fink, J.; Brust, M.; Bethell, D.; Schiffrin, D.J. *Nature* **1998**, *396*, , 444.

(42) (a) Donath, E.; Sukhorukov, G. B.; Caruso, F.; Davis, S. A.; Mo¨hwald, H. *Angew. Chem., Int. Ed*. **1998**, *37*, 2202. (b) Mandal, T. K.; Fleming, M. S.; Walt, D. R. *Chem. Mater*. **2000**, *12*, 3481.

(43) Swanson, Tatge, Natl. Bur. Stand. (U.S.), Circ. 539, **1953**,1, 31

(44) Mandal, S.; Roy, D.; Chaudhari, R.V.; Sastry, M. *Chem. Mater*. **2004**, *16*, 3714. Basu, S.; Mapa, M.; Gopinath, C.S.; Doble, M.; Bhaduri, S.; Lahiri, G.K. *J. Catal*. **2006**, *239,* 154 (c) Vilella, M.J.; de Miguel, S.R.; Scelza, O.A. *Chemical Engineering Journal*, **2005**, *114*, 11433. (d) Li, C.-H.; Yu, Z. –X.; Yao, K.-F.; Ji, S. –F.; Lian,J. J. Mol. Catal. A, **2005**, *226*, 101.

(45) Pasricha, R.; Swami, A.; Sastry, M. *J. Phys. Chem. B.* **2005**, *109,* 19620

Chapter VII

Conclusion

Satisfaction lies in the effort, not in the attainment, full effort is full victory. (Mahatma Gandhi)

The salient features of the work detailed in the thesis and possible avenues for future work are briefly discussed.

Summary of the work

Synthesis of nanomaterials with fascinating optical and electronic properties is the result of an interdisciplinary effort of various researchers. Colloidal metal nanoparticles especially gold and silver are of importance as they are biocompatible and had been used in a variety of applications ranging from drug delivery [1], anti bacterial-agents [2] to catalysis [3]. The properties of nanomaterials can be largely altered by tuning the shape and size of the nanoparticles [4], hence there has been much of interest in the synthesis of 2D, 1D and anisotropic nanostructures like nanowires, nanorods, nanotriangles, nanosheets, nanofibres and so on. The use of air-water interface for the two dimensional (2D) assembly of hydrophobized nanoparticles and synthesis of anisotropic nanostructures is the objective of this thesis. Various aspects have been covered in the process of the study.

It has been shown that presence of a lipid monolayer reduces the surface tension of aqueous subphase resulting in long range assembly of metal nanoparticles at the air water interface. We have further shown the effect of deposition pressure, nature of lipid monolayer and solvent in controlling the long range ordering at the air water interface. After the study we could conclude that only when the interactions between particles are strong enough and there is sufficient time for assembly, a perfect monolayer is formed.

Among all the interactions that drive self assembly, the use of electrostatic interactions for multilayer formation is very attractive. It has been shown that colloidal gold particles can be incorporated in ODA films by simple spreading of the organic films on the colloidal solution containing nanoparticles having a net charge. Moreover in addition to the shape (nanoscale curvature) of the colloidal particle surface, the chemical nature of the colloidal particle also plays an important role in the electrostatic binding at the air water interface.

The transmetallation reaction between a sacrificial nanoparticle and more noble metal ions in solution has emerged as a novel method for creating unique hollow and bimetallic nanostructures. In our report we have exploited the built in anisotropy of air-water interface and coupled it with the transmetallation reaction for the synthesis of

nanostructures having interesting morphologies. It has been further shown that the transmetallation reaction can be modulated by the insertion of an electrostatic barrier in the form of an ionizable lipid monolayer between the silver nanoparticles and the aqueous gold ions that impacts the gold nanoparticle assembly. The same reaction has been carried out at the liquid-liquid interface , taking advantage of the close packing of the silver nanoparticles at the interface for the synthesis of interconnected bimetallic nanoribbons. The electrical and sensor properties of films composed of silver nanoparticles (Ag-NPs) and the bimetallic film which has been synthesized as the result of the core metal galvanic exchange reaction were compared to investigate the effect of the morphology and assembly of the nanoparticles on the electronic and gas sensing properties of nanostructures. Transmetallation reaction between silver nanoparticles and gold ions has also been carried out in solution, in the presence of halide ions. We have highlighted the crucial role of halide ions on the evolution of the different morphologies of gold nanostructures. Cl^- ions are known to form an ordered layer on the (111) lattice plane of gold and thus have a greater probability of passivating (111) face [5]. Further the Br^- and I^- ions can replace the adsorbed Cl^- ions. Based on these arguments it has been demonstrated that Br^- and I^- ions, having better ability to bind with gold surface. Thus the presence of Br^- favors the formation of thin shells in solution which are not possible in the presence of other halide ions and the presence of I^- ions promotes the formation of interconnected aggregated structures .

A time dependent systematic study using transmetallation between sacrificial hydrophobic nickel nanoparticles assembled and constrained at the air-water interface and aqueous subphase containing platinum ions ($PtCl_6^{2-}$) has been carried out enabling us to detail the morphological, structural and compositional, changes involved in such a heterogeneous reaction on nanoscale at room temperature. The reaction resulted in the synthesis of catalytically active porous platinum nanoparticles.

Scope for future work

The presence of hydrocarbon bed at the air-water interface results in synthesis of 2D assemblies of nanoparticles. The effect of mixture of anionic and cationic lipids in

varying ratios on the assembly of the nanoparticles at the air water interface will be worth noticing. We saw the sintering of nanoparticles of a particular size, in a pattern on increase of surface pressure at the air-water interface in case of Au-ODA in chloroform, spread on hydrocarbon bed. This raises the possibility that the size-dependence of particle stability might be exploited for nanopatterning.

To use the electrostatic interaction between the lipid monolayer and the nanoparticles as a successful separation technique, experiments with organic molecules which can bind to glass beads and have a free positive charge to bind to the negatively charged nanoparticles need to be taken up.

The interconnected nanostructures formed at the liquid-liquid interface after the galvanic exchange reaction and the ones formed at the air water interface could be further taken up HRTEM studies to investigate the direction of growth and the compositional mapping of the both. This will give an insight on the growth pattern of the nanostructures at two different interfaces.

The rate of the reaction of subphase platinum ions with the hydrophobized nickel nanoparticles monolayer may further be modulated by positioning a suitable layer of organic molecule that can act as barrier between the nanoparticles and the subphase. This may result in the synthesis of nanostructures with interesting morphologies and better catalytic properties. Galvanic exchange between the nickel nanoparticles and gold ions can also be taken up at the air water interface and the resultant assembly can be studied for the change in magnetic properties in addition to catalytic properties.

Reference

(1) Paciotti, G.; Myer, L.; Weinreich, D.; Goia, D.; Pavel, N; Maclaughlin, R.; Tamarkin, L. *Drug Delivery*, **2004**, *11*, 169.

(2) Lee, H. J.; Yeo, S. Y.; Jeong, S. H. *J. Mater. Sc*., **2003,** *38*, 2199.

(3) (a) Hirai, H.; Wakabayashi, H.; Komiyama, M. *Chem. Lett*., **1983**, 1047. (b) Ahmadi, T. S.; Wang, Z. L.; Green, T. C.; Henglein, A.; El-sayed, M. A.; *Science*, **1996**, *272*, 1924.

(4) Jin, R.; Cao, Y.; Mirkin, C. A.; Kelly, K. L.; Schatz G. C.; Zheng, J. G. *Science*, **2001**, *294*, 1901.(b) Shankar, S. S.; Rai, A.; Ankamwar, B.; Singh, A.; Ahmad, A.; Sastry, M. *Nat. Mater.*, **2004**, *3*, 482. (c) Jana, N. R.; Gearheart, L.; Murphy, C. J. *Adv. Mater*. **2001**, *13*, 1389. (d) Sun, Y.; Mayers, B.; Herricks, T.; Xia, Y. Nano Lett. **2003**, *3*, 955. (e) Caswell, K. K.; Bender, C. M.; Murphy, C. J. *Nano Lett*., **2003**, *3*, 667. (f) Sun, Y.; Xia, Y. *Analyst*, **2003**, *128*, 686

(5) Gao, P. Weaver, M. J. *J. Phys. Chem.*, **1986**, *90*, 4057.

LIST OF PUBLICATIONS

1. Transmetallation reaction between hydrophobic silver nanoparticles and aqueous chloroaurate ions at the air-water interface, **Pasricha, R**.; Swami, A.; Sastry, M. *J. Phys. Chem. B.* **2005**, *109,* 19620.
2. Shape and size selective separation of gold nanoclusters by competitive complexation with octadecylamine monolayer at the Air-Water Interface, **Pasricha, R**.; Singh A.; Sastry, M. *J. Colloid Interface Sci.*, Communicated, **2007.**
3. Controlling the assembly of hydrophobized gold nanoparticles at the air-water interface by varying the interfacial tension, **Pasricha, R**.; Swami, A.; Sastry, M. *J. Nanosci. Nanotech.*, Communicated, **2007.**
4. Synthesis of Ag-Au bimetallic film at liquid–liquid interface and its application in vapor sensing, **Pasricha, R**.; Singh A.; Sastry, M. Communicated, **2007.**
5. Synthesis of catalytically active porous platinum nanospheres by transmetallation reaction and proposition of the mechanism **Pasricha, R**.; Bala, T.; Sastry, M. *Small*, Communicated, **2007**.